

2013

Time and temperature dependence of viscoelastic stress relaxation in Au and Au alloy thin films

Kittisun Mongkolsuttirat
Lehigh University

Follow this and additional works at: <http://preserve.lehigh.edu/etd>

Recommended Citation

Mongkolsuttirat, Kittisun, "Time and temperature dependence of viscoelastic stress relaxation in Au and Au alloy thin films" (2013). *Theses and Dissertations*. Paper 1371.

This Dissertation is brought to you for free and open access by Lehigh Preserve. It has been accepted for inclusion in Theses and Dissertations by an authorized administrator of Lehigh Preserve. For more information, please contact preserve@lehigh.edu.

**Time and Temperature Dependence of
Viscoelastic Stress Relaxation in Au and Au
Alloy Thin Films**

By

Kittisun Mongkolsuttirat

Presented to the Graduate and Research Committee

of Lehigh University

in Candidacy for the Degree of

Doctor of Philosophy

in

Mechanical Engineering

Lehigh University

January 2013

Approved and recommended for acceptance as a dissertation in partial fulfillment of the requirements for the degree of Doctor of Philosophy.

Date

Accepted Date

Dissertation Advisor,
Prof. Richard P. Vinci

Committee Members:

Prof. Walter L. Brown

Prof. John P. Coulter

Prof. Terry L. Delph

Prof. Herman F. Nied

ACKNOWLEDGEMENTS

First and foremost, I would like to express my sincere appreciation to my advisor, Prof. Richard P. Vinci, to whom I am indebted for his time and valuable guidance from my Master degree throughout the Ph.D. program. Thank you for giving me the motivation, positive thinking and enthusiasm about my research. I am very pleased and honored to have the opportunity to work with him. I would also like to express my gratitude to Prof. Walter L. Brown for providing me with his valuable advices and constant supervision on the research. It is also my great pleasure to work with him who has remarkable amount of knowledge and expertise in bulge system. Thanks for his assistance and constructive suggestion with all types of technical problems. I would also like to express my special thanks for a great day I had on Thanksgiving with him and his family. Thank you very much for the hospitality. I am also grateful to both Professors for their time and effort spending on my dissertation writing.

I would also like to especially thank the other members of my research committee: Prof. John P. Coulter, Prof. Terry L. Delph, and Prof. Herman F. Nied - for their time and critical evaluation regarding my research.

I would also like to thank to my colleagues for helpful comments and support on this work. Special thanks to Jeffrey M. Biser for teaching and helping me how to operate sputtering deposition, and Mark J. McLean for teaching me how to use the bulge experiment. I am also grateful for the assistance and friendship of the faculty

staff who work in Mechanical and Material science department. Thanks to many lovely friends of Thai student society at Lehigh University for many activities and wonderful relationship during I stay here at Lehigh.

I wish to thank the Royal Thai Government for funding during studying here. In addition, this work was supported in part by the Defense Advanced Research Projects Agency (DARPA) N/MEMS S&T Fundamentals program under grant no. N66001-10-1-4006 issued by the Space and Naval Warfare Systems Center Pacific (SPAWAR).

Finally, I owe to my deep gratitude to my parents, my brother, and my sister for their unconditional support and endless encouragement throughout my life.

TABLE OF CONTENTS

| | |
|---|----|
| List of Tables..... | ix |
| List of Figures..... | xi |
| Abstract..... | 1 |
| 1. Introduction..... | 4 |
| 1.1 Background information..... | 4 |
| 1.2 Thin film fabrication and mechanical properties..... | 6 |
| 1.2.1 Thin film deposition methods..... | 6 |
| - Sputter deposition..... | 6 |
| - Cosputter deposition..... | 8 |
| - Reactive sputter deposition..... | 10 |
| 1.2.2 Thin film mechanical properties..... | 11 |
| - Solid solution strengthening..... | 12 |
| - Oxide dispersion strengthening..... | 16 |
| - Grain-size strengthening..... | 17 |
| 1.3 RF MEMS capacitive switch..... | 20 |
| 1.3.1 Switch design and operation..... | 20 |
| 1.3.2 Stress relaxation related to failure of the switch..... | 21 |
| 1.4 Viscoelasticity in thin metal films..... | 24 |
| 1.4.1 Definition and previous study..... | 24 |
| 1.4.2 Measurement techniques..... | 26 |
| 1.4.3 Commonly proposed mechanisms..... | 34 |
| 1.4.4 Modeling linear viscoelastic behavior..... | 42 |
| 1.4.5 Activation volume and dislocation mobility..... | 44 |
| 2. Experimental description..... | 49 |
| 2.1 Sample design and fabrication..... | 49 |

| | |
|---|-----|
| 2.2 Fabrication of Au and Au alloy thin films | 52 |
| 2.3 Microstructure and composition investigation | 56 |
| 2.4 Bulge testing..... | 57 |
| 2.4.1 The bulge measurement technique | 57 |
| 2.4.2 Bulge test setup for stress relaxation experiments..... | 62 |
| 2.4.3 Pressure ramp and relaxation testing | 63 |
| 3. Time and temperature dependence of stress and stress relaxation of Au, AuV and Au-V ₂ O ₅ films..... | 67 |
| 3.1 Characterization of thin films..... | 67 |
| 3.2 Stress relaxation of pure Au films..... | 69 |
| 3.2.1 Pressure ramp and relaxation results | 69 |
| 3.2.2 Steady state ramp and relaxation results..... | 72 |
| 3.2.3 Temperature dependence on relaxation behavior of Au film | 76 |
| 3.3 Effect of V and V ₂ O ₅ addition on stress relaxation of Au films | 82 |
| 3.3.1 Relaxation behavior of AuV films..... | 82 |
| 3.3.2 Relaxation behavior of AuV ₂ O ₅ films | 85 |
| 3.3.3 Effect of V and V ₂ O ₅ on stress relaxation | 87 |
| 3.4 Activation energy and possible mechanism | 91 |
| 3.4.1 Prony series and the Arrhenius equation | 91 |
| 3.4.2 Stretched exponential function | 93 |
| 3.4.3 The diffusion mechanism model | 96 |
| 3.4.4 Relaxation mechanism..... | 100 |
| 3.5 Summary | 107 |
| 4. Validity of linear viscoelastic models for pure Au thin films | 109 |
| 4.1 Linear viscoelasticity in Au thin film..... | 110 |
| 4.2 Strain rate dependence of stress and stress relaxation..... | 112 |
| 4.2.1 Effect of strain rates on pressure ramp results of Au thin film at 20 and 80 ° C..... | 114 |

| | |
|---|-----|
| 4.2.2 Effect of strain rates on relaxation results of Au thin film at 20 and 80 ° C | 116 |
| 4.3 The time dependent stress determined by linear viscoelastic model | 120 |
| 4.3.1 Simulation for multiple loading results | 122 |
| 4.3.2 Simulation for strain ramp results | 127 |
| 4.4 Summary | 127 |
| 5. The effect of solute concentration on relaxation behavior of AuV solid solutions | 129 |
| 5.1 Characterization of thin films | 129 |
| 5.2 Temperature dependence of relaxation behavior of AuV solid solution thin films | 133 |
| 5.2.1 Pure Au thin film | 134 |
| 5.2.2 Solid solution of AuV 0.89 at. % | 136 |
| 5.2.3 Solid solution of AuV 2.20 at. % V | 138 |
| 5.2.4 Solid solution of AuV 4.50 at. % | 140 |
| 5.2.5 Discussion of temperature dependence on AuV films. | 141 |
| 5.3 Effect of V on relaxation behavior of Au thin film | 149 |
| 5.3.1 At 20 °C | 149 |
| 5.3.2 At 50 °C | 150 |
| 5.3.3 At 80 °C | 150 |
| 5.3.4 Discussion of concentration dependence on AuV films | 151 |
| 5.3.5 Modeling of creep strain rate | 154 |
| 5.4 Summary | 157 |
| 6. Grain size effect on relaxation behavior of Au films | 159 |
| 6.1 Characterization of Au thin films deposited at different substrate temperatures | 159 |
| 6.2. Temperature dependence of relaxation behavior of Au films with different grain sizes | 163 |
| 6.3. Effect of grain size on relaxation behavior of Au thin films | 168 |
| 6.4. Summary | 172 |

| | |
|---|-----|
| 7. Activation volume and dislocation mobility in viscoelastic behavior of Au and Au alloy thin films..... | 174 |
| 7.1 Repeated stress relaxation..... | 177 |
| 7.2 Activation volume results and discussion..... | 181 |
| 7.2.1 Apparent activation volume..... | 181 |
| 7.2.2 Physical activation volume..... | 186 |
| 7.3 The density of mobile dislocation results and discussion..... | 190 |
| 7.4 Summary..... | 197 |
| 8. Conclusions and future work..... | 198 |
| 8.1 Conclusions..... | 198 |
| 8.2 Future work..... | 200 |
| 9. References..... | 204 |
| VITA..... | 208 |

LIST OF TABLES

| | |
|---|-----|
| Table 1.1 The values of solute misfit and local change modulus of Au alloys | 15 |
| Table 1.2 Characteristics of obstacles for dislocation glide. | 40 |
| Table 3.1 The temperature dependence of SiN properties..... | 71 |
| Table 3.2 Prony series constants of Au film at steady state for 20-80 °C..... | 81 |
| Table 3.3 Prony series constants of AuV film at steady state for 20-80 °C..... | 84 |
| Table 3.4 Prony series constants of AuV ₂ O ₅ film at steady state for 20-80 °C. | 87 |
| Table 3.5 Three hours modulus decay of Au, AuV and AuV ₂ O ₅ at different temperatures..... | 89 |
| Table 3.6 Fitting Prony coefficients of Au, AuV and AuV ₂ O ₅ | 92 |
| Table 3.7 Activation energies of Au, AuV and AuV ₂ O ₅ taken from average slope of linear fits from Figure 3.24. | 93 |
| Table 3.8 Parameter fit of stretched exponential function for Au, AuV, and AuV ₂ O ₅ | 94 |
| Table 3.9 parameter values of diffusional model for Au, AuV, and AuV ₂ O ₅ | 98 |
| Table 4.1 Fitting Prony series constants of Au film at steady state for 20 and 80 °C. | 111 |
| Table 4.2 Value of strain rates corresponding to pressure rates shows the fastest strain rate is 300 times the slowest strain rate. | 113 |
| Table 4.3 Properties of Au film at steady state of 20 and 80 °C for different strain rates. | 115 |
| Table 5.1 Percent V content estimated by EDS software. | 131 |
| Table 5.2 Estimated value of flow stress for AuV films..... | 155 |
| Table 5.3 Material parameters of Au film for creep rate equation at 10 ⁻⁹ /s..... | 156 |

Table 7.1 The conditions of repeated stress relaxation testing of Au and Au alloy
films. 179

LIST OF FIGURES

| | |
|---|----|
| Figure 1.1 Schematic diagram of DC sputtering system. ¹² | 7 |
| Figure 1.2 Cross-sectional view of magnetron sputtering arrangement. ¹² | 8 |
| Figure 1.3 Sputter yield vs atomic number of elements such as Au, Ti, and V for the sputtering gas of Ar ⁺ . ¹⁴ | 9 |
| Figure 1.4 Au-V (Gold-Vanadium) phase diagram. ¹⁵ | 10 |
| Figure 1.5 Critical shear stress for solid solutions of Au..... | 14 |
| Figure 1.6 Specific hardening $d\tau_p/dc^{2/3}$ vs. the combined misfit and elasticity parameters. | 15 |
| Figure 1.7 Hardness vs. at % V of AuV and AuV ₂ O ₅ films measured by nanoindentation. ¹⁰ | 17 |
| Figure 1.8 Hardness or strength of a material as a function of the grain size. ²⁹ | 18 |
| Figure 1.9 Inverse Hall-Petch behavior in nanocrystalline Cu ($H - H_0$ denoted the hardness increment, D the grain size). ³⁰ | 19 |
| Figure 1.10 Top view and cross section of RF MEMS capacitive switch. ³³ | 20 |
| Figure 1.11 Schematic diagram of operation of RF MEMS capacitive switch. | 21 |
| Figure 1.12 Elastic, plastic, and viscoelastic/anelastic behavior of materials. | 24 |
| Figure 1.13 Typical stress-strain curves for Au films with grain size 200 nm illustrate the strong rate sensitivity observed by Emery and Povirk. ³⁷ | 26 |
| Figure 1.14 SEM image of microtensile test chip of Haque and Saif. ⁵² | 30 |
| Figure 1.15 (a) Schematic of indenter and specimen surface geometry, ⁵⁴ (b) Indentation loading and unloading curves. ⁵⁵ | 31 |
| Figure 1.16 a) Flow of vacancies from A-type to B-type boundaries and (b) strain produced in a hypothetical rectangular grain in Nabarro-Herring creep. ⁶³ | 35 |
| Figure 1.17 Flow of vacancies for Coble creep. ⁶³ | 36 |

| | |
|---|----|
| Figure 1.18 Relaxation of an initially uniform shear stress distribution by grain boundary sliding. ⁶⁶ | 37 |
| Figure 1.19 The bowing of a dislocation pinned at point A and B under applied stress. | 41 |
| Figure 1.20 The strain and stress in a three-step experiment. ⁴ | 43 |
| Figure 1.21 (a) Stress and strain of Al film at constant pressure of 30 torr for 1 hour, (b) Same film but different step pressure step: 30 torr for 30 min and down to 10 torr for 30 min, and (c) The time-dependent modulus deduced from (a) and (b). ⁹ | 44 |
| Figure 1.22 Schematic procedure and parameters of repeated stress relaxation. ⁸² | 47 |
| Figure 2.1 Bulge sample a) bottom view and b) cross section view..... | 50 |
| Figure 2.2 Sample fabrication for bulge testing..... | 52 |
| Figure 2.3 Experimental setup of bulge system..... | 57 |
| Figure 2.4 Schematic demonstration of bulge test in the bulge chamber. | 58 |
| Figure 2.5 Electrical setup for the capacity measurement. | 59 |
| Figure 2.6 Schematic of bulge test and description of bulge parameters when gas pressure > 0. | 60 |
| Figure 2.7 Schematic demonstration of bulged shape in thin film when P> 0 torr. ... | 61 |
| Figure 2.8 Schematic of strain versus time for a) Pressure ramp and b) Relaxation testing..... | 64 |
| Figure 2.9 Typical results of bulge experiments a) Pressure ramp and b) Relaxation testing..... | 65 |
| Figure 2.10 Flow chart of experimental procedure of bulge testing for viscoelastic films. | 66 |
| Figure 3.1 SEM and AFM images of sputtered Au, AuV(5.4 at.%V), and AuV ₂ O ₅ (5.4 at.%V) thin films | 68 |
| Figure 3.2 EDS results for AuV and AuV ₂ O ₅ films compared to the standard thin film of 4.5 at%V. | 69 |

| | |
|--|----|
| Figure 3.3 Initial relaxation behavior of Au/SiN film at 20 °C for a) pressure ramp and b) relaxation testing..... | 70 |
| Figure 3.4 Initial relaxation behavior of a free standing Au film at 20 °C for a) pressure ramp and b) relaxation testing. | 72 |
| Figure 3.5 Residual stress, modulus, and 3 hrs modulus decay of composite Au/SiN at 20 °C from the first run to steady state condition. | 74 |
| Figure 3.6 Relaxation of normalized modulus of composite Au/SiN at 20 °C from the first run to steady state condition. | 75 |
| Figure 3.7 Relaxation of normalized modulus of free standing Au at 20 °C from the first run to steady state condition. | 75 |
| Figure 3.8 Pressure ramp results in each run carried out each day on a single Au/SiN film providing residual stress and modulus. | 76 |
| Figure 3.9 Relaxation of normalized modulus of Au/SiN for each temperature (20, 50, 70 and 80 °C) from the first run to steady state condition. | 77 |
| Figure 3.10 Stress and strain curve of unloading segment at steady state of free standing Au for each temperature to determine plane-strain modulus and residual stress..... | 79 |
| Figure 3.11 Residual stress before and after exercising at 80 °C as a function of temperature. | 79 |
| Figure 3.12 Normalized modulus relaxation at steady state of free standing Au. | 80 |
| Figure 3.13 Normalized modulus relaxation of free standing Au at steady state fitted with four-term Prony series model a) linear scale, b) logarithmic scale. | 81 |
| Figure 3.14 Pressure ramp results in each run carried out each day of AuV/SiN providing residual stress and modulus..... | 83 |
| Figure 3.15 Relaxation of normalized modulus of AuV/SiN for each temperature (20, 50, 70 and 80 °C) from the first run to steady state condition. | 83 |
| Figure 3.16 Normalized modulus of a free standing AuV film at steady state for various temperatures fitted with a Prony series model. | 84 |

| | |
|--|-----|
| Figure 3.17 Pressure ramp results in each run carried out each day of AuV ₂ O ₅ /SiN providing residual stress and modulus. | 85 |
| Figure 3.18 Relaxation of normalized modulus of AuV ₂ O ₅ /SiN for each temperature (20, 50, 70 and 80 °C) from the first run to steady state condition. | 86 |
| Figure 3.19 Normalized modulus of a free standing AuV ₂ O ₅ film at steady state for various temperatures fitted with a Prony series model. | 87 |
| Figure 3.20 Pressure ramp results show residual stress and plane-strain modulus of Au, AuV and Au V ₂ O ₅ at steady state. | 88 |
| Figure 3.21 Normalized modulus of films at steady state for various temperatures fitted with Prony series model a) Au, b) AuV, and c) AuV ₂ O ₅ | 89 |
| Figure 3.22 Comparison of relaxation modulus of Au, AuV, and AuV ₂ O ₅ at each temperature (20, 50, 70 and 80 °C). | 90 |
| Figure 3.23 Temperature dependence of 3 hours modulus decay for Au, AuV and AuV ₂ O ₅ | 90 |
| Figure 3.24 Logarithmic plot of Prony coefficient values as a function of the inverse temperature for 3 different films (a) Au, (b) AuV and (c) AuV ₂ O ₅ | 93 |
| Figure 3.25 Normalized relaxation curves of Au, AuV, and AuV ₂ O ₅ fitted with stretched exponential function. | 95 |
| Figure 3.26 The activation energy extracted by stretched exponential function. | 95 |
| Figure 3.27 Schematics diagrams of a thin film with grain boundary and surface diffusion. | 96 |
| Figure 3.28 stress relaxation curves of Au film at a) 20 and b) 80 °C. The solid lines are fitted by the diffusion model. | 98 |
| Figure 3.29 The activation energies deduced by the grain boundary diffusivity as a function of temperature. | 99 |
| Figure 3.30 a) A dislocation segment rigidly pinned at the two points in the same Peierls energy trough, b) the advance of a dislocation through the Peierls potential by separation of the double kink in the dislocation. | 102 |

| | |
|---|-----|
| Figure 3.31 A schematic diagram showing the bowing out of a dislocation loop with several double kinks pinned at two point A and B with distance L apart on grain boundary. | 104 |
| Figure 3.32 The logarithmic plot of the sum of Prony coefficient as a function of the inverse temperature. | 107 |
| Figure 4.1 Relaxation modulus of the Au film at 20 and 80 °C at the constant strain 0.001..... | 111 |
| Figure 4.2 Normalized modulus of Au thin film at different strains of 0.0005 and 0.001 at two temperatures (a) 20 °C and (b) 80 °C..... | 112 |
| Figure 4.3 Pressure and strain versus time for different pressure rates from 8 torr/sec to 0.025 torr/sec. | 113 |
| Figure 4.4 Stress and strain curve of Au/SiN at 20 and 80 °C at different strain rates. | 114 |
| Figure 4.5 The effect of strain rates on Au film properties at 20 and 80 °C of a) residual stress, b) plane strain modulus and c) stress at strain 0.1%. | 116 |
| Figure 4.6 Linear time scale of stress relaxation results at different strain rates from $10^{-4} - 3 \times 10^{-7} \text{ s}^{-1}$ at 20°C (a) overall relaxation and (b) only stress relaxation section. | 117 |
| Figure 4.7 Logarithmic time scale of stress relaxation results at different strain rates from $10^{-4} - 3 \times 10^{-7} \text{ s}^{-1}$ at 20°C (a) overall relaxation and (b) only stress relaxation section. | 118 |
| Figure 4.8 Linear time scale of stress relaxation results at different strain rates from $10^{-4} - 3 \times 10^{-7} \text{ s}^{-1}$ at 80°C (a) overall relaxation and (b) only stress relaxation section. | 118 |
| Figure 4.9 Logarithmic time scale of stress relaxation results at different strain rates from $10^{-4} - 3 \times 10^{-7} \text{ s}^{-1}$ at 20°C (a) overall relaxation and (b) only stress relaxation section. | 119 |
| Figure 4.10 strain versus time for linear viscoelastic model. | 121 |
| Figure 4.11 Comparison of relaxation results on linear time scale at different strain rates at 20°C between (a) the experiment and (b) linear viscoelastic model. | 123 |

| | |
|---|-----|
| Figure 4.12 Comparison of relaxation results on logarithmic time scale at different strain rates at 20°C between (a) the experiment and (b) linear viscoelastic model. . | 124 |
| Figure 4.13 Comparison of relaxation results on linear time scale at different strain rates at 80°C between (a) the experiment and (b) linear viscoelastic model. | 124 |
| Figure 4.14 Comparison of relaxation results in logarithmic time scale at different strain rates at 80°C between (a) the experiment and (b) linear viscoelastic model. . | 125 |
| Figure 4.15 Comparison of experiment and simulation results for multiple loading parts at a strain rate of 10^{-4} s^{-1} at 20 °C including the recovery part shown in the inset. | 126 |
| Figure 4.16 Comparison of experiment and simulation results for multiple loading parts at a strain rate of 10^{-4} s^{-1} at 80 °C including the recovery part shown in the inset. | 126 |
| Figure 4.17 Comparison of experiment and simulation results for strain ramp results at the strain rate a) 10^{-4} s^{-1} and b) $3 \times 10^{-7} \text{ s}^{-1}$ at 20 °C. | 127 |
| Figure 5.1 EDS results for the set of AuV films show differences at the V peak related to the different V concentrations..... | 130 |
| Figure 5.2 SEM images of pure Au and AuV at 0.89, 2.2, 4.5 at. % V..... | 132 |
| Figure 5.3 Relaxation of normalized modulus of pure Au thin film for each temperature (20, 50 and 80 °C) from the first run to steady state condition. | 134 |
| Figure 5.4 Steady-state relaxation curves for each temperature of pure Au film. | 135 |
| Figure 5.5 Relaxation of normalized modulus of AuV 0.89 at. % V thin film for each temperature (20, 50 and 80 °C) from the first run to steady state condition. | 136 |
| Figure 5.6 Steady-state relaxation curves for each temperature of AuV 0.89 at. % V. | 137 |
| Figure 5.7 Relaxation of normalized modulus of AuV 2.2 at. % V thin film for each temperature (20, 50 and 80 °C) from the first run to steady state condition. | 138 |
| Figure 5.8 Steady-state relaxation curves for each temperature of AuV 2.2 at. % V. | 139 |
| Figure 5.9 Relaxation of normalized modulus of AuV 4.5 at. % V thin film for each temperature (20, 50 and 80 °C) from the first run to steady state condition. | 140 |

| | |
|--|-----|
| Figure 5.10 Steady-state relaxation curves for each temperature of AuV 4.5 at. %V. | 141 |
| Figure 5.11 Amount of plasticity in each run, from the first to the steady state condition of a pure Au film at successive temperatures of 20, 50 and 80 °C and for a film tested only at 80 °C..... | 144 |
| Figure 5.12 Time dependence of the amount of plasticity observed in the first run at each successive temperature in the Au film..... | 144 |
| Figure 5.13 Temperature dependence of 3 hour normalized modulus for AuV films. | 145 |
| Figure 5.14 Temperature dependence of anelastic creep strain for a pure Au film generated from steady state stress relaxation data at a fixed stress of 100 MPa. | 146 |
| Figure 5.15 Natural log of creep rates vs. 1/T for AuV films..... | 148 |
| Figure 5.16 The effect of V concentration on relaxation behavior of AuV solid solutions at 20 °C. | 149 |
| Figure 5.17 The effect of V concentration on relaxation behavior of AuV solid solutions at 50 °C. | 150 |
| Figure 5.18 The effect of V concentration on relaxation behavior of AuV solid solutions at 80 °C. | 150 |
| Figure 5.19 Concentration dependence of 3 hour normalized modulus for each temperature at steady state. | 152 |
| Figure 5.20 Concentration dependence of creep strain for a set of AuV films at room temperature converted from stress relaxation at fixed stress 100 MPa. | 153 |
| Figure 5.21 Concentration dependence on creep strain rate of AuV films at 20, 50, and 80 °C..... | 153 |
| Figure 5.22 Predicted contour for $\dot{\gamma} = 10^{-9}$ /s for creep rate of dislocation glide equation, compared with the experimental data for pure Au film. | 156 |
| Figure 5.23 Deduced the creep rate as a function of stress and temperature from creep rate equation of dislocation glide, compared to the creep rate from stress relaxation experiment..... | 157 |

| | |
|--|-----|
| Figure 6.1 SEM images show the Au film at elevated temperature a) with Ti and b) without Ti as adhesive layer. | 160 |
| Figure 6.2 SEM images show the different grain sizes of Au thin films deposited at different temperatures. | 161 |
| Figure 6.3 Grain size measurement by using a) linear intercept method and b) software program of <i>Image J</i> | 162 |
| Figure 6.4 The relationship of average grain size of pure Au and Au alloy thin films and substrate temperature. | 163 |
| Figure 6.5 The relationship between substrate temperature during deposition and room temperature residual stress in pure Au thin films. | 164 |
| Figure 6.6 Steady-state relaxation curves for each temperature of Au at RT substrate temperature (d= 60 nm). | 165 |
| Figure 6.7 Steady-state relaxation curves for each temperature of Au at 100 °C substrate temperature (d= 240 nm). | 165 |
| Figure 6.8 Steady-state relaxation curves for each temperature of Au at 200 °C substrate temperature (d= 460 nm). | 166 |
| Figure 6.9 Steady-state relaxation curves for each temperature of Au at 300 °C substrate temperature (d= 570 nm). | 166 |
| Figure 6.10 Steady-state relaxation curves for each temperature of Au at 400 °C substrate temperature (d= 605 nm). | 167 |
| Figure 6.11 Temperature dependence of Au with various grain sizes on normalized modulus. | 168 |
| Figure 6.12 The effect of grain size on relaxation behavior of Au films at 20 °C. | 169 |
| Figure 6.13 The effect of grain size on relaxation behavior of Au films at 50 °C. | 169 |
| Figure 6.14 The effect of grain size on relaxation behavior of Au films at 80 °C. | 170 |
| Figure 6.15 Grain size dependence on normalized modulus of Au films. | 171 |
| Figure 6.16 Simulated creep curves from relaxation measurements for Au films with various grain sizes a) 20 °C, b) 50 °C and c) 80 °C. | 172 |

| | |
|---|-----|
| Figure 7.1 SEM images and estimated grain size of Au, AuV and AuV ₂ O ₅ thin films. | 179 |
| Figure 7.2 Repeated stress relaxation curves at steady state showing four cycles with time interval of 200 second a) large grain Au and b) Au, AuV and AuV ₂ O ₅ | 181 |
| Figure 7.3 Example of the fitting curve of the first stress relaxation for apparent activation volume in Au. | 182 |
| Figure 7.4 Repeated stress relaxation and 3 hour stress relaxation including the fitting of apparent activation volume of Au film. | 183 |
| Figure 7.5 Apparent activation volume as a function of run number for Au and Au alloy films. | 185 |
| Figure 7.6 A plot of apparent activation volume at steady state vs. stress decay ($\Delta\tau$) of Au and Au alloy films. | 186 |
| Figure 7.7 Physical activation volume as a function of run number for Au and Au alloy films. | 187 |
| Figure 7.8 Apparent and physical activation volume as a function of applied stress. | 188 |
| Figure 7.9 The effect of temperature on activation volume for Au thin films. | 189 |
| Figure 7.10 The effect of alloy compositions on activation volume of Au alloy thin films. | 189 |
| Figure 7.11 The effect of grain size on activation volume for Au thin films. | 190 |
| Figure 7.12 The mobile dislocation density as a function of time assuming various strain-hardening coefficients (K) for Au films deposited at room temperature. | 192 |
| Figure 7.13 The estimated value of the mobile dislocation density at t = 200 seconds assuming various value of K for Au and Au alloy films. | 193 |
| Figure 7.14 Comparison of mobile dislocation density as a function of time for Au and Au alloy films when K is reasonably estimated at 1000 MPa. | 193 |

Abstract

Radio frequency (RF) switches based on capacitive MicroElectroMechanical System (MEMS) devices have been proposed as replacements for traditional solid-state field effect transistor (FET) devices. However, one of the limitations of the existing capacitive switch designs is long-term reliability. Failure is generally attributed to electrical charging in the capacitor's dielectric layer^{1, 2} that creates an attractive electrostatic force between a moving upper capacitor plate (a metal membrane) and the dielectric. This acts as an attractive stiction force between them that may cause the switch to stay permanently in the closed state. The force that is responsible for opening the switch is the elastic restoring force due to stress in the film membrane. If the restoring force decreases over time due to stress relaxation, the tendency for stiction failure behavior will increase. Au films have been shown to exhibit stress relaxation even at room temperature.^{3, 4} The stress relaxation observed is a type of viscoelastic behavior that is more significant in thin metal films than in bulk materials.

Metal films with a high relaxation resistance would have a lower probability of device failure due to stress relaxation. It has been shown that solid solution and oxide dispersion can strengthen a material without unacceptable decreases in electrical conductivity. In this study, the viscoelastic behavior of Au, AuV solid solution and AuV₂O₅ dispersion created by DC magnetron sputtering are investigated using the gas pressure bulge testing technique in the temperature range from 20 to

80°C. The effectiveness of the two strengthening approaches is compared with the pure Au in terms of relaxation modulus and 3 hour modulus decay. The time dependent relaxation curves can be fitted very well with a four-term Prony series model. From the temperature dependence of the terms of the series, activation energies have been deduced to identify the possible dominant relaxation mechanism.

The measured modulus relaxation of Au films also proves that the films exhibit linear viscoelastic behavior. From this, a linear viscoelastic model is shown to fit very well to experimental steady state stress relaxation data and can predict time dependent stress for complex loading histories including the ability to predict stress-time behavior at other strain rates during loading.

Two specific factors that are expected to influence the viscoelastic behavior-degree of alloying and grain size are investigated to explore the influence of V concentration in solid solution and grain size of pure Au. It is found that the normalized modulus of Au films is dependent on both concentration (C) and grain size (D) with proportionalities of $C^{1/3}$ and D^2 , respectively. A quantitative model of the rate-equation for dislocation glide plasticity based on Frost and Ashby⁵ is proposed and fitted well with steady state anelastic stress relaxation experimental data.

The activation volume and the density of mobile dislocations is determined using repeated stress relaxation tests in order to further understand the viscoelastic relaxation mechanism. A rapid decrease of mobile dislocation density is found at the

beginning of relaxation, which correlates well with a large reduction of viscoelastic modulus at the early stage of relaxation. The extracted activation volume and dislocation mobility can be ascribed to mobile dislocation loops with double kinks generated at grain boundaries, consistent with the dislocation mechanism proposed for the low activation energy measured in this study.

1. Introduction

1.1 Background information

Thin films play important roles in many applications, especially as structural and electronic components in microelectromechanical system (MEMS) devices. A MEMS device designed for radio frequency (RF) applications is the RF MEMS capacitive switch. This switch involves metal-on-dielectric contact, with the switching operation accomplished by mechanical movement. One of the main mechanical failures of the switch is due to the stiction between the top, thin film metal layer and the dielectric layer.^{1, 2} Since a large voltage is required to operate the switch from the open to the closed state, electrical charge can accumulate in the dielectric layer. This charge creates an electrostatic attractive force between the metal membrane and the dielectric layer which can cause the switch to fail to open when the activating voltage is removed.^{2, 6} The opening force is provided by tensile stress in the thin metal membrane. If the elastic restoring force decreases over time due to stress relaxation in the membrane, the tendency for this mode of failure will increase.

It has been shown that the viscoelastic behavior of thin films is a primary consideration in evaluating the reliability of films for MEMS switch performance.^{4, 7} Au thin films are particularly employed for RF MEMS switches because of their high electrical conductivity, chemical inertness, and resistance to oxidation and corrosion.⁶

However, since Au films exhibit significant stress relaxation behavior at room temperature,^{8,9} they can fail in MEMS capacitive switch applications.

In bulk metals, one common way to strengthen a material and reduce the stress relaxation is by creating metal alloys. However, due to the limited manufacturing methods available for fabrication of thin films and the electrical requirements for applications of RF MEMS, there are not many options for controlling alloy composition and microstructure. Alloying the metal films must not result in loss of the desirable electrical properties or the ease of processing. It has been shown that solid solution and oxide dispersion strengthening can achieve high hardness while retaining reasonable electrical conductivity, and both methods are compatible with standard thin film processing techniques.¹⁰ These classes of materials are therefore potential candidates to begin to understand the effects of alloying on stress relaxation.

Furthermore, the MEMS capacitive switch must be able to operate under various applied strain rates and operating temperatures. It has been reported that relaxation in gold is strongly dependent on both temperature and strain rate.^{8, 9} Increasing temperature increases both the magnitude and rate of stress relaxation,⁷ making switches made with this material more vulnerable to failure at high temperature. However, nothing has been published about the temperature dependence of stress relaxation of solid solution and oxide-dispersion strengthened gold thin films. Hence, investigation of such films at different temperatures and strain rates is important to predicting the reliability of capacitive MEMS switches.

Some other material properties that are expected to influence the viscoelastic behavior of Au and Au alloys are also investigated, such as the effect of grain size and the effect of solute concentration. Furthermore the mechanism responsible for stress relaxation in thin films has been studied through the determination of the activation energy, activation volume and density of mobile dislocations in the materials.

1.2 Thin film fabrication and mechanical properties

In the semiconductor industry, fabrication of integrated circuits requires placing many different thin film layers of different metals and insulators in direct contact with one another. The desired materials may be in layers from tens of nanometers to micrometers in thickness. For MEMS devices, Au thin films are often the order of one to several micrometers thick. As noted above, Au is often chosen for its electrical conductivity and its chemical inertness.

1.2.1 Thin film deposition methods

There are many different physical and chemical techniques for depositing thin films. However, the objective of this thesis is not to cover all techniques and only Physical Vapor Deposition (PVD)¹¹ including sputtering, cosputtering, and reactive cosputtering are discussed.

- Sputter deposition

In sputter deposition, a vapor flux from a solid target surface is produced when the solid surface is bombarded with energetic particles such as accelerated ions.

This is typically achieved by applying a negative voltage to the target in an inert gas environment such as Ar. The Ar^+ ions created in the glow discharge that is formed are accelerated toward the target, ejecting atoms of the target material which then deposit on a substrate. Three fundamental hardware configurations for thin film coating consist of DC sputtering, RF sputtering, and the magnetron arrangements. Figure 1.1 shows schematically the essential arrangement for DC sputtering.

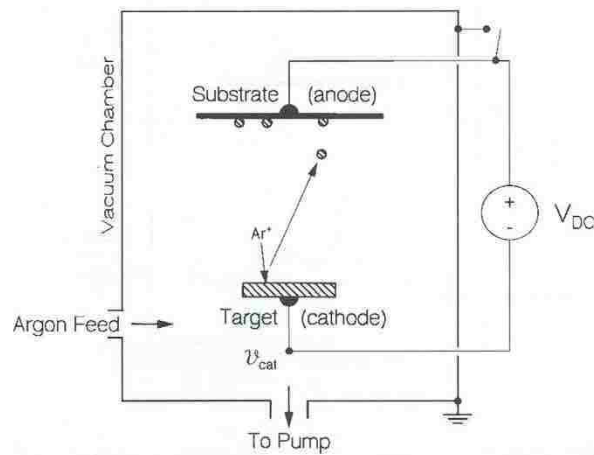


Figure 1.1 Schematic diagram of DC sputtering system.¹²

In magnetron sputtering, magnets are placed under the target with a north pole-oriented magnet at the center and a ring of south pole-oriented magnets in a band at the edge of the target as presented in Figure 1.2. Magnetron sources are superior to diode sources because they provide a magnetic field that confines the motion of electrons near the target surface, causing denser plasma. This leads to improved sputtering efficiency, higher deposition rate and a reduction in substrate bombardment.¹³

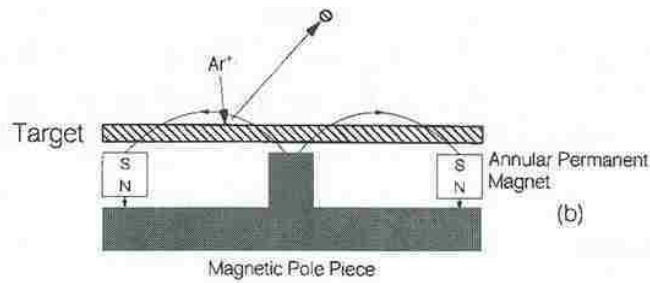


Figure 1.2 Cross-sectional view of magnetron sputtering arrangement.¹²

- Cosputter deposition

The cosputter deposition technique is sputtering as described above but using more than one target material. Cosputter deposition is used in this study to fabricate Au-V solid solution thin films. We use two alloy targets (A, B) in the sputtering system. The composition of the sputtered alloy films is generally controlled by regulating the power to the individual sputtering targets. Figure 1.3 shows the sputter yields vary periodically with the element's atomic number such as Au, Ti, and V for sputtering with Ar^+ at 400eV.

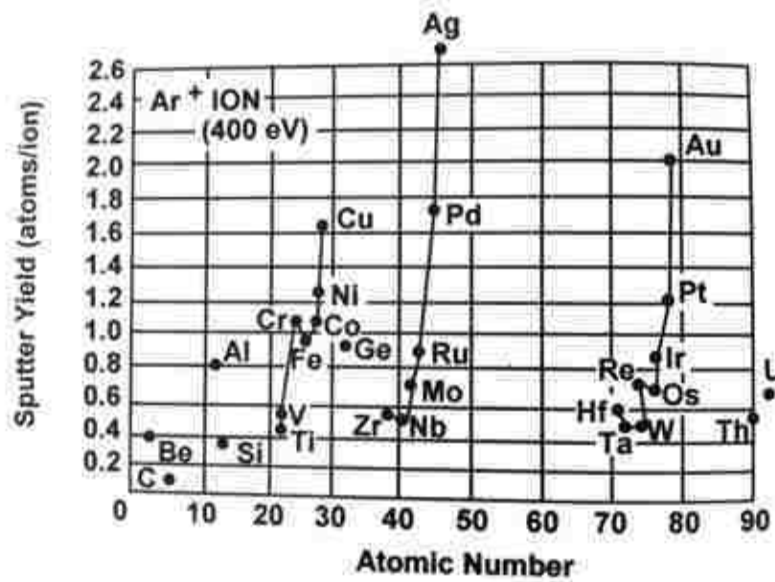


Figure 1.3 Sputter yield vs atomic number of elements such as Au, Ti, and V for the sputtering gas of Ar^+ .¹⁴

In this work, the binary alloy Au-V is selected and fabricated as a solid solution thin film. The Au-V phase diagram contains single and multiple phases as shown in Figure 1.4. In the composition range of less than 13 at % or 4 wt % of V in Au matrix, a solid solution with no intermetallic compounds exists. A AuV solid solution is expected to have similar structure as pure Au and acts as a model material to study solid solution strengthening on stress relaxation behavior.

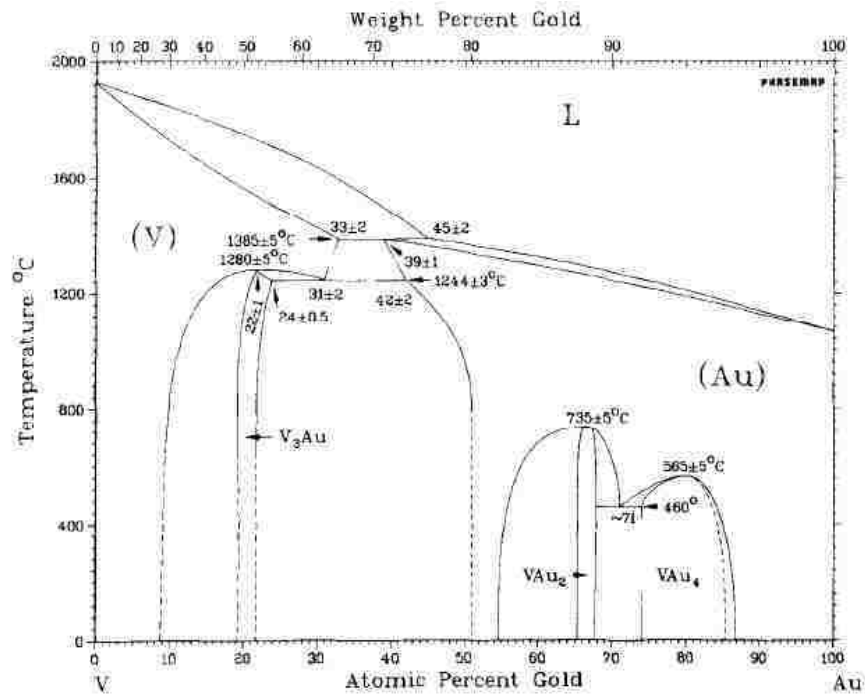


Figure 1.4 Au-V (Gold-Vanadium) phase diagram.¹⁵

- Reactive sputter deposition

Reactive sputter deposition is the sputtering of an elemental target in the presence of a gas that will react with the target material to deposit a compound or multiphase thin film.^{16, 17} In this method, Ar is typically used as the main sputtering gas to deposit films from Au and V metallic targets. For oxide compound thin films, O₂ is added to react with one or more of the metals during deposition, in our case with V, creating oxide material automatically. Thin oxide films processed by reactive sputter deposition can be low cost and have high purity, but it is difficult to control the critical composition of the process.¹⁸ Insufficient O₂ will lead to incomplete oxidation of the film. On the other hand, when the sputtering rate is below the gas adsorption rate at the target, then ‘poisoning’ of the target can occur. Severe

oxidation of the target surface under high O₂ conditions significantly decreases sputtering rate. Thus a suitable amount of oxygen partial pressure is required to create desirable thin films.

1.2.2 Thin film mechanical properties

Since thin films have been used primarily as structural components in a variety of applications, the mechanical properties of thin films are critical for potential reliability of the devices. These properties can be partially explained by the microstructure of thin films. The final microstructure of a thin film on a rigid substrate is controlled by the deposition process and any subsequent thermal treatment. Often, thin metal films have either a columnar grain structure or a finer microstructure with smaller equiaxed grains.

One of the important microstructures of typical films is their small grain size. The hardness and strength of the films increase as the grain size decreases following the Hall-Petch relation. The flow stresses of thin metal films deposited on rigid substrates are therefore obviously higher than those observed in the corresponding bulk metal. The flow stress also tends to increase with decreasing film thickness. This is because the geometrical constraints on the films, which obstruct dislocation motion. Based on bulk material behavior, solid metals are generally assumed to have small viscoelastic behavior at room temperature due to their crystalline structures. However, when the metals have nanoscale grain size as they may in thin film materials, they tend to show room temperature viscoelasticity.¹⁹

In summary, the mechanical properties of thin films are different from those of bulk materials. This can be explained by their microstructure, their large surface to volume ratio, and the importance of attachment of a film to its substrate which influences dislocation motion.²⁰ In order to strengthen thin films, we can increase the number of dislocation interactions with other dislocations (strain hardening), solute atoms (solid solution strengthening), grain boundaries, precipitates (precipitation hardening), and dispersoids (dispersion strengthening). The rest of the chapter briefly discusses only three strengthening mechanism related to this study: solid solution strengthening, oxide dispersion strengthening, and grain boundary strengthening.

- Solid solution strengthening

A solid solution is compositionally homogeneous. The solute (impurity) atoms are randomly distributed throughout the matrix and form either a substitutional or an interstitial solid solution. It has been shown that the addition of solute results in an attendant increase in yield and tensile strength compared to pure metals. For example, Bannuru's results¹⁰ showed that solid solutions of V in Au films have greater hardness than pure Au. This strengthening results from elastic, electrical and chemical interactions between solute atoms and dislocations.²¹ Of these, the elastic interactions are the most important and will be discussed here. The strengthening due to elastic interactions is the result of stress fields surrounding the solutes and dislocations. The following parameters are used to characterize the solute atoms in their interactions with dislocations:²²

- 1) The size misfit measured by the percentage change in the lattice parameter (or Burger vector b) on alloying (concentration c)

$$\delta = \frac{1}{b} \cdot \left(\frac{db}{dc} \right) \quad \mathbf{1.1)}$$

- 2) The change of the shear modulus G with alloying as a measure of the change in binding on the introduction of the solute atom

$$\eta = \frac{1}{G} \cdot \left(\frac{dG}{dc} \right) \quad \text{and} \quad \eta' = \eta / (1 + |\eta|/2) \quad \mathbf{1.2)}$$

Both of these interactions are of long range and can be calculated approximately by elasticity theory. At close distances between a dislocation and a solute atom, there is a “core” interaction which is of short range and thermally activated. It is useful to exclude the core interaction by measuring alloy hardening in the temperature range where the critical shear stress is no longer temperature dependent, thus obtaining the so-called “Plateau stress” τ_p .

According to Fleischer²³ and Labusch²⁴, the contribution of solid solution hardening τ_p to the total critical shear strength depends on the concentration c , the exponents p and q , and a hardening parameter ε which is a combination of δ and η' .

$$\tau_p = G \cdot \varepsilon^p c^q / Z + \tau_{00} \quad \mathbf{1.3)}$$

where Z is constant, and τ_{00} is the critical resolved shear stress of pure metal.

Eq.1.3) can therefore give the relationship to predict the relative strengthening effects of different solute atoms on a particular solvent. For example, Jax et al.²²

investigated the solid solution hardening τ_p of Au-In, -Cd, -Ga, -Zn, and -Ag. The values of τ_p were determined at temperature above 500 K by the usual single slip transformation in compression in an Instron machine. Figure 1.5 shows the results of concentration dependence of the plateau stress τ_p of Au alloys. Based on their measurement of critical resolved shear stress, the relationship of strength and concentration of Au alloys is well described as $\tau_p \propto c^{2/3}$.

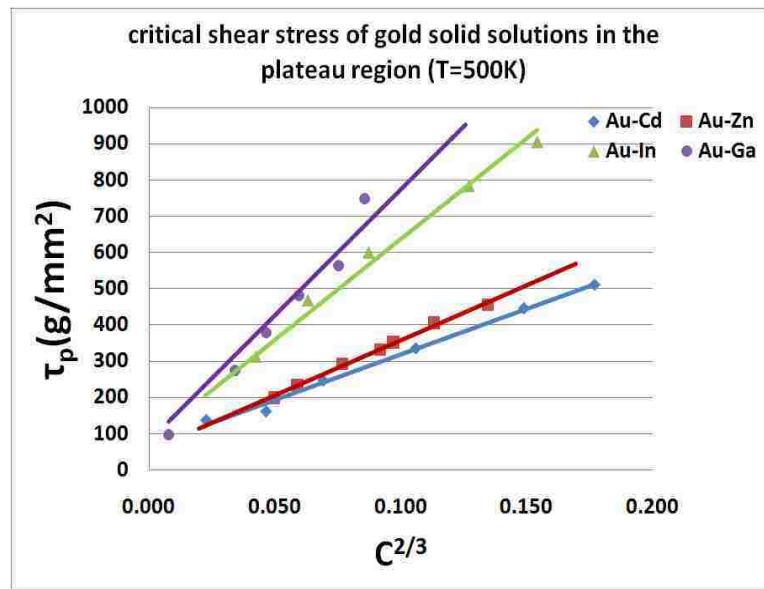


Figure 1.5 Critical shear stress for solid solutions of Au.

Some papers describe the solid solution hardening in alloys as either the size effect or the modulus effect alone.^{22, 25} However, the results of Jax et al. prove that it is impossible to fully explain the hardening by only one parameter. For example, based on the value of size misfit alone as presented in Table 1.1, Au-Ga should be harder than Au-Ag, but much softer than Au-Cd, Au-Zn, Au-In. This is not the case since Ga has the strongest effect in this series of Au alloys as shown in Figure 1.5. It is observed that the influence of solid solution hardening in these alloys is a

combination of parameters of solute misfit and the change of modulus. Jax et al.²² suggested the combination which matches quite well in shear stress from their experiment. The expression is given by $\varepsilon = |\eta'| + 16|\delta|$. The degree of solid solution hardening ($d\tau_p/dc^{2/3}$) of Au as it depends on ε is plotted in Figure 1.6. The results provide the data about which alloying elements exhibit higher solid solution hardening.

| Alloy | Solute misfit(δ) | η' |
|-------|---------------------------|---------|
| Au-Ga | -0.013 | -1.29 |
| Au-Cd | 0.043 | 0.17 |
| Au-Zn | -0.048 | -0.19 |
| Au-In | 0.075 | -0.6 |
| Au-Ag | -0.004 | 0.35 |

Table 1.1 The values of solute misfit and local change modulus of Au alloys

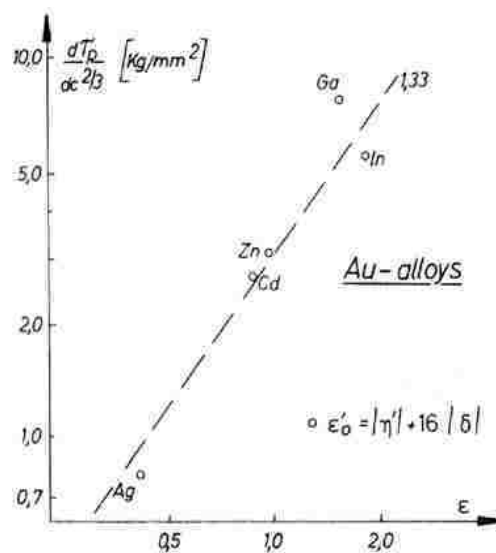


Figure 1.6 Specific hardening $d\tau_p/dc^{2/3}$ vs. the combined misfit and elasticity parameters.

There are also publications considering the hardening effect of materials other than Au alloys. Wesemann²⁶ prepared molybdenum alloys with Cr, Re, Ta, Ti, and

W additions and measured the mechanical properties at room temperature (including Vickers hardness measurements). They found that Mo-Cr showed the highest solid solution hardening followed by Ti, Ta, and Re, which matches the expectations of the combined misfit and elasticity model.

- Oxide dispersion strengthening

This type of strengthening is advantageous at elevated temperature where a microstructure can be more stable than other alloys due to the very high melting point of oxide particles. The oxide particles that are homogeneously dispersed in the metal matrix block dislocation motion and also restrict high temperature recrystallization that would lead to larger grain size and reduced mechanical strength.²⁷ The strength of the oxide dispersion-strengthened alloys is therefore due to the factors of particle size, volume fraction (particle spacing), deforming vs non-deforming type, particle shape (spherical or non-spherical) and the kind of the boundary between the particle and the surrounding matrix. It is evident that yield strength increases as a function of oxide volume fraction (decreasing particle spacing).^{21, 27} The relationship between particle spacing and oxide volume fraction can be defined by²¹

$$\lambda = \frac{2d}{3f}(1 - f) \quad \mathbf{1.4)}$$

where λ is particle spacing or “mean free path”, d is particle size, and f is volume fraction.

The dispersoid is effective in blocking the movement of dislocations, demanding that a higher stress be applied to a dislocation to cut through the finely

dispersed particles. Previous work on mechanical properties in terms of hardness of Au-V₂O₅ dispersion used nanoindentation at room temperature.¹⁰ The results shown in Figure 1.7 demonstrate that Au-V₂O₅ films have a greater hardness at a given V concentration than solid solutions.

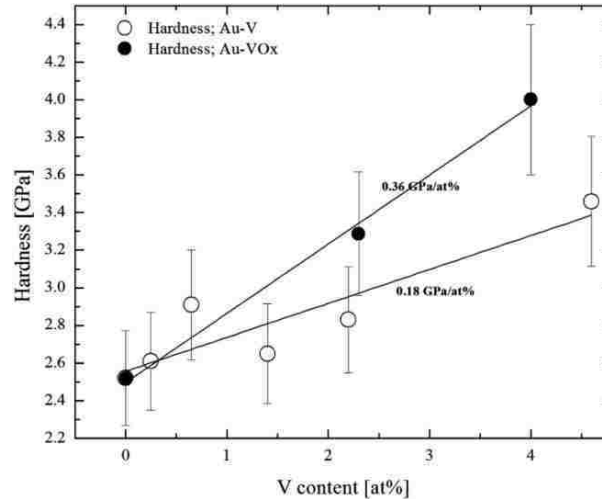


Figure 1.7 Hardness vs. at %V of AuV and AuV₂O₅ films measured by nanoindentation.¹⁰

- Grain-size strengthening

The presence of grain boundaries can greatly influence the mechanical properties of a material due to the interactions between dislocations and grain boundaries. There are two important roles of the grain boundary which act as a barrier to dislocation motions. The first role is the difficulty for dislocation to pass through two different grain orientations. The others is the atomic disorder within a grain boundary region which contributes to a discontinuity of slip planes from one grain to the next.²⁸ Typically, a fine-grained material is stronger than a coarse-

grained material due to a greater total grain boundary area. The classical effect of grain size on yield stress can be described by the Hall-Petch equation:

$$\sigma_y = \sigma_0 + kd^{-1/2} \quad 1.5)$$

where σ_0 is the intrinsic flow stress, d is grain size and k is a material constant coefficient. It is noted that Eq 1.5) is not valid for both very large grain and extremely fine grain materials as shown in Figure 1.8.

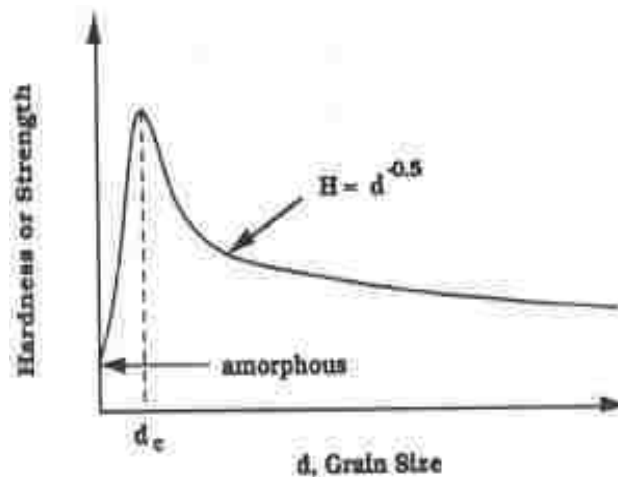


Figure 1.8 Hardness or strength of a material as a function of the grain size.²⁹

The condition of grain size strengthening is based on the pile-ups of dislocation loops against grain boundaries. This mechanism must break down when a material reaches a maximum strength at a critical grain size, d_c , at which the distance between the dislocations piling up against the grain boundaries become comparable to the grain size.³⁰ For Cu, as an example, the critical grain size which can be termed “strongest grain size” is estimated to be approximately 50 nm which is consistent with experimental results by Chokshi et al.³¹ as shown in Figure 1.9. The plastic

behavior of a material below the critical grain size is not fully clear. Some authors reported some possible mechanisms for such a softening effect due to coble creep, grain boundary sliding and grain boundary triple junctions.³²

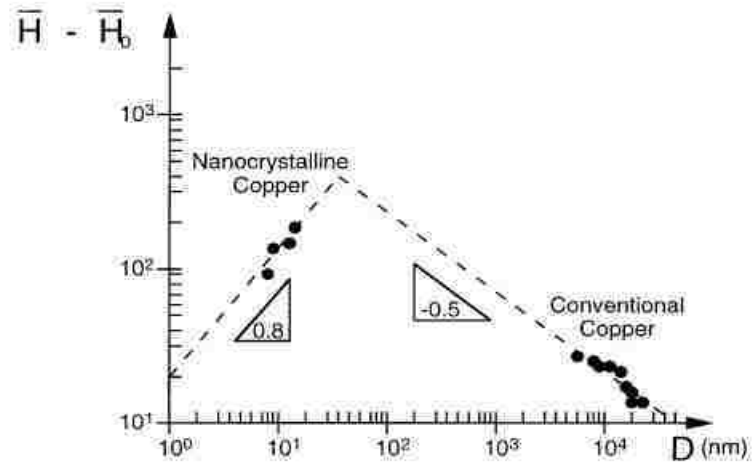


Figure 1.9 Inverse Hall-Petch behavior in nanocrystalline Cu ($\bar{H} - \bar{H}_0$ denoted the hardness increment, D the grain size).³⁰

1.3 RF MEMS capacitive switch

1.3.1 Switch design and operation

An RF MEMS capacitive switch is one major application of MEMS devices designed for radio frequency (RF) applications as shown in Figure 1.10.³³ It offers several advantages such as reduced weight, low power consumption, high linearity, low insertion loss, and potentially low cost as compared to solid state switches.³⁴ This switch involves metal-on-dielectric contact, with the switching operation accomplished by mechanical movement. Figure 1.10 shows the switch with a thin metal film membrane which is clamped at both ends. Beneath the membrane and spaced a few micron below is an electrode coated by a dielectric layer.

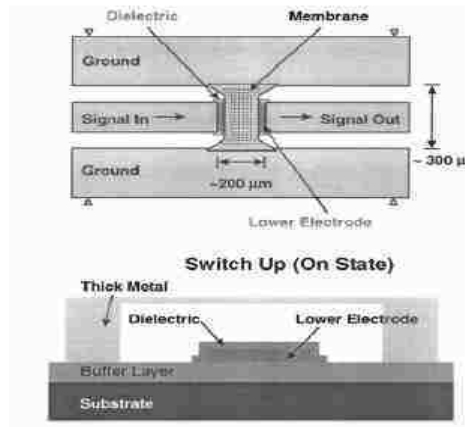


Figure 1.10 Top view and cross section of RF MEMS capacitive switch.³³

When a voltage is applied to the lower electrode, the membrane is pulled down until it suddenly comes in contact with the dielectric, which is called the “down” state. In this state, the RF signal is shorted to ground and no RF signal flows along the transmission line output. In order to move the switch from “down” state to

“up” state, the voltage is removed from the bottom electrode, and elastic restoring forces in the moving part of the device enable the membrane to return to its “up” state. In the “up” state, the membrane is suspended above the bottom electrode, and the gap is relatively large allowing the RF signal to pass through the device.

A schematic diagram showing “up” and “down” states of an RF MEMS capacitive switch is shown in Figure 1.11. It is noted that capacitive switches can also be made using cantilever beams, clamped at only one end. This study focuses only the capacitive switches on the fixed-fixed beam design.

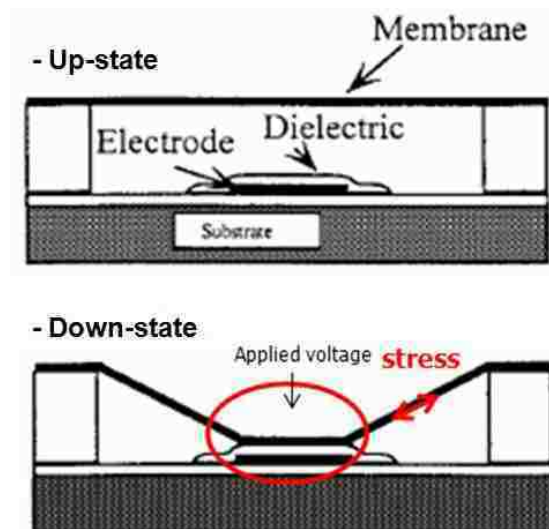


Figure 1.11 Schematic diagram of operation of RF MEMS capacitive switch.

1.3.2 Stress relaxation related to failure of the switch

One of the major concerns of MEMS components is the reliability for long-term applications. For RF capacitive MEMS switches, the primary failure mechanism is the “stiction” between the metal layer (top electrode) and the dielectric

layer covering the bottom electrode.^{1, 2} Since a large voltage is required to actuate a switch, there can be a significant amount of charge accumulation in the dielectric layer of the devices. This charge creates an electrostatic attractive force between the metal membrane and the dielectric layer which can cause the switch to fail to reopen when the activating voltage is removed.⁶ However, dielectric charging is not the only mechanism that contributes to stiction failure of a switch. There is also a mechanical component related to the stress in the membrane. The force associated with the stress in this membrane opposes the electrostatic force to return the switch to an open state, thus it is known as the “restoring force”. If the membrane stress relaxes over time, the corresponding elastic restoring force will also decrease with time, which increases the tendency for this failure behavior.

It has been reported that the time-dependent mechanical response of a typical metal thin film used in an RF MEMS switch consists of a combination of two distinct components: viscoelastic and viscoplastic.^{4, 7} Stress relaxation by either component will reduce the restoring force, but only the viscoplastic component is a permanent change. The viscoplastic component can be exhausted by doing multiple stress relaxation cycles (i.e., repeatedly applying a constant load for a fixed time) or a single cycle for a long time until a film reaches a steady state condition, after which it shows only a viscoelastic response.⁷ In this study, the multiple relaxation cycles are chosen rather than a single cycle to allow for frequent evaluations of the remaining viscoplasticity. This implies that it may be possible to “burn in” a device to achieve a more stable condition by exhausting the viscoplastic relaxation prior to the final

testing of device performance. However, the viscoelastic behavior will continue to reduce the restoring force in the membrane and influence the reliability of the switch even after all permanent relaxation is complete. If the viscoelastic relaxation can be accurately predicted and/or reduced by proper alloying, it may be possible to design the RF MEMS to be highly reliable even with viscoelastic behavior present.

1.4 Viscoelasticity in thin metal films

1.4.1 Definition and previous study

Viscoelastic (or anelastic) behavior is an intermediate behavior between elastic and plastic behavior. Viscoelasticity is different from elasticity and plasticity since it is time dependent but involves no permanent deformation as shown in Figure 1.12.

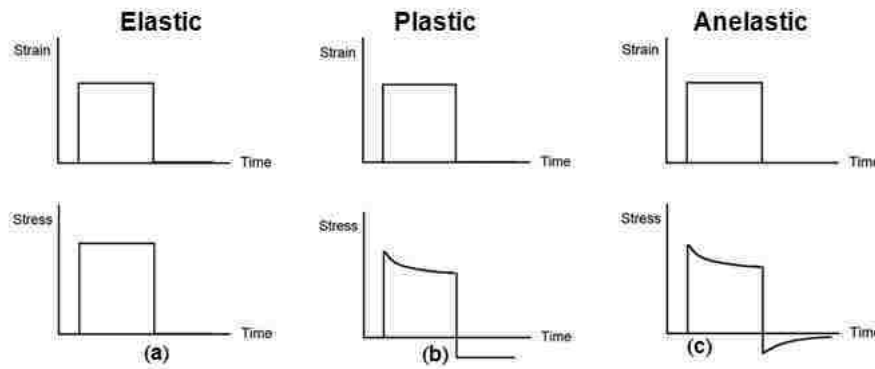


Figure 1.12 Elastic, plastic, and viscoelastic/anelastic behavior of materials.

Viscoelasticity gives rise to some common phenomena which are known as creep, and relaxation. Creep is a deformation of a material under constant stress and the strain increases with time. In contrast, stress relaxation is the gradual decrease of stress when the material is held at constant strain.³⁵ Since the real conditions of RF MEMS switches matches well with constant strain operation, stress relaxation is the focus of this study.

Common metals, such as steel or aluminum, exhibit small effects of some viscoelastic response at room temperature and at small strain. However, the fine

grain structure in thin films influences mechanical properties including viscoelasticity. Many researchers have reported that several thin film materials exhibit time dependent deformation as a result of creep and relaxation. Au films which are commonly used in MEMS switches exhibit significant stress relaxation at room temperature. Yan et al.⁴ reported that a 27 % reduction in the effective elastic modulus occurs over a three-day period under constant strain conditions at room temperature. The operating temperature range of RF MEMS switches typically exceeds room temperature. Higher temperatures are expected to have an influence on relaxation behavior.^{8, 9} McLean et al.⁷ reported that relaxation is strongly dependent on temperature in the temperature range of 20-80 °C. They showed that increasing temperature increases both the magnitude and rate of stress relaxation, making switches made with this material more vulnerable to failure at high temperature.

Additionally, viscoelastic behavior is observed to be sensitive to strain rate. The strain rate dependence of thin films has been widely studied for all standard properties: elastic, viscoelastic, and plastic behavior. Emery et al.^{36, 37} studied fine-grained Au films (grain size less than 500 nm) at various strain rates over two orders of magnitude ($5 \times 10^{-6} \text{ s}^{-1}$ to $5 \times 10^{-4} \text{ s}^{-1}$) by uniaxial tensile test. The results showed that at room temperature, these fine-grained films demonstrated significant strain rate dependence of yield stress and tensile strength as shown in Figure 1.13. They suggested that the climb-and-glide of dislocations was the most likely deformation mechanism. The strain rate dependence of Au films was also observed by Chastiotis et al.³⁸ with a greater extension of the strain rate from 10^{-6} - 10^{-2} s^{-1} . The results

showed that the properties of Au films with regard to the strain rate dependence are in agreement with Emery's results.

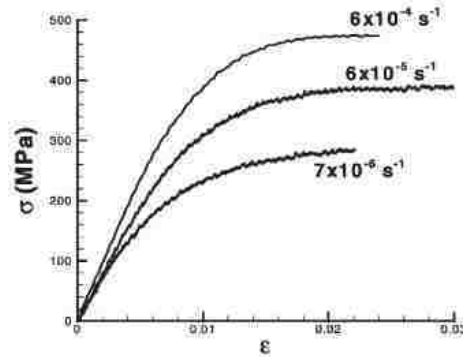


Figure 1.13 Typical stress-strain curves for Au films with grain size 200 nm illustrate the strong rate sensitivity observed by Emery and Povirk.³⁷

1.4.2 Measurement techniques

It is well known that the mechanical properties of thin films are different from those of bulk materials due to the small scale of these materials. Thin film mechanical properties can be measured by several techniques such as substrate curvature,³⁹ microtensile testing,^{3, 40} nanoindentation,⁴¹ and bulge test.⁴² This section presents an overview of some of the most common techniques for measuring the mechanical properties of thin films.

- Substrate curvature method

Measurement of the curvature induced in a wafer by the stress in a thin film on its surface is one of the most widely used techniques for the determination of the film stress.

The curvature of a substrate is typically evaluated by scanning the film surface with a laser beam, detecting the reflected signal, and determining the changing angle of reflection. Once the radius of curvature is known, the stress in the film may be calculated by using Stoney equation.⁴³ In this equation, the properties of the substrate are required as well as the thickness of the films.

$$\sigma = \frac{M_s t_s^2}{6t_f} \left(\frac{1}{R_1} - \frac{1}{R_2} \right) \quad \mathbf{1.6)}$$

where t_f is the film thickness, t_s is the substrate thickness, M_s is elastic biaxial modulus of the substrate, R_1 is spherical radius of curvature of the composite film/substrate neutral plane, R_2 is the spherical radius of curvature of the bare substrate mid-plane/neutral plane, and σ is the biaxial stress in the thin film.

Additionally, this method can be used to study the mechanical properties when a thin film on a substrate is thermally cycled. Differences in thermal expansion between the film and substrate lead to changes in the stresses in the film and substrate as the temperature is changed, resulting in spherical deformation of the substrate.⁴⁴ The amount of stress change is given by considering the biaxial plane stress of the film.

$$\Delta\sigma = M \Delta\alpha \Delta T \quad \mathbf{1.8)}$$

where M is biaxial modulus of the film, $\Delta\alpha$ is the linear coefficient of thermal expansion (CTE) difference of the film and substrate. The coefficient of thermal expansion and the biaxial modulus of the film can be determined by using two known different substrates, such as Si, Ge or sapphire.⁴⁵

The advantages of the substrate curvature techniques are that it is rapid and nondestructive.⁴⁶ However, if there is nonuniformity in film stress or thickness, measurement of curvature over less than the full substrate will lead to error in the calculation stress.^{46, 47} One of the limitations of the substrate curvature method is that the applied stress and temperature cannot be varied independently due to the direct relationship between them.

- Microtensile testing

In this method, a sample is usually loaded at a constant strain rate and the stress is measured by a load cell whose output voltage is proportional to the applied force. Simple measurement and straightforward interpretation of results is one of the main advantages of tensile testing. However, the difficulties of the uniaxial tensile test are in fabricating a small and stress-free specimen, aligning and gripping the specimen, generating small forces and measuring strain.⁴⁸ Several methods are used to measure the small strain such as strain gauge, interferometric strain, and atomic-force microscopy. For example, Sharpe et al.⁴⁹ applied ISDG (interferometric strain/displacement gage) which is a noncontacting optical technique for measuring strain or displacement between two reflective gage markers, and used an air bearing to avoid the friction in the loading system during the testing process. Chasiotis and Knauss⁵⁰ employ Atomic Force Microscope (AFM) or Scanning Tunneling Microscope (STM) to measure surface topologies of deforming specimens for strain measurement.

The manipulation of the samples is one of the difficult procedures of microtensile testing. The sample with micro and nanoscale features is often fragile and cannot be handled with conventional tools. One can accomplish the specimen handling by mounting the specimen on a support structure that is large or stiff enough to handle easily with typical tools. In recent years, the rapid development of MEMS technology creates another possible microtensile technique. A MEMS-based testing device involves photolithography and surface micromachining techniques to pattern a specimen of desired geometry. Haque and Saif^{51, 52} applied the MEMS-based tensile testing platforms in which the specimen is co-fabricated with the testing apparatus to perform tensile testing of metal films. Co-fabrication has the clear advantage of perfect alignment and gripping. Figure 1.14⁵² shows a microtensile platform of Haque and Saif which utilizes flexure beams for alignment and force measurement, and is small enough for in situ experimentation inside an SEM or TEM. This structure involves tensile loading using a piezoactuator at the right end of the chip and the difference between two markers (A and B) gives the elongation of the specimen.

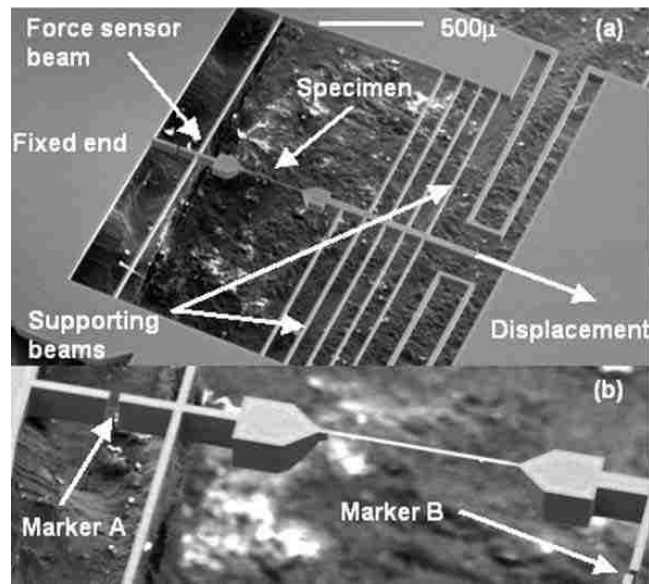


Figure 1.14 SEM image of microtensile test chip of Haque and Saif.⁵²

- Nanoindentation

One of the most popular techniques used to measure mechanical properties such as hardness, elastic modulus, residual stress, viscoelastic behavior, and fracture toughness is nanoindentation.⁵³ The nanoindentation method determines the area of contact by measuring the depth of penetration of the indenter into the specimen surface. Many indenter shapes such as Berkovich, Cube corner, and Vickers have been applied for this purpose. With a known geometry of the indenter, it provides an indirect measurement of contact area at full load and then hardness and reduced modulus are estimated by analyzing the load-displacement curve. Figure 1.15 shows indentation load displacement data for loading and unloading, and important measured parameters.^{54, 55} These simple load displacement curve of nanoindentation can measure properties of hardness, creep, and elastic modulus.

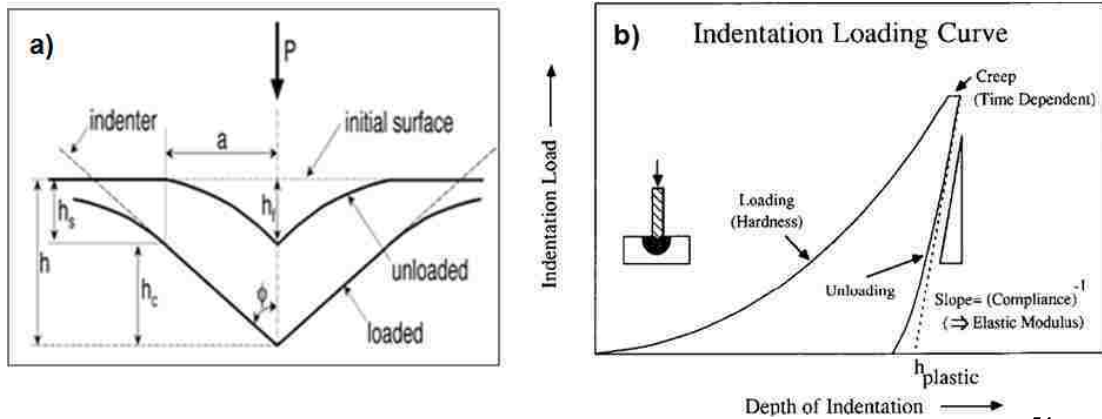


Figure 1.15 (a) Schematic of indenter and specimen surface geometry,⁵⁴ (b) Indentation loading and unloading curves.⁵⁵

In this figure, h is indentation depth, and h_c is contact depth $=h_{max}-h_s$. When the indenter deforms the surface, the contact area (A_c) is calculated from the geometry of the indenter which is a function of contact depth h_c , $A = f(h_c)$. For an ideal Berkovich indenter $A=24.56 h_c^2$ whereas $A= 2.598 h_c^2$ for a cube corner indenter.⁵³

The hardness (H) of the thin film is calculated by $H = P_{max}/A_c$, where P_{max} is the maximum applied force and A_c is the contact area.

The elastic modulus of the material can be determined from the unloading curve. The slope identified in Figure 1.15 is proportional to the modulus, which is often determined using a technique developed by Oliver and Pharr.⁵⁴ However, since the measured elastic behavior during unloading reflects both the indenter (i) and specimen (s) stiffness in series, the measurement really results in E_r which is known as the reduced modulus. It is a function of the Young's modulus and the Poisson ratio for both indenter and specimen. If the indenter is much stiffer than the film, as

is often the case, then the reduced modulus is close to the indented material's plane strain modulus, $E/(1-\nu^2)$.

$$\frac{1}{E_r} = \frac{1 - \nu_s^2}{E_s} + \frac{1 - \nu_i^2}{E_i} \quad 1.7)$$

Creep behavior can be assessed if the load is held constant, and the indenter sinks into the material in a time dependent deformation. The rate of movement of the indenter can be characterized as a strain-rate effect in indentation given by $\dot{\epsilon} = \left(\frac{1}{h}\right) \left(\frac{dh}{dt}\right)$.⁵⁵

There are several advantages of the indentation method: no special sample preparation is required and the test is quick and inexpensive. However, care must be taken when interpreting indentation results, since the hardness is a function only of applied load and projected contact area. The placement of the indenter in different positions of the samples such as over the center of a grain, over a boundary, or over a region of high dislocation density will lead to different observed properties.⁵⁶ The determination of the contact area is rather difficult if the material piles up or sinks in around the indentation. Also, the hardness value can be affected by the substrate. In order to avoid this effect, the indentation used to make the hardness measurement must be small compared to the film thickness.

- Bulge test

The bulge test is often used for characterizing the mechanical properties of thin films. The test is based on measuring the deflection of a membrane under an applied pressure and converted into a stress-strain curve for the films. Standard

semiconductor fabrication is required for sample preparation. Thin film windows can be free-standing films by removing the thick substrate from underneath the film in a lithographically defined area. A requirement in free-standing film sample preparation is to always keep the film in tension so it does not go into compression and wrinkle. If the film alone would be in compression, a composite membrane may be fabricated consisting of the film of interest on an additional film which has sufficient tension to maintain the composite membrane in tension. The initial position of the flat membrane (in tension) before bulging is a very important value for an accurate interpretation of the result.⁵⁷ The height of the films can be measured by several methods, such as laser interferometry,^{42, 58, 59} laser scanning to measure the bulge curvature,⁶⁰ or by capacitance-based measurement.^{4, 7}

The major advantage associated with bulge testing is the capability for testing freestanding films. This advantage does not exist for testing by nanoindentation and wafer curvature techniques. Both techniques fail when the film thickness becomes extremely small. Bulge measurements of free standing films can give more precise results than for films attached with the substrates.

Bulge testing was chosen in this study to investigate time and temperature dependence of viscoelastic stress relaxation in Au and Au alloy thin films. The detailed explanation of the bulge test will be further discussed in Chapter 2, section 2.

1.4.3 Commonly proposed mechanisms

Several fundamental mechanisms have been identified for the observed viscoelastic behavior of thin films, such as diffusional creep, grain boundary sliding, power law creep, and obstacle-controlled dislocation glide. For example, Hyun et al.⁹ used a membrane resonance method to perform stress relaxation experiments on aluminum thin films of varying thickness, and reported a dislocation locking mechanism for the reduction in relaxation rate with an increase in thickness. Kalkman et al.¹⁹ conducted dynamic bulge tests on thin films (W, Al, and Au) and observed stress relaxation at room temperatures with a frequency dependence in Young's modulus and measurable relaxation time constants. Grain boundary sliding was claimed to be the predominant effect causing stress relaxation at room temperature. Here, a few of the important mechanisms will be given in this section.

- Diffusional creep

The viscoelastic mechanisms can also be accomplished by atomic diffusion, either by bulk diffusion, or grain boundary diffusion. Bulk diffusion (Nabarro-Herring creep) involves stress-directed flow of vacancies from tensile to compressive grain boundaries. Consider a cube-shaped grain in a polycrystal deforming at high temperatures under the stress shown in the Figure 1.16(a). The vacancy concentration in equilibrium with a grain boundary will be different for boundary A than for boundary B. If grain boundaries act as sources and sinks for point defects, a concentration gradient of point defects, generally the vacancies, is set up. Vacancies will start to flow from boundary A to boundary B along path AB. If vacancies move

along path AB, atoms have to move along a path BA. Vacancies and atoms move in opposite directions. Atoms are being removed from boundary B and are plated on boundary A. A grain will change shape because atoms are removed from grain boundaries B and put into grain boundaries A, producing a creep strain shown in Figure 1.16(b). The strain rate resulting from Nabarro-Herring creep can be described by^{61, 62}

$$\dot{\epsilon}_{\text{NH}} = \frac{C_1 D_B \Omega}{k T D^2} \sigma \quad \text{1.8}$$

where C_1 is a constant, D_B is the bulk diffusivity, Ω is the atomic volume, k is Boltzman's constant, T is temperature, D is grain diameter, and σ is applied stress.

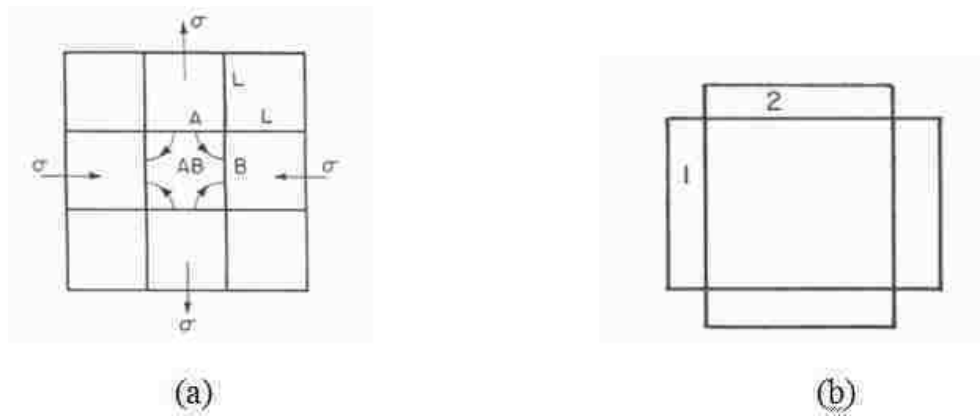


Figure 1.16 a) Flow of vacancies from A-type to B-type boundaries and (b) strain produced in a hypothetical rectangular grain in Nabarro-Herring creep.⁶³

Vacancies can transfer from tensile boundaries to those under compression not only through the grain but also along the grain boundaries. Consider then the transfer of vacancies only along a narrow zone adjacent to the grain boundary. This diffusional creep process, involving vacancy transfer along grain boundaries, is

generally called Coble creep⁶⁴ as shown in Figure 1.17. Let the width of this narrow zone be δ . The area of grain boundary zone intersecting a unit area of a polycrystal of average grain diameter, d , is given by (δ/d) . However, diffusion along this narrow grain boundary zone is determined not by lattice self-diffusion but by grain boundary diffusion. The Coble creep rate associated with diffusional flow along grain boundaries becomes⁶⁵

$$\dot{\epsilon}_C = \frac{C_2 D_{GB} \delta \Omega}{k T D^3} \sigma \quad 1.9)$$

where D_{GB} = grain boundary self-diffusion coefficient, C_2 = constant, σ = applied stress, Ω = atomic volume, k = Boltzman's constant, T = temperature and D = grain diameter. Since Coble creep is more sensitive to grain size than Nabarro-Herring creep, it is expected that Coble creep will dominate the creep rate in very fine grained materials.

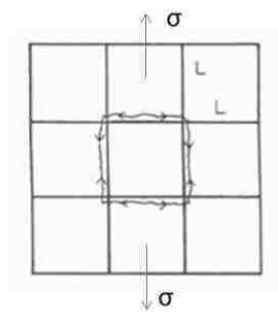


Figure 1.17 Flow of vacancies for Coble creep.⁶³

- Grain boundary sliding

Grain boundaries can slide between two adjacent grains under an applied stress. The shear stress which initially acts across a boundary is gradually reduced through viscous slip while the grain corners sustain more and more of the total shearing force.⁶⁶ Figure 1.18 presents how the sliding process occurs. With applied shear stress, it causes grain 1 to slide over grain 2 to build up opposing stresses at the triple junctions of the grain boundaries. This relaxation process will continue until the shear stress has dropped to zero across most of the length of the boundary. When low stress is applied, the distortion at the edge of the boundary is purely elastic. Once the applied stress is removed, the distortion subjects the boundary to a reverse shear stress and produces the elastic aftereffect. In the case of complete recovery, this internal shear stress drives the recovery process until the grain boundary returns to its original condition and there is no distortion at the edge of the boundary.

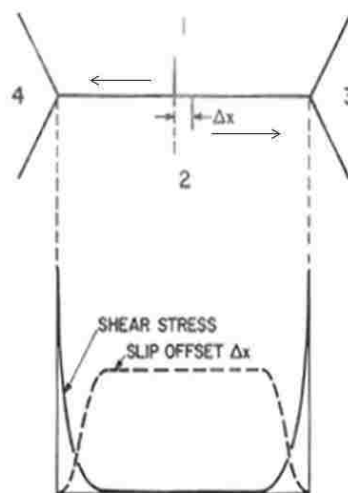


Figure 1.18 Relaxation of an initially uniform shear stress distribution by grain boundary sliding.⁶⁶

Zener⁶⁷ has calculated the relaxation modulus(E_R) in the presence of grain boundary sliding under the simplifying assumptions of isotropic material and spherical grains. He obtained the relaxed modulus compared to the unrelaxed modulus as given by

$$\frac{E_R}{E_U} = \frac{1}{2} \left(\frac{7 + 5\nu}{7 + \nu - 5\nu^2} \right) \quad \mathbf{1.10}$$

where ν is Poisson's ratio. For a material with $\nu = 0.44$, the modulus decay with grain boundary sliding is 29% which is very large relaxation. However, this effect depends on the assumption that grain boundary sliding can occur entirely across the boundary. If the material is anisotropic or the grain sliding is obstructed by grain boundary roughness, the modulus decay will be much smaller. Although grain boundary sliding is a commonly referred to relaxation mechanism, it is usually not an independent deformation, as it requires other deformations to be active.

- Power law creep

At intermediate to high stress and high temperature, the deformation of a material can be accomplished by diffusion-controlled movement of dislocations. Dislocation creep includes the movement of dislocations by diffusional transport of vacancies under the influence of applied stress. Such a motion is termed climb and requires a rearrangement of atoms, again by vacancy diffusion. As grain boundaries are not a major factor, the strain rate is not strongly affected by grain size, but the resistance to the climb process is such that there is strong stress dependence. Also, it

is temperature dependent since a diffusion process is involved. Thus, the equation has the form⁶⁸

$$\dot{\epsilon} = \frac{A_3 \sigma^m}{T} e^{\frac{-Q}{RT}} \quad \mathbf{1.11)}$$

where m varies with material and test conditions.

Some studies report power law creep to be responsible for stress relaxation of some metal films at high stress/or temperature. For example, Hwang et al.³⁹ studied the deformation mechanism of electroplated Cu films and believed that the dominant deformation mechanism is power-law creep at temperatures between 180 °C and 400 °C.

- Obstacle-controlled dislocation glide

Below the ideal shear strength and at low temperatures, deformation can be accomplished by the movement of dislocations. This motion is almost always hindered by obstacles such as other dislocations, solute atoms or precipitates, or grain boundaries. The strengthening effect of a material depends on the strength of obstacles as classified in Table 1.2,⁵ where ΔF is the total free energy or the activation energy required to overcome the obstacles without aid from external stress, $\hat{\tau}$ is the shear strength without thermal energy, μ is the shear modulus and b is Burgers' vector.

| <i>Obstacle strength</i> | ΔF | τ | <i>Example</i> |
|--------------------------|-------------------|------------------------------|---|
| Strong | $2 \mu b^3$ | $> \frac{\mu b}{\ell}$ | Dispersions; large or strong precipitates (spacing ℓ) |
| Medium | $0.2-1.0 \mu b^3$ | $\approx \frac{\mu b}{\ell}$ | Forest dislocations, radiation damage; small or weak precipitates (spacing ℓ) |
| Weak | $< 0.2 \mu b^3$ | $\ll \frac{\mu b}{\ell}$ | Lattice resistance; solution hardening (solute spacing ℓ) |

Table 1.2 Characteristics of obstacles for dislocation glide.

The strain rate resulting from discrete-obstacle controlled plasticity is given by⁵

$$\dot{\gamma} = \dot{\gamma}_0 \left(\frac{\sigma_s}{\mu} \right)^2 \exp \left[- \frac{\Delta F}{kT} \left(1 - \left(\frac{\sigma_s}{\tau} \right)^p \right)^q \right] \quad \mathbf{1.12}$$

where p and q are parameters that depend on the obstacle. For discrete obstacles, p and q are equal to 1. For plasticity limited by lattice resistance, Raffo⁶⁹ proposed the choice of p=3/4 and q=4/3 for the best fit to experimental data of tungsten.

Consider a dislocation pinned at two ends by obstacles that are spaced at a distance l apart as presented in Figure 1.19.

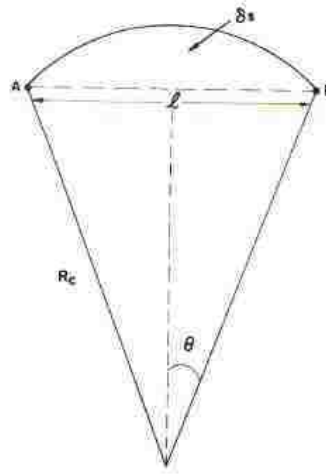


Figure 1.19 The bowing of a dislocation pinned at point A and B under applied stress.

An applied stress (σ) causes a bowing of a dislocation and the radius of curvature (R_c) between pinning points is given by⁶⁶

$$R_c = \frac{1}{2} Gb/\sigma \quad \mathbf{1.13)}$$

where G is shear modulus and b is burger vector. The dislocation moves back when the applied stress is removed which is time dependent behavior. The area (δs) swept out by a dislocation under a stress (σ) is

$$\delta s = \frac{1}{12} \left(\frac{l^3}{R_c} \right) \quad \mathbf{1.14)}$$

If the crystal material has a certain number of dislocation segments per unit volume (N_V), the strain due to the dislocation bowing is

$$\varepsilon = b(\delta s)N_V \quad \mathbf{1.15)}$$

The difference between the modulus with and without dislocation (the modulus defect), ΔG , can be expressed⁶⁶

$$\frac{\Delta G}{G} = \frac{1}{6} \rho l^2 \quad \mathbf{1.16)}$$

where G is the modulus in the absence of dislocations, and $\rho = N_v l$ is dislocation density.

1.4.4 Modeling linear viscoelastic behavior

Linear viscoelasticity is a type of viscoelastic behavior that adds the condition that the time dependent modulus is independent of the magnitude of stress and strain. Then the stress relaxation can be calculated by using the Boltzman Superposition Principle. Boltzman proposed that (1) the time dependent stress depends on strain history, and (2) each strain step makes an independent contribution to the final stress relaxation so that final stress relaxation can be obtained by the simple addition of each incremental strain as given by the equation:⁷⁰

$$\sigma(t) = \sigma_0 + \varepsilon_0 E(t) + \int_0^t E(t - \xi) \frac{d\varepsilon(\xi)}{d\xi} d\xi \quad \mathbf{1.17)}$$

where σ_0 is the residual stress, ε_0 is $\varepsilon(t=0 \text{ sec})$, $\frac{d\varepsilon(\xi)}{d\xi}$ is the strain rate, and $E(t)$ is the time dependent modulus which is given by

$$E(t) = E_0 \left(1 - \sum_{i=1}^N P_i \left(1 - e^{-\frac{t}{\tau_i}} \right) \right) \quad \mathbf{1.18)}$$

where E_0 is the instantaneous modulus of the films, P_i is i 'th Prony constant and τ_i is i 'th time constant.

It has been reported that the viscoelastic behavior in Au thin films is linear at room temperature.⁴ The evidence for this is presented as identical results of time dependence of stress at different strains by using a bulge capacitance system. Yan et al.⁴ showed a more stringent test of linearity for Au films at room temperature by using multiple step changes of strains as presented in Figure 1.20. The linear viscoelastic model and superposition were used to calculate the stress relaxation as it depended on time. The good match between the experimental data and the simulation were reported, and verified that linear viscoelasticity and superposition are appropriate descriptions of the Au films.

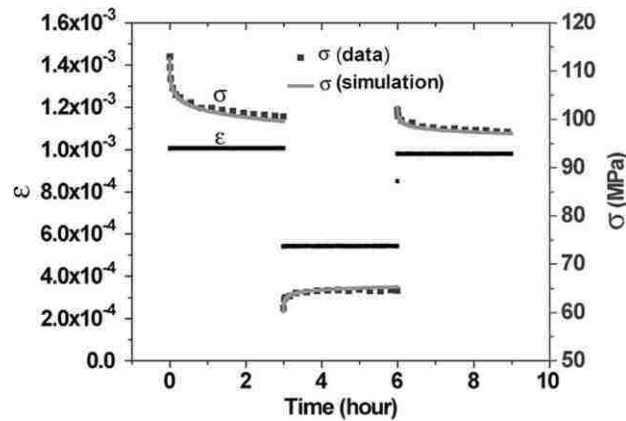


Figure 1.20 The strain and stress in a three-step experiment.⁴

Hyun et al.⁹ also reported the linear viscoelastic behavior of different materials other than Au by using stress relaxation experiment. Figure 1.21 shows results of a stress relaxation experiment which validates the linear viscoelastic

behavior. The elastic modulus measurement shows that strain steps produced by different bulge pressure steps lead to the same elastic modulus decay over time, fulfilling linearity requirements.

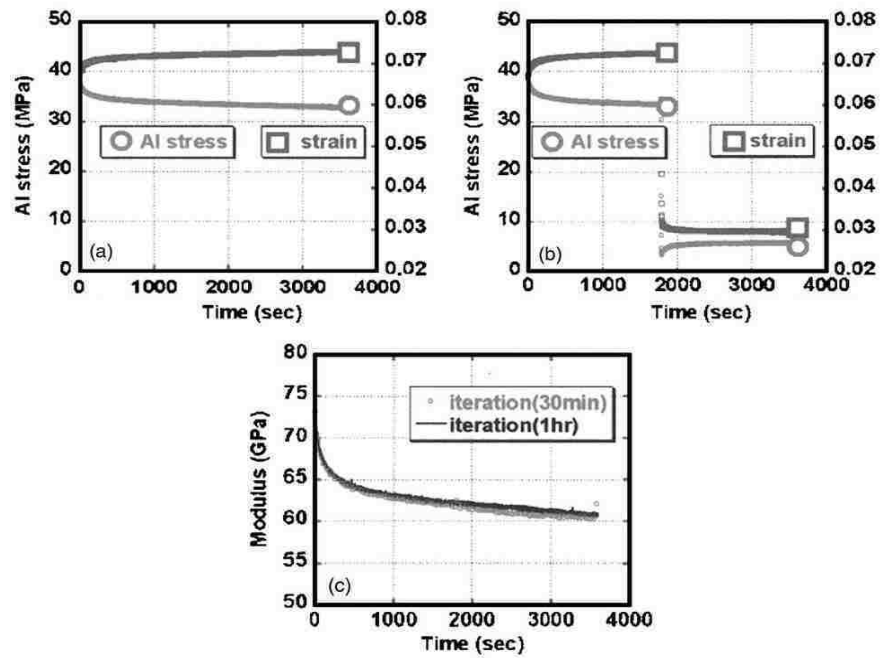


Figure 1.21 (a) Stress and strain of Al film at constant pressure of 30 torr for 1 hour, (b) Same film but different step pressure step: 30 torr for 30 min and down to 10 torr for 30 min, and (c) The time-dependent modulus deduced from (a) and (b).⁹

1.4.5 Activation volume and dislocation mobility

It is well known that dislocation mobility of nanoscale materials which controls plastic deformation is usually thermally activated. Therefore, the activation volume which is one of the thermal activation parameters is the key issue to identify

the possible deformation mechanism in the materials. The plastic strain rate ($\dot{\gamma}$) dependence on temperature can be written in the Arrhenius equation.^{71,72}

$$\dot{\gamma} = \dot{\gamma}_0 \exp\left(-\frac{G(\tau^*)}{kT}\right) \quad \mathbf{1.19}$$

where $G(\tau^*)$ is the stress-dependent activation energy for the thermally activated dislocation motion, k is the Boltzman constant. The activation volume (v^*) can be defined as⁷¹

$$v^* = kT \left(\frac{\partial \ln \dot{\gamma}}{\partial \tau^*}\right) = MkT \left(\frac{\partial \ln \dot{\epsilon}}{\partial \sigma^*}\right) \quad \mathbf{1.20}$$

where σ^* and τ^* are the thermal component of applied stress and shear stress, respectively, and M is the conversion factor from shear stress to uniaxial tensile stress. The activation volume can be measured by several techniques such as uniaxial tensile testing,^{73, 74} nanoindentation,^{75, 76} strain rate jump test,⁷⁷ and stress relaxation.^{78, 79} The first two methods commonly measure the flow stress (σ_f) or hardness (H) as a function of strain rate ($\dot{\epsilon}$) and determine the activation volume from the slope of a linear fit of $\ln \dot{\epsilon}$ versus σ_f or H .

Strain rate jump test is a transient test which observes the change in stress ($\Delta\tau$) when the strain rate is suddenly changed from $\dot{\gamma}_1$ to $\dot{\gamma}_2$. V_a which is the apparent activation volume can be defined by the formula.⁸⁰

$$V_a = kT \left(\frac{\ln \left(\frac{\dot{\gamma}_1}{\dot{\gamma}_2} \right)}{\Delta\tau} \right) \quad \mathbf{1.21)}$$

Another type of transient test is stress relaxation. The apparent activation volume is determined from the first stress relaxation and can be expressed as⁸⁰

$$\Delta\tau(t) = -\frac{kT}{V_a} \ln \left(1 + \frac{t}{C_r} \right) \quad \mathbf{1.22)}$$

where $\Delta\tau$ is the decay of shear stress as a function of time (t) and C_r is the time constant. Based on the Orowan equation,⁸¹ the shear strain rate ($\dot{\gamma}$) is a consequence of two parameters: the dislocation velocity (v) and mobile dislocation density (ρ_m) as $\dot{\gamma} = b\rho v$. To separate a contribution of two variation to strain rate, repeated stress relaxation tests are performed to determine physical activation volume (V^*).^{80, 82}

$$V^* = kT \frac{\ln \left(\frac{\dot{\gamma}_{i2}}{\dot{\gamma}_{f1}} \right)}{\Delta\tau} \quad \mathbf{1.23)}$$

where $\dot{\gamma}_{i2}$ and $\dot{\gamma}_{f1}$ is the onset of stress relaxation² and the end of stress relaxation 1, respectively. The schematic procedure of repeated stress relaxations is presented in Figure 1.22.⁸²

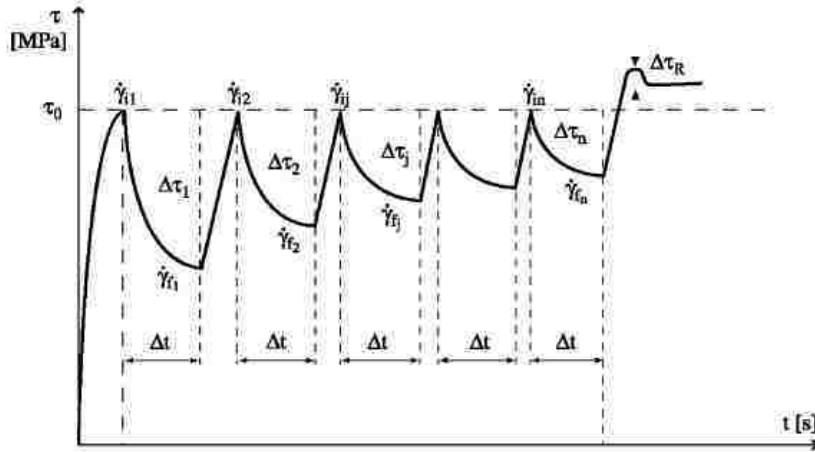


Figure 1.22 Schematic procedure and parameters of repeated stress relaxation.⁸²

Since the change in stress is fast enough to assume the dislocation density is the same, the physical activation volume incorporates the stress dependence of the dislocation velocity only. In contrast, the apparent activation volume characterizes the stress dependence of the mobile dislocation density. The mobile dislocation density (ρ_m) and the dislocation velocity (v) can be expressed by a power relation⁸⁰

$$\frac{\rho_m}{\rho_{m0}} = \left(\frac{v}{v_0}\right)^\beta \quad 1.24)$$

where ρ_{m0} and v_0 is the initial mobile dislocation density and dislocation velocity, respectively. The mobile dislocation density during a stress relaxation test can be expressed by

$$\frac{\rho_m}{\rho_{m0}} = \left(\frac{C_r}{C_r + t}\right)^{\beta/(1+\beta)} \quad 1.25)$$

where β is defined as $\beta = \frac{\Omega}{1+K/M} - 1$, K is a strain-hardening coefficient, M is the elastic modulus of the specimen-machine system, and Ω is the ratio of V_a to V^* . Repeated stress relaxation was proposed to determine physical activation volume (V^*), which relates to the V_a as $\Omega = V_a/V^*$.

Activation volume has been measured to obtain insight into the rate-controlling deformation mechanism. For example, Kobrinsky⁸³ measured the activation volume by stress relaxation in Ag films by observing the characteristics of dislocation motion by in situ Transmission Electron Microscopy (TEM). They conclude the value of activation volume with supporting TEM results is consistent with forest dislocation-obstacle controlled plasticity.

2. Experimental description

This chapter describes the experimental set up for the research on time and temperature dependence of stress and stress relaxation in Au and Au alloy films. The first part of the chapter discusses the sample design and fabrication. The second part discusses the process development for the pure and alloy films; subsequent characterization of microstructure and composition are described as well. The rest of the chapter involves the bulge measurement technique which includes the experimental setup for pressure ramp and relaxation testing. It is noted that all results presented in chapters 3-7 of this dissertation were obtained by the same experimental procedures of bulge testing that are presented in this chapter.

2.1 Sample design and fabrication

Gas pressure bulge testing requires some specific samples whose design is shown in Figure 2.1. The thin film membrane is suspended over a window 12 mm by either 2 or 3 mm in the center of a 20 mm by 20 mm Si die. The bulge samples are fabricated by using standard semiconductor fabrication methods as shown in Figure 2.2.

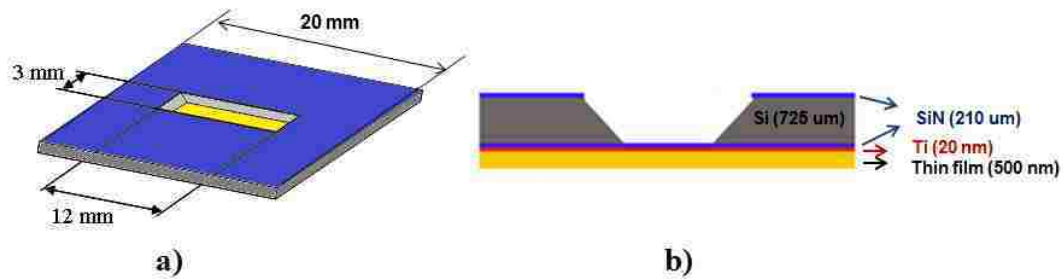


Figure 2.1 Bulge sample a) bottom view and b) cross section view.

Silicon dies are coated on both sides with 210 nm of SiN; the back side SiN is patterned to create a window of 3 mm (or 2 mm) by 12 mm using standard photolithography; the silicon in the window is partially etched with KOH concentration of 45 % (weight) and a temperature of 85 °C until the silicon is left at approximately 60-100 um. A 20 nm film of Ti is then sputter deposited on the front side as an adhesive layer over the SiN. Finally, Au or Au alloy thin films are deposited by DC magnetron sputtering on the Ti. The deposition and patterning of the SiN films was previously carried out at Bell Laboratories. The etching of the silicon and the deposition of metal thin films were done at Lehigh. Details of these steps will be presented in a following section.

Bulge experiments require a tensile residual stress in the membranes that are to be bulged. If the unpressurized membrane stress ever becomes compressive the membrane buckles and/or wrinkles and it becomes very difficult to acquire reliable results.⁸⁴ If the as-deposited thin Au film is in a compressive state the composite membrane of Au plus SiN may not be because the SiN film by itself is in tension. However, because the typical Au films in the thesis are 500 nm thick and the SiN is

only 210 nm thick the Au compressive stress cannot be very large for the composite to remain tensile.

If the Au as deposited is in a strongly compressive state or if the Au film is to be measured after removal of the SiN so there is no balancing tensile stress as there is in the composite membrane, there is another way to proceed. After deposition the Au plus SiN plus the remaining thickness of Si substrate not yet etched away can be annealed at elevated temperature. Raising the temperature will increase the compressive stress in the Au film because of the difference in thermal expansion of the Au and the Si substrate. Once a certain critical temperature is reached, plastic yielding in the Au will take place. Because the Au is supported by the stiffness of the silicon substrate this compressive plastic deformation of the Au will take place without distortion of the Au film. When the composite is returned to lower temperature the Au is put in tension because of the differential thermal expansion of Au and Si. The remaining Si substrate can then be etched away. In this study, some thin films after deposition were annealed at 260 °C for 2 hours and cooled to room temperature. The remaining Si was then etched away in KOH leaving the SiN plus Au in tension. This pre-etching annealing procedure even allows the removal of the SiN layer because the Au itself is in tension. Studies of free standing Au can then be carried out.

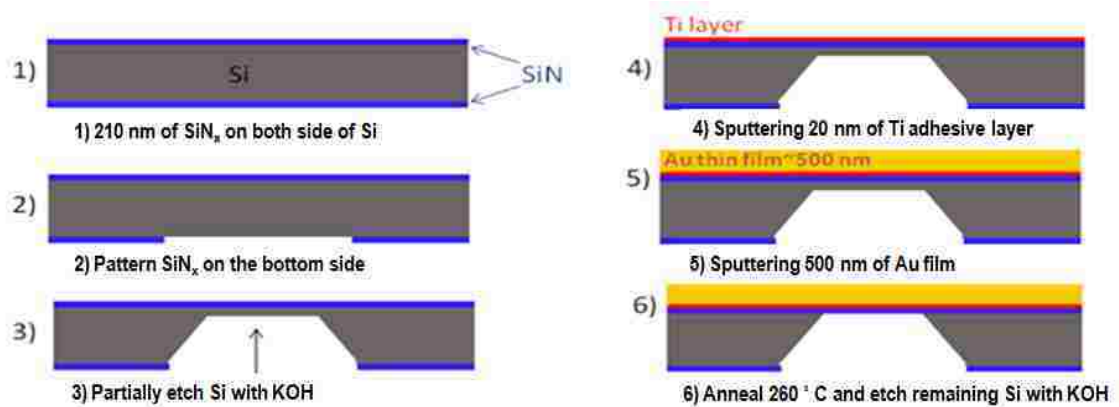


Figure 2.2 Sample fabrication for bulge testing.

2.2 Fabrication of Au and Au alloy thin films

For this research, the three types of thin films that are fabricated are as follows:

1. Pure Au films with normal and different grain sizes.
2. Solid solution AuV films with different V compositions.
3. Oxide dispersion strengthened Au films by addition of V₂O₅ nanoparticles.

All three types of thin films are produced by DC magnetron sputtering using a system obtained from AJA international (ATC2200 sputtering system). The metal thin films are deposited on bulge substrates by the sputtering guns carrying elemental targets. For example, we use only two guns in the sputter chamber to deposit pure Au films with a Ti adhesion layer. For Au alloy films, such as AuV or AuV₂O₅, we require three sputter targets in the guns consisting of Au, V and Ti.

1. Conditions for deposition of pure Au films.

- The base pressure is about $5-7 \times 10^{-7}$ Torr.
- The deposition of Au thin films requires 2 guns – Au and Ti
- The height of the substrate is set to 4 inches on the indicator which is the distance from the top of the chamber to the substrate.
- The substrate is rotated during deposition to provide uniform film thickness.
- A film of Titanium is deposited as an adhesive layer between the substrate and the Au films.
 - The angle of the Titanium gun is set at 4 on the indicator which is about 61.3° from the horizontal (based on AJA drawing).
 - The sputtering gas is Ar at a pressure of 4 mTorr.
 - The gun power is 150 W and the deposition time is 2.50 min. As the deposition rate is 8 nm/min, the thickness of the Titanium film is about 20 nm.
- A film of Au is deposited
 - The angle of Au gun is set at 4 on the indicator.
 - The sputtering gas is Ar at pressure 4 mTorr.
 - The gun power of Au is fixed at 150 W. Using a deposition time of 10 minutes and determining film thickness by using a step height measurement from an optical profilometer with a high resolution optical sensor (STIL: CHR 150-N), the

deposition rate of pure Au was approximately 50 nm/min. The thickness of all thin films was therefore approximately 500 nm. We also determine the deposition rate of Au by measuring the mass of a glass slide before and after deposition for a certain time. With the known density of Au and the deposited area of the glass slide (7.5 cm x 5 cm), we calculate the thickness of the thin film on the glass slide and determine the deposition rate. The two methods provide approximately the same deposition rates.

- A series of pure Au thin films with various grain sizes is deposited at different substrate temperatures controlled by a temperature controller (AJA international model SHQ 2001-C) from room temperature to 400 degree Celsius.

2. Condition of deposition processes of solid solution (AuV)

- The base pressure is about $5-7 \times 10^{-7}$ Torr.
- The deposition of solid solution thin films is prepared by cosputter deposition and requires 3 guns – Au, V and Ti.
- The temperature of the sputtering is nominally room temperature.
- The V gun operates in the Self Run Mode via Sparc-LE (Small Package Arc Repression Circuit), with the DC power periodically pulsed between zero and the set point.
- The height of the substrate is set to 4 inches on the indicator.

- The substrate is rotated during deposition to maintain uniform film thickness and homogeneous composition.
- A film of Titanium is deposited as an adhesive layer between the substrate and the AuV film.
 - The angle of Titanium gun is set at 4 on the indicator.
 - The sputtering gas is Ar at pressure 4 mTorr,
 - The gun power is 150 W and the deposition time is 2.5 min.
As the deposition rate is 8 nm/min, the thickness of the Titanium film is about 20 nm
- The deposition of AuV thin film requires 2 guns –Au and V
 - The angle of Au and V guns are set at 4 on the indicator.
 - The sputtering gas is Ar at 4 mTorr.
 - The films are prepared with five different power settings for the V gun: 0, 25, 60, 150, and 200 watt in order to vary the V composition while the power of Au gun is constant at 150 watt.

3. Condition of deposition processes of Au V₂O₅

AuV₂O₅ thin films are successfully fabricated by reactive co-sputtering. The basic conditions of the deposition process are the same as for the Au-V thin films described above. In order to deposit AuV₂O₅ films, oxygen is introduced separately into the deposition chamber to facilitate reaction with V and formation of VO_x compound. In this study, the optimum amount of oxygen is 0.1 mtorr.⁸⁵ It is

introduced into the chamber first. Then, the total pressure of Ar and O₂ is brought up to 4 mTorr by admitting Ar.

The power of the two guns is 150 W for Au and 200W for V which gives a deposition rate at 1.14 nm/s. Using a deposition time of 7 min 19 second, the thickness of AuV₂O₅ thin films is approximately 500 nm.

2.3 Microstructure and composition investigation

1. Scanning Electron Microscopy (SEM: Hitachi 4300VP) is used to investigate the surface microstructure of the Au and Au alloy thin films, especially grain size. Magnification at 50X is used to compare different grain sizes produced at different deposition temperatures. The mean lineal intercept method following ASTM standard E112-88 is applied to estimate the grain size of the thin films.

2. Atomic Force Microscopy (AFM: DI3000) was applied to some films to clearly show the surface and to quantitatively measure film roughness.

3. Rutherford Back Scattering (RBS) is a technique to analyze the true film composition. It was used to calibrate the composition of one film. The true composition of that V/Au film, 4.5 at. %V, was determined by Dr. Stephen Menasian of Rutgers University for a sample deposited by Bannuru.⁸⁶

4. Energy Dispersive spectrometry (EDS) is used to determine the relative composition of the elements present in a sample. The EDS system relates the

quantitative intensity of x-rays emitted to their x-ray energy. The energy of a peak identifies the element while the relative amount of that element is determined from the area under the peak. EDS can only give relative element quantities but when calibrated with an absolute standard thin film composition obtained by Rutherford Back Scattering (RBS) the true composition of other films can be determined.

2.4 Bulge testing

2.4.1 The bulge measurement technique

Time and temperature dependence of viscoelastic stress relaxation in Au and Au alloy thin films are measured by using bulge testing.⁴²

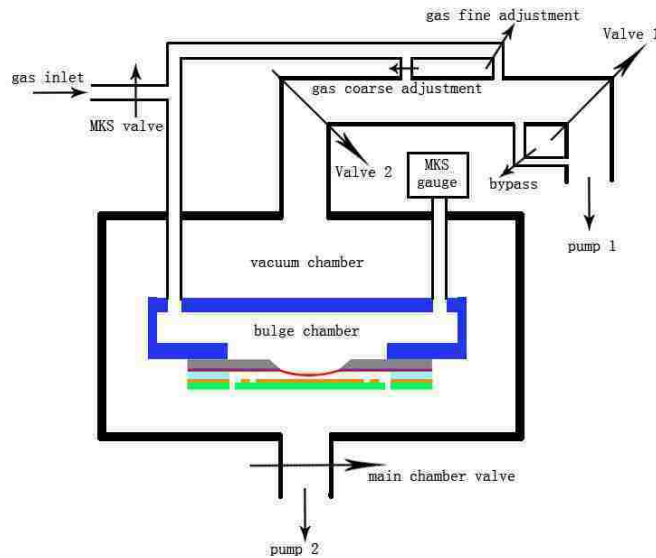


Figure 2.3 Experimental setup of bulge system.

As shown in the Figure 2.3, our bulge test system has two chambers: the vacuum chamber and the bulge chamber which is inside the vacuum chamber.

Figure 2.4 shows an enlarged view of the inside of the bulge chamber. A thin film sample is placed in the bulge chamber and the chamber evacuated. The fixed capacitor plate is 6 mm by 6 mm and is surrounded by a closely spaced grounded guard ring to limit the fringing field. The capacitor plate is positioned over the center of the membrane and separated from it by a metal spacer that surrounds the membrane. There are 8 heaters embedded in the stainless steel base of the chamber to enable measurements at elevated temperature.

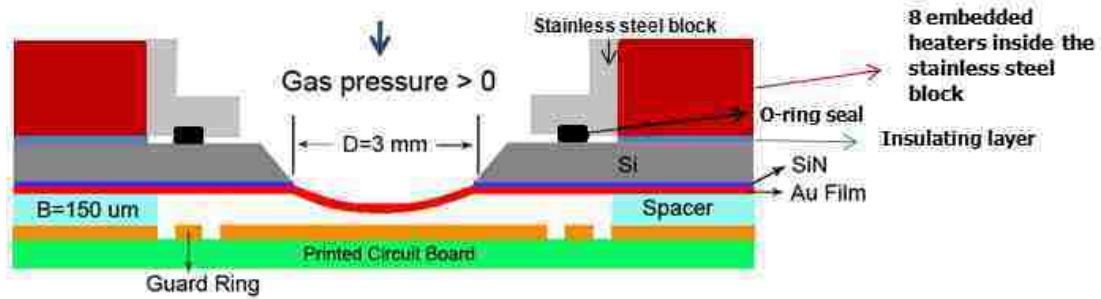


Figure 2.4 Schematic demonstration of bulge test in the bulge chamber.

A pressure (P) of N_2 gas is applied to the bulge chamber and thus to one side of the sample membrane. The other side of the membrane is at the vacuum of the outer chamber. The pressure difference bulges the thin membrane. The applied pressure in the bulge chamber is controlled by an MKS (Type 250) pressure controller under command of a computer with a LabView program. The MKS controller adjusts the gas inlet valve to obtain the desired pressure as measured by the MKS pressure gauge.

The height (H) of the bulge provides information about the strain in the film. The height together with the pressure difference defines the stress. The bulge height

is determined by the change of capacitance between the bulged film and a fixed flat capacitor plate. To measure the capacity between the metal of the membrane and a fixed capacitor plate, a sine wave generator (Agilent, 33220 A) at a frequency of 100 kHz is applied to the membrane. A second generator at the same frequency and phase locked to the first but 180 out of phase with it is applied to a reference capacitor with a known capacitance of 0.5415 μF . The currents from the two generators through the two capacitors are summed in a charge sensitive preamplifier whose output is sent to a lock-in amplifier (SR 530). Figure 2.5 demonstrates the electrical setup for the capacity measurement.

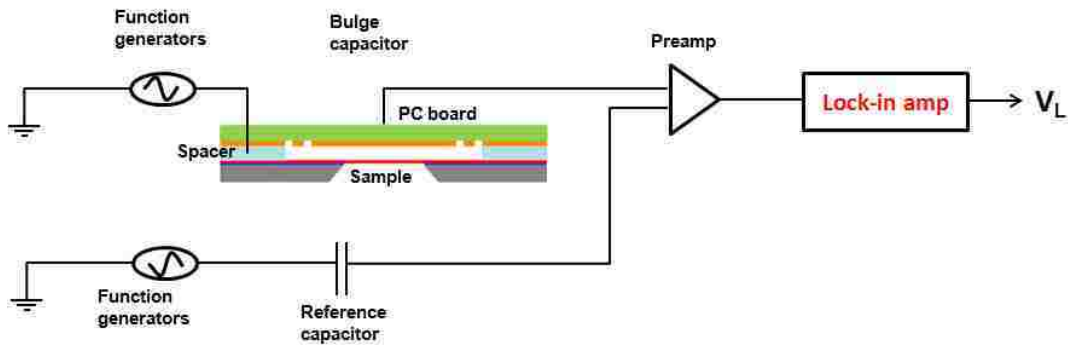


Figure 2.5 Electrical setup for the capacity measurement.

When the currents flowing through the two capacitors are approximately equal, the lock-in will show a value close to zero. At this balance setting, the ratio of the capacitance is inversely-proportional to the ratio of the amplitudes of the driving voltage:

$$U_1 \cdot C_1 \sim \frac{U_1}{Z_1} = U_2 \cdot C_2 \sim \frac{U_2}{Z_1} \quad \mathbf{2.1)}$$

Then when the capacitance of the bulge capacitor is changed by a change in bulge height, the currents are unbalanced and the lock-in amplifier will measure the difference.

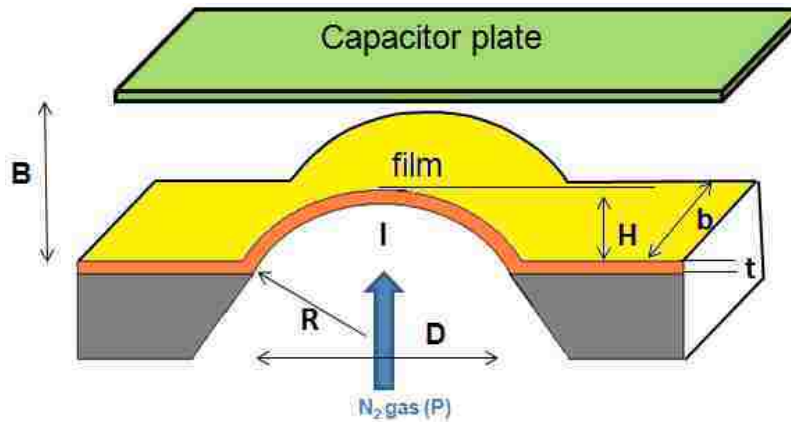


Figure 2.6 Schematic of bulge test and description of bulge parameters when gas pressure > 0 .

Figure 2.6 shows that a pressure (P) of N_2 gas is applied to create the pressure difference between both sides of the film and able to bulge the thin membrane. The shape of the bulged film can be assumed as a long cylinder fixed at the edge of the window as presented in Figure 2.7 taken by Optical Profilometer. Only the center 6 mm of the bulged film is considered since the height is uniform over this length and the shape can be treated as a thin-walled cylinder.

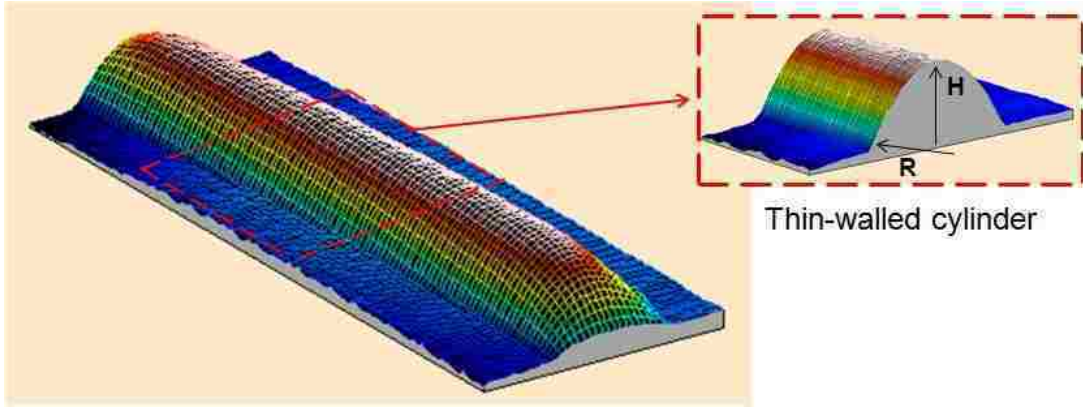


Figure 2.7 Schematic demonstration of bulged shape in thin film when $P > 0$ torr.

The bulge height (H) is determined by the change of the capacitance between the bulged film and a fixed flat capacitor plate by using the following equations:⁴

$$C = \epsilon_0 b \int_{-\frac{D}{2}}^{\frac{D}{2}} \frac{dx}{B - y(x)} \quad 2.2)$$

and

$$y(x) = \sqrt{R^2 - x^2} - \sqrt{R^2 - \frac{D^2}{4}} \quad 2.3)$$

where $y(x)$ is the bulge height at x , the integration yields

$$C = 4\epsilon_0 b \frac{\sqrt{4R^2 - D^2} \cdot \arctan\left(\frac{D}{\sqrt{4B\sqrt{4R^2 - D^2} - D^2}}\right)}{\sqrt{4B\sqrt{4R^2 - D^2} - D^2}} \quad 2.4)$$

and the geometry relation between H and R is

$$H = R - \sqrt{R^2 - \frac{D^2}{4}} \quad 2.5)$$

As indicated in Figure 2.6, P is the applied pressure, H is the bulge height, R is the bulge radius, b is the width of the capacitor plate, D is the width of the window, B is the gap spacing between the unbulged film and the capacitor plate.

Once R is obtained, the stress in the films can be calculated as the hoop stress acting on a thin-walled cylinder. This lead to the stress in terms of pressure as

$$\sigma = \frac{P \cdot R}{t} \quad 2.6)$$

and the strain ε of the film can be computed from

$$\varepsilon = \frac{l - D}{D} = \frac{2R \cdot \arcsin\left(\frac{D}{2R}\right) - D}{D} \quad 2.7)$$

where l is the length of the bulged film.

2.4.2 Bulge test setup for stress relaxation experiments

Based on the bulge test described above, stress relaxation is measured to determine the viscoelastic properties of the films. Stress relaxation in these experiments is the stress decay over time when the samples are subjected to constant strain. For most experiments conducted in this study, the films are maintained at a constant strain of 0.001 for 3 hours. The strain is held constant when the bulge height (H) is kept at a constant value by maintaining a constant bulge capacitance (C) during the 3 hour relaxation. The bulge height is controlled by a feedback loop of pressure introduced by the Labview program. Assume the thin film is maintained at the bulge height H_0 . When the stress in the film relaxes at a given pressure, the bulge height

will increase. Therefore, the pressure needs to be decreased to bring the bulge height back to the desired constant value. This pressure change, ΔP , is given by

$$\Delta P = \left(\frac{8t\sigma_0}{D^2} + \frac{64tMH_0^2}{D^4} \right) \cdot \Delta H \quad 2.8)$$

and

$$\Delta H = (H_0 - H_1) = \frac{3}{2} \cdot \left(\frac{\varepsilon_0 bD}{C_1} - \frac{\varepsilon_0 bD}{C_0} \right) \quad 2.9)$$

where H_0 and C_0 are the bulge height and bulge capacitance value that is to be kept constant, H_1 and C_1 are real-time bulge height and bulge capacitance, σ_0 is the residual stress of the film, M is the plane strain modulus. The value of Eq. 2.8) and 2.9) is to estimate the sensitivity needed in the feedback loop to hold the capacitance and H constant.

2.4.3 Pressure ramp and relaxation testing

Two experimental procedures are used to measure the relaxation behavior of the thin films. The first is a pressure ramp. The pressure from 0 torr is ramped up to reach a desired value before suddenly ramping down to 0 torr again at the same pressure rate. The typical time required for a pressure ramp rate of 4 torr/sec to increase the strain from 0 to 0.1% (0.001) is between 12 and 25 seconds, depending on the residual stress in the films. The pressure ramp test can be analyzed as a stress-strain curve from which the residual stress and plain strain modulus can be obtained. The residual stress is determined by the extrapolated y-intercept of the unloading segment of the stress-strain curve. The load and unload segments can have a different slope due to the fast relaxation during the short time period that the pressure ramp

occurs. The elastic modulus measured here is determined from the slope of the unloading segment of the stress-strain curve and is the plane-strain modulus due to the geometry of the film.^{42, 84}

The second procedure is stress relaxation testing which starts with a pressure ramp to a strain of 0.001 where it is held constant for 3 hours before ramping down to zero pressure. The strain is maintained at a constant value by the feedback loop program that controls the bulge height as described above. The relaxation results are characterized in terms of stress relaxation and normalized modulus relaxation. The normalized modulus is the plane strain modulus at a given time, $M(t) = \sigma(t)/\epsilon$, divided by the initial modulus, $M(t=0) = \sigma(t=0)/\epsilon$.

Figure 2.8 shows the schematic of strain versus time for pressure ramp and relaxation testing. The typical results of the two types of bulge experiments are shown in Figure 2.9.

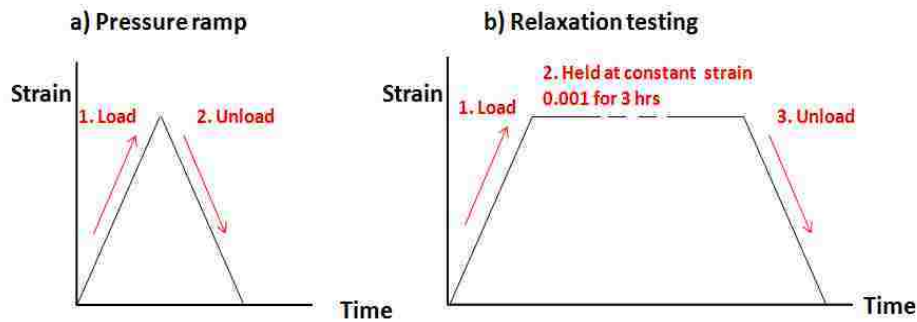


Figure 2.8 Schematic of strain versus time for a) Pressure ramp and b) Relaxation testing.

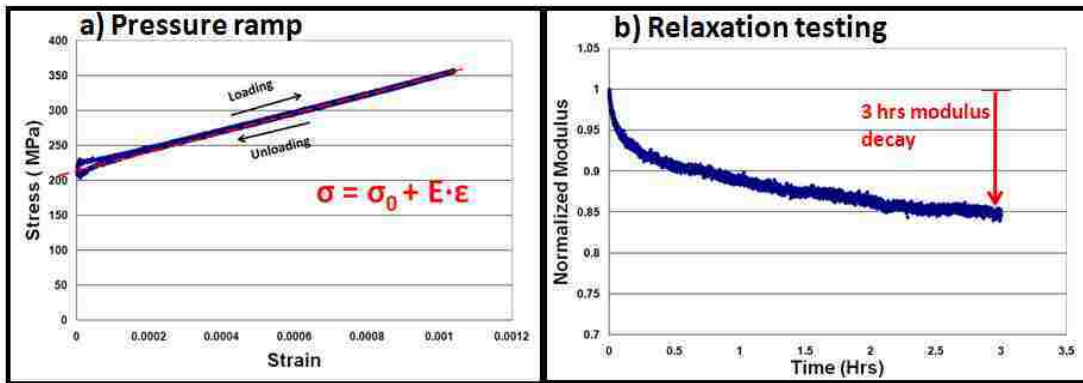


Figure 2.9 Typical results of bulge experiments a) Pressure ramp and b) Relaxation testing.

It has been shown that the initial relaxation behavior has two components, one viscoelastic (fully recoverable) and one viscoplastic.⁷ A “run” is a sequence of a pressure ramp and a 3 hour relaxation test. The sequence is performed multiple times to eliminate initial film plasticity and to bring a film to a steady state displaying only viscoelasticity. To allow time for full viscoelastic recovery at zero strain between runs, only one run is carried out per day. Each thin film requires from 3-5 runs at a single temperature to reach this steady state.

The temperature dependence of Au and Au alloy thin films is investigated in the temperature range from 20 to 80 °C. The flow chart below shows the experimental procedure for the films until the film reaches a steady state at each temperature. More details are given in the next chapter.

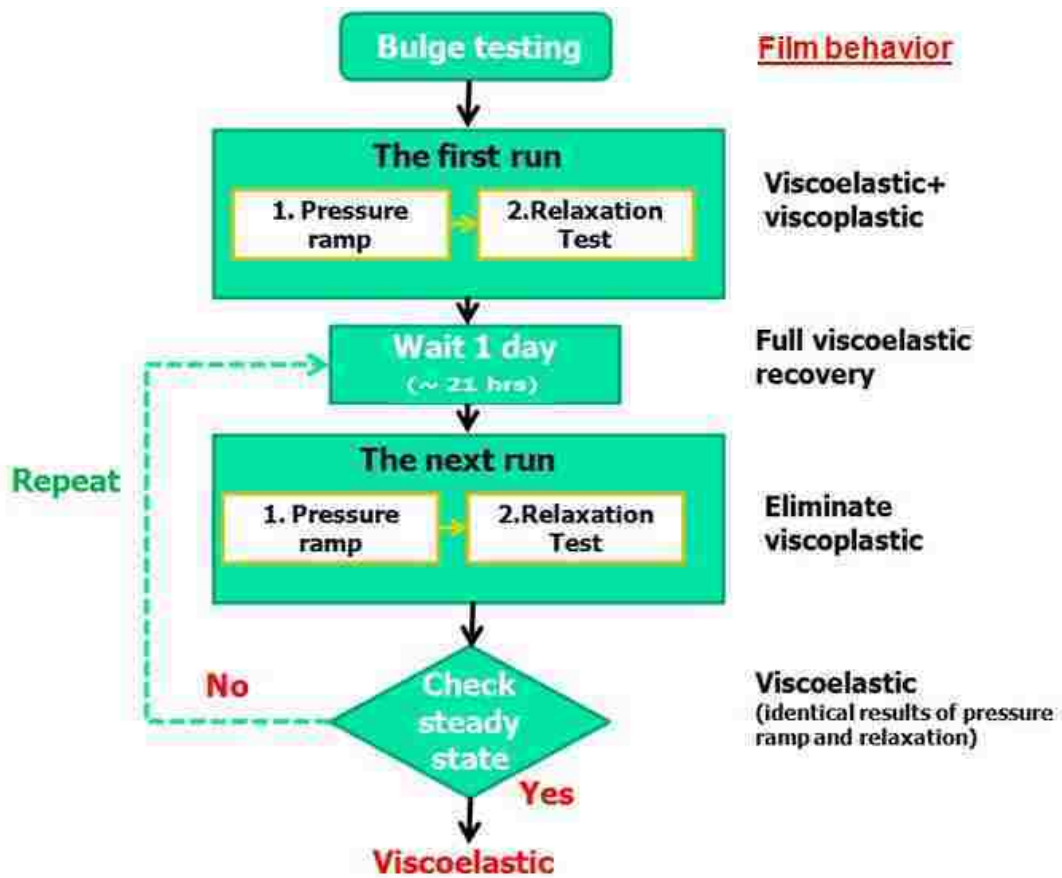


Figure 2.10 Flow chart of experimental procedure of bulge testing for viscoelastic films.

3. Time and temperature dependence of stress and stress relaxation of Au, AuV and Au-V₂O₅ films

In this study, stress relaxation and its temperature dependence for three types of thin films -pure Au, AuV solid solution and AuV₂O₅ dispersion- are investigated by using bulge testing over the temperature range 20-80 °C. Since stress relaxation of a thin film membrane in a MEMS capacitance switch can cause the lifetime of the switch to be shortened, the goal of this part of the investigation is improving the lifetime of the switch by identifying promising candidate membrane materials with less stress relaxation than pure Au over the temperature range of technological relevance. Vanadium (V) and vanadium oxide (V₂O₅) additions to Au are the candidate materials of this study.

3.1 Characterization of thin films

Figure 3.1 shows SEM and AFM images of Au, AuV and AuV₂O₅ films. The average grain sizes are estimated by using the mean linear intercept method based on the measurements along several lines in each image. The average grain size of Au, AuV and AuV₂O₅ films deposited at room temperature are approximately 100, 52 and 54 nm respectively. Smaller grain sizes are observed for AuV and AuV₂O₅ compared to Au. The AFM results show that there is no significant difference in the average roughness (R_a) for the three different types of film.

The V content of AuV and AuV₂O₅ is estimated from Scanning Electron Microscopy (SEM) with Energy Dispersive Spectrometry (EDS) software based on a calibrated AuV thin film as 4.5 at. %V. The EDS data shown in Figure 3.2 display the x-ray peaks associated with Au and V in Au alloy films. The quantitative V content can be estimated from the ratio of the characteristic V peak area to that measured for the calibrated 4.5 at. %V film. The concentration of V in the AuV and AuV₂O₅ films used for the alloy stress relaxation comparison is approximately 5.4 at. %V.

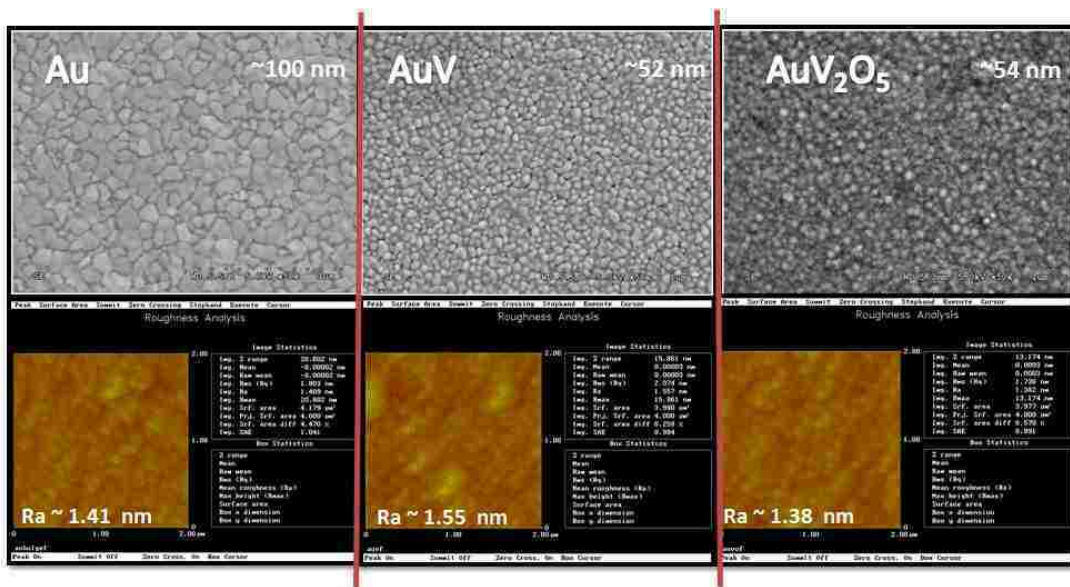


Figure 3.1 SEM and AFM images of sputtered Au, AuV(5.4 at.%V), and AuV₂O₅ (5.4 at.%V) thin films

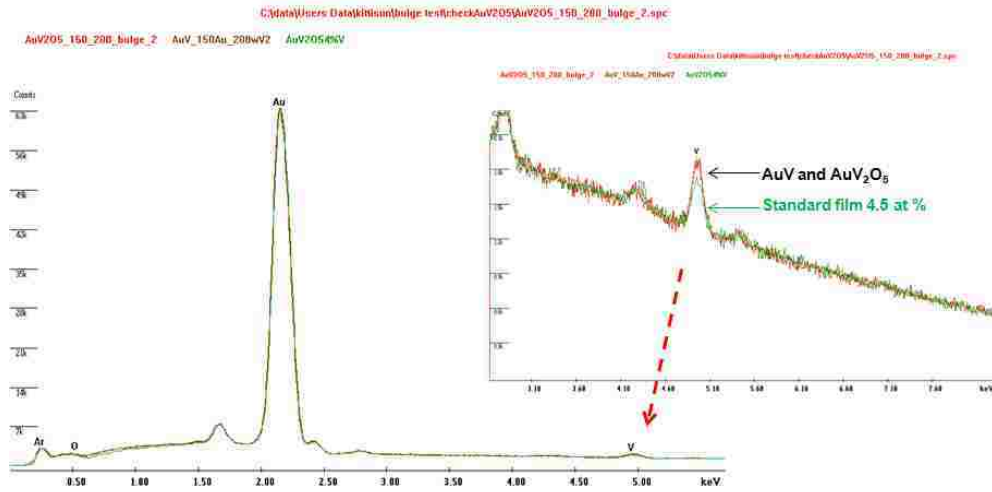


Figure 3.2 EDS results for AuV and AuV₂O₅ films compared to the standard thin film of 4.5 at% V.

3.2 Stress relaxation of pure Au films

3.2.1 Pressure ramp and relaxation results

A composite Au/SiN film is investigated at room temperature (20 °C) first, beginning with measurement of the residual stress and modulus of the film. A stress-strain curve as determined from a pressure ramp is shown in Figure 3.3 a). There are two quantities obtained by fitting the unloading half of the stress-strain curve. The first is the residual stress, 215 MPa, which is the extrapolated y-intercept. The second is the plane strain elastic modulus, 131 GPa, calculated from the slope of the unloading curve. The modulus computed from the pressure ramp is a plane strain modulus due to the geometry of the bulging thin film.⁸⁴ The plane strain modulus is related to the Young modulus, E, as $E/(1-\nu^2)$ where ν is Poisson's ratio. A pressure

ramp is run prior to each relaxation test primarily to define the residual stress (σ_0) at the beginning of the relaxation, but also to check the plane strain modulus.

Following the pressure ramp testing, a relaxation experiment is carried out on the film. The film is held at a constant strain of 0.1 % for 3 hours. The result of this test, $\sigma(t)$, together with the results from the pressure ramp previously carried out, determines the time dependent relaxation modulus ($M(t)$) given by

$$M(t) = \frac{\sigma(t) - \sigma_0}{\varepsilon(t)} \quad 3.1$$

and the normalized modulus which is the time dependent fraction of the initial modulus is given by $N.M(t) = M(t)/ M_0$, respectively. Figure 3.3 b) shows a typical normalized time dependent modulus of a composite Au/SiN film. The normalized modulus at 3 hours is 0.85, or, the modulus has decayed by 15% in 3 hours.

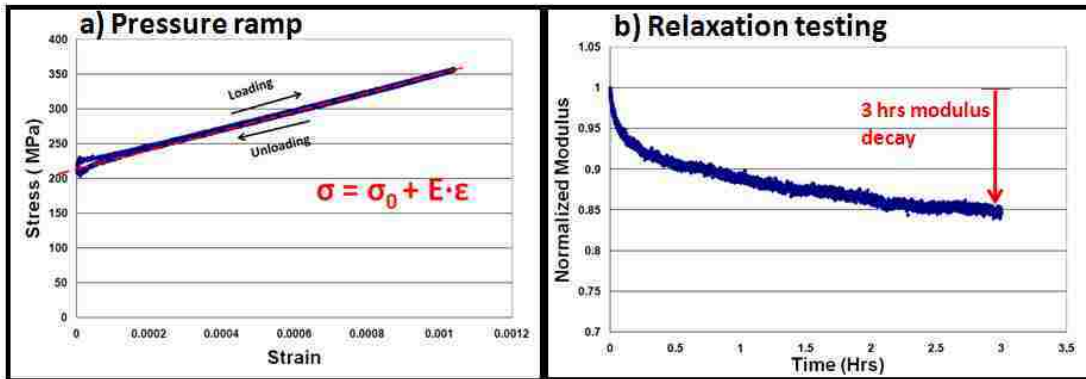


Figure 3.3 Initial relaxation behavior of Au/SiN film at 20 °C for a) pressure ramp and b) relaxation testing.

As mentioned earlier, since bulge experiments require the residual stress in the film before bulging to be in tension, the SiN is retained beneath the Au film. All

films in this study are measured as composite films. The stress and plane strain modulus of the Au film alone can be determined by extracting the properties of SiN from the composite films using the formula:

$$\sigma_{composite} = \frac{\sigma_{Au}t_{Au} + \sigma_{SiN}t_{SiN}}{t_{Au} + t_{SiN}} \quad 3.2)$$

and

$$M_{composite} = \frac{M_{Au}t_{Au} + M_{SiN}t_{SiN}}{t_{Au} + t_{SiN}} \quad 3.3)$$

where σ is stress, M is plane strain modulus and t is thickness. The thicknesses of the Au and SiN are 500 nm and 210 nm, respectively. The temperature dependence of SiN properties is shown in the Table 3.1. The modulus of approximately 226 GPa for the SiN film is consistent with other reports.⁸⁷

| Temperature | Residual stress (MPa) | Modulus (GPa) |
|-------------|-----------------------|---------------|
| 20 °C | 424.2 | 225.4 |
| 50 °C | 453.1 | 226.4 |
| 70 °C | 472.1 | 227.0 |
| 80 °C | 481.7 | 227.3 |

Table 3.1The temperature dependence of SiN properties.

The phrase “free standing Au thin film” is defined as the Au thin film from which the influence of SiN has been removed. The residual stress of the free standing Au film calculated from the composite Au/SiN film is 128 MPa and the plane strain modulus is 95 GPa which is consistent with the predicted plane strain modulus of 94.7 GPa based on the bulk Au Young’s modulus of 78 GPa and a Poisson’s ratio of 0.42.²⁷ The 3 hour normalized modulus of Au in the first run is 0.70. The resulting

unloading stress-strain curve and 3 hour normalized free standing modulus curve for the composite Au/SiN film shown in Figure 3.3 are shown in Figure 3.4.

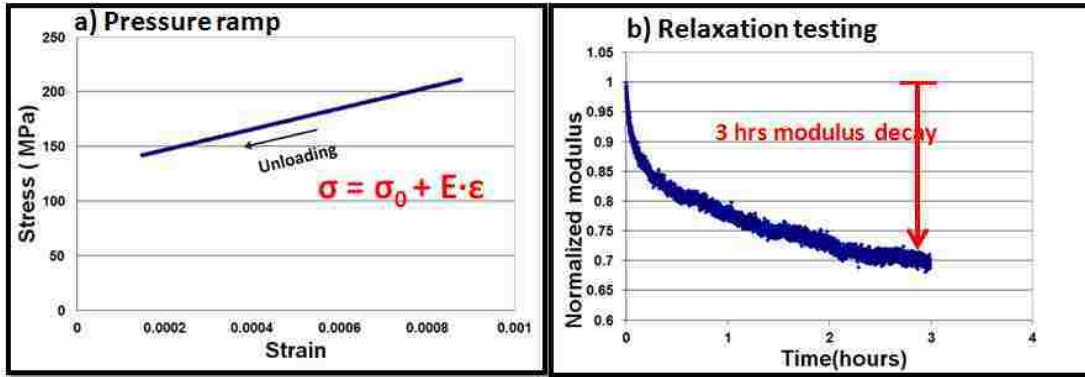


Figure 3.4 Initial relaxation behavior of a free standing Au film at 20 °C for a) pressure ramp and b) relaxation testing.

3.2.2 Steady state ramp and relaxation results

It has been reported that the mechanical response of thin Au films after fabrication consists of a combination of two distinct components: viscoelastic and viscoplastic.^{4, 7} The viscoplastic component can be exhausted by doing multiple relaxation runs until the film reaches a steady state condition at which the film shows only a viscoelastic response. In this steady state condition, any subsequent residual stress or relaxation experiment at the same temperature yields the same results.

In this study, one run, consisting of one pressure ramp, which defines the residual stress and plane strain modulus, and one 3 hour relaxation test, are carried out each day. The rest of the 24 hour period is provided for full recovery of anelasticity at zero strain. Such runs are repeated, one a day, until a steady state

condition is reached. With the first several runs, we observe the modulus decay and residual stress decrease from one run to the next until finally consecutive runs provide identical results and a steady state condition had been reached. The results show that the 3 hour modulus decay and the residual stress at steady state dropped to 6 % and 189 MPa, respectively. Figure 3.5 shows the observed composite residual stress, time-independent modulus, and modulus decay from multiple runs corresponding to viscoelastic and viscoplastic decays. There is no significant change of time-independent modulus from run to run. In contrast, we can see the residual stress and the total amount of relaxation at 3 hours decrease with the subsequent relaxation runs until they reach a steady-state condition. The decrease of the residual stress and the amount of relaxation result from some fraction of the first stress relaxation being due to viscoplasticity. When the film has both viscoplastic and viscoelastic stress relaxation components, the residual stress cannot fully recover to its original value after stress relaxation. Figure 3.5 shows that after the first relaxation, the film has a lower residual stress ($\sigma_0 = 198$ MPa) than the starting residual stress at 215 MPa. The residual stress drops to 189 MPa at steady state and now shows full stress recovery as expected for viscoelasticity. Also, the amount of relaxation, or modulus decay, drops from 15 % in the first run to a consistent value of 6 % at steady state. The relaxation at steady state is less than in the first run since there is only a viscoelastic contribution to the relaxation at steady state, while there are both viscoelastic and viscoplastic contributions in the first run. This observation suggests that the plastic relaxation can be a serious concern for switches in the beginning. Plasticity from the film

should be eliminated by exercising the film multiple times before switch operation. This will be beneficial for the performance of RF MEMS switches due to the decrease in the amount of relaxation.

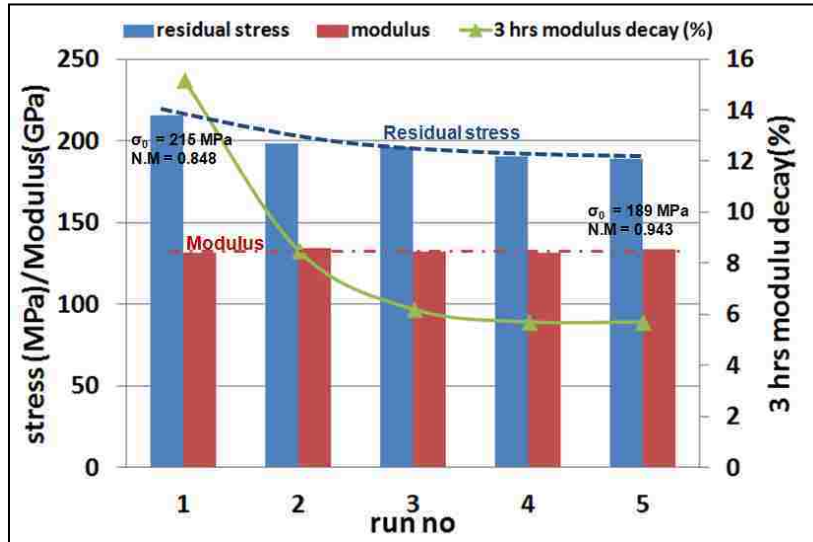


Figure 3.5 Residual stress, modulus, and 3 hrs modulus decay of composite Au/SiN at 20 °C from the first run to steady state condition.

Figure 3.6 shows the time dependence of the relaxation results in terms of normalized modulus vs time for successive 3 hours relaxations, the final values of which were shown in Figure 3.5. The normalized modulus of Au/SiN at the end of the first run is 0.848; at steady state it is 0.943. When we remove the contribution of the SiN film, which is totally elastic, from the composite Au/SiN results, we obtain the normalized modulus of free standing Au film as noted in Eq. 3.3). After the first run the normalized modulus is 0.70; after reaching steady state it is 0.886. The 3 hours modulus decay from the first run to steady state decreased from approximately 30 % to 11 % as presented in Figure 3.7.

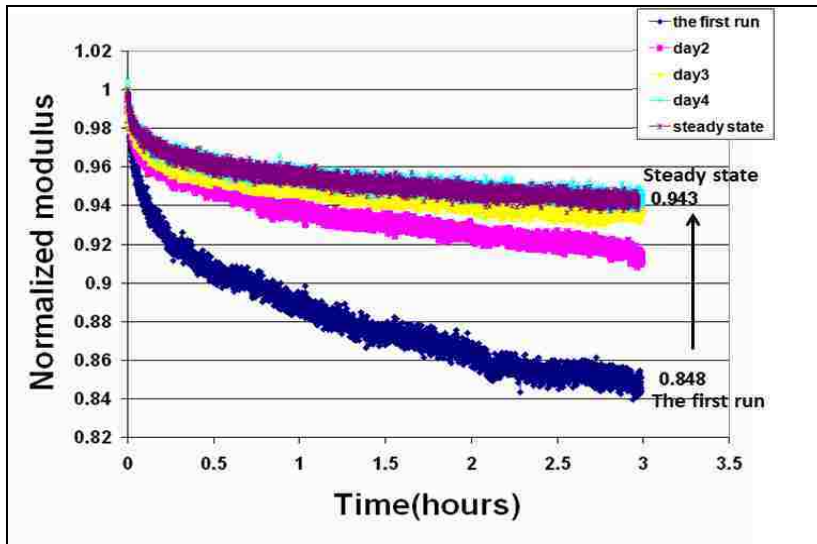


Figure 3.6 Relaxation of normalized modulus of composite Au/SiN at 20 °C from the first run to steady state condition.

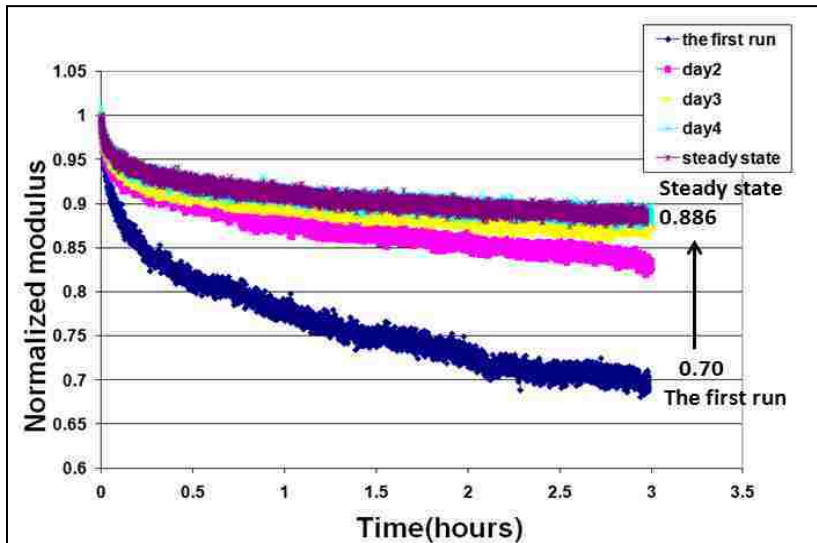


Figure 3.7 Relaxation of normalized modulus of free standing Au at 20 °C from the first run to steady state condition.

3.2.3 Temperature dependence on relaxation behavior of Au film

Temperature is expected to influence relaxation behavior because relaxation mechanisms each have a characteristic activation energy that must be overcome for the mechanism to operate. Once the relaxation behavior of the Au film tested at 20 °C reaches the steady state condition, the temperature is increased to 50, then to 70 and finally to 80 °C. At each temperature pressure ramp and relaxation runs are carried out, one a day, until steady state is reached, as in the experiments at 20 °C. The experiments are done with the composite Au/SiN film. Figure 3.8 shows pressure ramp results in each run carried out each day for Au/SiN providing residual stress and modulus. Then Figure 3.9 shows relaxation of normalized modulus of Au/SiN for each temperature (20, 50, 70 and 80 °C) versus time from the first run to steady state condition. Similar behavior from the first run to steady state is observed at elevated temperature as it was seen at room temperature.

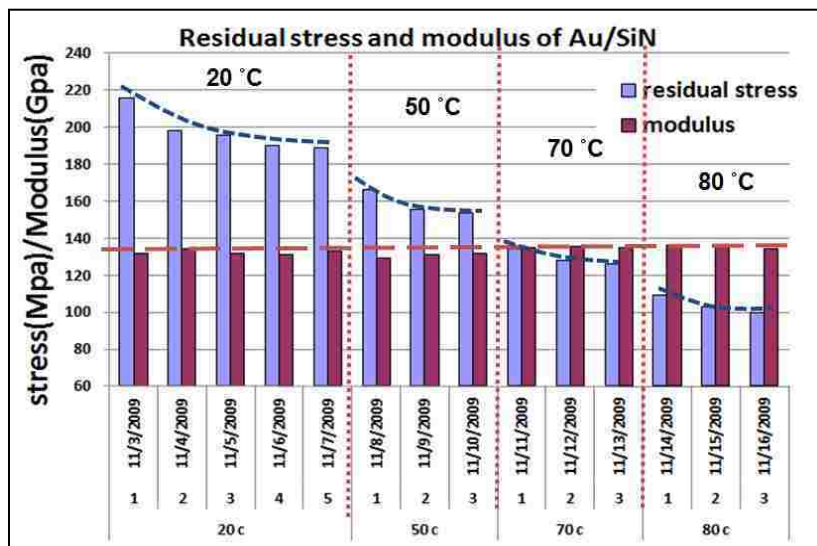


Figure 3.8 Pressure ramp results in each run carried out each day on a single Au/SiN film providing residual stress and modulus.

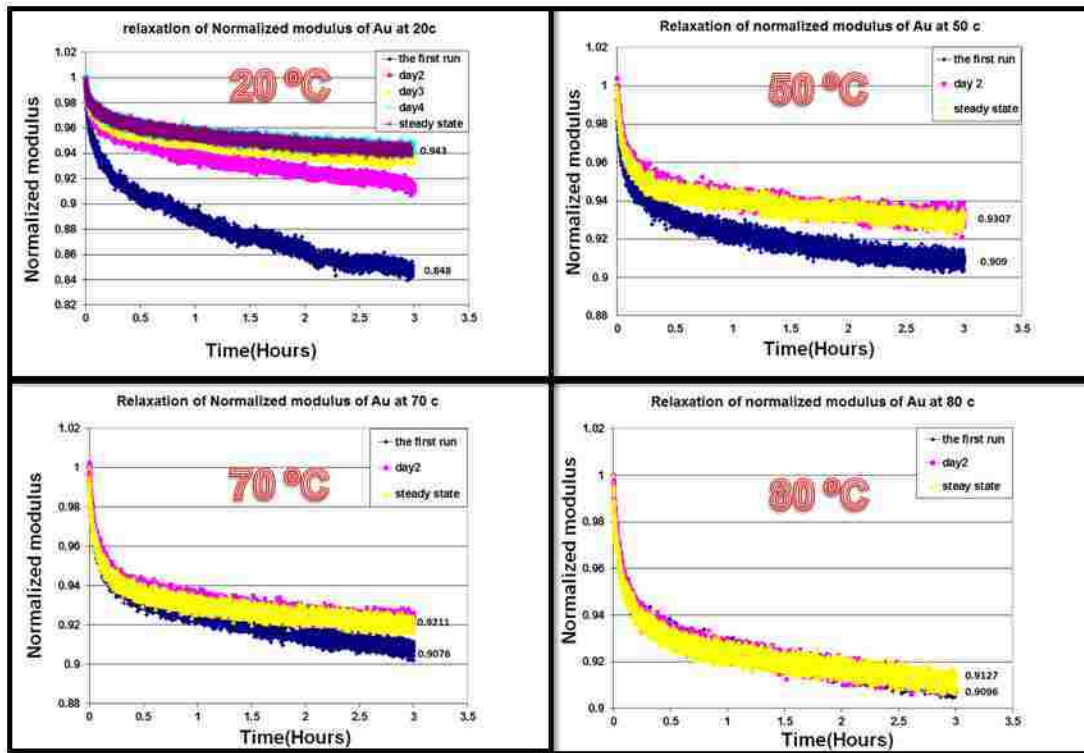


Figure 3.9 Relaxation of normalized modulus of Au/SiN for each temperature (20, 50, 70 and 80 °C) from the first run to steady state condition.

The experimental results of composite films are converted to results for free standing films. Only steady state results for each temperature are shown. Figure 3.10 shows the steady-state stress vs strain curves of the unloading segment for each temperature. The slope and the y-intercept of the curves give the plane-strain modulus and residual stress, respectively. The plane strain modulus, approximately 95 GPa, close to the literature value, is nearly independent of temperature as expected since the microstructure of the film is unchanged. However, as the temperature increases from 20 to 80 °C, the residual stress drops due to the difference of the thermal expansion coefficients of Si and Au. The influence of temperature on the residual stress at steady state is shown in the Figure 3.11. The plot shows that the

measured thermoelastic slope is higher than the expected value from the coefficient of thermal expansion (CTE) of Si, SiN and Au. The expected value of thermoelastic slope is about -1.7 MPa/°C, calculated by

$$\frac{d\sigma_0}{dT} = M_{Au}(\alpha_{Si} - \alpha_{Au}) \quad \mathbf{3.4)}$$

where M_{Au} is the biaxial modulus of Au film, and α_{Si} and α_{Au} are the linear coefficient of thermal expansion (CTE) of Si and Au.

This error in the measured slope can be the contribution of plasticity in the film at each temperature. After the plasticity is exhausted at the highest temperature (80 °C), we do the relaxation test again at 20 °C. This method exhausts additional plastic relaxation in the film that could not be exhausted at lower temperatures, giving a more accurate measurement of purely viscoelastic behavior. As a result of the plasticity exhausted at 80 °C, a decrease of residual stress of the film is observed at 20 °C. The resulting thermoelastic slope of the film agrees very well with the expected value of -1.7 MPa/°C.

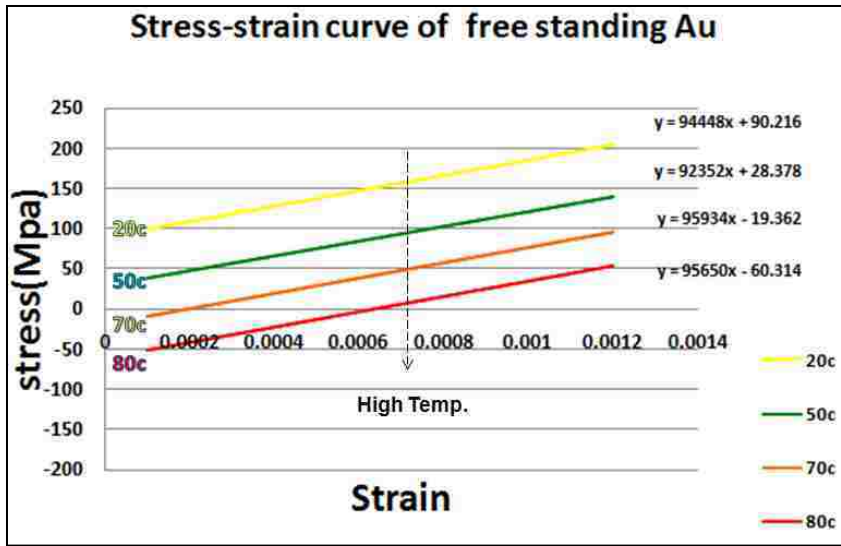


Figure 3.10 Stress and strain curve of unloading segment at steady state of free standing Au for each temperature to determine plane-strain modulus and residual stress.

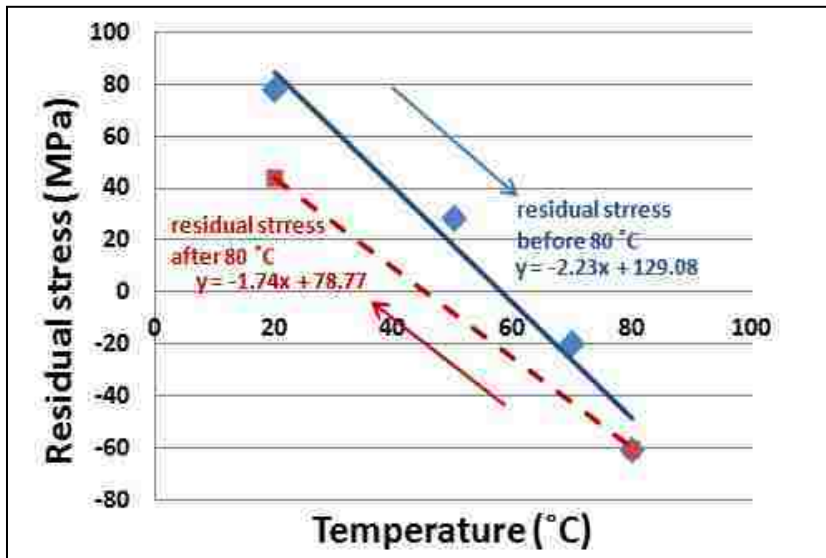


Figure 3.11 Residual stress before and after exercising at 80 °C as a function of temperature.

Figure 3.12 shows the normalized relaxation modulus of free standing Au at steady state for each temperature. The effect of temperature dependence on

relaxation behavior of the thin film is evident. The percentage of 3 hours modulus decay of the Au film is shown for comparison. When the temperature increases, the amount of modulus decays increase from 11.37 % at 20 °C, to 16.73 % at 80 °C.

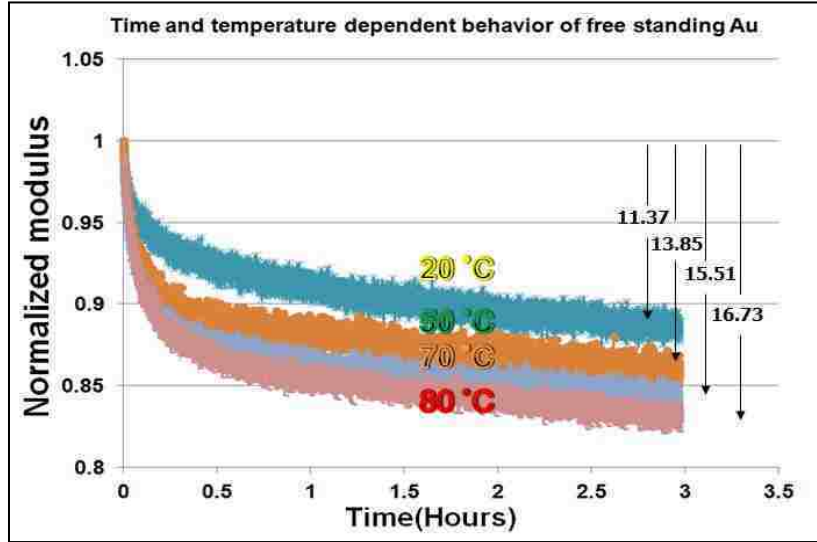


Figure 3.12 Normalized modulus relaxation at steady state of free standing Au.

Since the relaxation behavior of thin films has a complex time dependence, a Prony series (a sum of exponential decay functions) has been used to fit the relaxation curves.⁷ The form of normalized modulus function (N.M (t)) with a Prony series is given by

$$N.M(t) = 1 - \sum_{i=1}^N P_i (1 - e^{-\frac{t}{\tau_i}}) \quad 3.5$$

where P_i is i 'th Prony constant and τ_i is i 'th time constant.

A four-term Prony series is used to fit the relaxation curve results. For ease of comparison and to ensure sufficient weighting to achieve accurate fits at short times,

the time constants are fixed at $\tau=10, 100, 1000, \text{ and } 10000$ seconds. The Prony constants are obtained by least square fitting of Prony series equations to curves of normalized modulus. In Figure 3.13 the fitting curves are shown as solid lines overlaid on the normalized modulus results. The relaxation data are fitted very well by the four-term Prony series model as shown in both linear and log time displays. The fitted values of the Prony constants for the Au film are listed in the Table 3.2. Note that the trend of the relaxation curves in the Figure 3.13 b) implies that there is still further relaxation that will occur in the Au film after 3 hours.

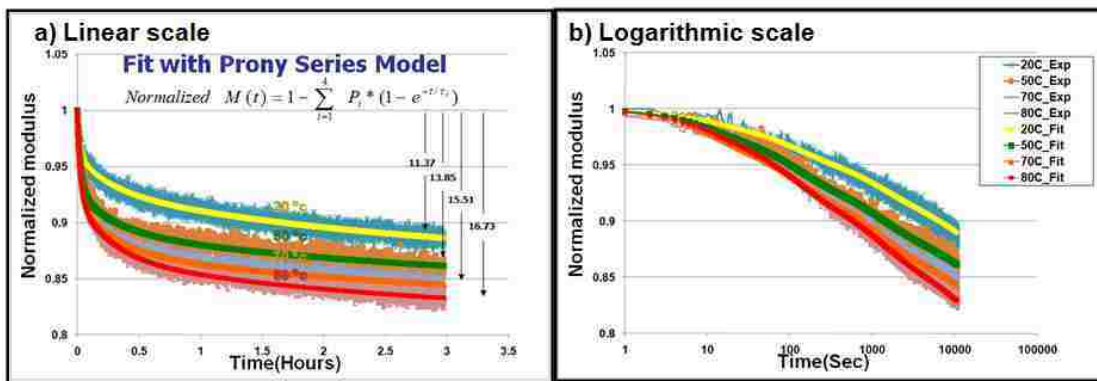


Figure 3.13 Normalized modulus relaxation of free standing Au at steady state fitted with four-term Prony series model a) linear scale, b) logarithmic scale.

| Temperature | Au | | | |
|-------------|-----------|------------|-------------|--------------|
| | P1 (10 s) | P2 (100 s) | P3 (1000 s) | P4 (10000 s) |
| 20 °c | 0.01193 | 0.02716 | 0.03395 | 0.05665 |
| 50 °c | 0.01943 | 0.04074 | 0.04326 | 0.05355 |
| 70 °c | 0.02725 | 0.04171 | 0.05141 | 0.05477 |
| 80 °c | 0.02247 | 0.05011 | 0.05335 | 0.06860 |

Table 3.2 Prony series constants of Au film at steady state for 20-80 °C.

3.3 Effect of V and V₂O₅ addition on stress relaxation of Au films

It has previously been shown that solid solution and oxide dispersion strengthening can increase hardness while retaining reasonable electrical conductivity, and both methods are compatible with standard thin film processing techniques.¹⁰ These materials are therefore potential candidates to begin to understand the effects of alloying on stress relaxation. The results below show the relaxation behavior of solid solution (AuV) and oxide dispersion (AuV₂O₅) strengthening at 5.4 at.% V. The experiments are done in the same way as that used for Au at 20, 50, 70 and 80 °C. Then the experimental results of the residual stress, plane strain modulus and normalized modulus relaxation of AuV and AuV₂O₅ films are determined and compared with the Au results.

3.3.1 Relaxation behavior of AuV films

Figure 3.14 shows the results of pressure ramp tests at each run from the first run to steady state of AuV/SiN. It shows that the plane strain modulus has almost no change when temperature changes and is also close to the value of Au/SiN. This is to be expected because the V content is quite low in the film and the modulus behavior is dominated by the Au matrix. Figure 3.15 shows that several 3 hour relaxations are conducted and repeated until steady state for each temperature.

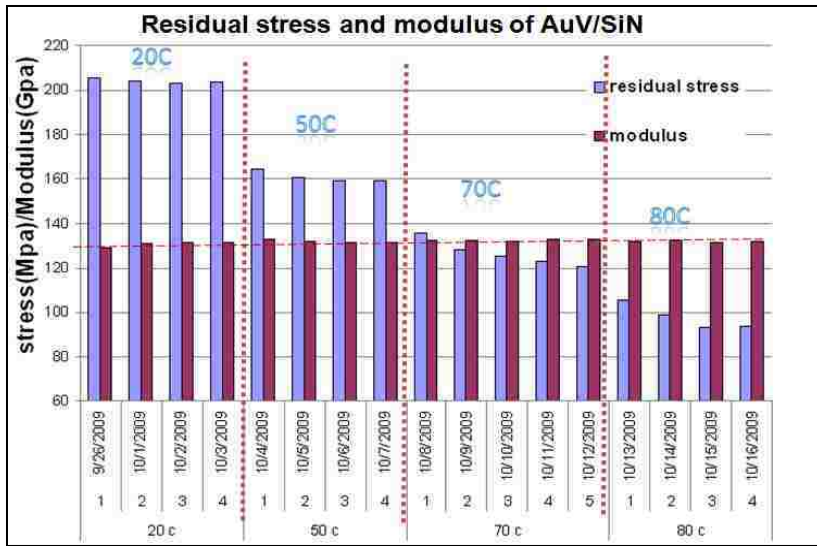


Figure 3.14 Pressure ramp results in each run carried out each day of AuV/SiN providing residual stress and modulus.

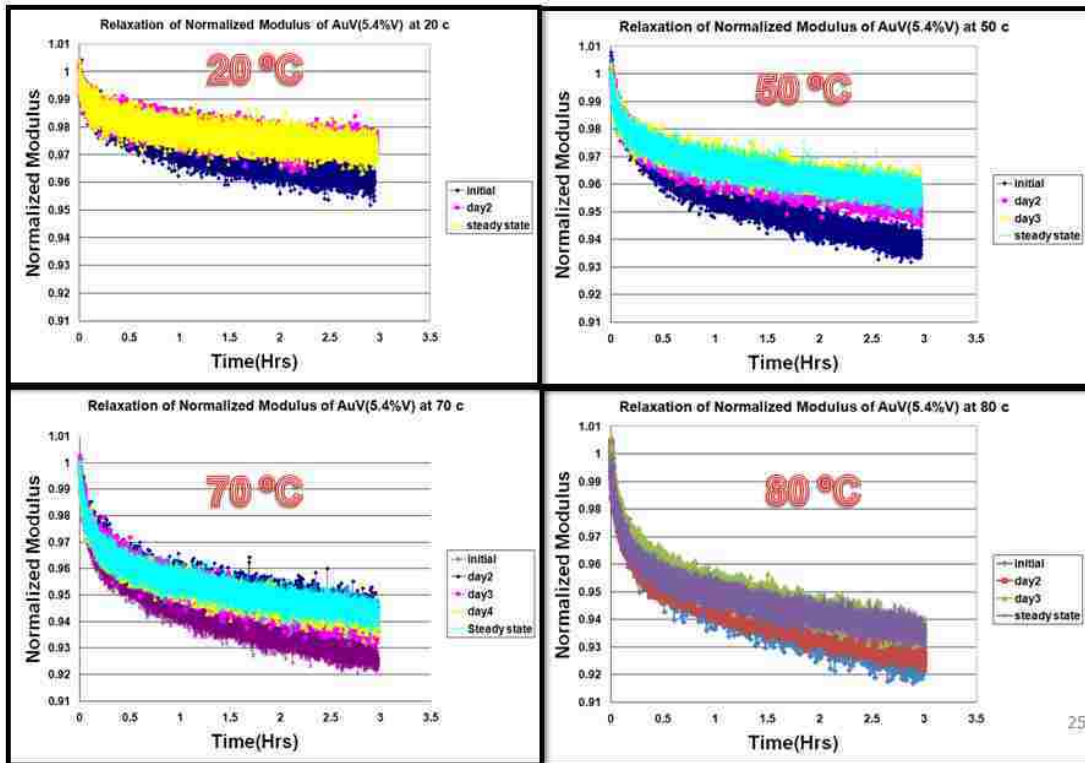


Figure 3.15 Relaxation of normalized modulus of AuV/SiN for each temperature (20, 50, 70 and 80 °C) from the first run to steady state condition.

Then the composite results are converted to results for free standing films. Figure 3.16 shows the normalized modulus of a free standing AuV film only at steady state for various temperatures fitted with a Prony series model. Also, Table 3.3 lists the values of the Prony series constants used to generate these curves. The 3 hour modulus decay of AuV films at 20, 50, 70 and 80 °C are 5.5, 8.7, 11.2, and 12.6 % respectively.

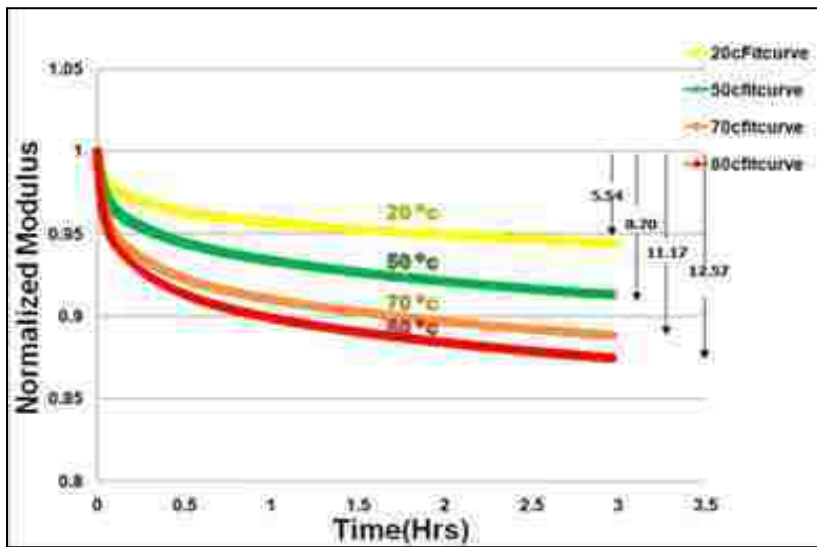


Figure 3.16 Normalized modulus of a free standing AuV film at steady state for various temperatures fitted with a Prony series model.

| Temperature | AuV | | | |
|-------------|-----------|------------|-------------|--------------|
| | P1 (10 s) | P2 (100 s) | P3 (1000 s) | P4 (10000 s) |
| 20 °C | 0.00025 | 0.01872 | 0.01477 | 0.03325 |
| 50 °C | 0.00050 | 0.02790 | 0.02176 | 0.05669 |
| 70 °C | 0.00065 | 0.03911 | 0.03387 | 0.05874 |
| 80 °C | 0.00072 | 0.04303 | 0.03858 | 0.06601 |

Table 3.3 Prony series constants of AuV film at steady state for 20-80 °C.

3.3.2 Relaxation behavior of AuV₂O₅ films

Repeated pressure ramp and relaxation experiments are conducted with AuV₂O₅/SiN specimens until a steady-state condition is reached, as has been done for Au/SiN and AuV/SiN. Figure 3.17 and Figure 3.18 show the measurement of pressure ramp results in terms of residual stress and modulus, and relaxation results in terms of normalized modulus vs time. Both results show multiple runs from the first run to steady state for each temperature.

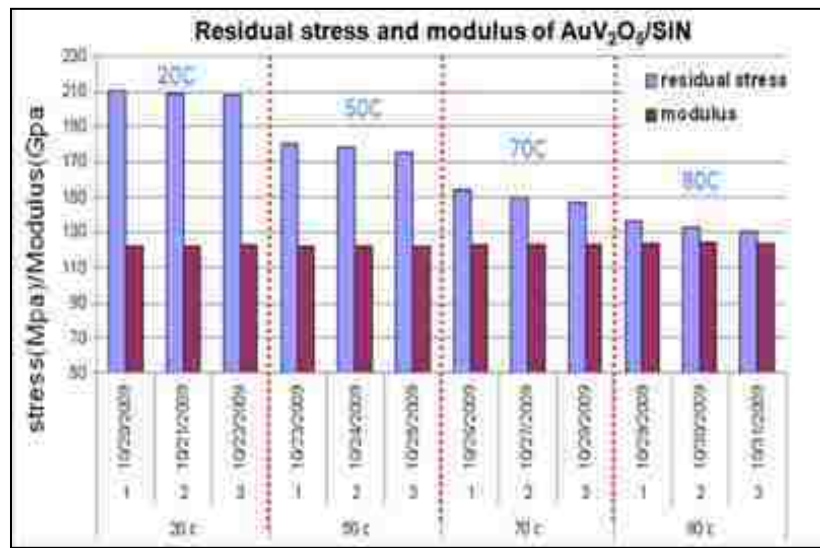


Figure 3.17 Pressure ramp results in each run carried out each day of AuV₂O₅/SiN providing residual stress and modulus.

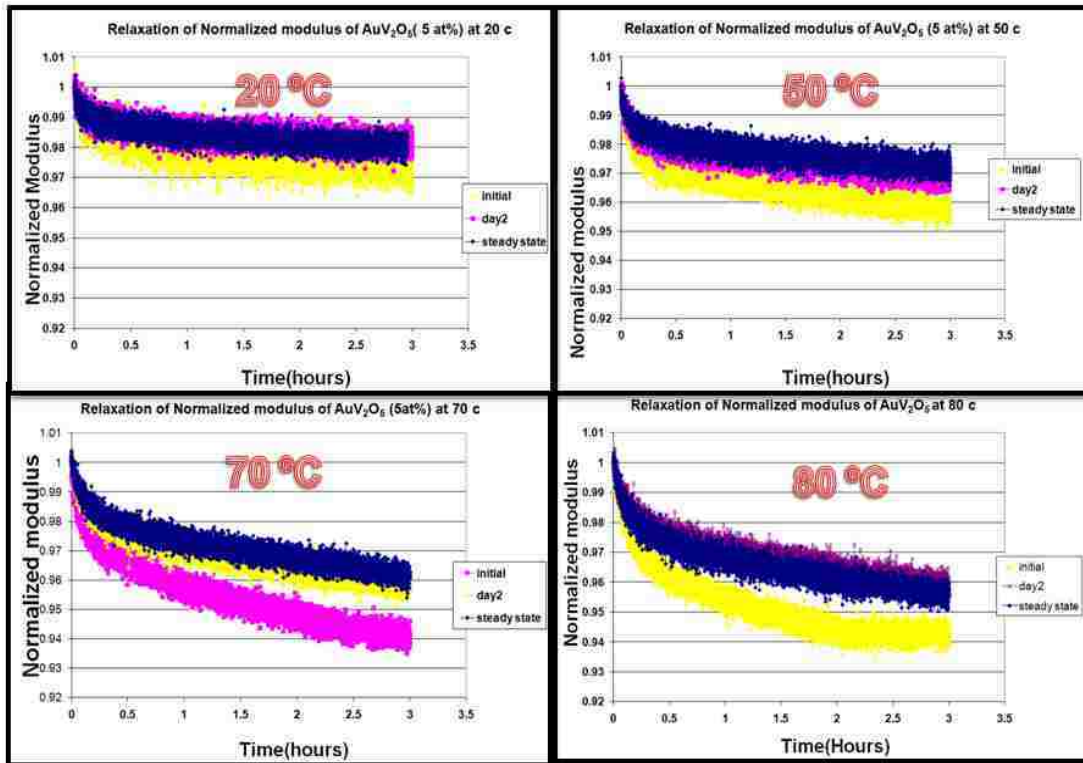


Figure 3.18 Relaxation of normalized modulus of AuV₂O₅/SiN for each temperature (20, 50, 70 and 80 °C) from the first run to steady state condition.

Then the results of AuV₂O₅ thin films are converted to results for free standing AuV₂O₅ films. Figure 3.19 shows the normalized modulus of a free standing AuV₂O₅ film at steady state for various temperatures fitted with a Prony series model. Table 3.3 lists the four-term Prony coefficient values for the normalized modulus function of AuV₂O₅. As seen in the Figure, the 3 hour modulus dropped by 4.22, 5.98, 8.01, and 9.25 % for 20, 50, 70 and 80 °C, respectively.

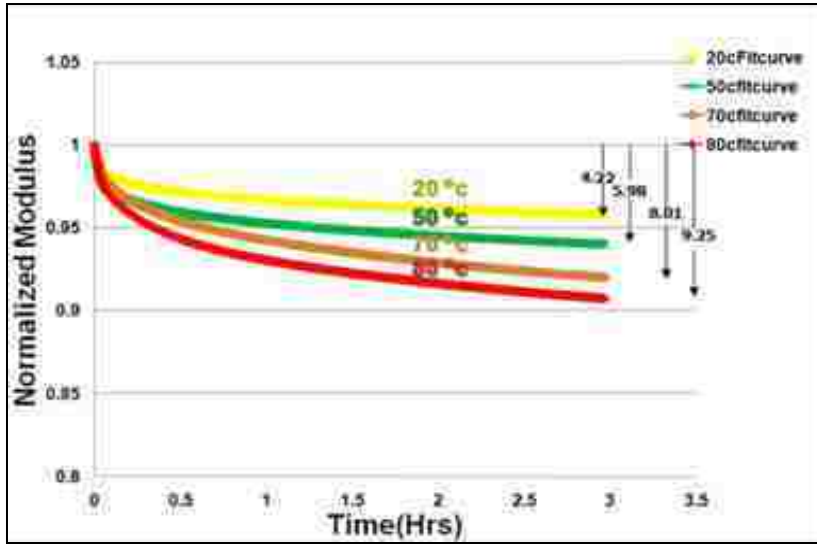


Figure 3.19 Normalized modulus of a free standing AuV_2O_5 film at steady state for various temperatures fitted with a Prony series model.

| Temperature | AuV_2O_5 | | | |
|-------------|--------------------------|------------|-------------|--------------|
| | P1 (10 s) | P2 (100 s) | P3 (1000 s) | P4 (10000 s) |
| 20 °C | 0.00168 | 0.01313 | 0.00967 | 0.02476 |
| 50 °C | 0.00270 | 0.01990 | 0.01318 | 0.03429 |
| 70 °C | 0.00297 | 0.02079 | 0.01717 | 0.06202 |
| 80 °C | 0.00400 | 0.02299 | 0.02699 | 0.06283 |

Table 3.4 Prony series constants of AuV_2O_5 film at steady state for 20-80 °C.

3.3.3 Effect of V and V_2O_5 on stress relaxation

In this part, the experimental results of the residual stress, plane strain modulus and normalized modulus relaxation of AuV and AuV_2O_5 films are compared with the Au results. In order to observe the effect of V and V_2O_5 of Au films, all relaxation results are converted to results of free standing thin films at steady state.

Also, all plots compared here showing 3 hour normalized modulus depict a Prony series fit, rather than the raw data, for clarity.

Measurements of residual stress and plane strain modulus of Au, AuV and AuV₂O₅ are presented in Figure 3.20. The same general behavior is observed for the three different films. The residual stress of the three thin films decreases with increasing temperature resulting in compressive stresses at some high temperatures, while the plane strain modulus is nearly temperature-independent.

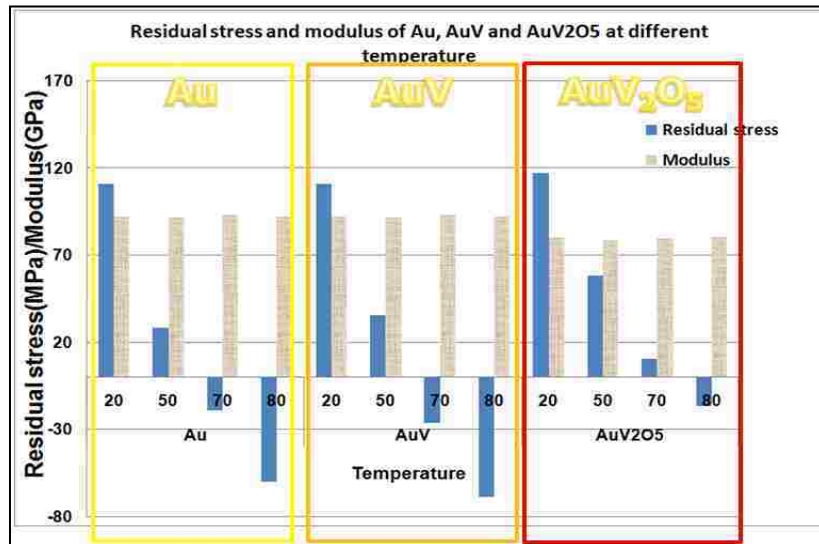


Figure 3.20 Pressure ramp results show residual stress and plane-strain modulus of Au, AuV and Au V₂O₅ at steady state.

Figure 3.21 shows the Prony series fits to the time and temperature dependence of the normalized modulus for the three films in the same y-scale. In all cases, it is observed that increasing the temperature produces larger modulus decay. The values of the 3 hour normalized modulus decays are given in Table 3.5. The addition of V or V₂O₅ to the Au films clearly reduces relaxation. While the 3 hours

modulus decays of Au over the 20-80 °C temperature range vary from 11.4-16.7 %, for AuV they decrease to 5.5-12.6 %, and for AuV₂O₅ they decrease even more to 4.2-9.3 %. The benefits of alloying are clear at all temperatures: even the 3 hour modulus decay of the AuV₂O₅ film at 80 °C is lower than that of pure Au at 20 °C. These results are clearly shown in Figure 3.22 for each temperature. Both sets of alloy films greatly reduce the relaxation behavior of the Au film and AuV₂O₅ shows more significant reduction than AuV. It is interesting to notice in Figure 3.23 that the dependence of 3 hours modulus decay on temperature for the three thin films shows almost linear trends.

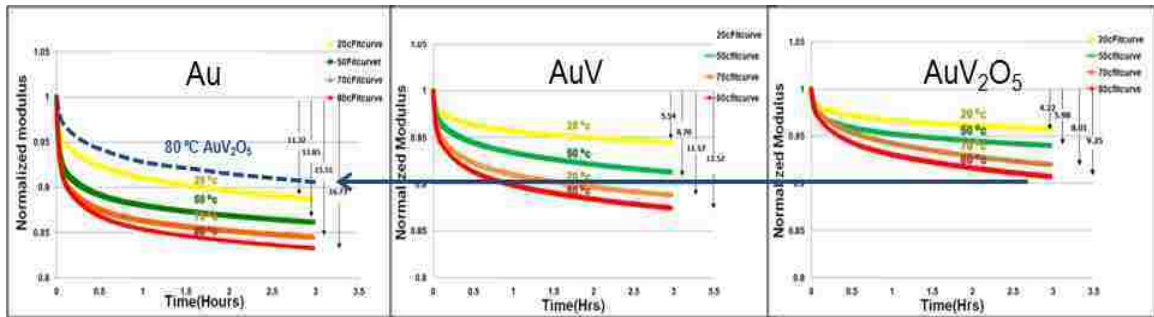


Figure 3.21 Normalized modulus of films at steady state for various temperatures fitted with Prony series model a) Au, b) AuV, and c) AuV₂O₅.

| Temperature | 3 hrs modulus decay(%) | | |
|-------------|------------------------|-------|---------------------------------|
| | Au | AuV | AuV ₂ O ₅ |
| 20 °C | 11.37 | 5.54 | 4.22 |
| 50 °C | 13.85 | 8.7 | 5.98 |
| 70 °C | 15.51 | 11.17 | 8.01 |
| 80 °C | 16.73 | 12.57 | 9.25 |

Table 3.5 Three hours modulus decay of Au, AuV and AuV₂O₅ at different temperatures.

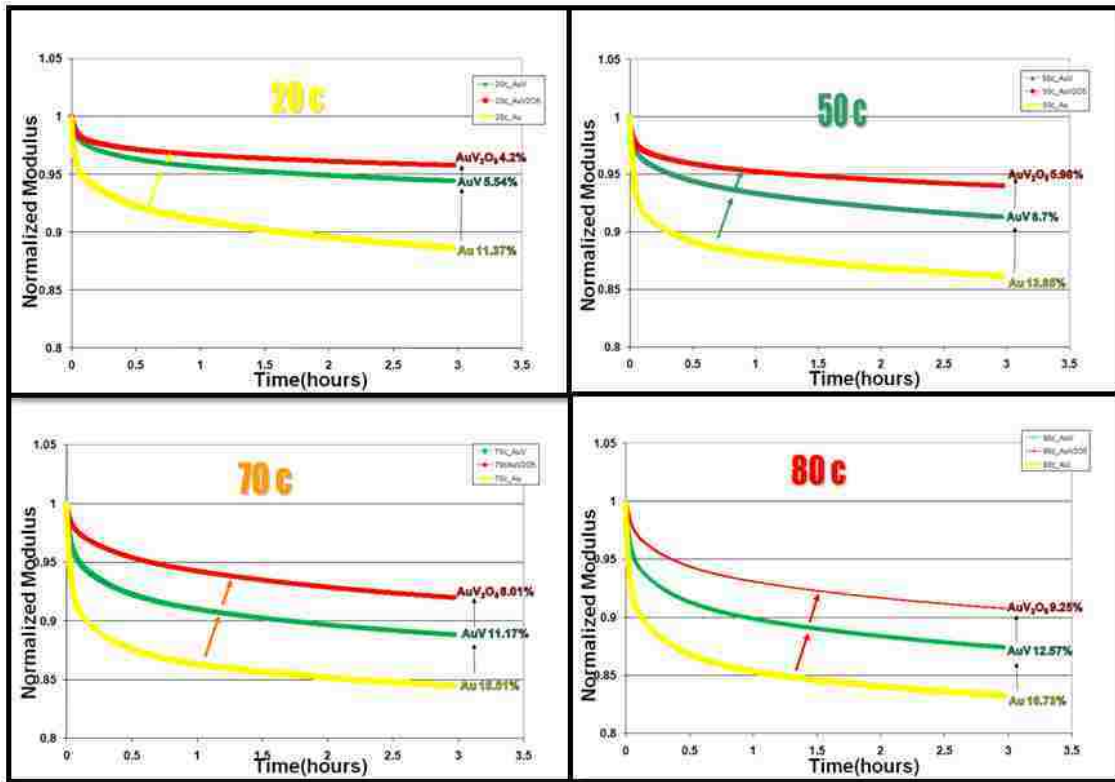


Figure 3.22 Comparison of relaxation modulus of Au, AuV, and AuV₂O₅ at each temperature (20, 50, 70 and 80 °C).

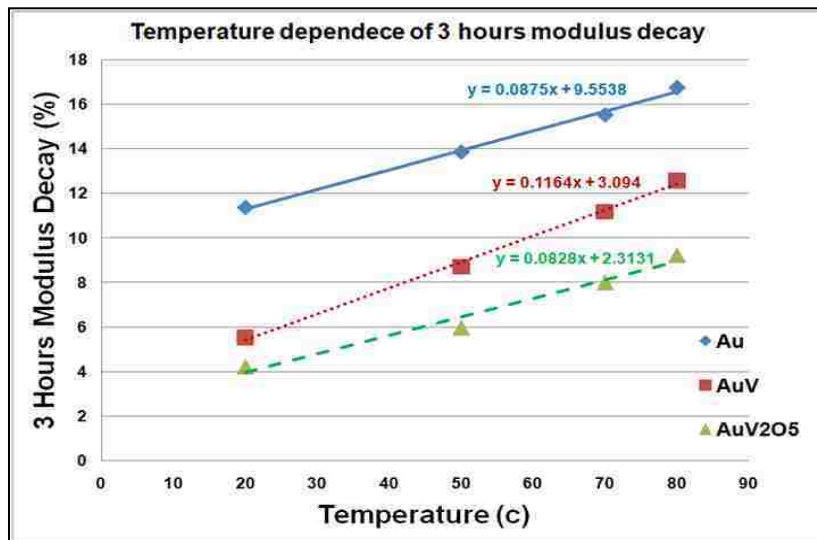


Figure 3.23 Temperature dependence of 3 hours modulus decay for Au, AuV and AuV₂O₅.

3.4 Activation energy and possible mechanism

Several fundamental mechanisms have been identified for the observed stress relaxation of thin films, such as grain boundary diffusion,⁸⁸⁻⁹⁰ grain boundary sliding,¹⁹ power law creep,³⁹ and dislocation glide.⁹ One of the methods to help identify relaxation mechanism for the observed viscoelastic behavior is extracting activation energy from the temperature dependence of some aspect of the relaxation behavior. In this study, three different approaches have been utilized: Prony series, stretched exponential function, and a diffusion model.

3.4.1 Prony series and the Arrhenius equation

The Arrhenius relation is applied to individual components of the Prony series

$$P_i = A \cdot \exp\left(\frac{-Q}{kT}\right) \quad 3.6)$$

where P_i is one of the four-term Prony series fitting constant, A is a pre-exponential factor, Q is the activation energy (eV), k is Boltzman constant ($8.617 \cdot 10^{-5}$ eV/K), and T is the temperature (Kelvin). Given this relationship, the slope of a plot of the natural log of a Prony constant vs $1/\text{temperature}$ is $-Q/k$. The Prony series coefficient values of three thin films are represented again in Table 3.6 to calculate the apparent activation energy. Figure 3.24 shows such a plot of the four Prony constants for each of the three different films. The slopes of the four lines for a single film are not identical as they would be expected to be if there is a single temperature dependent process controlling the relaxation. However, the variation is small so the average of the four slopes has been taken as the activation energy and the range of slopes is

indicated by the uncertainty given in Table 3.7. The extracted activation energies for Au, AuV and AuV₂O₅ are approximately 0.07, 0.13, and 0.12 eV respectively. These activation energies are small compared to the value reported by previous studies, all of which measured a combination of viscoplastic and viscoelastic relaxation.^{5, 89, 91, 92} It is conceivable that viscoplastic relaxation mechanisms active in Au involve obstacles to dislocation motion that are associated with significantly greater activation energies than the mechanism responsible for viscoelastic relaxation.

| Temperature | Au | | | | AuV | | | | AuV ₂ O ₅ | | | |
|-------------|-----------|------------|-------------|--------------|-----------|------------|-------------|--------------|---------------------------------|------------|-------------|--------------|
| | P1 (10 s) | P2 (100 s) | P3 (1000 s) | P4 (10000 s) | P1 (10 s) | P2 (100 s) | P3 (1000 s) | P4 (10000 s) | P1 (10 s) | P2 (100 s) | P3 (1000 s) | P4 (10000 s) |
| 20 °c | 0.01193 | 0.02716 | 0.03395 | 0.05665 | 0.00025 | 0.01872 | 0.01477 | 0.03325 | 0.00168 | 0.01313 | 0.00967 | 0.02476 |
| 50 °c | 0.01943 | 0.04074 | 0.04326 | 0.05355 | 0.00050 | 0.02790 | 0.02176 | 0.05669 | 0.00270 | 0.01990 | 0.01318 | 0.03429 |
| 70 °c | 0.02725 | 0.04171 | 0.05141 | 0.05477 | 0.00065 | 0.03911 | 0.03387 | 0.05874 | 0.00297 | 0.02079 | 0.01717 | 0.06202 |
| 80 °c | 0.02247 | 0.05011 | 0.05335 | 0.06860 | 0.00072 | 0.04303 | 0.03858 | 0.06601 | 0.00400 | 0.02299 | 0.02699 | 0.06283 |

Table 3.6 Fitting Prony coefficients of Au, AuV and AuV₂O₅.

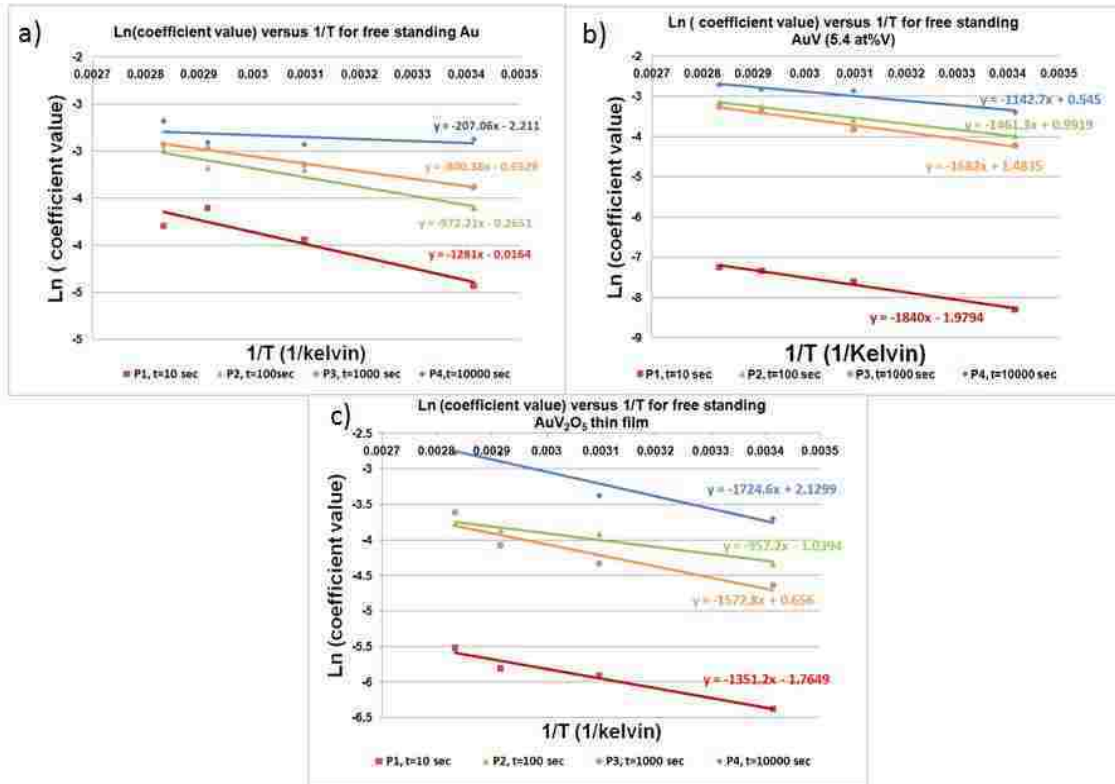


Figure 3.24 Logarithmic plot of Prony coefficient values as a function of the inverse temperature for 3 different films (a) Au, (b) AuV and (c) AuV₂O₅.

| Thin Films | Activation Energy(eV) |
|---------------------------------|-----------------------|
| Au | 0.07 ± 0.04 |
| AuV | 0.13 ± 0.03 |
| AuV ₂ O ₅ | 0.12 ± 0.03 |

Table 3.7 Activation energies of Au, AuV and AuV₂O₅ taken from average slope of linear fits from Figure 3.24.

3.4.2 Stretched exponential function

Relaxation behavior can also be described with a stretched exponential function rather than with a Prony series. This equation is a time dependent

exponential function which differs from a simple exponential by having one additional parameter called the stretching exponent beta (β). K is a rate constant, the reciprocal of a time constant.⁹³

$$M(t) = M_0 \exp(-Kt^\beta) \quad 3.7)$$

K can be assumed to be temperature dependent in this expression⁹⁴ and is given by $K=K_0 \cdot \exp(-E_k/kT)$, where E_k is the activation energy, k is the Boltzman constant and T is temperature.

Table 3.8 lists the parameter values (K and β) of the best-fit stretched exponential function for Au, AuV, and AuV₂O₅ which was used to match the relaxation curves. Figure 3.25 shows the stretched exponential fits of three films to typical normalized relaxation curves. The stretched exponential fit quality is not as good as that previously found for the Prony series, but the general temperature trends are still captured. Activation energies can be deduced from plots of the natural log of K vs. reciprocal temperature as shown in Figure 3.26 for all three film types. The activation energies deduced in this way are very similar to those deduced from the Prony series. This is not surprising since the same data of time dependent normalized modulus is being used in both approaches.

| Temperature@ | Au | | AuV | | AuV2O5 | |
|--------------|-------|---------|-------|---------|--------|---------|
| | K | β | K | β | K | β |
| 20 | 0.093 | 0.242 | 0.044 | 0.250 | 0.033 | 0.236 |
| 50 | 0.126 | 0.171 | 0.068 | 0.271 | 0.048 | 0.228 |
| 70 | 0.144 | 0.163 | 0.093 | 0.237 | 0.059 | 0.336 |
| 80 | 0.155 | 0.174 | 0.105 | 0.239 | 0.071 | 0.307 |

Table 3.8 Parameter fit of stretched exponential function for Au, AuV, and AuV₂O₅.

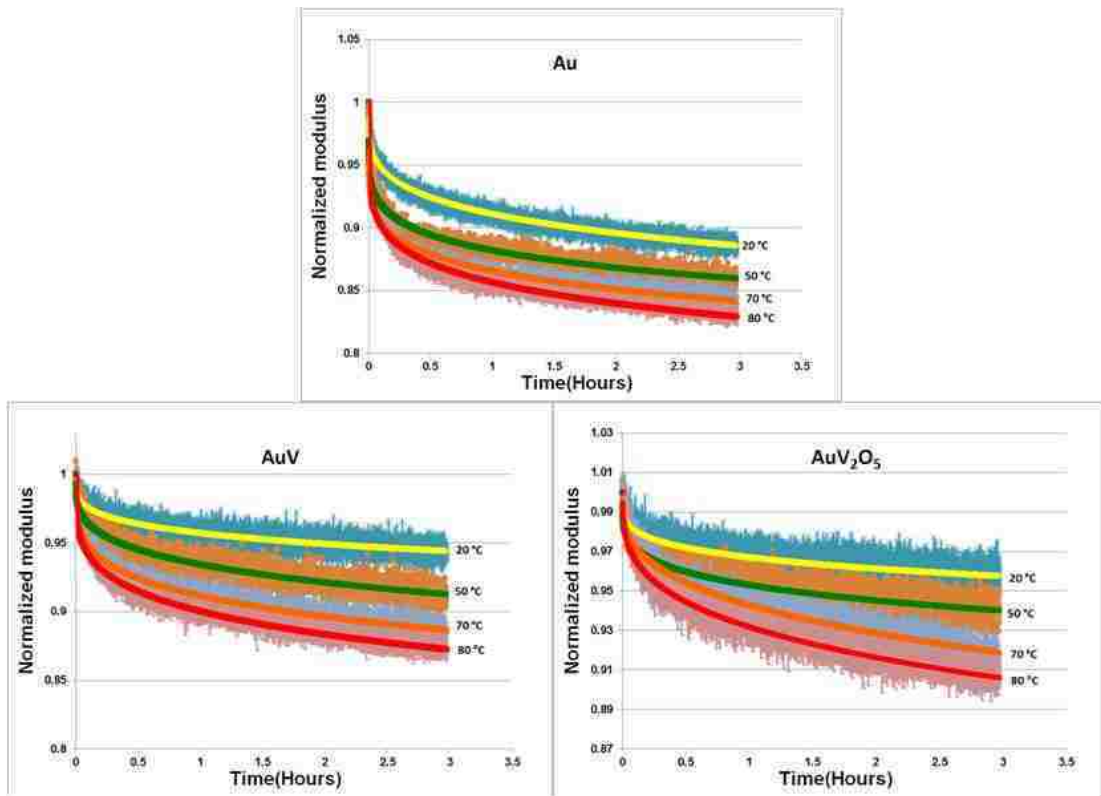


Figure 3.25 Normalized relaxation curves of Au, AuV, and AuV₂O₅ fitted with stretched exponential function.

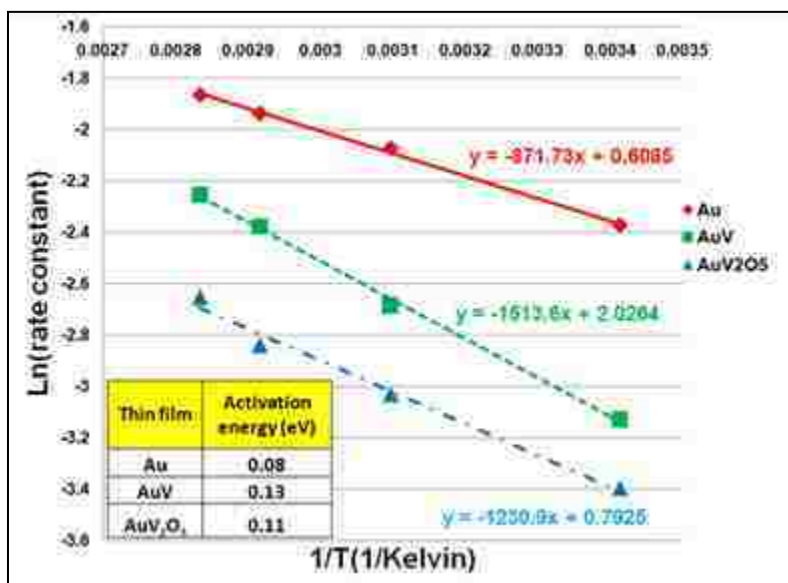


Figure 3.26 The activation energy extracted by stretched exponential function.

3.4.3 The diffusion mechanism model

Since grain boundary diffusion is often associated with time dependent processes in thin films because of the relatively small grain sizes in such films, we examine the diffusion mechanism model proposed by Gan and Ho^{95, 96} as responsible for our observations of modulus relaxation. These authors developed the model for stress relaxation based on the mass transport by diffusion along the free surface and the grain boundaries, but neglecting lattice diffusion and diffusion along the film/substrate interface. Figure 3.27 schematically illustrates the model structure for a film consisting of two-dimensional grains of a constant length l with grain boundaries of height h perpendicular to the film/substrate interface. The chemical potential is defined by the local curvature for the surface and the normal stress for the grain boundaries. The gradient of chemical potential drives atoms to diffuse into or out of grain boundaries.

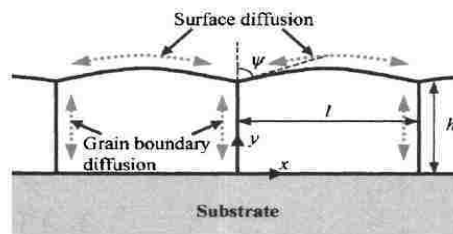


Figure 3.27 Schematics diagrams of a thin film with grain boundary and surface diffusion.

However, in practice, surface diffusion is usually faster than grain-boundary diffusion. Then with the assumption of infinitely fast surface diffusion and the kinetics is controlled by grain-boundary diffusion, their stress relaxation function is given by^{21, 22}

$$\sigma(t) = \sigma_{\infty} + (\sigma_0 + \sigma_{\infty}) \frac{8}{\pi^2} \sum_{n=0}^{\infty} \frac{\exp(-\frac{t}{\tau_n})}{(2n+1)^2} \quad 3.8)$$

where

$$\tau_n = \left(\frac{4kTh^2l}{(2n+1)^2\pi^2M\Omega\delta_B D_{B0}} \right) \exp\left(\frac{Q_B}{kT}\right) \quad 3.9)$$

where T is temperature, h is film thickness, l is grain size, Q_B is activation energy for grain-boundary diffusion, M is biaxial modulus, Ω is atomic volume, δ_B is grain boundary width, D_{B0} is pre-exponential factor for grain boundary diffusivity, σ_0 is the initial stress, and σ_{∞} is the zero-creep stress.

The grain-boundary diffusivity at various temperatures can be obtained by fitting Eq. 3.8) to stress relaxation curves. With the other parameters fixed, the grain boundary diffusivity, $\delta_B D_B = \delta_B D_{B0} \cdot \exp(-Q_B/kT)$, is varied to minimize the error in the fitting curves. Figure 3.28 shows an example of stress relaxation results of the Au film at 20 and 80 °C fitted with the diffusion model, in comparison with the experimental data. The grain boundary diffusivity value $\delta_B D_B$ of the Au, AuV and AuV₂O₅ at 20, 50, 70 and 80 °C are listed in the Table 3.9 with the film structure and material parameters. Compared to the Prony series fits, the diffusivity model fits are very poor. Nonetheless, an activation energy can still be extracted.

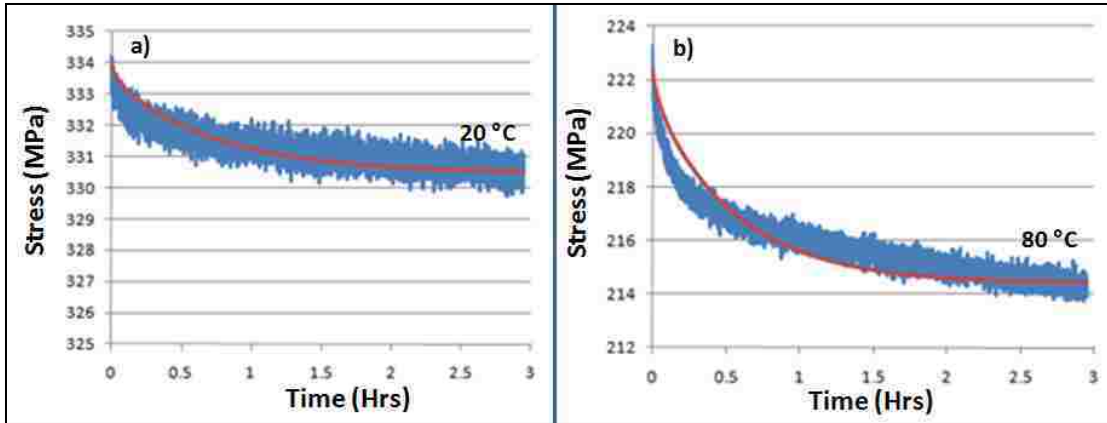


Figure 3.28 stress relaxation curves of Au film at a) 20 and b) 80 °C. The solid lines are fitted by the diffusion model.

| Parameter values | Au | AuV | AuV ₂ O ₅ |
|---|---|---|---|
| Film thickness (h) | 500 nm | 500 nm | 500 nm |
| Average grain size (l) | ~ 100 nm | ~52 nm | ~54 nm |
| Atomic volume (Ω) | $1.7 \times 10^{-29} \text{ m}^3$ | $1.7 \times 10^{-29} \text{ m}^3$ | $1.7 \times 10^{-29} \text{ m}^3$ |
| Grain-boundary diffusivity ($\delta_B D_B$) | | | |
| 20 °C | $2.53 \times 10^{-23} \text{ m}^2/\text{s}$ | $1.10 \times 10^{-23} \text{ m}^2/\text{s}$ | $1.20 \times 10^{-23} \text{ m}^2/\text{s}$ |
| 50 °C | $4.68 \times 10^{-23} \text{ m}^2/\text{s}$ | $1.34 \times 10^{-23} \text{ m}^2/\text{s}$ | $1.65 \times 10^{-23} \text{ m}^2/\text{s}$ |
| 70 °C | $5.43 \times 10^{-23} \text{ m}^2/\text{s}$ | $1.72 \times 10^{-23} \text{ m}^2/\text{s}$ | $1.80 \times 10^{-23} \text{ m}^2/\text{s}$ |
| 80 °C | $5.60 \times 10^{-23} \text{ m}^2/\text{s}$ | $1.98 \times 10^{-23} \text{ m}^2/\text{s}$ | $1.95 \times 10^{-23} \text{ m}^2/\text{s}$ |
| Activation energy (Q_B) | 0.12 eV | 0.09 eV | 0.07 eV |

Table 3.9 parameter values of diffusional model for Au, AuV, and AuV₂O₅.

With the relationship of the diffusivities and the Arrhenius equation, the activation energies are obtained from the slopes of plots of the natural log of diffusivity versus $1/T$. Figure 3.29 shows the activation energies extracted by the diffusion mechanism model. The activation energies for Au, AuV and AuV₂O₅ are 0.12, 0.09, 0.07 eV, respectively. These activation energies are, again, all small -on the order of 0.1 eV.

We observe that almost all of the time dependence introduced by the diffusion model of Gan and Ho comes from the first-term time constant ($n=1$). The second term is reduced in importance by a factor of 25 by the denominator of the sum. This is essentially the same as fitting the experimental modulus decay data with a single exponential decay as though it were a single term Prony series. This is the reason for the poor fit that it provides to the experimental relaxation data as shown in Figure 3.28. If the model allowed for different diffusion coefficients (for example because of different grain boundary geometries) each of these could be represented by a separate sum and the fitting would become effectively a multiterm Prony series.

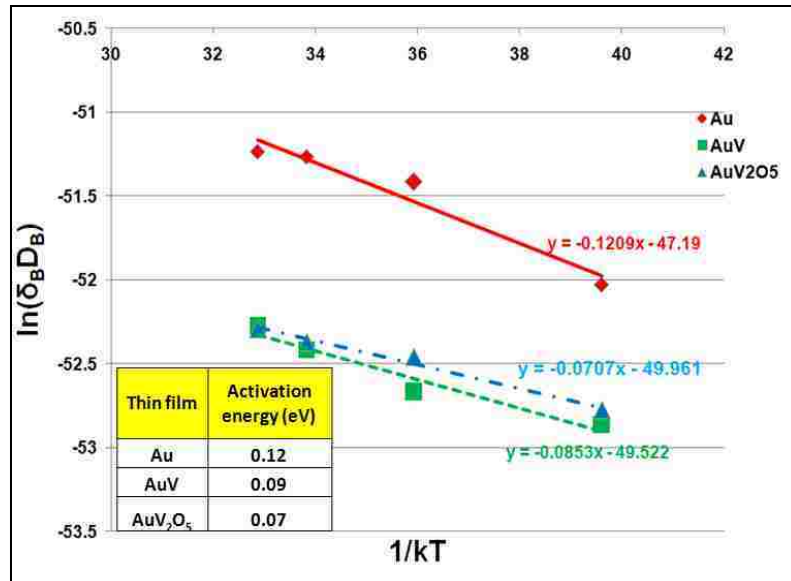


Figure 3.29 The activation energies deduced by the grain boundary diffusivity as a function of temperature.

3.4.4 Relaxation mechanism

In this part, we examine two possible relaxation mechanisms of the thin films based on Frost and Ashby⁵: grain boundary diffusion and low temperature plasticity based on dislocation glide.

The diffusion mechanism which is applicable for small grain sizes is discussed first. The activation energies deduced in sections 3.4.1 – 3.4.3 above all are small, approximately 0.1 eV. This value is extremely low compared with values for grain boundary diffusion from the literature.^{5, 89, 91, 92} It is approximately 10 times lower than the activation energy reported for diffusion in bulk Au.⁵ In Au films, Hummel and Geier reported the activation energy of 0.98 eV in the temperature range of 260- 380 °C.⁹¹ Activation energies in the range between 0.35-0.6 eV were given for diffusion mechanisms in Au films above 100 °C.^{89, 92} Diffusion mechanisms are primarily active at high temperature.⁵ Also, when the diffusion models are applied to the relaxation curves as presented in section 3.4.3, the model does not provide a good fit to the experiment. It is reasonable to conclude that grain boundary diffusion is not a dominant mechanism responsible for viscoelastic stress relaxation based on the low activation energy this study determined in the low temperature range of 20 -80 °C.

Dislocation glide is another possible mechanism that is active at low temperature. The movement of dislocations in low temperature plasticity is obstacle-limited because of their interactions with other dislocations, solutes or precipitates, grain boundaries, or lattice resistance.⁵ It is helpful to use the activation energy to

characterize obstacles by their strength. Weak obstacle strength (e.g. due to lattice resistance or solution strengthening) is defined when the activation energy less than $0.2\mu b^3$ (where μ is the shear modulus and b is the magnitude of the Burger's vector). Assuming a Burgers vector of 0.288 nm and a shear modulus of 27 GPa, $0.2 \mu b^3$ is approximately 0.8 eV. Medium strength obstacles (forest dislocations or weak precipitates) are defined as $0.2-1.0\mu b^3$, or as large as 4 eV for Au. Strong obstacles (strong precipitates or dispersions) have activation energies as large as $2.0 \mu b^3$, or 8 eV for Au. A weak obstacle strength is therefore in agreement with the activation energy in this study for all three materials despite the differences in composition. The weak "obstacle" known as lattice resistance or Peierls resistance limits dislocation movement through interaction with the atomic structure itself, whereas solution hardening involves interaction with lattice distortions associated with solution atoms.

In this study, an attractive possible mechanism which controls the dislocation velocity is known as the dislocation double kink mechanism. Kinks are defined as steps of atomic dimension in the dislocation line that are fully contained in the glide plane of the dislocation. A double kink is formed when two kinks of opposite character develop along a single dislocation. Consider the movement of a dislocation line which is rigidly pinned in two points situated in the same Peierls energy trough as shown in Figure 3.30. Double-kinks may be generated by several mechanisms such as the applied stress and thermal energy or the movement of the dislocations. The green circles symbolize the last atom on the inserted half-plane of an edge dislocation situated in the Peierls potential energy curve. Dashed lines in the Figure

represent the potential energy of a dislocation along a close-packed direction in the lattice. The activation energy of a double kink, which is approximately equal to $2W_k$ (where W_k is the energy of a kink), is given by⁹⁷

$$2W_k = \frac{\lambda}{\pi} \left(\frac{2\lambda b W_0 \sigma_p}{\pi} \right)^{1/2} \quad \mathbf{3.10}$$

where $\lambda \approx b$ is the wavelength of the Peierls potential, which is similar to the Burgers vector b , σ_p is the Peierls stress, and $W_0 \approx \mu b^2/2$ is the line tension of the dislocation.

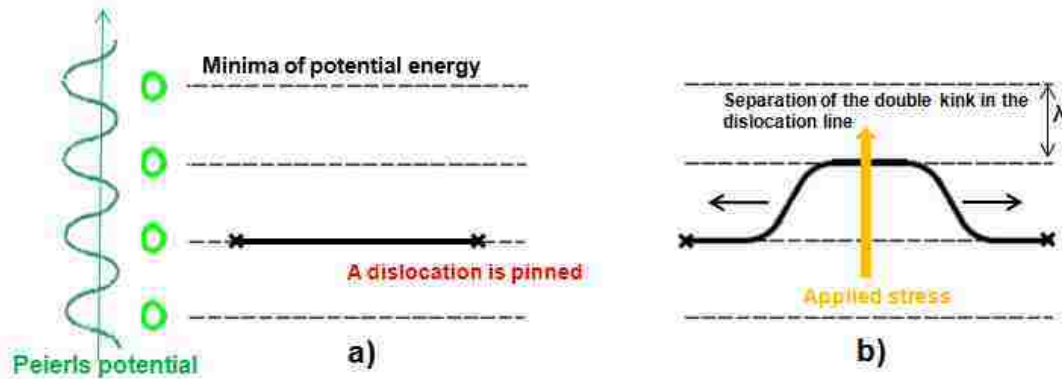


Figure 3.30 a) A dislocation segment rigidly pinned at the two points in the same Peierls energy trough, b) the advance of a dislocation through the Peierls potential by separation of the double kink in the dislocation.

With the mixed action of a mechanical stress applied to the dislocation and of stresses coming from thermal fluctuations, a bulge (double-kink) appears on the dislocation. Figure 3.31 shows the configuration of a dislocation segment moving forward by one step under the applied shear stress with double-kink generation. The dislocation segment can be considered as a portion a dislocation loop pinned at a grain boundary. Once a double-kink has been formed, the two single kinks can be

driven laterally spread out from each other, allowing the dislocation to pass one Peierls valley to the next causing the dislocation loop to expand. It is believed that the thermally activated formation and propagation of a double-kink on a pinned loop under the action of an applied stress should lead to a relaxation effect in the bulge test with fixed strain over time. If the applied stress is too small to cause dislocation glide without the assistance of thermal fluctuations, temperature and time dependence of the dislocation motion should result. As the loop expands, the resulting increase in line tension should provide an increase in resistance to further expansion, gradually decreasing the expansion rate and, therefore, the stress relaxation rate. When the applied stress is removed, the line tension or elastic stored energy in the bulged dislocation loop will bias the motion of the dislocation in order to retract the dislocation loop to the original location. If the dislocations fully return to their initial location then the material shows full viscoelastic recovery. If there is some permanent displacement between the initial and final condition, perhaps associated with unpinning from the original obstacles or increased pinning due to interaction with other obstacles, the material shows some permanent viscoplasticity which is not fully recoverable, as seen in the experimental results above.

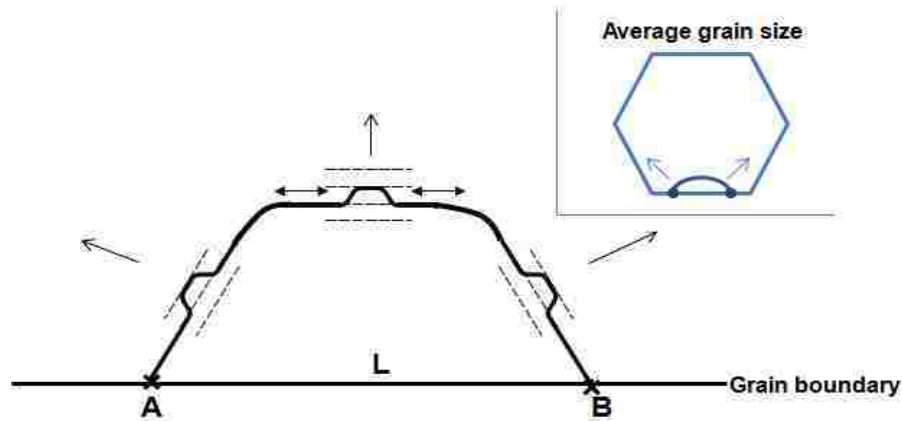


Figure 3.31 A schematic diagram showing the bowing out of a dislocation loop with several double kinks pinned at two point A and B with distance L apart on grain boundary.

According to this model, the presence of solute atoms or oxide dispersion particles alters the pinning distance, the mean free path for dislocation glide, and the magnitude of the Peierls stress. These changes should modify the resistance to loop expansion, but not the fundamental nature of the rate-determining obstacle (i.e., the lattice resistance).

One of the best ways to prove that a double kink mechanism is responsible for our relaxation results would be by comparison of the activation energies of our Au and Au alloy thin films with double kink simulation or analytical models. However, this is difficult because of the unavailability or uncertainty of the properties of solutes and dislocations, such as single-kink energy, Peierls stress, secondary Peierls barrier to kink migration, single-kink mobility, solute-kink interaction energies, solute misfit, etc. Instead we can take two approaches to address the possible double-kink

mechanism. First, we can compare of our activation energies with the known double kink nucleation energy for materials similar to Au. Second, we can compare our experimental observation of rate and temperature dependence with the double kink simulation model.

Firstly, based on the analytical double kink model developed by Hirth and Lothe,⁹⁸ if the rate of the double kink nucleation limits the dislocation motion, the activation energy can be estimated to be approximately half of the energy of double kink nucleation. Lytton et al^{99, 100} studied the low temperature creep of a single crystal of pure aluminum and reported an activation energy at 0.15 eV. Similar values of activation energy for Cu and Al were experimentally measured at 0.1 and 0.2 eV, respectively, for kink pair formation observed by internal friction measurement.¹⁰¹ It is reasonable to expect that the activation energy for Au is similar to that for other materials with structures similar to Au (i.e. FCC). Also, based on Eq. 3.10) for double kink formation, $Q = 2 W_k$, we can determine the Peierls stress (σ_p):

$$\sigma_p \approx \left(\frac{\pi Q}{4\lambda}\right)^2 \frac{\pi}{\lambda b^3 \mu} \quad \mathbf{3.11)}$$

Using $Q \approx 0.1$ eV, $\lambda = b = 0.288$ nm, and $\mu = 27$ GPa, the estimated Peierls stress is 32 MPa. This value is in good agreement with literature value of Peierls stress for FCC metals derived from experiment results, which vary from 20 to 30 MPa.¹⁰²

Second, a published dislocation double kink model is discussed to compare the model and experimental results. One of the double kink models is proposed by

Deo et al.^{103, 104} They present a Kinetic Monte Carlo method for simulating dislocation motion in pure Ta and Ta alloys related to the kink model. The model considers the motion of a dislocation on a particular glide plane, while the solute atoms are distributed in 3 dimensions. There are two interactions: a short-range interaction between a dislocation core and the solute and a long-range interaction of solute misfit and dislocation stress fields. The prediction of dislocation velocities is available for alloys in the effects of solute-core interaction energy, solute misfit and solute concentration. In this study, the summation of the Prony series coefficients is used as overall measurement of the temperature dependence for comparison with the double kink simulation model. Figure 3.32 shows the logarithm of the sum of Prony coefficient as a function of the inverse temperature for Au, AuV, and AuV₂O₅. We found that the results in Figure 3.32 are consistent with double kink model predictions of the dependence on these parameters as follows.

- Dislocation motion is thermally activated: stress relaxation is thermally activated.
- The rate of dislocation motion decreases with increasing solute addition: AuV and AuV₂O₅ have lower rates at all temperatures compared to Au.
- The dislocation velocity decreases with increasing dislocation-solute interaction energy and solute misfit: V₂O₅, which must have a much larger misfit than V, has a lower relaxation rate compared to AuV at the same % V.

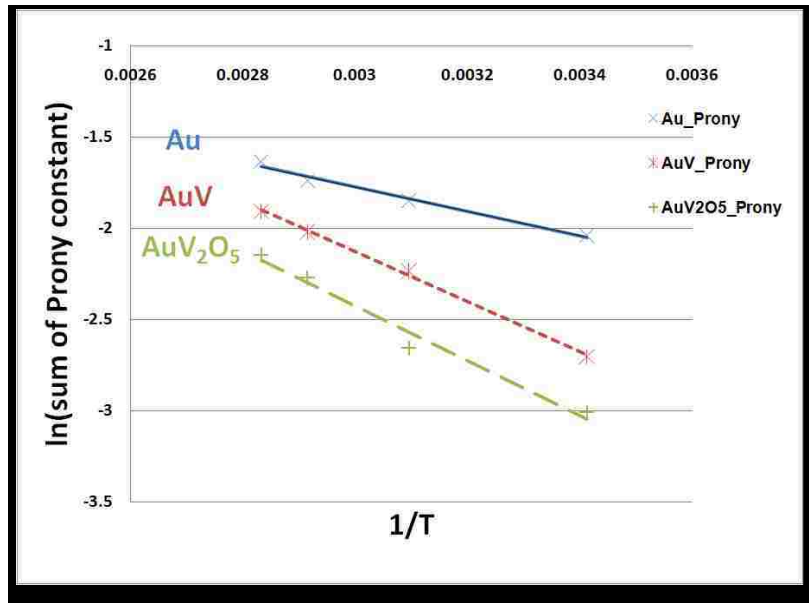


Figure 3.32 The logarithmic plot of the sum of Prony coefficient as a function of the inverse temperature.

3.5 Summary

Pure Au, solid solution AuV, and oxide dispersion strengthened AuV₂O₅ films are fabricated by DC magnetron sputtering at 500 nm thicknesses. The viscoelastic behavior of thin films of Au in comparison with thin films of AuV and AuV₂O₅ is investigated by using bulge technique. Solid solution (V) and oxide dispersion (V₂O₅) additions to Au thin films significantly decrease the magnitude and rate of viscoelastic modulus decay compared to pure Au in the 20 to 80 °C temperature range. The activation energies determined for modulus decay are small, on the order of 0.1 eV. These small energies, the low temperature, and the relatively larger effect of V₂O₅ compared with V lead us to conclude that the most probable mechanism for

viscoelastic modulus decay in Au and in the alloys investigated is due to double kink generation and reversible motion of dislocations in these materials.

4. Validity of linear viscoelastic models for pure Au thin films

It has been reported that the viscoelastic behavior of Au thin films is linear at room temperature after they have been conditioned so that all viscoplastic deformation has been exhausted.⁴ Additionally, the viscoelastic behavior is observed to be sensitive to strain rate. However, it has not been reported whether the linear property is still true at higher temperatures or at different strain rates. This study is designed to provide more experimental data of linear viscoelasticity of Au films by using gas pressure bulge testing at 20 and 80 °C. The influence of strain rate on the viscoelastic behavior of Au films is also investigated in the range 10^{-7} - 10^{-4} s⁻¹. Most reports describing the stress relaxation in thin films ignore the initial loading period and the strain rate effects during it which might result in an error in determination of their mechanical properties. The experiments presented in this chapter will address the impact of strain rate over more than three orders of magnitude and during the period of loading prior to the start of stress relaxation at constant strain. Finally, the quantitative analysis of the linear viscoelastic model and superposition will be carried out to predict the time dependence of stress at different strain rates. The goal of this work is to establish whether fully conditioned Au films are linearly viscoelastic, and if it is possible to predict the time dependent stress for different temperatures and strain rates in Au films that exhibit fully-recoverable viscoelastic deformation.

4.1 Linear viscoelasticity in Au thin film

In order to investigate the linear viscoelastic behavior of Au thin films, stress relaxations at constant strain are measured at two different strain amplitudes by using gas pressure bulge testing. It is noted that the tests are conducted on Au thin films on 210 nm tensile films of SiN. Two temperatures of 20 and 80 °C are investigated. The relaxation measurements have been made using the same experimental procedure as described earlier in which stress relaxation is followed for 3 hours at a constant applied strain of 0.1 %. This strain state is achieved following a pressure ramp from an initial applied strain of zero. A “run”, a sequence of a pressure ramp and a relaxation test, is performed only once per day to allow the film time to experience full viscoelastic recovery at zero strain before the next run. Such runs are repeated, one a day, until the film reaches a steady state condition. The pressure ramp and relaxation testing results that will be presented here are only after the steady state condition has been reached.

Figure 4.1 shows the time and temperature dependence of the normalized modulus of a Au film at 20 and 80 °C. It is observed that as the temperature increases, the modulus decay increases. Increasing the temperature from 20 to 80 °C causes the 3 hours modulus decay to increase from 5.4% to 8 %. Also, shown in Figure 4.1 with the solid line is a four-term Prony series fit to the relaxation data given by

$$N. M(t) = 1 - \sum_{i=1}^N P_i (1 - e^{-\frac{t}{\tau_i}}) \quad 4.1$$

The time constants (τ_i) are fixed at one per decade (10, 100, 1000, and 10000 second). The values of four Prony constants (P_i) at 20 and 80 °C are listed in Table 4.1. Figure 4.1 b) is plotted with a logarithmic time scale to clearly show the early time relaxation which is important in the next section to predict the time dependent stress.

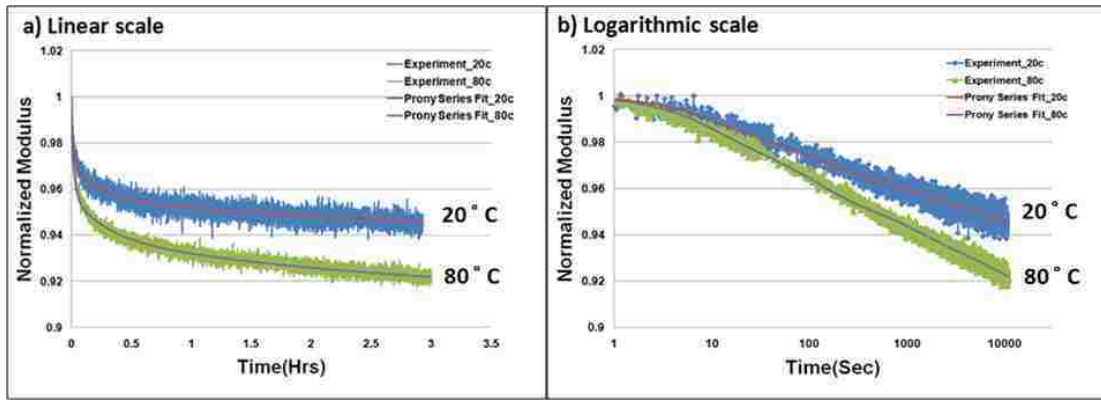


Figure 4.1 Relaxation modulus of the Au film at 20 and 80 °C at the constant strain 0.001.

| Temperature (°c) | P1 (t=10 s) | P2 (t=100 s) | P3 (t=1000s) | P4 (t=10000 s) |
|------------------|-------------|--------------|--------------|----------------|
| 20 °c | 0.0120 | 0.0136 | 0.0168 | 0.0203 |
| 80 °c | 0.0167 | 0.0210 | 0.0221 | 0.0279 |

Table 4.1 Fitting Prony series constants of Au film at steady state for 20 and 80 °C.

Figure 4.2 shows the time dependence of normalized relaxation on a linear scale and a logarithmic scale when the pressure is applied to the Au film from zero to

the two different strain levels of 0.0005 and 0.001, then held at a constant value for 3 hours for both 20 and 80 °C. The identical behavior of the normalized modulus for the two different strain levels demonstrates linear viscoelasticity in the Au thin film.

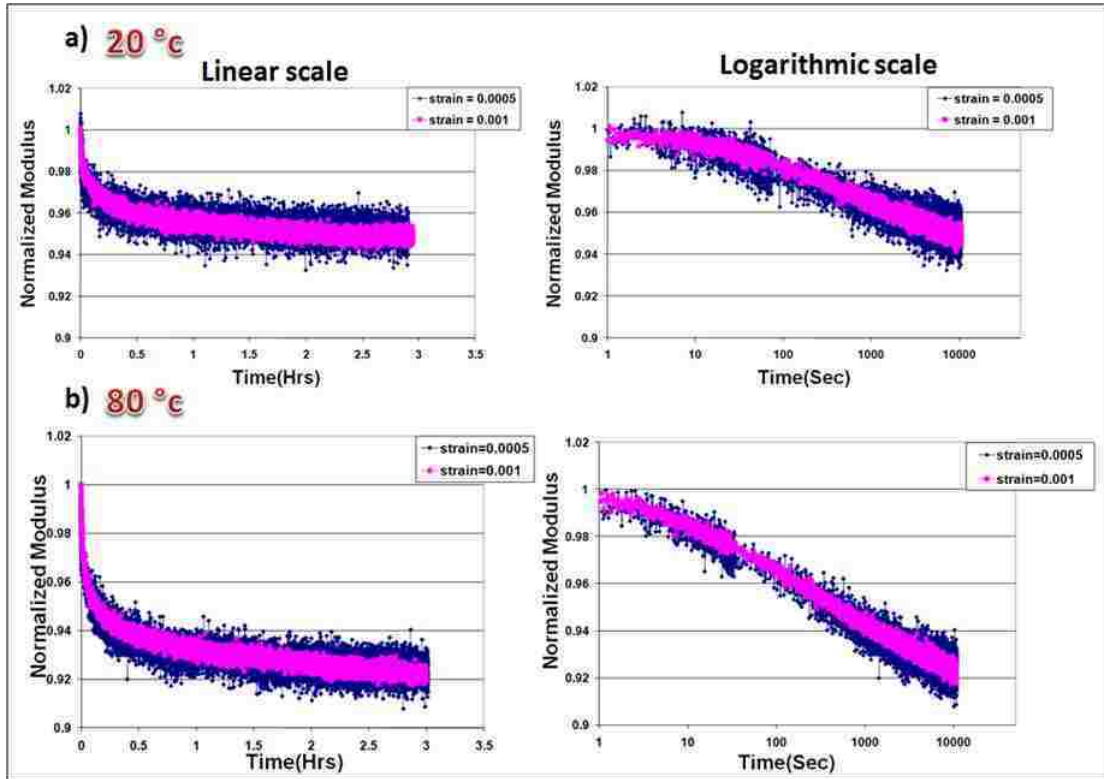


Figure 4.2 Normalized modulus of Au thin film at different strains of 0.0005 and 0.001 at two temperatures (a) 20 °C and (b) 80 °C.

4.2 Strain rate dependence of stress and stress relaxation

In order to examine the dependence of strain rate on the mechanical properties of a Au film, we apply five different pressures ramps to the Au film. A pressure ramp up from zero to 100 torr and back to zero is carried out at a rate of 8, 4, 1, 0.25, or 0.025 torr/sec which correspond to strain rates of $1.07 \times 10^{-4} \text{ s}^{-1}$, 5.36×10^{-5}

s^{-1} , $1.34 \times 10^{-5} s^{-1}$, $3.38 \times 10^{-6} s^{-1}$, and $3.36 \times 10^{-7} s^{-1}$ respectively. Figure 4.3 shows a schematic plot of pressure versus time (solid line) corresponding to strain rate versus time (dashed line). The strain is not quite linear with time, but it is adequately represented by a constant strain rate. The strain rates are determined by the slope of strain with time on the loading part of each curve. Also, Table 4.2 shows the value of strain rates corresponding to pressure rates. It is observed that strain rates are simply the pressure rates times a factor. The fastest strain rate is about 300 times the slowest strain rate.

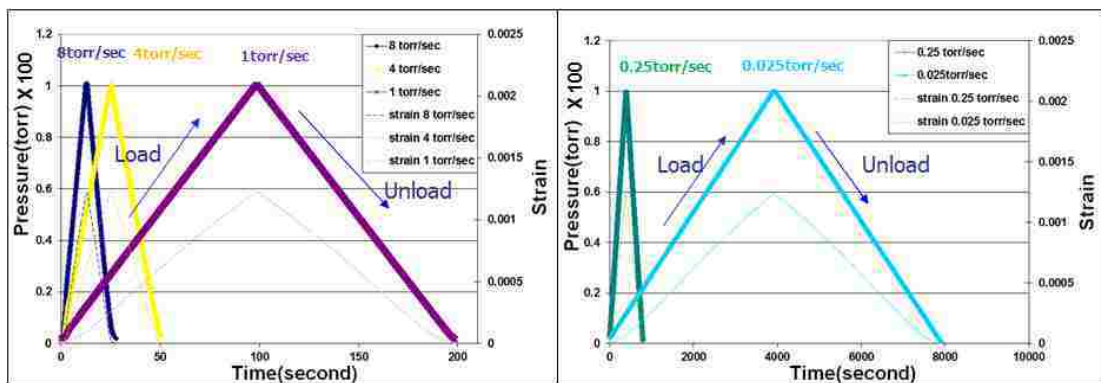


Figure 4.3 Pressure and strain versus time for different pressure rates from 8 torr/sec to 0.025 torr/sec.

| | | | | | |
|--------------------------|-----------------------|-----------------------|-----------------------|-----------------------|-----------------------|
| Pressure rate (Torr/Sec) | 0.025 | 0.25 | 1 | 4 | 8 |
| Strain rate | 3.36×10^{-7} | 3.38×10^{-6} | 1.34×10^{-5} | 5.34×10^{-5} | 1.07×10^{-4} |

Table 4.2 Value of strain rates corresponding to pressure rates shows the fastest strain rate is 300 times the slowest strain rate.

4.2.1 Effect of strain rates on pressure ramp results of Au thin film at 20 and 80 ° C

The pressure ramp test for different strain rates from $3.4 \times 10^{-7} - 1.07 \times 10^{-4} \text{ s}^{-1}$ are applied to a Au film at 20 and 80 °C. Figure 4.4 shows a set of stress-strain curves spanning the entire set of strain rates. The unloading curves have been used to determine the residual stress, plane strain modulus, and stress at a strain 0.1 % in the Au film. Table 4.3 lists the measured mechanical properties for 20 and 80 °C.

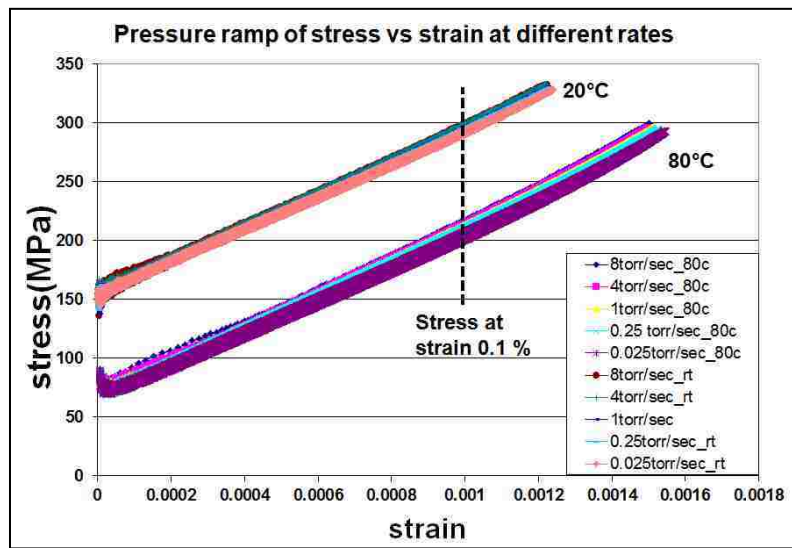


Figure 4.4 Stress and strain curve of Au/SiN at 20 and 80 °C at different strain rates.

| Temperature | Pressure rate (torr/sec) | Strain rate (s^{-1}) | Residual stress (MPa) | Plane strain modulus(GPa) | Stress at 0.1% strain (MPa) |
|-------------|--------------------------|--------------------------|-----------------------|---------------------------|-----------------------------|
| 20 °c | 0.025 | 3×10^{-7} | 152.84 | 136.83 | 293.20 |
| | 0.25 | 3×10^{-6} | 153.30 | 139.03 | 295.60 |
| | 1 | 1×10^{-5} | 153.50 | 140.30 | 297.20 |
| | 4 | 5×10^{-5} | 152.80 | 143.32 | 299.10 |
| | 8 | 1×10^{-4} | 152.14 | 143.23 | 300.80 |
| 80 °c | 0.025 | 3×10^{-7} | 62.54 | 136.50 | 206.87 |
| | 0.25 | 3×10^{-6} | 62.99 | 139.04 | 210.52 |
| | 1 | 1×10^{-5} | 63.21 | 141.40 | 212.94 |
| | 4 | 5×10^{-5} | 62.88 | 143.50 | 215.44 |
| | 8 | 1×10^{-4} | 62.61 | 144.50 | 217.36 |

Table 4.3 Properties of Au film at steady state of 20 and 80 °C for different strain rates.

In order to quantify the effect of strain rate on viscoelastic properties, the properties are plotted vs. the logarithmic strain rate. Figure 4.5 shows the effect of strain rate on Au film properties at 20 and 80 °C. The Au film at 80 °C shows the same behavior of strain rate dependence as at 20 °C. The values of residual stress are similar for the different strain rates due to the original property of the thin film. In contrast, the plane strain modulus and stress at any strain such as 0.1% are strain rate dependent. As the strain rate decreases, the modulus and any specific stress decrease caused by relaxation are presented in Figure 4.5b) and c). These results are consistent with Emery and Povirk's results^{36, 37} for tensile behavior of Au films at room temperature. Emery et al. reported that the properties of fine-grained Au films (grain size less than 500nm) have a dependence on the strain rate, in contrast with coarse-grained Au films.

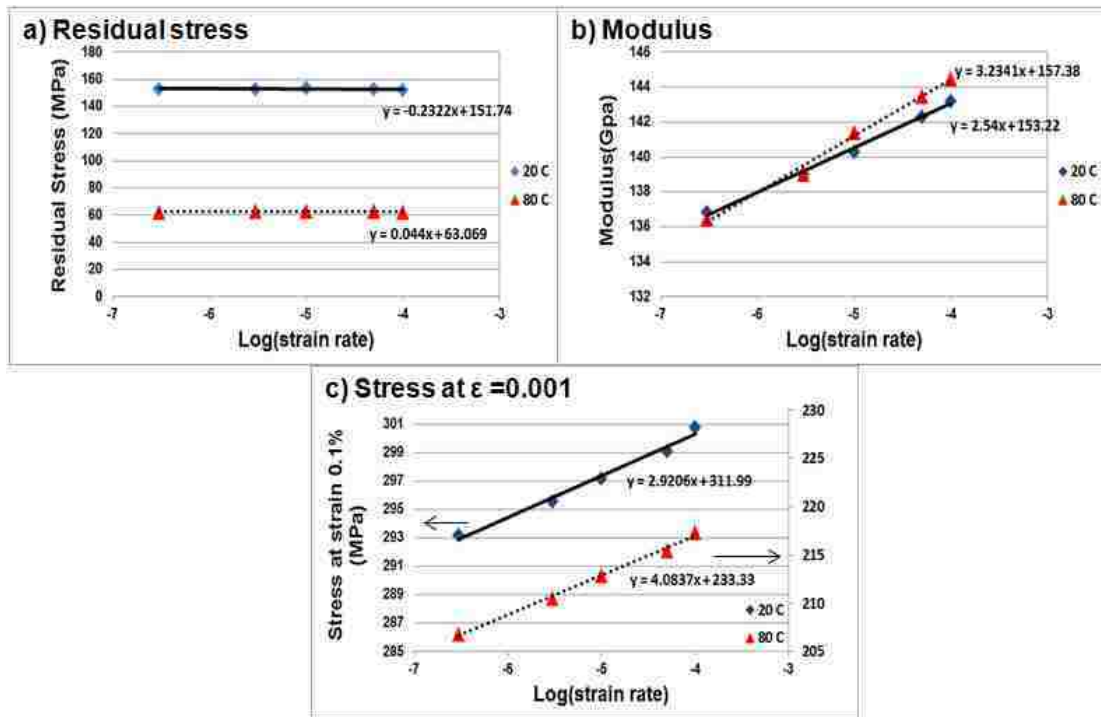


Figure 4.5 The effect of strain rates on Au film properties at 20 and 80 °C of a) residual stress, b) plane strain modulus and c) stress at strain 0.1%.

4.2.2 Effect of strain rates on relaxation results of Au thin film at 20 and 80 °C

At each strain rate, the 3 hour relaxation experiments are conducted until the Au film reaches a steady state condition - the completely recoverable, viscoelastic state. The response during the loading for various strain rates are considered here for stress relaxation. The overall relaxation experiment at different strain rates for 20 °C is shown on a linear scale and a logarithmic scale in Figure 4.6 and Figure 4.7, including the loading, relaxation and unloading segments. Figure 4.6 b) and Figure 4.7 b) focus on the relaxation part to clearly demonstrate the significant difference during the transition between the loading and relaxation segments. The results are

shown on a logarithmic time scale since they are more clearly presented in the loading part. First, the relaxation curves overlap to a substantial extent, and the degree of relaxation is the same after the full 3 hour-stress relaxation for each loading rate case. Second, for the slow loading rate cases there are obviously “stress pop-ups” at the point where there is a change from the loading segment to the relaxation segment. However, this stress overshoot is quickly eliminated and the relaxation curve soon follows the same path as the other cases. This is because a significant amount of relaxation has already taken place during the loading segment of the slower strain rate cases, so at the time when the loading-to-relaxation transition takes place the slow strain rates cases exhibit slower stress relaxation. This behavior is also seen in 80 °C at two different strain rates of 10^{-4} and 10^{-7} s^{-1} as shown in Figure 4.8 and Figure 4.9.

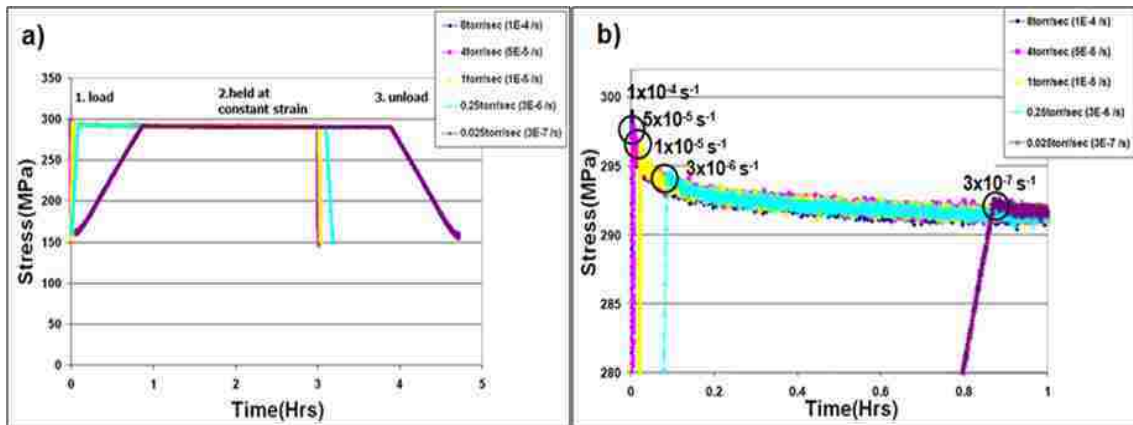


Figure 4.6 Linear time scale of stress relaxation results at different strain rates from 10^{-4} – $3 \times 10^{-7} \text{ s}^{-1}$ at 20°C (a) overall relaxation and (b) only stress relaxation section.

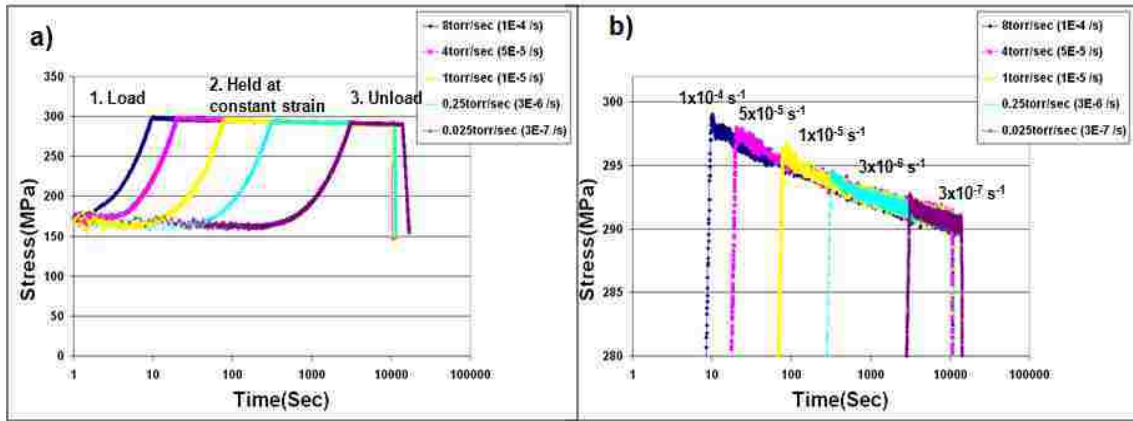


Figure 4.7 Logarithmic time scale of stress relaxation results at different strain rates from $10^{-4} - 3 \times 10^{-7} \text{ s}^{-1}$ at 20°C (a) overall relaxation and (b) only stress relaxation section.

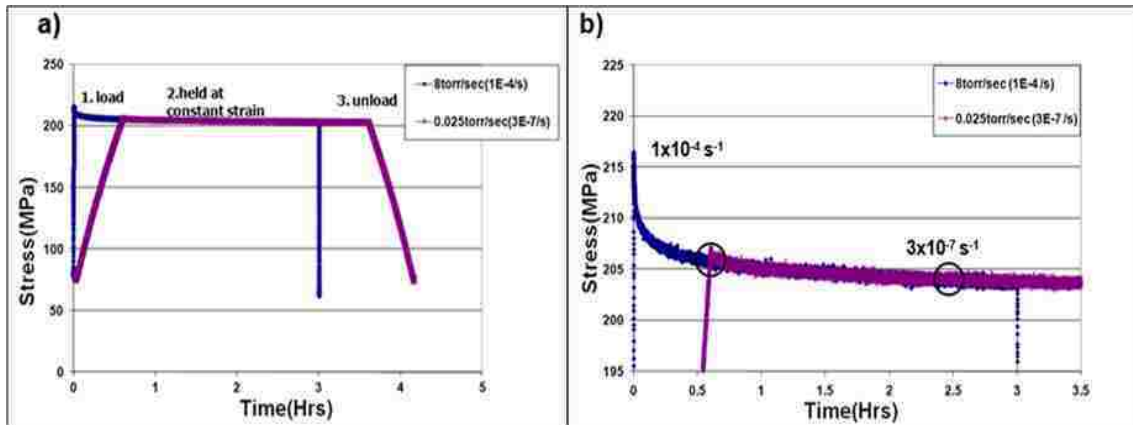


Figure 4.8 Linear time scale of stress relaxation results at different strain rates from $10^{-4} - 3 \times 10^{-7} \text{ s}^{-1}$ at 80°C (a) overall relaxation and (b) only stress relaxation section.

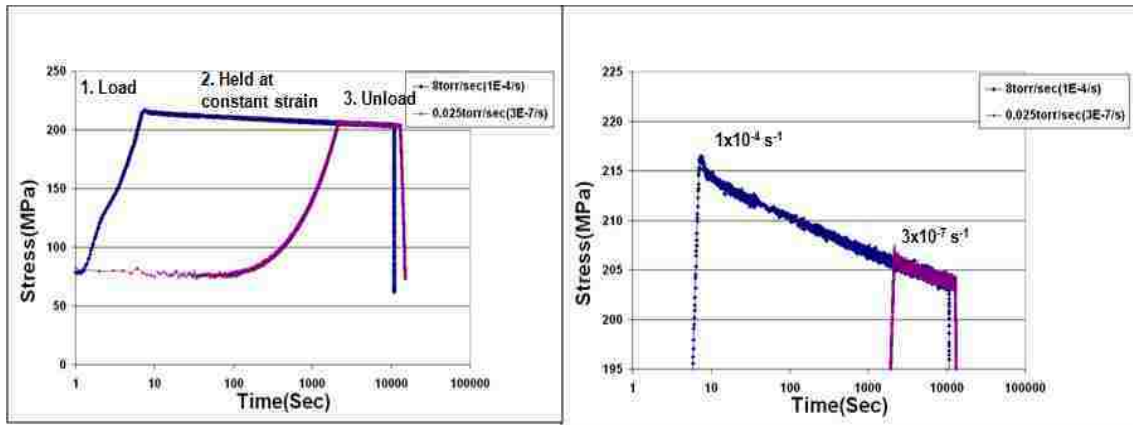


Figure 4.9 Logarithmic time scale of stress relaxation results at different strain rates from $10^{-4} - 3 \times 10^{-7} \text{ s}^{-1}$ at 20°C (a) overall relaxation and (b) only stress relaxation section.

4.3 The time dependent stress determined by linear viscoelastic model

Since the thin Au films exhibit linear viscoelasticity, we should be able to determine the time dependence of the stress for any time dependent applied strain using linear superposition. Figure 4.10 shows strain versus time for the model used to evaluate the applicability of linear superposition to Au film viscoelastic relaxation. The experimental data of stress dependence in the first three parts (segment 1-3) is measured continuously during the 3 hour stress relaxation experiment. During the recovery period (segment 4), the stress is determined by brief, individual, intermittent, strain ramp measurements that assess the time-dependent stress state. This approach is necessary because the film is flat when the applied strain is zero, so changes in stress cannot be evaluated by the bulge test.

$$\begin{array}{llll}
 \varepsilon(t) = \varepsilon_1 \cdot t / (t_1 - t_0) & ; t_0 < t \leq t_1 & d\varepsilon/dt = \varepsilon_1 / (t_1 - t_0) & ; t_0 < t \leq t_1 \\
 \varepsilon_1 & ; t_1 < t \leq t_2 & 0 & ; t_1 < t \leq t_2 \\
 \varepsilon_1 - \varepsilon_1 \cdot t / (t_3 - t_2) & ; t_2 < t \leq t_3 & -\varepsilon_1 / (t_3 - t_2) & ; t_2 < t \leq t_3 \\
 0 & ; t_3 < t \leq t_4 & 0 & ; t_3 < t \leq t_4
 \end{array} \tag{4.2}$$

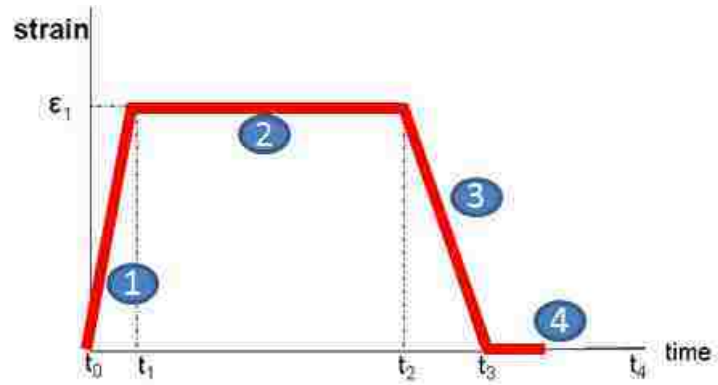


Figure 4.10 strain versus time for linear viscoelastic model.

The stress as a function of time can be calculated by superposition as:

$$\sigma(t) = \sigma_0 + \varepsilon_0 E(t) + \int_0^t E(t - \xi) \frac{d\varepsilon(\xi)}{d\xi} d\xi \quad 4.3$$

where σ_0 is the residual stress, ε_0 is the instantaneous applied strain, $\frac{d\varepsilon(\xi)}{d\xi}$ is the strain rate, and $E(t)$ is time dependent modulus which is given by

$$E(t) = E_0 \left(1 - \sum_{i=1}^N P_i \left(1 - e^{-\frac{t}{\tau_i}} \right) \right) \quad 4.4$$

where E_0 is the instantaneous modulus of the films, P_i is i 'th Prony constant and τ_i is i 'th time constant.

The result is:

Step 1: $t_0 < t \leq t_1$

$$\sigma_1(t) = \sigma_0 + \frac{E_0 \cdot \varepsilon_1}{t_1} \cdot \left(t - \sum P_i t + \sum P_i \tau_i - \sum P_i \tau_i \cdot e^{-\frac{t}{\tau_i}} \right) \quad 4.5$$

Step 2: $t_1 < t \leq t_2$

$$\sigma_2(t) = \sigma_0 + \frac{E_0 \cdot \varepsilon_1}{t_1} \cdot \left(t_1 - \sum P_i t_1 + \sum P_i \tau_i \cdot e^{-\frac{(t-t_1)}{\tau_i}} - \sum P_i \tau_i \cdot e^{-\frac{t}{\tau_i}} \right) \quad 4.6$$

Step 3: $t_2 < t \leq t_3$

$$\sigma_3(t) = \sigma_0 + \frac{E_0 \cdot \varepsilon_1}{t_1} \cdot \left(t_1 - \sum P_i t_1 + \sum P_i \tau_i \cdot e^{-\frac{(t-t_1)}{\tau_i}} - \sum P_i \tau_i \cdot e^{-\frac{t}{\tau_i}} \right) - \frac{E_0 \cdot \varepsilon_1}{(t_3-t_2)} \cdot \left(t - \sum P_i t + \sum P_i \tau_i - t_2 + \sum P_i t_2 - \sum P_i \tau_i \cdot e^{-\frac{(t-t_2)}{\tau_i}} \right) \quad 4.7$$

The first section of Eq. 4.7 is equal to Eq. 4.6. Thus,

$$\sigma_3(t) = \sigma_2(t) - \frac{E_0 \cdot \varepsilon_1}{(t_3-t_2)} \cdot \left(t - \sum P_i t + \sum P_i \tau_i - t_2 + \sum P_i t_2 - \sum P_i \tau_i \cdot e^{-\frac{(t-t_2)}{\tau_i}} \right) \quad 4.8$$

where $\sigma_2(t)$ is Eq 4.6 and it is function of time.

Step 4: $t_3 < t \leq t_4$

$$\sigma_4(t) = \sigma_2(t) - \frac{E_0 \cdot \varepsilon_1}{(t_3-t_2)} \cdot \left(t_3 - \sum P_i t_3 + \sum P_i \tau_i \cdot e^{-\frac{(t-t_3)}{\tau_i}} - t_2 + \sum P_i t_2 - \sum P_i \tau_i \cdot e^{-\frac{(t-t_2)}{\tau_i}} \right) \quad 4.9$$

4.3.1 Simulation for multiple loading results

By using the four-term Prony series derived from the experimental relaxation experiment associated with loading at 8 torr/sec, which provides the best available data for short times because it is the most rapid loading rate, we can predict stress as a function of time during loading and stress relaxation segments at other, lower, strain rates. The relaxation function in the form of a Prony series for Au at 8 torr/sec was presented earlier in Figure 4.1 and Table 4.1. The loading and stress relaxation are shown in experimental segments 1 and 2 in Figure 4.10. Eq. 4.5) and 4.6), which correspond to the loading and relaxation parts, provide a model to simulate the time

dependence stress in the Au film if the starting conditions (σ_0 , E_0 and ϵ_1) are known. Using the Prony series for a Au film at 8 torr/sec, simulations for 5 experiments at lower strain rates have been carried out. The comparison of the experimental and simulation results at 20 °C is given in Figure 4.11 and Figure 4.12 for linear and logarithmic time scales, respectively. There is a good match of experimental data and simulation giving further verification that linear viscoelasticity is an appropriate description of Au film. The same validity of the linear model is also applicable at 80 °C as shown in Figure 4.13 and Figure 4.14. It is particularly noteworthy that the stress overshoot at the peak stress of each loading segment is captured by the simple superposition model without any need to resort to a special transient relaxation model that would pertain only to the initial loading behavior.

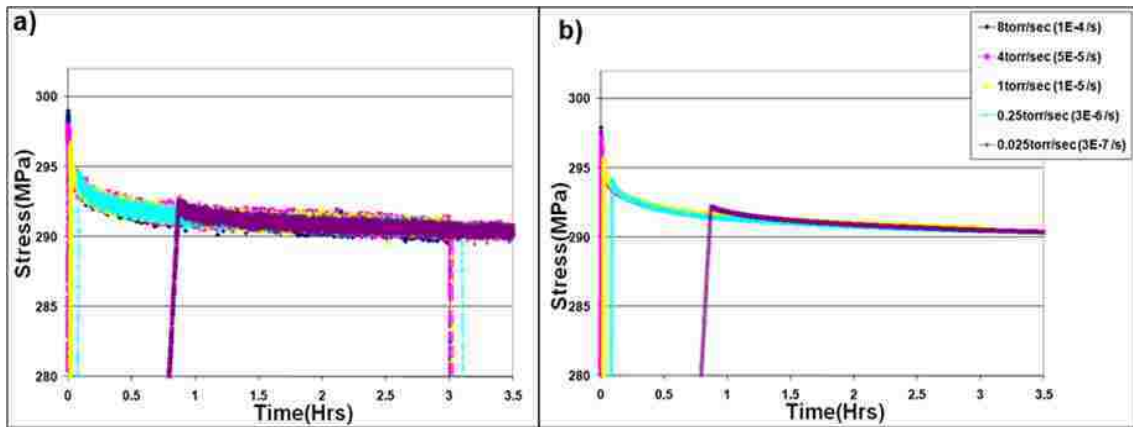


Figure 4.11 Comparison of relaxation results on linear time scale at different strain rates at 20°C between (a) the experiment and (b) linear viscoelastic model.

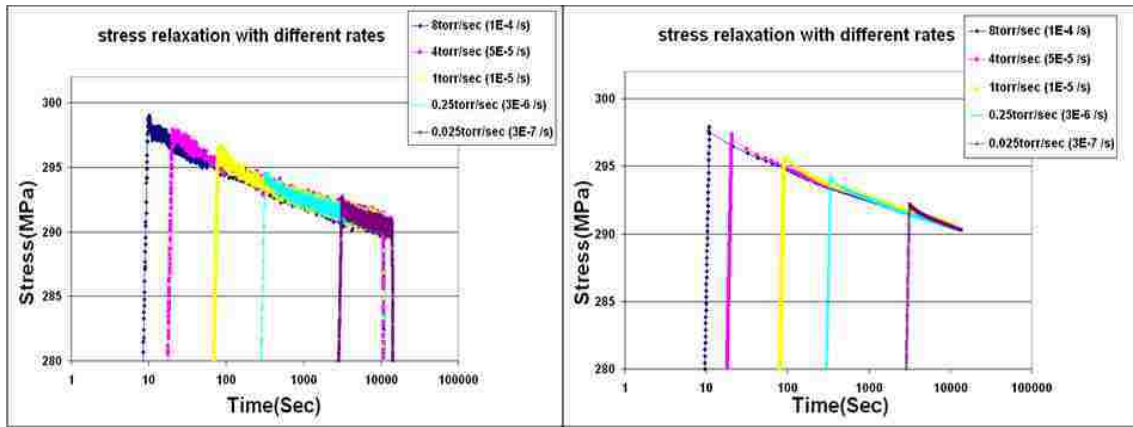


Figure 4.12 Comparison of relaxation results on logarithmic time scale at different strain rates at 20°C between (a) the experiment and (b) linear viscoelastic model.

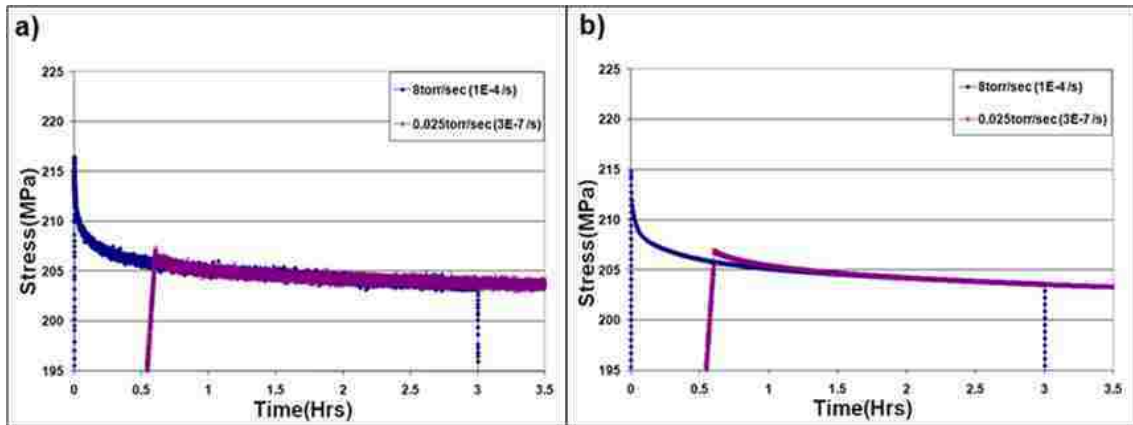


Figure 4.13 Comparison of relaxation results on linear time scale at different strain rates at 80°C between (a) the experiment and (b) linear viscoelastic model.

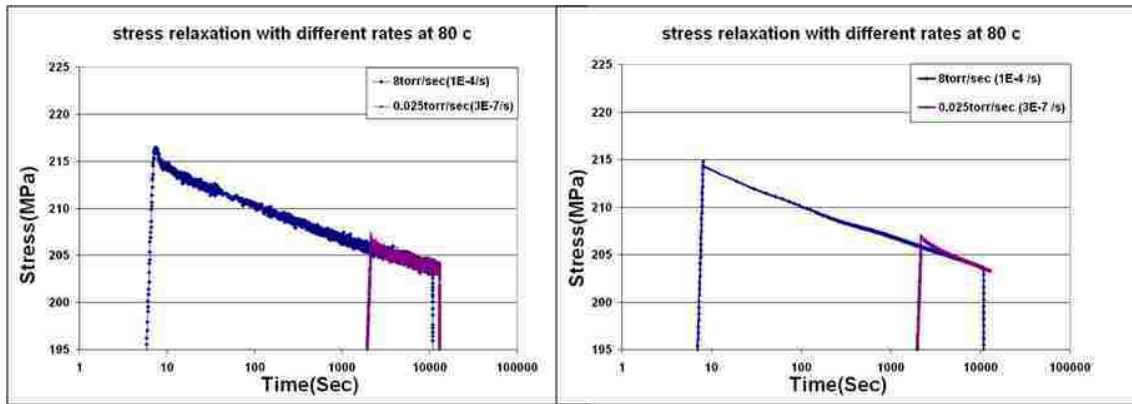


Figure 4.14 Comparison of relaxation results in logarithmic time scale at different strain rates at 80°C between (a) the experiment and (b) linear viscoelastic model.

The stress function of multiple loading process as presented in Figure 4.10 can be derived by using Eq. 4.5)-4.9). Figure 4.15 and Figure 4.16 show the experimental data and the viscoelastic expectation for the stress during more complex imposed strain/time dependence including loading, constant strain, unloading, and recovery parts at 20 and 80 °C. Accurate simulation of time dependent stress in thin films can be useful for structural devices, such as RF MEMS switches, to predict the mechanical effect under complex conditions. For example, the restoring force in RF MEMS switch can be estimated using predictable time-dependent stress.

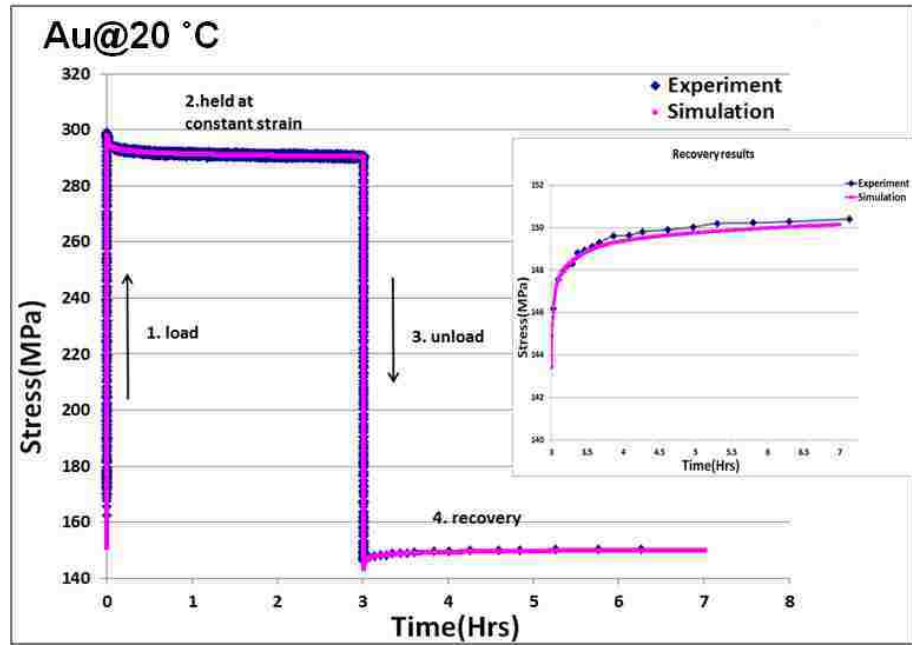


Figure 4.15 Comparison of experiment and simulation results for multiple loading parts at a strain rate of 10^{-4} s^{-1} at $20 \text{ }^\circ\text{C}$ including the recovery part shown in the inset.

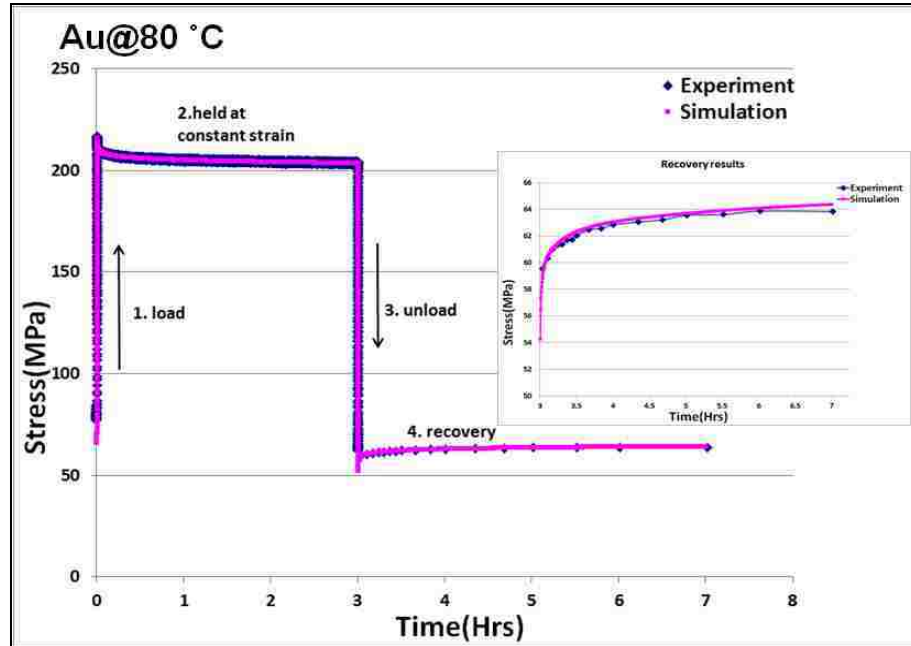


Figure 4.16 Comparison of experiment and simulation results for multiple loading parts at a strain rate of 10^{-4} s^{-1} at $80 \text{ }^\circ\text{C}$ including the recovery part shown in the inset.

4.3.2 Simulation for strain ramp results

The linear model is also applied to simulate strain ramp results for comparison to the experimental results. Figure 4.17 shows the experimental data and the viscoelastic expectation for the stress during a strain ramp at 20 °C for a) 8 torr/sec (strain rate $1 \times 10^{-4} \text{ s}^{-1}$) and b) 0.025 torr/sec (strain rate $3 \times 10^{-7} \text{ s}^{-1}$).

It is shown that the linear viscoelastic model provides an excellent fit to both simple and complicated loadings including relaxation and strain ramping which further indicates the linear viscoelastic behavior of the Au film.

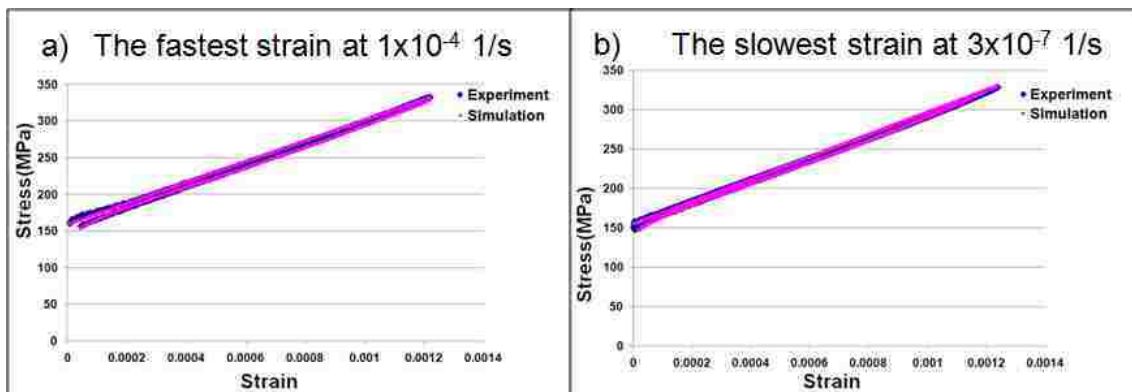


Figure 4.17 Comparison of experiment and simulation results for strain ramp results at the strain rate a) 10^{-4} s^{-1} and b) $3 \times 10^{-7} \text{ s}^{-1}$ at 20 °C.

4.4 Summary

The Au thin films characterized in this study show linear viscoelasticity at both 20 and 80 °C after having been conditioned to remove all potential for substantial viscoplastic deformation. The normalized time dependent modulus is

identical at two different strain levels, a basic requirement of linear viscoelasticity. Using this time dependent modulus in a superposition model of time dependent stress in response to a variety of different imposed time dependent strains, the simulation and the experimental results are in good agreement, providing further verification of the conclusion that the Au thin films are linearly viscoelastic.

5. The effect of solute concentration on relaxation behavior of AuV solid solutions

It is known that solid solution additions can play a crucial role for strengthening of metals. In bulk materials, increasing the concentration of the solute typically results in an attendant increase in yield and tensile strength. The effects of concentration on mechanical properties of thin films have also been investigated to some degree. However, there is still no information in the literature on the concentration dependence of relaxation behavior for solid solutions. This study is designed to explore the effect of V concentration on sputter-deposited AuV films (at approximately 1 to 5 at % V) on relaxation behavior at 20, 50, and 80 °C. AuV films with different concentrations will be compared in terms of normalized modulus or the 3-hour modulus decay. Since the solid solution strengthening mechanism is a major contribution to film strengthening and the primary viscoelastic stress relaxation mechanism active in Au is based on dislocation motion, it is expected that increasing V content in the AuV alloys will increase the relaxation resistance. The degree of stress relaxation which relates to the strength of the materials should be dependent on V content. The goal is to develop a quantitative model for the effect of solute concentration on relaxation of AuV films.

5.1 Characterization of thin films

AuV solid solution with different V concentrations were deposited and fabricated as 500 nm thick bulge samples, as described earlier. The various

compositions of V were created by adjusting the power of the V sputtering gun. The Au target gun was fixed at 150 watt and the power of the V target gun was varied between 0 watt and 120 watt. The V content of each thin film was determined from SEM analysis in combination with EDS software. Figure 5.1 shows the zoomed spectrum in the region of the V peak; the different area of each peak relates to the different compositions.

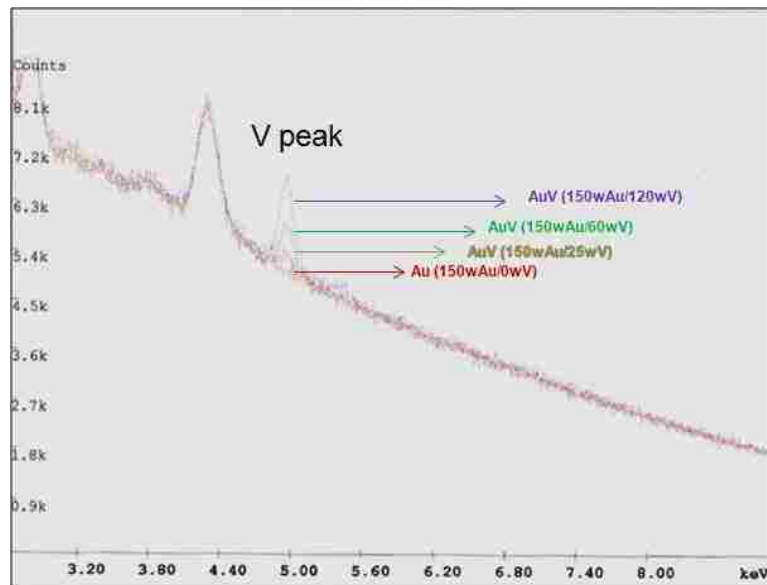


Figure 5.1 EDS results for the set of AuV films show differences at the V peak related to the different V concentrations.

The quantitative V content of each sample can be estimated by using the ratio of characteristic x-ray intensity of V peak area to that measured from the calibrated 4.5 at. %V film, and the ratio should be equal to the ratio of V content.¹⁰⁵ Following the k ratio formula, the results are shown in Table 5.1.

$$\frac{C_i}{C_s} = \frac{I_i}{I_s} = K_i \quad \mathbf{5.1}$$

where C_i = composition of sample (unknown), C_s = composition of standard, I_i = x-ray intensity above background from the i 'th sample, and I_s = x-ray intensity above background from the standard sample.

| Power Au (Watt) | Power V (Watt) | at. % V |
|--------------------|-------------------|---------|
| 150 | 0 | 0 |
| 150 | 25 | 0.89 |
| 150 | 60 | 2.2 |
| 150 | 120 | 4.5 |

Table 5.1 Percent V content estimated by EDS software.

SEM images show the grain size of the films in Figure 5.2. By using the mean linear intercept method, the average grain size in AuV solid solution at 0, 0.89, 2.2 and 4.5 at.% V are approximately 115, 110, 93 and 90 nm, respectively. The decrease in grain size due to the addition of V is not very large in this study.

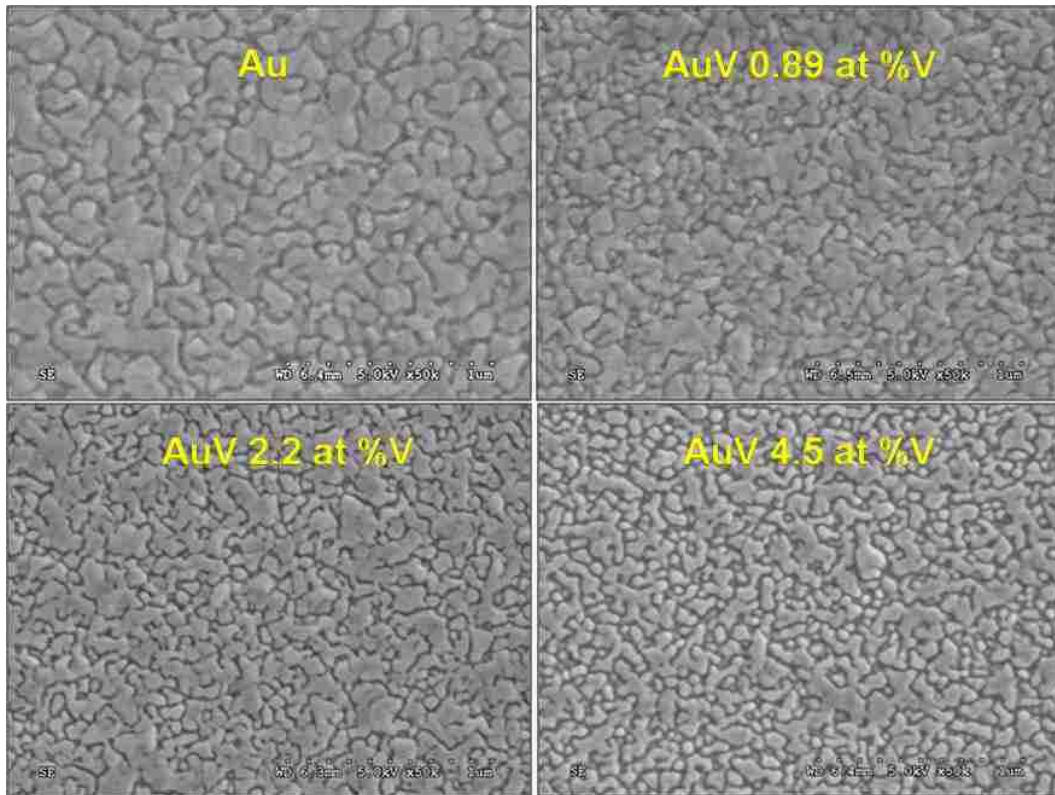


Figure 5.2 SEM images of pure Au and AuV at 0.89, 2.2, 4.5 at. %V.

5.2 Temperature dependence of relaxation behavior of AuV solid solution thin films

In this part, we characterize the temperature dependence of viscoelasticity of sputter-deposited solid solution strengthened Au-V films with 0, 0.89, 2.2, and 4.5 at.% V. It is noted again that although all films in the experiment are composite films with a SiN layer beneath the metal, we convert the results of the composite films to free standing films by subtracting the elastic contribution of the SiN film. Then, a four-term Prony series is used, with fixed time constants of 10, 100, 1000 and 10,000 seconds, to fit the experimental results of free standing films. All results after that are shown in terms of a Prony series fit, rather than the raw data, for clarity.

For each film within the set of AuV films, the results are shown in two parts. The first one is the experimental results of relaxation curves showing the initial condition and steady-state condition at 20, 50 and 80 °C, in order. At each temperature, repeated relaxation experiments are conducted until a steady-state condition is reached, as has been described before. The second one shows only the steady-state relaxation curves for each temperature. The steady-state relaxation curves are shown in terms of four-term Prony series fits, rather than the raw data.

5.2.1 Pure Au thin film

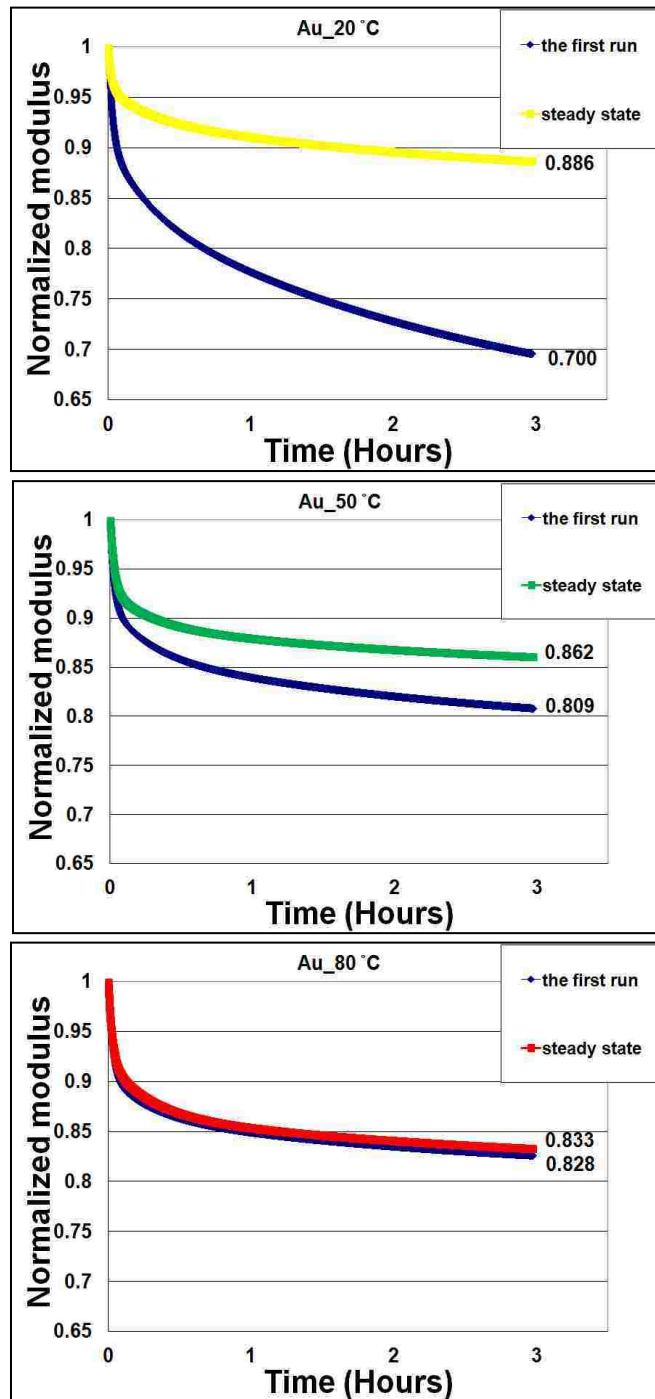


Figure 5.3 Relaxation of normalized modulus of pure Au thin film for each temperature (20, 50 and 80 °C) from the first run to steady state condition.

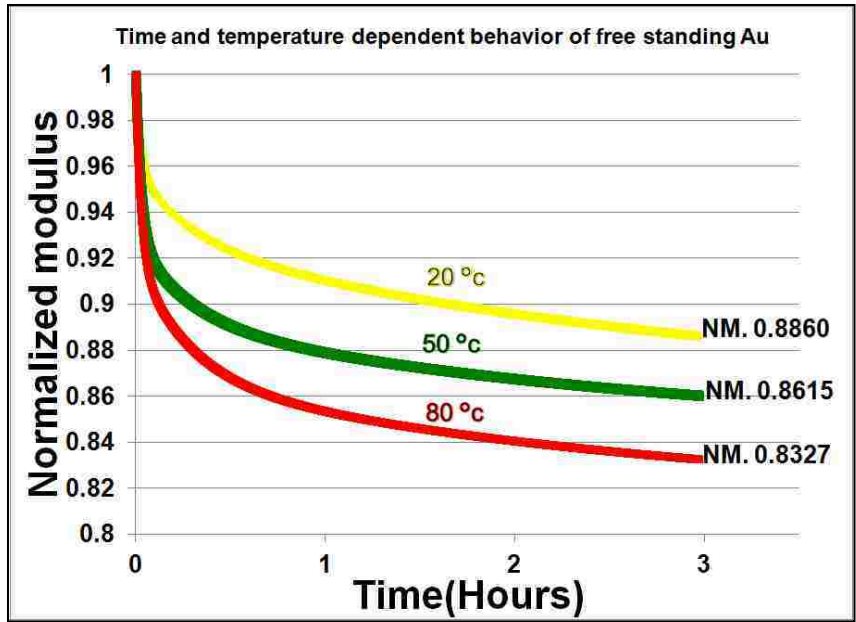


Figure 5.4 Steady-state relaxation curves for each temperature of pure Au film.

5.2.2 Solid solution of AuV 0.89 at. %

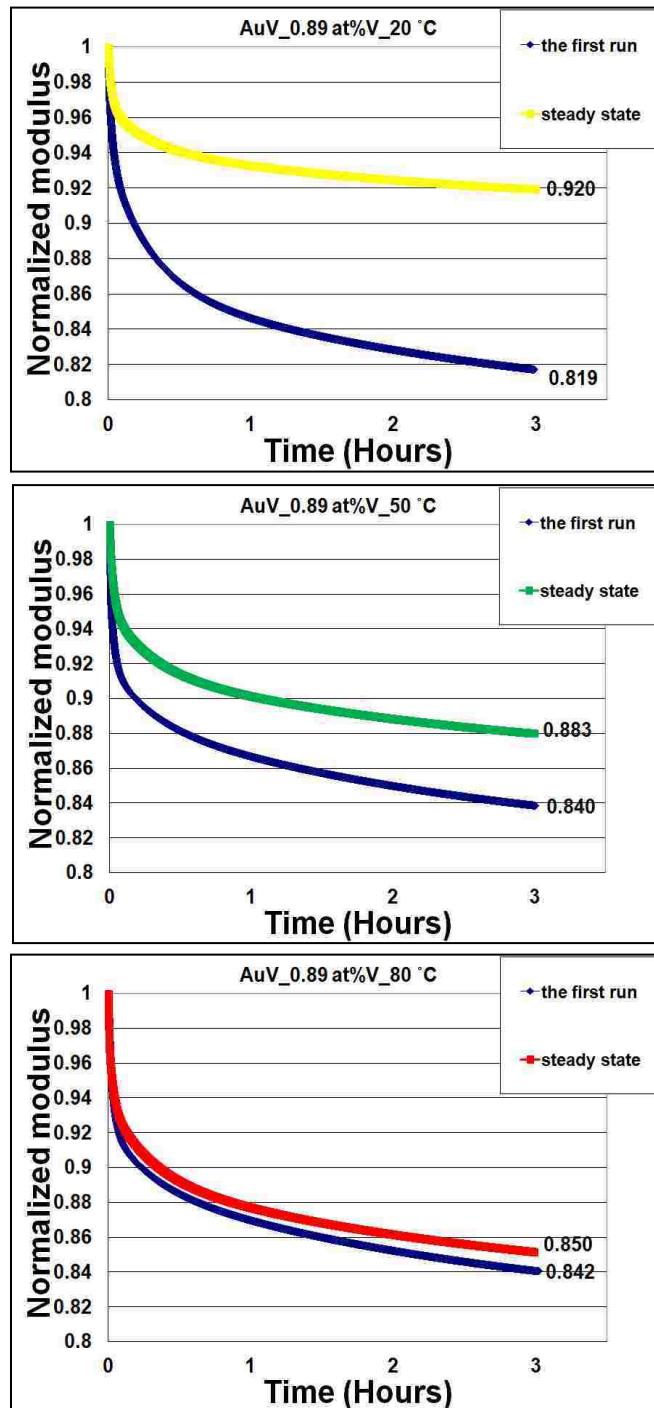


Figure 5.5 Relaxation of normalized modulus of AuV 0.89 at. %V thin film for each temperature (20, 50 and 80 °C) from the first run to steady state condition.

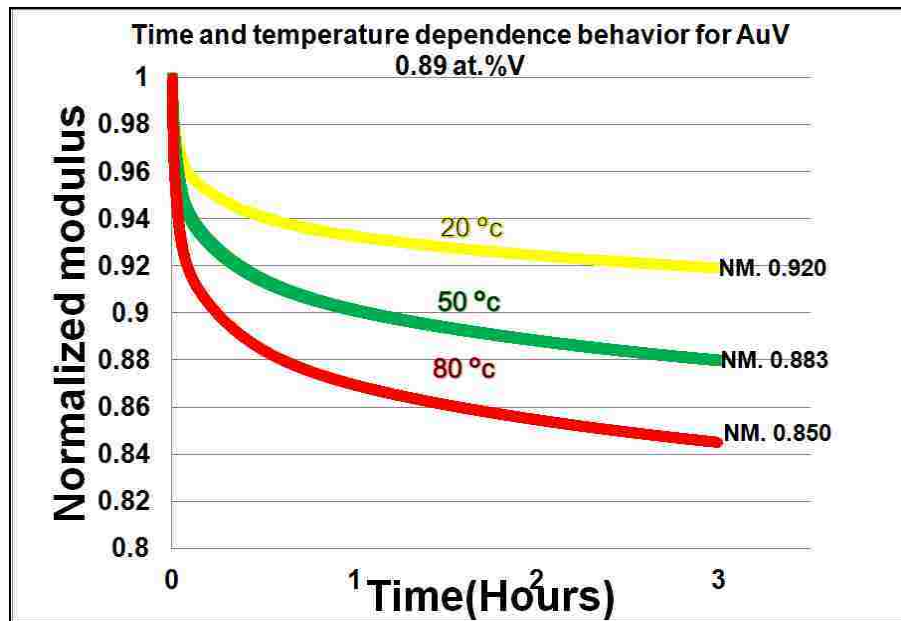


Figure 5.6 Steady-state relaxation curves for each temperature of AuV 0.89 at.%V.

5.2.3 Solid solution of AuV 2.20 at. %V

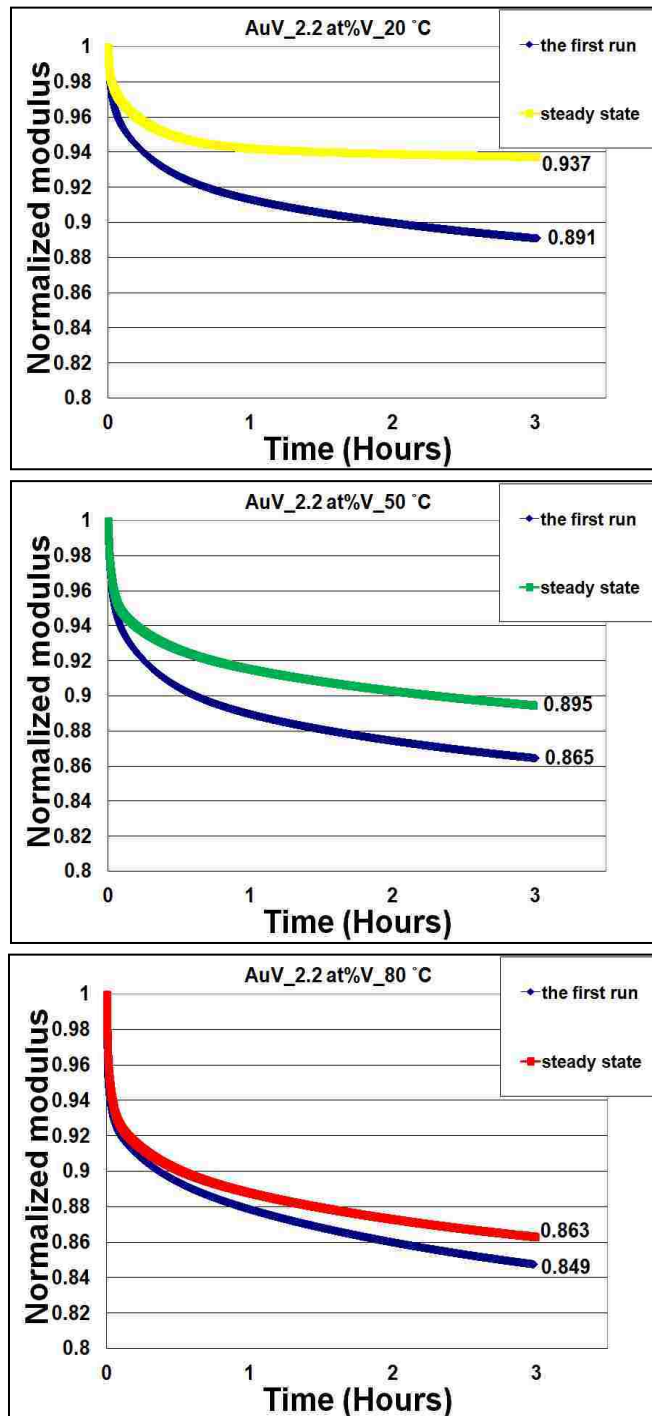


Figure 5.7 Relaxation of normalized modulus of AuV 2.2 at. %V thin film for each temperature (20, 50 and 80 °C) from the first run to steady state condition.

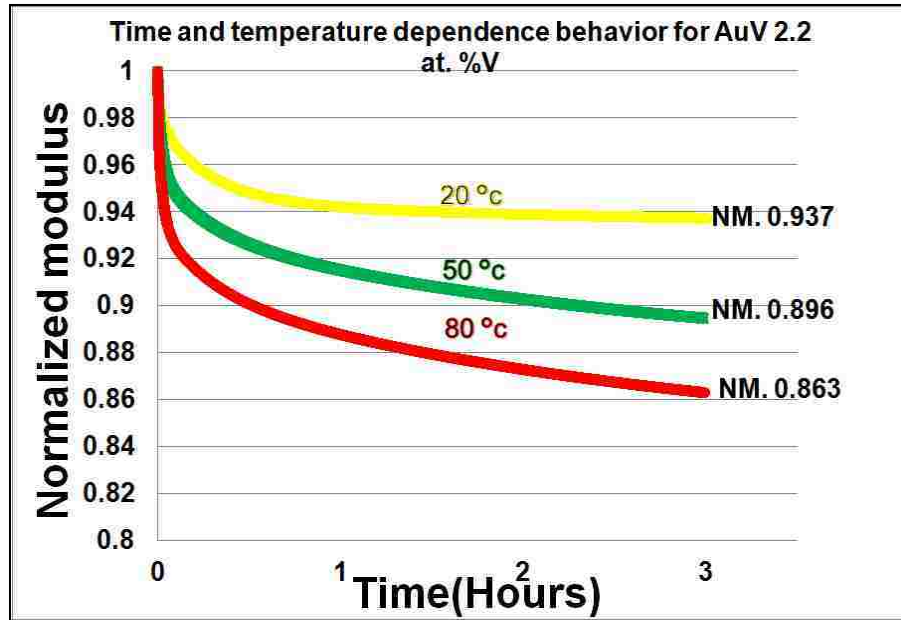


Figure 5.8 Steady-state relaxation curves for each temperature of AuV 2.2 at. %V.

5.2.4 Solid solution of AuV 4.50 at. %

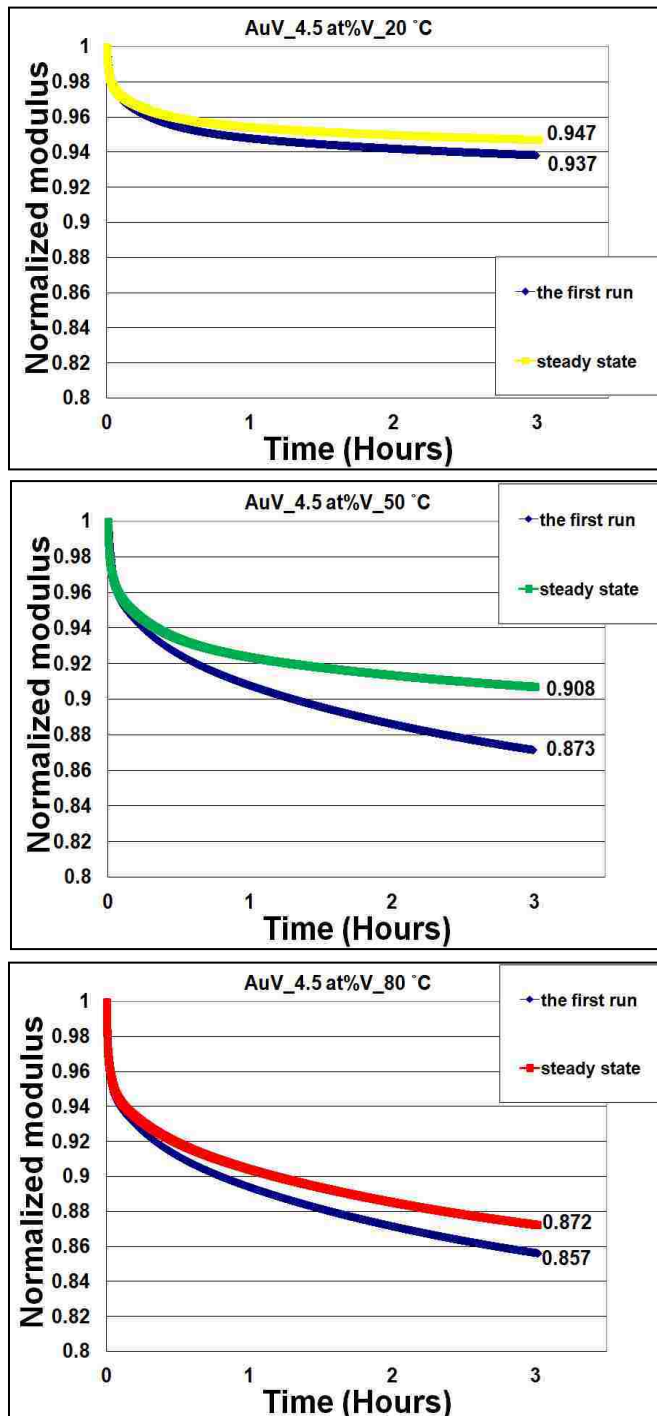


Figure 5.9 Relaxation of normalized modulus of AuV 4.5 at. %V thin film for each temperature (20, 50 and 80 °C) from the first run to steady state condition.

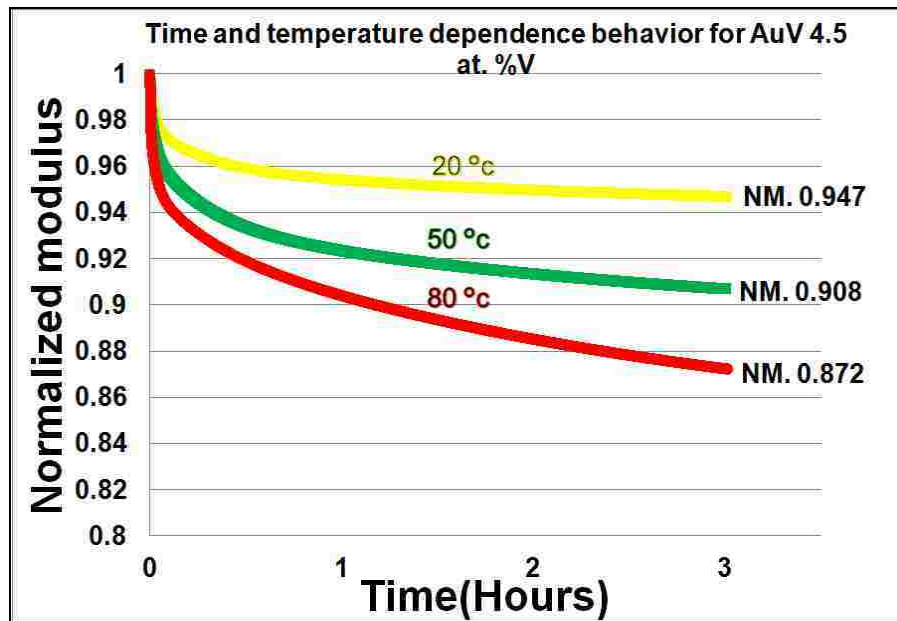


Figure 5.10 Steady-state relaxation curves for each temperature of AuV 4.5 at. %V.

5.2.5 Discussion of temperature dependence on AuV films.

The important things that we observed for relaxation behavior of the set of AuV films are:

1. Repeated relaxation experiments are required to reach a steady state condition in which there is only anelasticity for all AuV films at 20, 50, and 80 °C.

The steady state results show that with increasing temperature, both the initial anelastic modulus relaxation rate and the overall amount of modulus decay increase. Although all of the films reach a steady-state condition at each temperature, there is still further plasticity seen at the next higher temperature.

The amount of plasticity at the end of 3 hours from the first run to the steady-state run is shown in terms of the difference in the normalized modulus between steady state and that run. A pure Au film is used as a representative example. Figure 5.11 shows that increasing the temperature to 50 and 80 °C after the film had reached its limiting plastic deformation at a lower temperature enables additional plastic relaxation that was not accessible at the lower temperature in three hours. However, the additional plasticity at each higher temperature is much smaller than that at the lower temperature where it had been previously tested. When most of the plasticity possible in a film already occurred at 20 °C, only a small additional amount occurred at 50 °C and a very small additional amount more at 80 °C.

The observation that there is more plasticity at low temperature than at high temperature in single temperature testing may be surprising. Note in Figure 5.11 that the film at higher temperature (80 °C after 20 and 50 °C) requires only a single run to reach a steady-state condition whereas multiple runs were required at low temperature. This is evident also in the time dependence of the deformation as shown in Figure 5.12 which shows that reaching steady state is much quicker at the higher temperature. It suggests that low temperature plastic deformation influences the amount of deformation that occurs at higher temperature, as though it were changing the material structure. For example, if the mobile dislocation density decreased during the 20 and 50 C relaxations due to dislocation pinning, it is possible that the additional thermal energy associated with raising the temperature to 80 C reactivated only a small fraction of the pinned dislocations.

Figure 5.11 also shows the modulus change associated with viscoplasticity exhibited by a pure Au film tested immediately at 80 °C without previous tests at 20 and 50 °C. The total amount of modulus change (the sum of the modulus change in each run) is estimated from the graph. While the total amount of modulus change due to plasticity of the film at 80 °C after 20 and 50 °C is about 0.31, which includes the total plasticity at 20, 50 and 80 °C, the total normalized modulus change of the film tested only at 80 °C is only 0.18. It is also interesting to note that the total normalized modulus change associated with testing immediately at 80 °C is smaller even than the change associated with testing only at 20 °C. This could be related to the lower residual stress present at elevated temperature, but a clear relationship has not been demonstrated. All together, the complicated viscoplastic relaxation behavior implies that there is not only a temperature effect on the extent of viscoplastic deformation, there is a thermal-mechanical history effect as well.

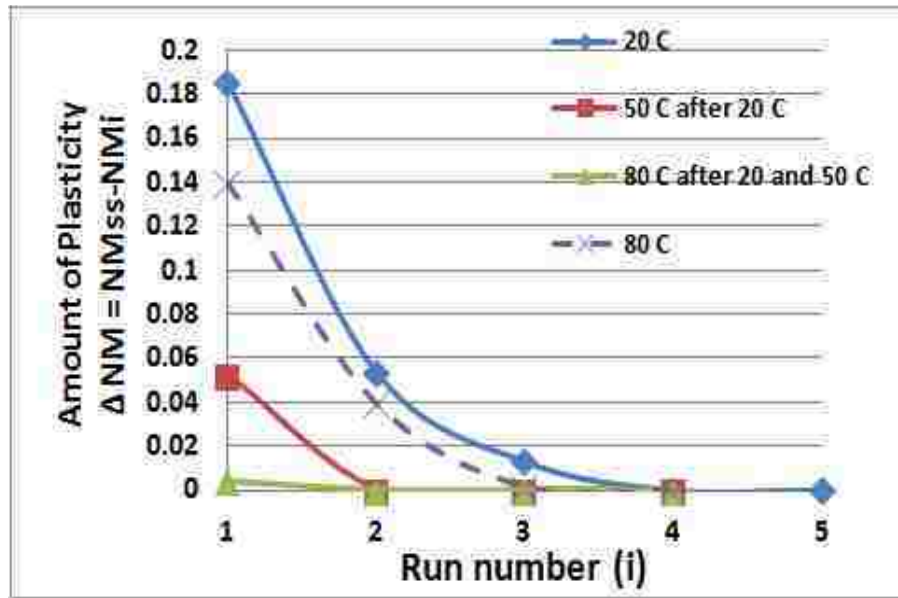


Figure 5.11 Amount of plasticity in each run, from the first to the steady state condition of a pure Au film at successive temperatures of 20, 50 and 80 °C and for a film tested only at 80 °C.

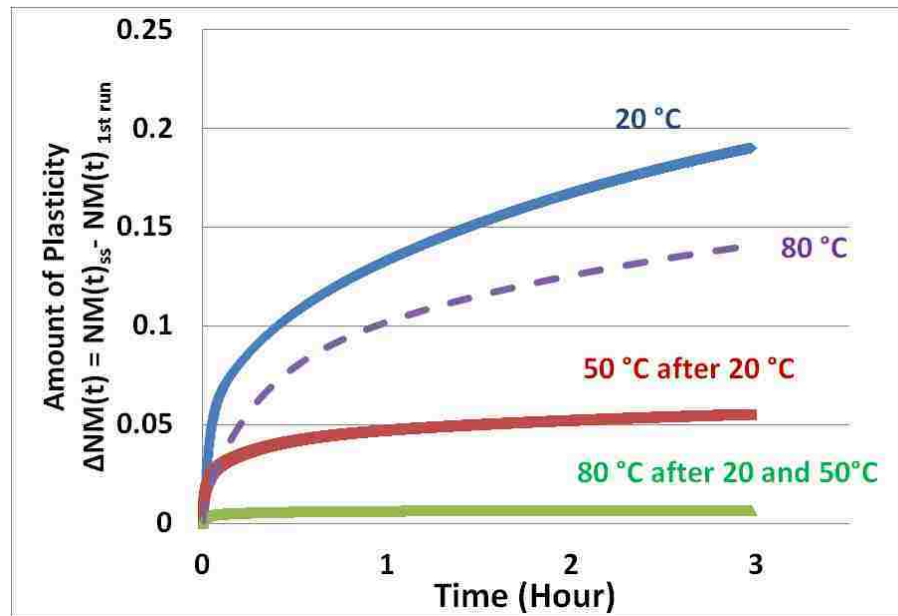


Figure 5.12 Time dependence of the amount of plasticity observed in the first run at each successive temperature in the Au film.

2. It is interesting to investigate the 3 hour normalized modulus as a function of temperature. We observe in Figure 5.13 that the normalized modulus changes for all AuV thin films show almost linear trends.

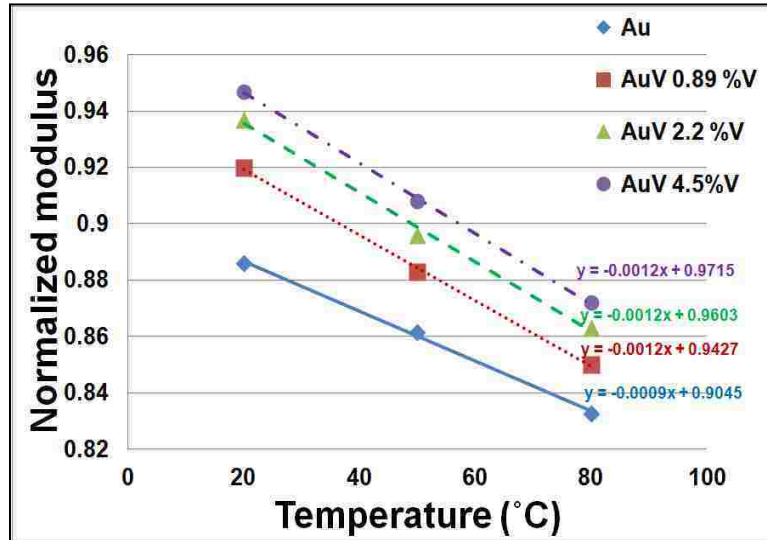


Figure 5.13 Temperature dependence of 3 hour normalized modulus for AuV films.

3. While some applications like RF MEMS switches are modeled well by ideal stress relaxation conditions (stress change at constant strain), other applications may be closer in nature to ideal creep conditions (strain change at constant stress). Also, many prior studies of time-dependent deformation in bulk materials have been performed under creep conditions. Therefore, in order to investigate the temperature dependence of creep properties at constant stress so that the strain rate can be predicted and compared to established creep models, we use steady state stress relaxation data to simulate anelastic creep curves. Since the films have been proven to be linearly viscoelastic, a linear superposition model can be used to simulate the strain that would be present if a sample were strained at

constant stress (rather than stress relaxed at constant strain). In order to generate the creep strain, additional incremental stresses must be added to a stress relaxation curve to maintain the film at a constant stress. This is equivalent to performing a long series of brief strain relaxation experiments, each of which begins at the same stress. The total creep at time t is therefore the product of the superposition of incremental stress and a general function of time. If the time increments associated with the additional incremental stresses are very short, a reasonable representation of a creep curve should result. Figure 5.14 shows predicted creep strain curves for a pure Au film at 20, 50 and 80 °C held at a constant stress of 100 MPa that were calculated according to this procedure.

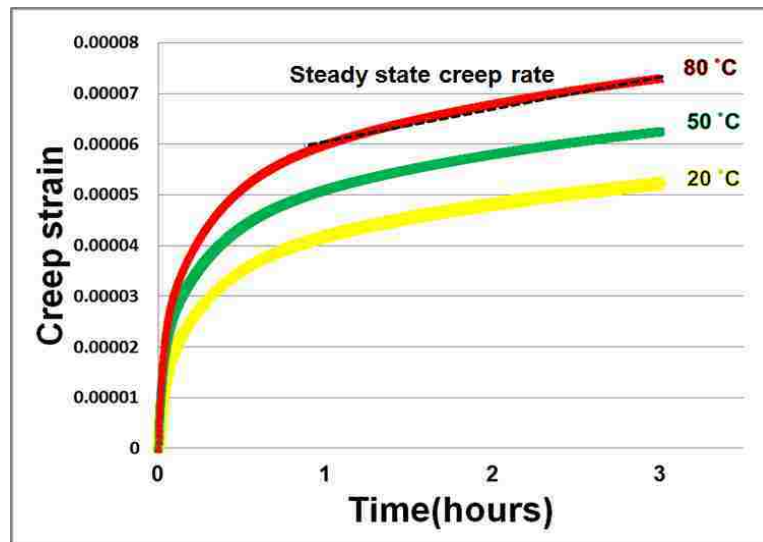


Figure 5.14 Temperature dependence of anelastic creep strain for a pure Au film generated from steady state stress relaxation data at a fixed stress of 100 MPa.

Note that under creep loading conditions the strain continues to change at a significant rate even after 3 hours. In fact, it appears that after the time 1-1.5 hours, a steady state creep rate is being established. Based on the creep strain at constant

stress for each temperature as shown in Figure 5.14, the steady state creep rate is determined from the slope of creep versus time between one and three hours during which the rate of creep is approximately constant.

The equation governing the rate of steady state creep is

$$\text{creep rate} = \dot{\epsilon} = A\sigma^n \exp\left(-\frac{Q}{KT}\right) \quad 5.2)$$

where Q = activation energy, n= stress exponent, A= constant, K is the Boltzman constant, and T is the temperature.

This equation can be rearranged into the form:

$$\ln\dot{\epsilon} = \ln A + n \ln \sigma - Q/KT \quad 5.3)$$

Given this relationship, if the stress is kept constant and the temperature varied, the activation energy Q can be determined by plotting the natural log of creep rate against the reciprocal of temperature.

All stress relaxation results of AuV films are converted to creep strain versus time with a fixed stress at 100 MPa and the approximate steady-state creep rate determined. The temperature dependence of the creep rate is plotted as the natural log of creep rate vs. reciprocal temperature (1/T) in Figure 5.15. The plot shows a definite temperature dependence and the activation energies extracted from the slope are also extremely small, in the range of 0.04-0.11 eV. These are consistent with the activation energy values found by the temperature dependence of the stress relaxation Prony coefficients. This is not surprising since the creep data is derived directly from

the stress relaxation data, and should therefore show the same fundamental temperature dependence.

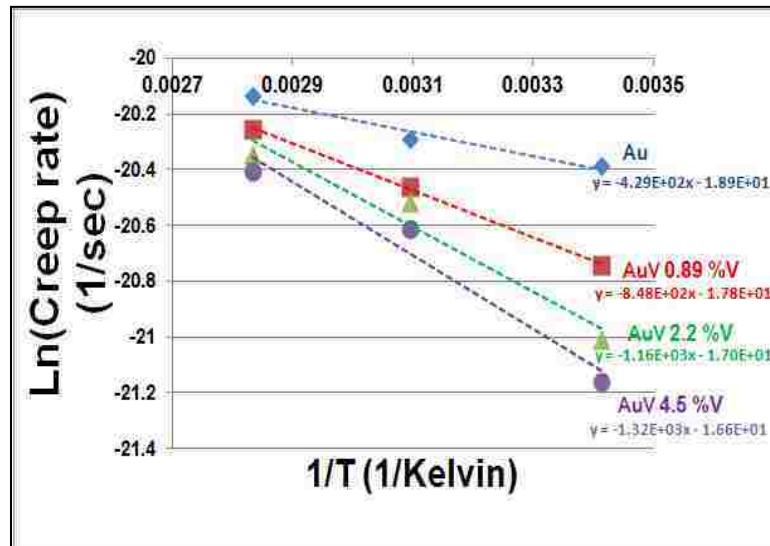


Figure 5.15 Natural log of creep rates vs. 1/T for AuV films.

5.3 Effect of V on relaxation behavior of Au thin film

Since the addition of vanadium is associated with increased relaxation resistance or normalized modulus, it is expected that the strength of relaxation should be dependent on V concentration. The effectiveness of the solid solution is shown in terms of 3 hour normalized modulus at 20, 50, and 80 °C. The dependence of V can be shown for relaxation at a steady-state viscoelastic condition. The trends of both relaxation and creep strain rate with % concentration of V are established and a quantitative model is developed to predict these two relationships.

5.3.1 At 20 °C

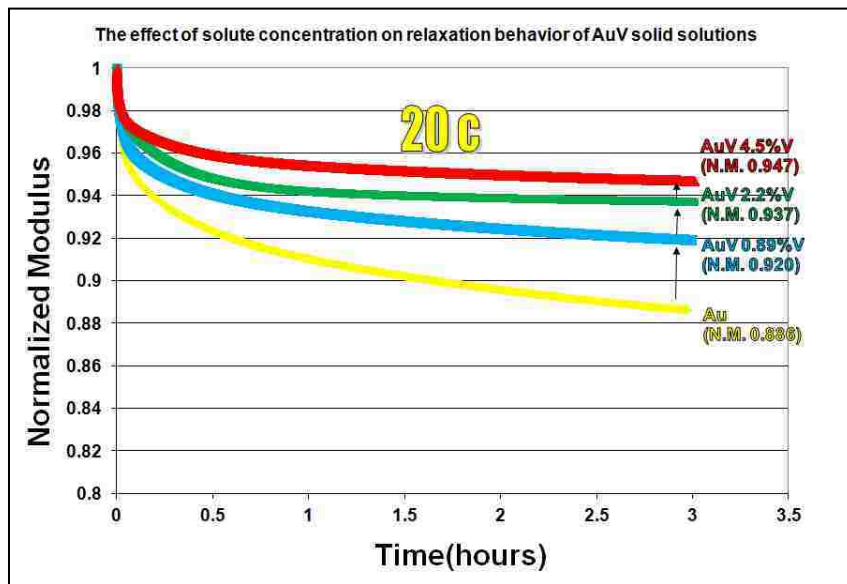


Figure 5.16 The effect of V concentration on relaxation behavior of AuV solid solutions at 20 °C.

5.3.2 At 50 °C

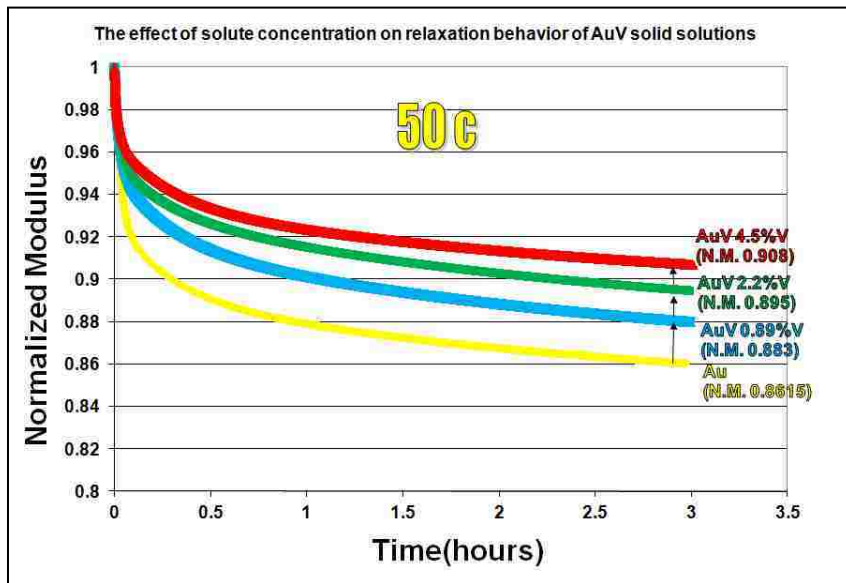


Figure 5.17 The effect of V concentration on relaxation behavior of AuV solid solutions at 50 °C.

5.3.3 At 80 °C

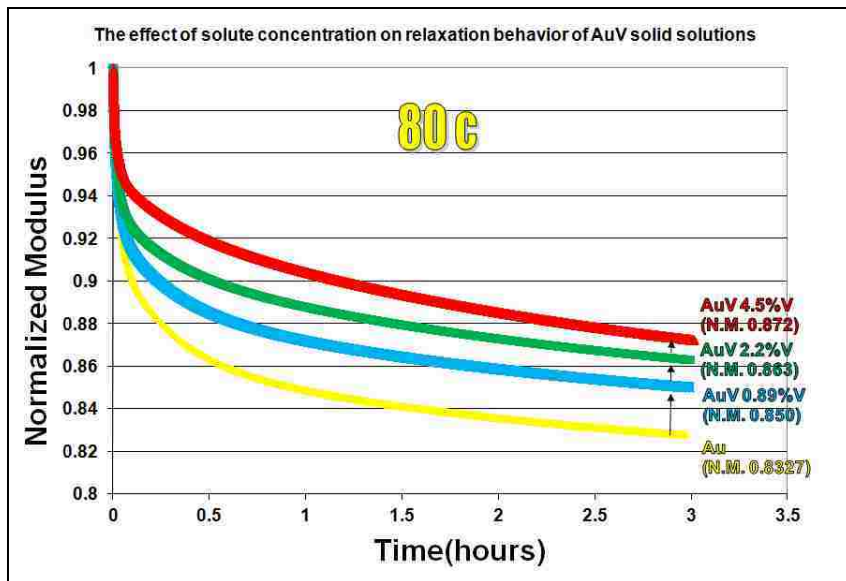


Figure 5.18 The effect of V concentration on relaxation behavior of AuV solid solutions at 80 °C.

5.3.4 Discussion of concentration dependence on AuV films

Based on the normalized modulus results of the films during three hours of relaxation, we observe that the solid solution strengthening mechanism is a major contributor to reduced stress relaxation. The relaxation resistance increases with an increasing concentration of V. At each temperature, a concentration dependence of $\sim C^{1/3}$ (where C is the V concentration) for the relaxation at a steady-state viscoelastic condition has been established as shown in Figure 5.19.

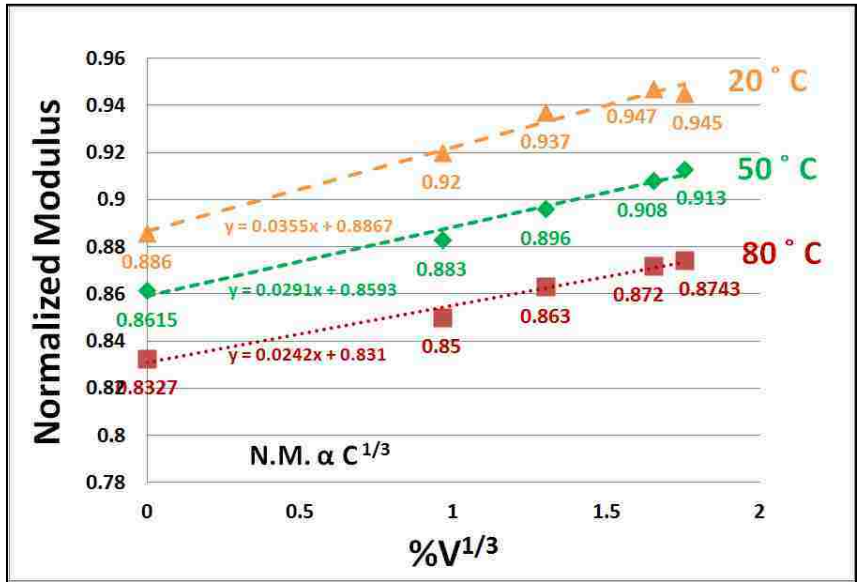


Figure 5.19 Concentration dependence of 3 hour normalized modulus for each temperature at steady state.

Also, we determine the creep strain rates as a function of concentration for a set of AuV films at 20, 50 and 80 °C. First, the creep strain curves of the AuV films are determined based on the stress relaxation curves, as described before. Figure 5.20 shows an example of creep curves of AuV films as a function of time at room temperature. The steady-state creep rates are found by taking the linear portion of the creep strain vs time. Figure 5.21 shows the concentration dependence and estimated creep strain rate at three different temperatures of 20, 50, and 80 °C. A $C^{1/3}$ dependence has been shown to match the creep behavior of AuV solid solution films, as expected from the concentration dependence of stress relaxation behavior.

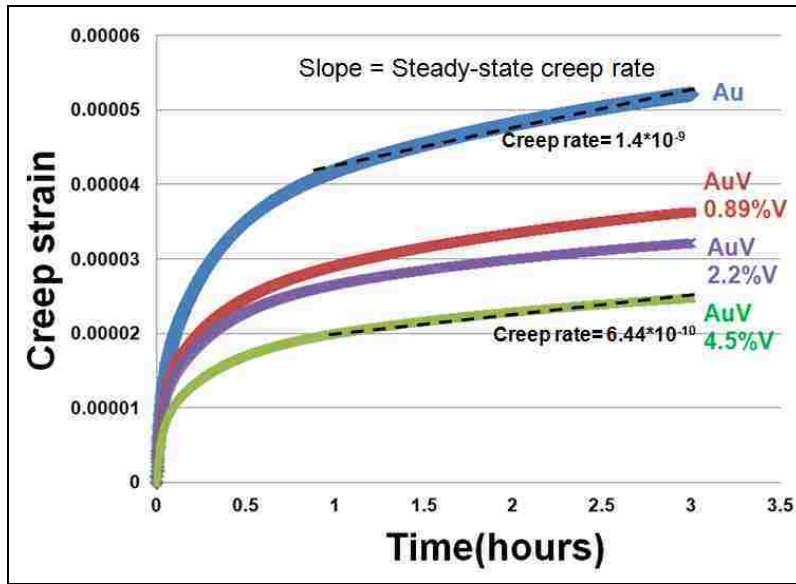


Figure 5.20 Concentration dependence of creep strain for a set of AuV films at room temperature converted from stress relaxation at fixed stress 100 MPa.

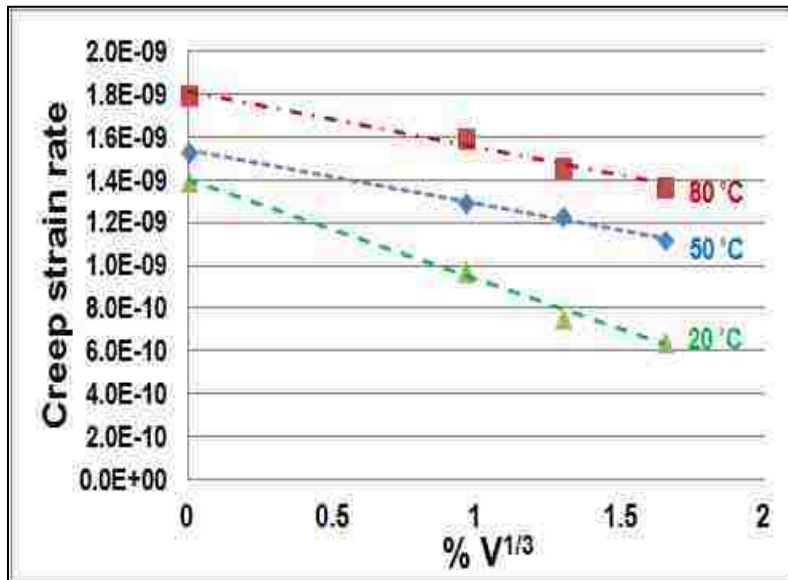


Figure 5.21 Concentration dependence on creep strain rate of AuV films at 20, 50, and 80 °C.

5.3.5 Modeling of creep strain rate

It is proposed that a dislocation-based mechanism involving the nucleation and movement of double-kinks is the most likely mechanism responsible for the observed viscoelasticity for pure Au and AuV solid solution films. A quantitative model of the rate-equation for dislocation glide plasticity is⁵

$$\dot{\gamma} = \dot{\gamma}_p \left(\frac{\sigma_s}{\mu}\right)^2 \cdot \exp - \left\{ \frac{\Delta F_p}{kT} \left[1 - \left(\frac{\sigma_s}{\tau_p}\right)^p \right]^q \right\} \quad \mathbf{5.4)}$$

where $\dot{\gamma}$ is shear strain rate,

σ_s is shear stress which is related to the tensile stress (σ_1) by $\sigma_1/\sqrt{3}$,

$\dot{\gamma}_p$ can be treated as a constant and obtained by fitting data from experiment,

ΔF_p is activation energy,

τ_p is the flow stress at 0 K or the stress forcing the dislocation through the obstacle with no help from thermal energy,

μ is the shear modulus, and

p and q are parameters which show the measured strength of material varies with temperature.

In order to determine τ_p , the stress properties of the films are required. In the case of a metal thin film with small grain size, the yield stress (σ_{YS}) is given by

$$\sigma_{YS} = \sigma_i + \sigma_{Hall-Petch} \quad \mathbf{5.5)}$$

where σ_{YS} is often approximated as 1/3 of the hardness measured by nanoindentation.^{106, 107} Hardness results of AuV films as a function of V concentration are available from the measurements of Bannuru.¹⁰

σ_i is some intrinsic flow stress of a film, which is approximately $\sqrt{3} \cdot \tau_p$

$\sigma_{Hall-Petch}$ related to the grain size effect property in which the Hall-Petch relationship is $k \cdot d^{-0.5}$, where d is grain size and k is a material constant coefficient. The literature value^{108, 109} of the Hall-Petch coefficient for Au is about 3 GPa(nm)^{-0.5}.

Then, all parameters can be calculated to determine τ_p by Eq. 5.6) and presented in Table 5.2.

$$\frac{1}{3}H = \sqrt{3} \cdot \tau_p + kd^{-0.5} \quad 5.6)$$

| %V | Hardness(GPa)* | σ_{ys} (MPa) | σ_i for pure or alloy(MPa) | τ_p (MPa) |
|------|----------------|---------------------|-----------------------------------|----------------|
| 0 | 2.50 | 833.33 | 326.24 | 188.4 |
| 0.89 | 2.70 | 899.26 | 392.17 | 226.4 |
| 2.2 | 2.99 | 996.30 | 489.20 | 282.4 |
| 4.5 | 3.50 | 1166.67 | 659.57 | 380.8 |

Table 5.2 Estimated value of flow stress for AuV films.

Based on creep rate equation for glide (Eq 5.4), the experimental data for a pure Au film at a creep strain rate of $\dot{\gamma} = 10^{-9}/s$ is compared with the prediction of Eq 5.4), with various combinations of p and q. An analysis of the predicted contour for creep rate at $\dot{\gamma} = 10^{-9}/s$ is plotted with a normalized shear stress and homologous temperature map as shown in Figure 5.22. It justified the best choice of p and q at 1 and 2, respectively, for the best fit. Table 5.3 lists the parameters used for the prediction creep rate at $10^{-9}/s$.

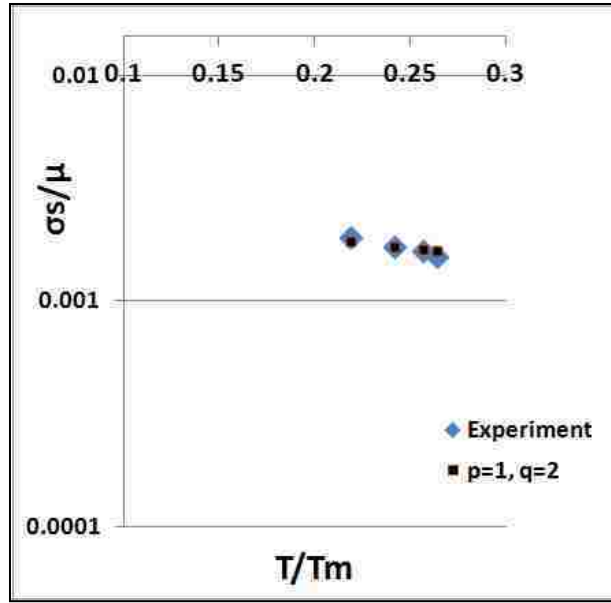


Figure 5.22 Predicted contour for $\dot{\gamma} = 10^{-9}/s$ for creep rate of dislocation glide equation, compared with the experimental data for pure Au film.

| Parameters of Au | Value |
|-------------------------------------|-----------------------------------|
| μ , shear modulus | 30000 MPa |
| ΔF , activation energy | 1.12×10^{-20} J |
| k , Boltzman constant | 1.38×10^{-23} J/K |
| H , Hardness | 2.5 GPa |
| k , Hall-Petch coefficient | $3 \text{ GPa}(\text{nm})^{-0.5}$ |
| τ_p of Au | 188.4 MPa |
| $\dot{\gamma}_p$, fitting constant | 0.0017 sec^{-1} |
| p and q | 1 and 2 |

Table 5.3 Material parameters of Au film for creep rate equation at $10^{-9}/s$

With the parameters of Au obtained by fitting data to Eq 5.4) compared to the experiment, we now have the values of $\dot{\gamma}_p$, p , and q at 0.0017 sec^{-1} , 1, and 2, respectively. Then we can develop a quantitative model for the effect of %V on the creep rate as a function of stress and temperature. Figure 5.23 shows the values of creep strain rate derived from a stress relaxation experiment compared with the creep

rate simulation derived from Eq 5.4) at a tensile stress of 100 MPa at room temperature for AuV films. The agreement between the quantitative model and experiment is reasonably good. This implies that the procedure for converting stress relaxation rate to creep strain rate is appropriate under the conditions established for the AuV films studied here.

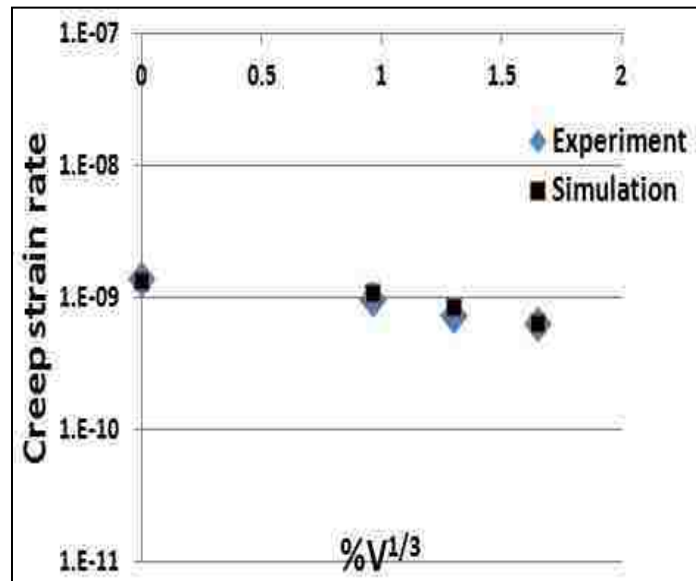


Figure 5.23 Deduced the creep rate as a function of stress and temperature from creep rate equation of dislocation glide, compared to the creep rate from stress relaxation experiment.

5.4 Summary

The effect of V concentration on AuV films (at approximately 1 to 5 at %V) on relaxation behavior at 20, 50, and 80 °C is investigated using gas pressure bulge testing. It is found that increasing the concentration of the V improves the relaxation

resistance of Au film at all temperatures. Both initial and steady-state normalized modulus are well described by a concentration dependence of $X_V^{1/3}$.

Creep strain curves are simulated based on experimental viscoelastic stress relaxation results using Boltzman superposition. The creep rates derived from creep curves show temperature dependence related to steady state creep rate equation. The activation energies estimated from the temperature dependence of the creep rate are extremely small which are in good agreement with the temperature dependence of Prony series coefficients. The results also show that even the trend of the creep rate on V concentration is proportional to $X_V^{1/3}$.

Furthermore, a quantitative model of rate-equation for dislocation glide is developed to predict the creep rate as a function of stress and temperature for AuV films. A rate-equation for a dislocation-based mechanism model is fitted to the experimental data. From the data we could determine the variable parameter of p and q to be 1 and 2 which gives the best fit.

6. Grain size effect on relaxation behavior of Au films

It is well known that the size of the grains in a metal influences the mechanical properties. Typically, a fine-grained material is stronger than a coarse-grained material due to greater interactions between dislocations and grain boundaries. Increasing the grain size results in a decrease of flow stress as shown in the Hall-Petch equation. If dislocation motion is the primary mechanism of stress relaxation then a small grain size would be expected to have less relaxation. But, if grain boundary diffusion plays a role then the opposite should be true. However, it seems that the effect of grain size on stress relaxation in Au films over the range of temperatures of interest has not been reported. In this chapter, a series of pure Au films is fabricated to explore a range of grain sizes by controlling the substrate temperature during deposition. Time and temperature dependence of stress relaxation in pure Au films with different grain sizes will be investigated over the range of 20-80 °C. The goal of this work is to establish trends in relaxation with grain size and temperature. The expectation is that faster stress relaxation will be observed at larger grain size, consistent with a dislocation-based mechanism.

6.1 Characterization of Au thin films deposited at different substrate temperatures

A series of Au thin films with various grain sizes was fabricated by DC magnetron sputtering from a single target of Au. Films with various grain sizes can be fabricated by controlling the substrate temperature during deposition from room

temperature to 400 °C. Increasing the substrate temperature during deposition is known to strongly affect the grain size of Au thin films.¹⁴ For fabrication of Au films at elevated substrate temperature it is important to omit the Ti adhesive layer to avoid diffusion of Ti into the Au. Ti diffusion into Au changes the microstructure of the Au as can be observed in SEM images in Figure 6.1. Without the presence of the Ti layer, it is quite impossible to keep the Au film attached on the substrate during immersion with KOH. Therefore, the Au films in this study are deposited on the SiN on fully etched Si dies, not partially etched Si as was used earlier.

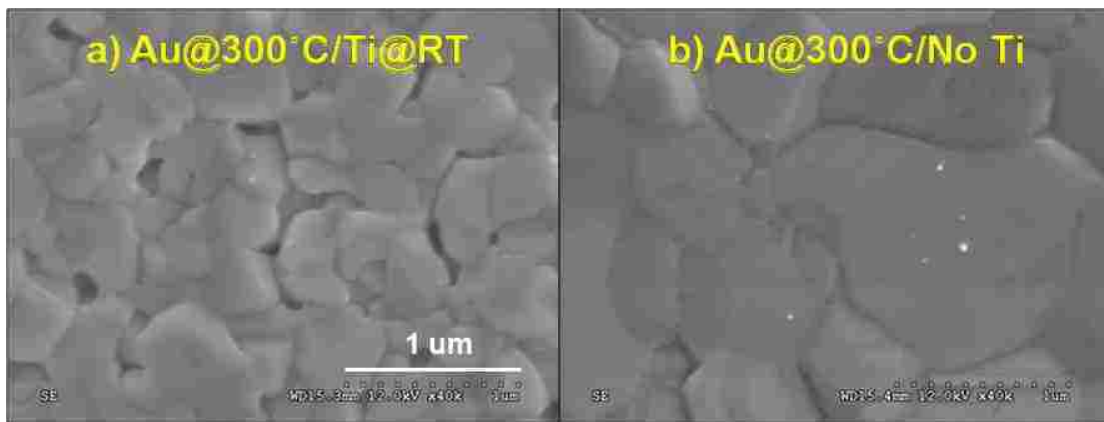


Figure 6.1 SEM images show the Au film at elevated temperature a) with Ti and b) without Ti as adhesive layer.

Scanning Electron Microscopy (SEM) is used to investigate the grain size of the Au thin films. Magnification at 50X is used for the comparison. The results are in Figure 6.2.

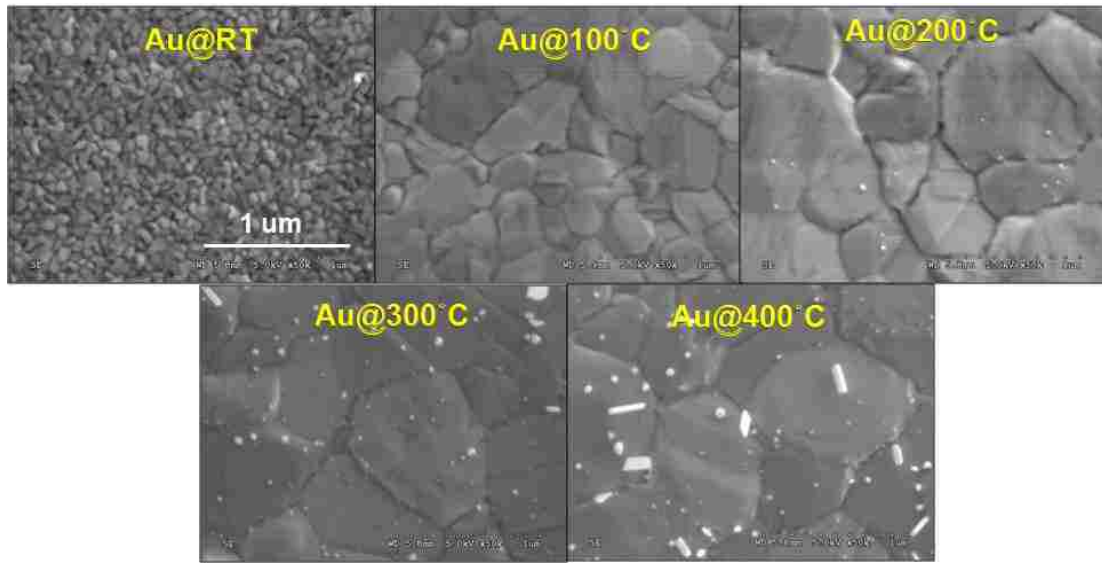
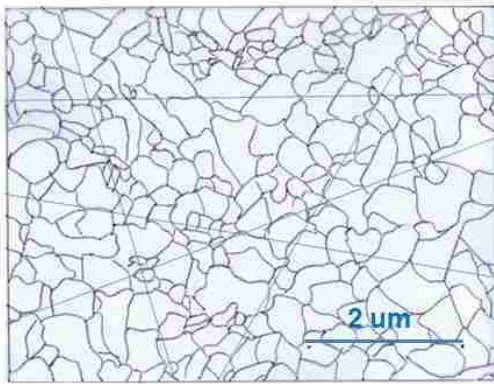


Figure 6.2 SEM images show the different grain sizes of Au thin films deposited at different temperatures.

Two methods are applied to estimate the grain size of the thin films. The first is the mean lineal intercept method following ASTM standard E112-88. The second is done with the software program called *Image J*. All boundaries can be revealed clearly by producing SEM images, then tracing the boundaries out manually using a transparent film and a felt pen. The resulting drawing can be processed by using the two mentioned methods as presented in Figure 6.3. The relationship between the substrate temperature and the average grain size based on the average of the two methods of pure Au thin films is shown in Figure 6.4. The grain size of Au is obviously increasing with increasing substrate deposition temperature. An attempt was made to fabricate a series of AuV and AuV₂O₅ films with the various grain sizes for comparison to the pure Au. However, large grain sizes could not be achieved in the Au alloy films because the alloying elements interfere with normal grain growth

by decreasing grain boundary mobility. Although the films were deposited at temperatures up to 300 °C, the grain size increase is relatively small compared to pure Au films as shown in Figure 6.4. Annealing after deposition also had little effect on grain size for the alloy films. On the positive side, these findings indicate that the grain size in Au alloy films will be very stable over time, and thus any benefits associated with small grain size will be retained even if the films are exposed to elevated temperatures.

a) Linear intercept method



b. Software program :Image J

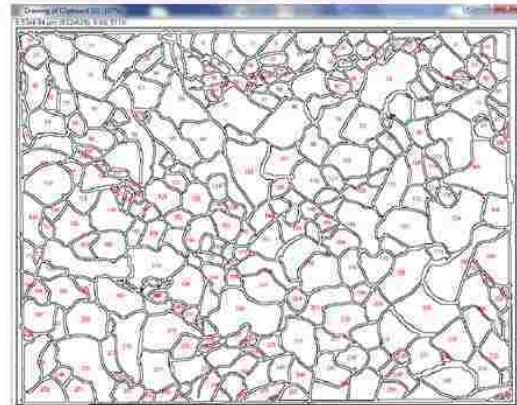


Figure 6.3 Grain size measurement by using a) linear intercept method and b) software program of *Image J*.

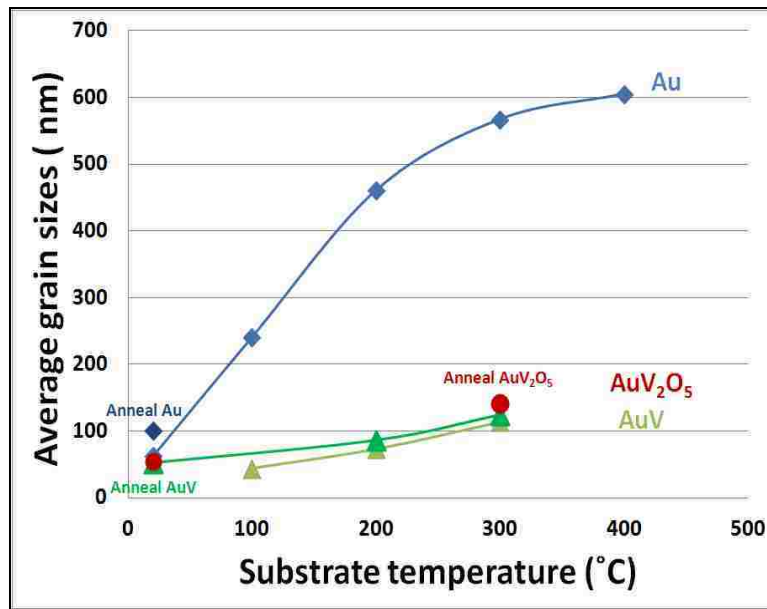


Figure 6.4 The relationship of average grain size of pure Au and Au alloy thin films and substrate temperature.

6.2. Temperature dependence of relaxation behavior of Au films with different grain sizes

Various substrate temperatures not only influence the grain size but also the residual stress of the films. In bulge testing, the residual stress is measured by a pressure ramp before doing a 3 hour relaxation experiment. The residual stresses in the pure Au films are shown in Figure 6.5 as related to the substrate deposition temperature. The residual stress at room temperature increases from 37 MPa to 110 MPa as the substrate temperature during deposition increases from room temperature to 400 °C. As seen in this plot, there are two stages to the increase. The residual stress increases quickly when the substrate temperature increases from RT to 100 °C. At higher temperatures the residual stress is almost constant, increasingly only

slightly when the substrate temperature is higher than 100 °C. This behavior indicates that there probably is plastic yielding when the stress is greater than about 90 MPa during cool down after deposition leading to a nearly constant residual stress level determined more by the plasticity than by the maximum substrate temperature.

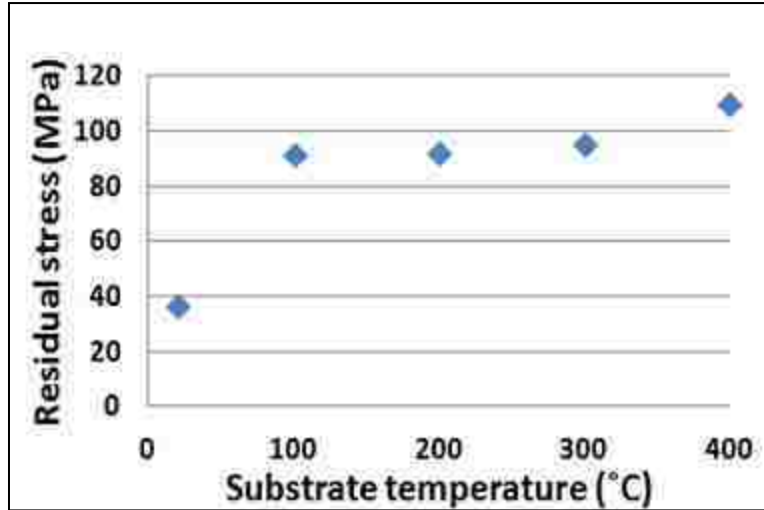


Figure 6.5 The relationship between substrate temperature during deposition and room temperature residual stress in pure Au thin films.

Temperature dependence of viscoelastic behavior in the set of Au films with different grain sizes is characterized by stress relaxation measurements using bulge testing, as before. The results below show only the steady-state condition of free-standing films after exercising the films multiple times. At each grain size, normalized modulus as a function of time is plotted with a Prony series fit at 20, 50 and 80 °C.

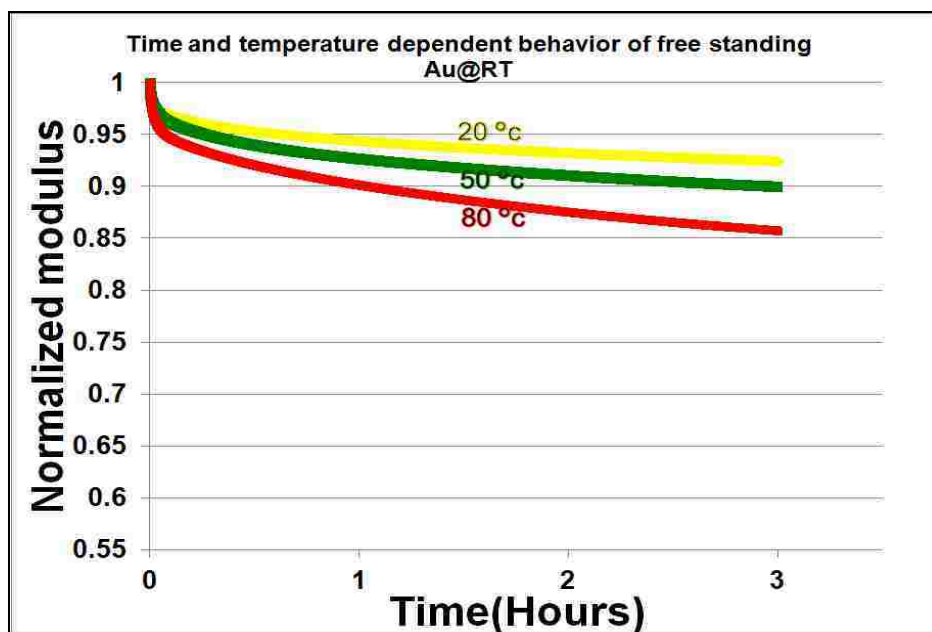


Figure 6.6 Steady-state relaxation curves for each temperature of Au at RT substrate temperature (d= 60 nm).

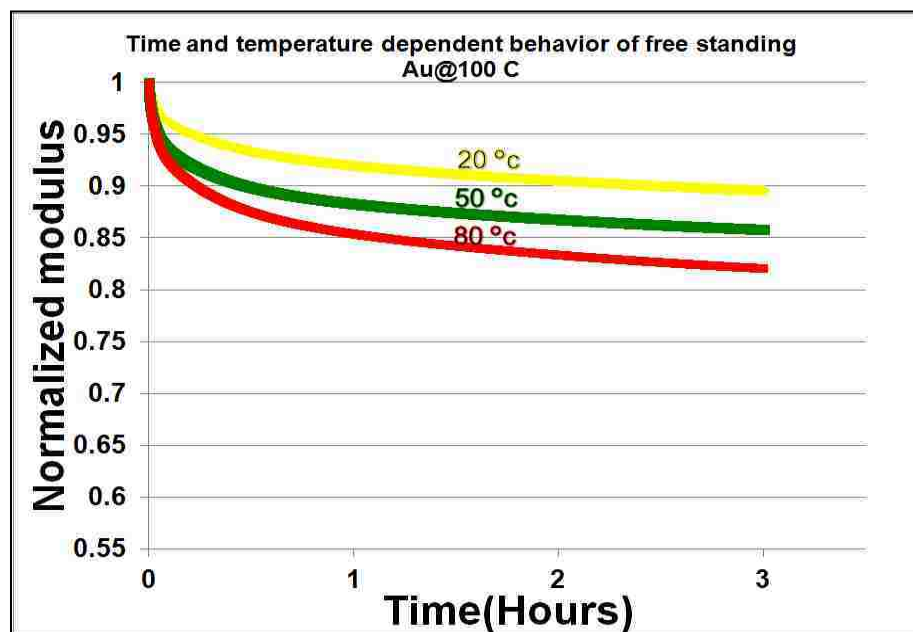


Figure 6.7 Steady-state relaxation curves for each temperature of Au at 100 °C substrate temperature (d= 240 nm).

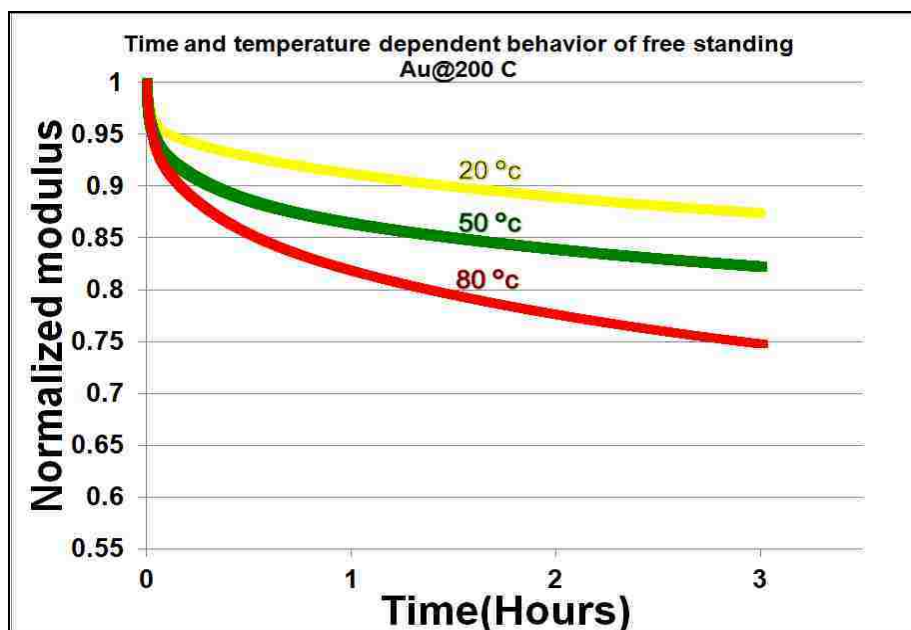


Figure 6.8 Steady-state relaxation curves for each temperature of Au at 200 °C substrate temperature (d= 460 nm).

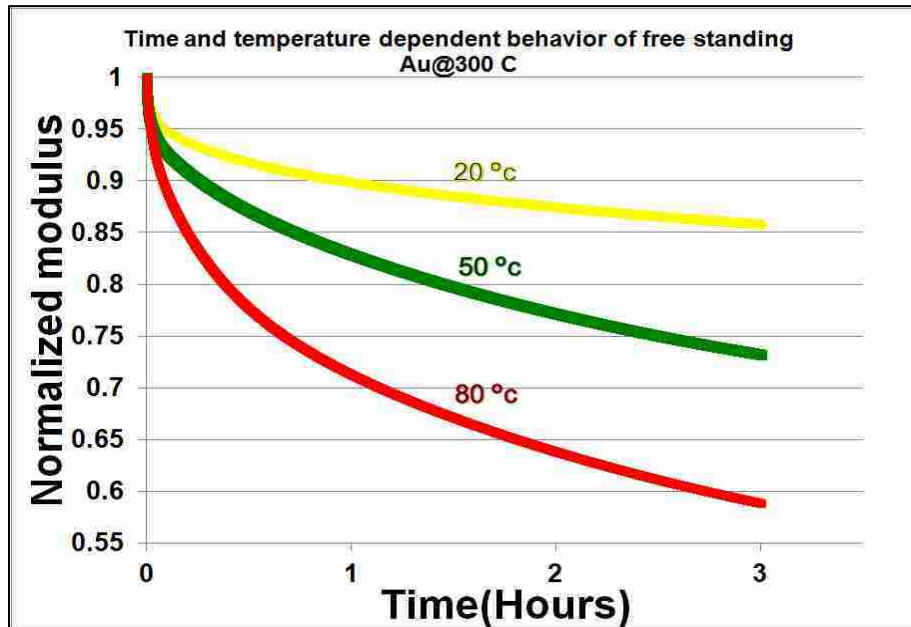


Figure 6.9 Steady-state relaxation curves for each temperature of Au at 300 °C substrate temperature (d= 570 nm).

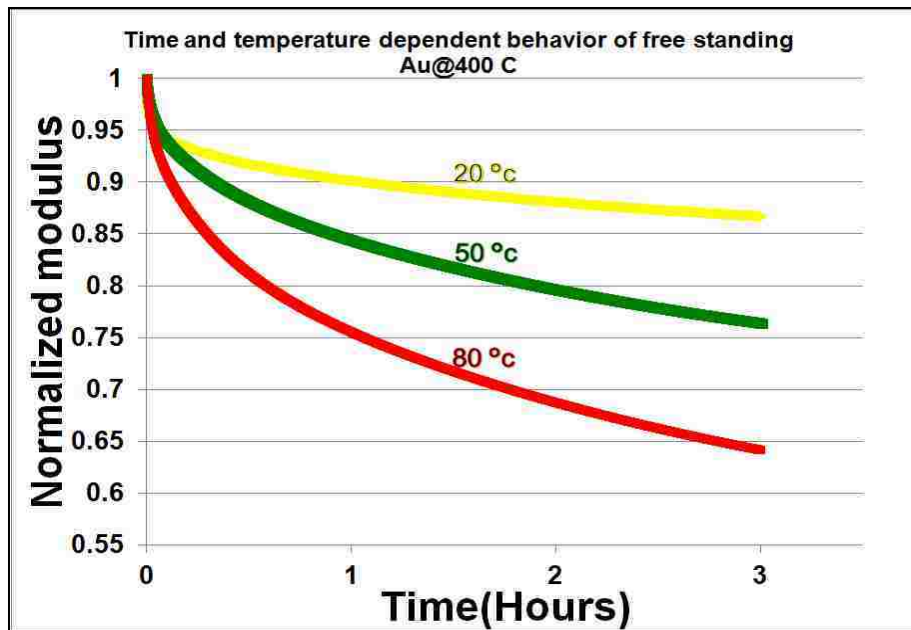


Figure 6.10 Steady-state relaxation curves for each temperature of Au at 400 °C substrate temperature (d= 605 nm).

The temperature dependence of relaxation behavior is the same for all Au films with various grain sizes. Increasing temperature from 20-80 °C increases the amount of relaxation in the films. However, it can be observed that the temperature dependence on relaxation more strongly affects the larger grain sizes as shown by the slope of the Figure 6.11.

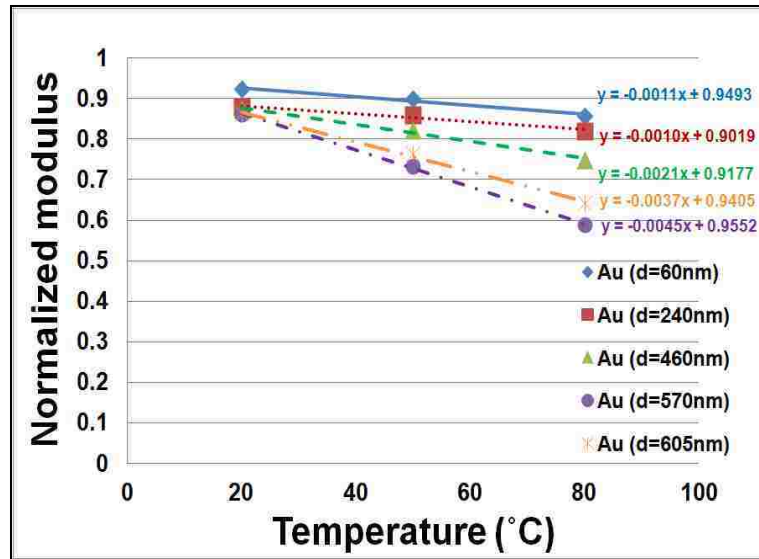


Figure 6.11 Temperature dependence of Au with various grain sizes on normalized modulus.

6.3. Effect of grain size on relaxation behavior of Au thin films

We have seen that grain size affects relaxation behavior. Faster stress relaxation is observed at larger grain size which is consistent with the dislocation-based mechanism described before. There is an unexpected result for the relaxation of Au at $D=605$ nm compared to Au at $D=570$ nm since the relaxation of Au at $D=605$ nm is higher than relaxation of Au at $D=570$ nm. The reason remains unclear at this point. Figure 6.12-Figure 6.14 show that the larger grain size leads to more relaxation not only at room temperature (20 °C) but also at the higher temperature (80 °C). At higher temperature there is a more rapid increase in the amount of relaxation with grain size. Thus, while Au with larger grain size can provide better electrical conductivity, it may be detrimental to the performance of a switch, particularly at elevated temperature.

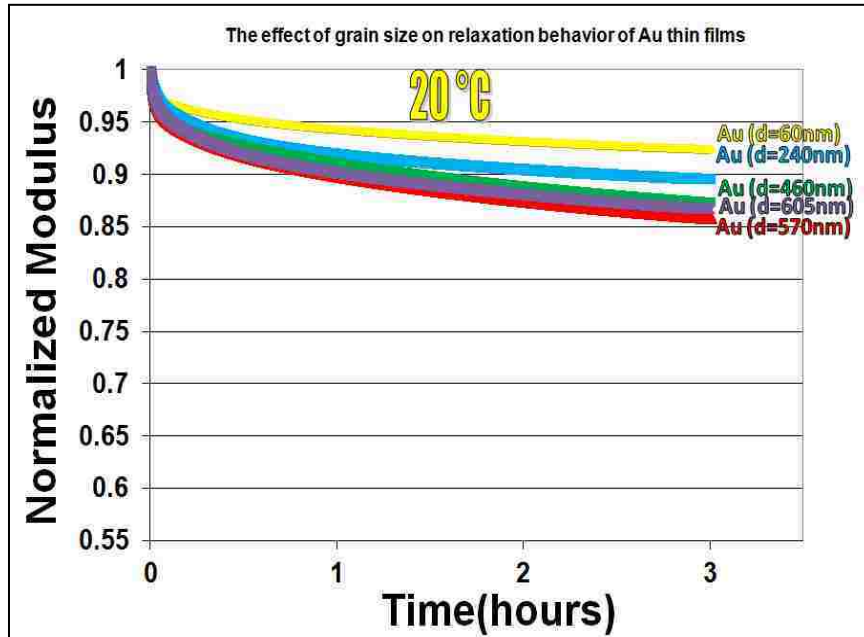


Figure 6.12 The effect of grain size on relaxation behavior of Au films at 20 °C.

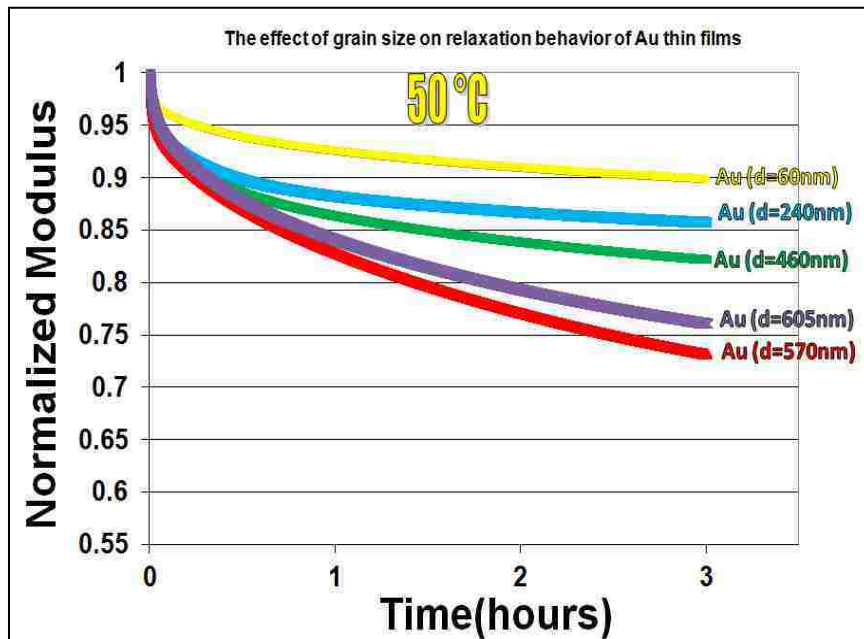


Figure 6.13 The effect of grain size on relaxation behavior of Au films at 50 °C.

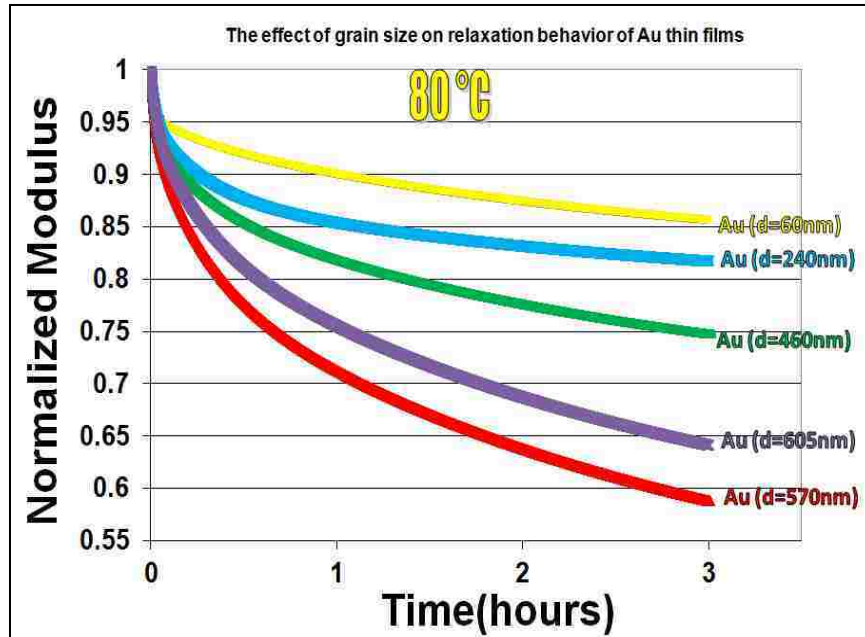


Figure 6.14 The effect of grain size on relaxation behavior of Au films at 80 °C.

Consistent with a dependence of relaxation rate on grain size, the three-hour normalized modulus of the films is also dependent on the grain size (D). Figure 6.15 shows the grain size dependence of the three hour normalized modulus is proportional to D^2 .

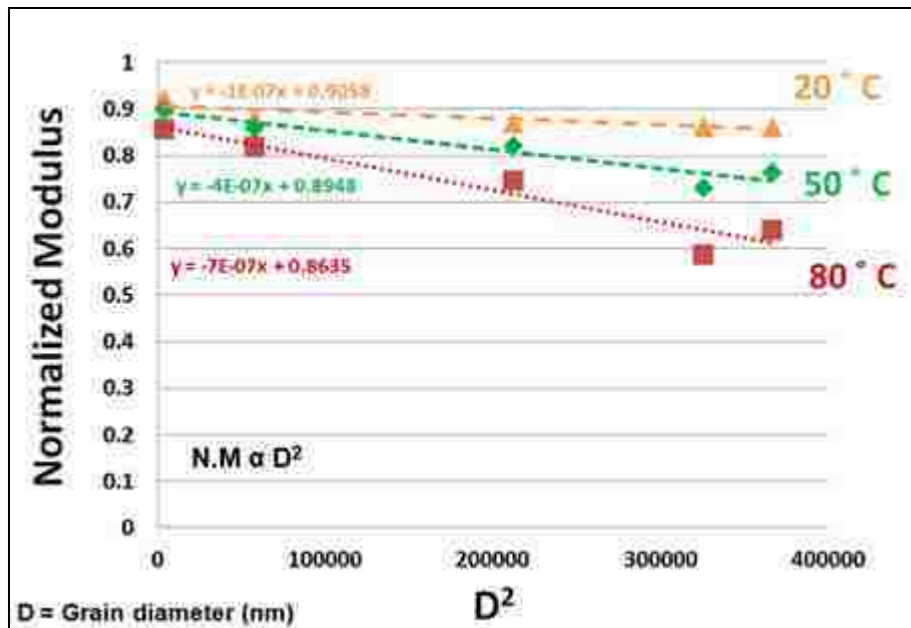


Figure 6.15 Grain size dependence on normalized modulus of Au films.

We can also determine the creep strain and steady state creep rate of Au films from relaxation measurements at fixed strain assuming linear viscoelastic behavior. The creep strain can be seen from the amplitude of the creep curve y-axis and the steady state creep rate can be estimated from the slope. Not surprisingly, the amount of creep and the steady state creep rate are also found to increase with increasing the grain size, particularly at elevated temperature, consistent with the relaxation behavior. Figure 6.16 shows calculated creep curves for Au films with various grain sizes at 20, 50 and 80 °C.

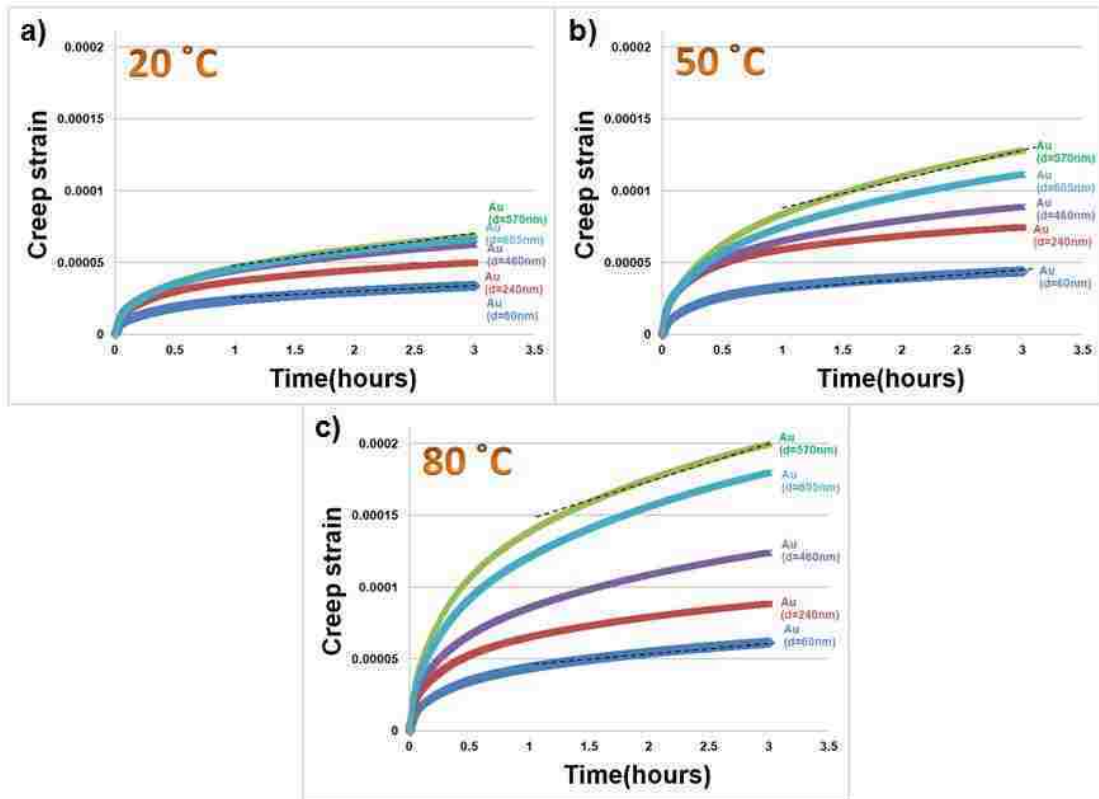


Figure 6.16 Simulated creep curves from relaxation measurements for Au films with various grain sizes a) 20 °C, b) 50 °C and c) 80 °C.

6.4. Summary

Au films with various grain sizes are fabricated using different substrate temperatures during sputtering. The viscoelastic behavior of these pure Au films with different grain sizes is investigated over the temperature range of 20–80 °C. All of the films show a similar temperature dependence. Increasing the temperature increases the amount of relaxation of the films. It is found that there is an effect of grain size on the normalized modulus and creep rate as a result. Increasing the grain size results in a decrease of normalized modulus and an increase in relaxation rate, particularly at

the highest temperature. These results agree with a dislocation-based mechanism, where the grain boundaries can be a barrier to dislocation loop movement or can act as sources for dislocations that provide backstresses that limit loop expansion. The trend of normalized modulus (N.M) with grain size (D) was shown to be proportional to D^2 .

7. Activation volume and dislocation mobility in viscoelastic behavior of Au and Au alloy thin films.

In previous chapters (Chapter 3), the activation energy of the stress relaxation process was determined so that a likely viscoelastic stress relaxation mechanism could be identified. The activation energy has a direct physical interpretation in the case of stress-assisted, thermally activated movement of a dislocation. In order to move from one metastable equilibrium position to another, a dislocation must pass through a higher energy state, the magnitude of which is determined by the nature of the obstacle that creates the energy barrier. At higher temperatures, thermal energy provides significant assistance to a dislocation overcoming the activation barrier and so the plastic strain rate (or the stress relaxation rate, in our case) is higher than at lower temperatures. Experimentally, the activation energy, Q_e , can be related to the strain rate and the temperature by¹¹⁰

$$Q_e = kT^2 \left(\frac{\partial \ln \dot{\epsilon}}{\partial T} \right)_\tau \quad \mathbf{7.1}$$

The applied stress plays a critical role in overcoming the activation barrier, and can alter the activation enthalpy of the barrier. A related thermodynamic quantity called the experimental activation volume, V_e , has therefore been defined to characterize this dependence in terms of the strain rate at constant temperature.¹¹⁰

$$V_e = kT^2 \left(\frac{\partial \ln \dot{\epsilon}}{\partial \tau} \right)_T \propto \left(\frac{dW}{d\tau} \right)_T \quad 7.2)$$

As shown by Eq. 7.2, the activation volume is proportional to the work, W , needed to move a dislocation segment of a certain length forward by a certain distance.¹¹¹ While the activation volume does not always have a clear physical meaning, it may sometimes be interpreted as the product of the Burgers vector of the dislocation and the area swept out by the movement of a dislocation from a metastable state to the activated state.¹¹¹

Activation volume can be measured by observing the changes in strain rate and the changes in stress that occur during a single stress relaxation experiment. This analysis of the changes, however, gives only the “apparent” activation volume (V_a). In order to determine the “true” or “physical” activation volume (V^*) it is necessary to remove the effects of machine stiffness and strain hardening. This is usually done by performing repeated stress relaxation tests and then analyzing the relationship between the change in applied stress at each transition and the ratio of the strain rate at the end of one relaxation test and the strain rate at the beginning of the next relaxation test.

One advantage to characterizing the activation volume in addition to the activation energy is that the activation volume can be used to estimate the dislocation velocity (v) and mobile dislocation density (ρ_m) as well as the nature of the obstacle involved in the glide process. In principle, this allows a comparison to published results of these quantities for other materials. However, based on a survey of the

literature, the activation volume and mobile dislocation density have previously been determined in bulk materials and in nanoscale materials during plastic deformation using measurements performed in the plastic regime (i.e., after the yield stress has been exceeded). None of these studies consider viscoelastic stress relaxation at low stress. The strain used in the present study is in the range of viscoelastic behavior, not plastic deformation. In addition, we note that many of the publications report the activation volume only for pure metal films such as Ag,⁸³ Ni,⁷³ and Cu,¹¹² so it is interesting to extend the experiments to other materials such as alloy metals. It has been recognized that alloy films can achieve higher relaxation resistance than pure metals. In this study, two strengthening mechanisms, AuV solid solution and AuV₂O₅ dispersion, are investigated as alloys and compared with pure Au.

With this in mind, in this chapter additional bulge experiments with sputtered Au and Au alloy films are performed using repeated stress relaxation in order to determine the apparent and physical activation volume, and density of mobile dislocations. The purpose of the present study is to determine these quantities in Au and Au alloy films at different test conditions in the range of viscoelastic behavior, thereby providing the first data of this kind. The influence of parameters such as applied stress, temperature, alloy composition and grain size on activation volume and mobile dislocation density are examined. This study will provide the groundwork for a deeper understanding of viscoelastic relaxation behavior and its mechanism.

7.1 Repeated stress relaxation

As described in section 1.3.5, repeated stress relaxation is one type of transient mechanical test that can be used to determine the activation volume and provide the mobile dislocation density.

The procedure of repeated stress relaxation used in these experiments starts with a pressure ramp to measure the residual stress and the modulus of the film, and to identify the pressure required to produce a strain of either 0.001 or 0.002. This pressure is needed to establish the constant strain in the first of the repeated relaxation cycles. Following this preliminary ramp test, four cycles of repeated stress relaxation and reloading are conducted.

In each cycle, the pressure is applied to bulge a sample until it reaches a desired strain, then strain is kept constant and stress relaxation is measured over time. In this study, the constant strain for the first cycle is chosen as either 0.001 or 0.002 which is in the range of viscoelastic and viscoplastic behavior. The strain magnitude is chosen to give sufficiently large stresses to cause measurable relaxation. The stress decay during this first constant strain period is observed over a time interval of 200 seconds during which the stress decays by $\Delta\tau$. The sample is then reloaded by increasing the gas pressure to produce the same stress level as at the beginning of the first constant strain period and then allowed to relax again over a 200 second time interval. Naturally, this means that the constant strain values changes from one relaxation cycle to the next. The stress relaxation of the sample is repeated for a total

of four cycles of 200 seconds. Following the four cycles of repeated relaxation a three hour relaxation is carried out. This whole sequence is called a run.

Following the first run, the sequence is repeated several times in order to get rid of the viscoplastic component of the relaxation as described previously. Such runs are repeated at a rate of one run per day, allowing the film about 21 hours to recover viscoelastically at zero strain following the run, until the film reaches a steady state condition at which the film shows only viscoelastic response. From this type of experiment, we can observe the development of the film from the first run, which contains viscoelastic and viscoplastic components, to a run at a steady state condition which is only viscoelastic. In each run only the first 200 sec cycle of the four repeated stress relaxations is used to determine the apparent activation volume. It gives the same result as we obtain if we use the first 200 sec of our data on 3 hour relaxations from Chapter 3-6. All four cycles of repeated stress relaxation are used to determine the physical activation volume from the change in relaxation rate immediately before and after each increment in the stress.

Repeated stress relaxation experiments on sputtered Au, AuV and AuV₂O₅ films are carried out under different test conditions as shown in Table 7.1. The strain values in the table are those applied during the first stress relaxation cycle in the sequence of four in a single run. The microstructures of the investigated films are determined by SEM images as presented in Figure 7.1.

| Samples | Strain | Temperature Testing |
|---|--------|---------------------|
| 1. Au@large grain size (d=605 nm) | 0.001 | RT |
| | 0.002 | RT |
| 2. Au@normal grain size (d = 100 nm) | 0.002 | RT |
| | 0.002 | 80 °C |
| 3. AuV | 0.001 | RT |
| 4. AuV ₂ O ₅ | 0.001 | RT |

Table 7.1 The conditions of repeated stress relaxation testing of Au and Au alloy films.

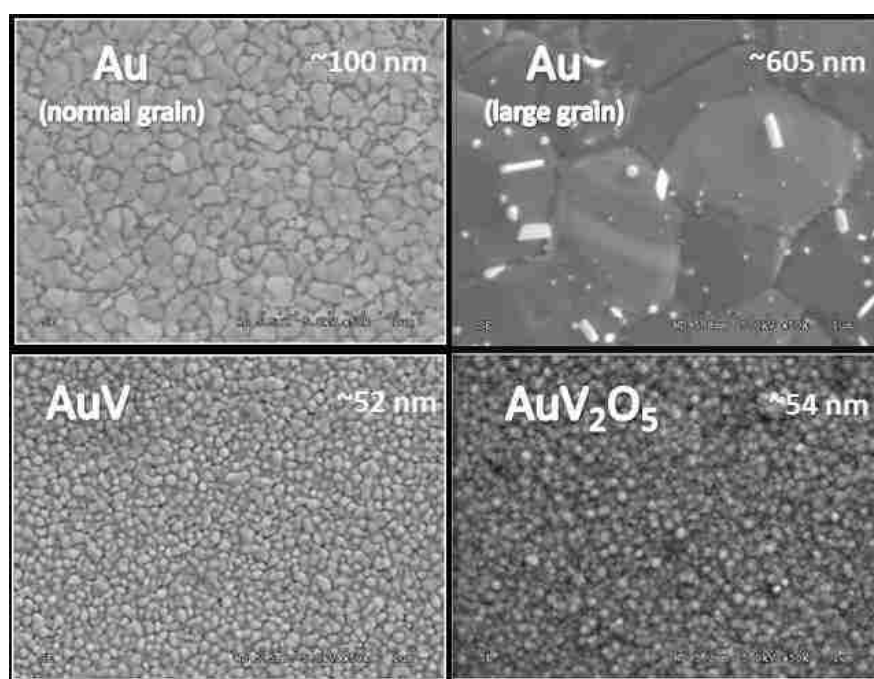


Figure 7.1 SEM images and estimated grain size of Au, AuV and AuV₂O₅ thin films.

The data for the final run (when the film has reached steady state) of repeated stress relaxation for Au and Au alloy films are shown in Figure 7.2. Other, earlier, runs of repeated stress relaxation show similar trends. It is observed that the stress in

each film at the beginning of the first 200 sec stress relaxation is different due to differences in residual stress. Figure 7.2a) shows the Au with large grain size at two different strain levels. The stress drop at a strain of 0.002 is larger than at a strain of 0.001. However, the modulus decay for these two strain levels is identical at steady state because the response is linear viscoelastic. For example, in Figure 7.2a), the large grain Au is initially strained to 0.001 (at stress level 178 MPa). The first relaxation cycle starts at stress level 178 MPa, and decreases over a time interval of 200 sec, by 3 MPa. Then, the film is reloaded to the same stress level, 178 MPa, and relaxes by 1.3 MPa during the second 200 sec, then reloaded to 178 MPa again, etc. (for four cycles).

Comparing the Au, AuV and AuV₂O₅ results in Figure 7.2b), AuV₂O₅ has the least amount of stress relaxation, as expected, while Au exhibits the most stress relaxation in each cycle. During consecutive relaxation cycles, we observe a continuing decrease in stress drop ($\Delta\sigma_i$) with increasing number of relaxation cycles for both Au and Au alloy films. This can be seen from the horizontal dashed lines in Figure 7.2. As the relaxation cycles continue, it is reasonable to assume that the dislocation velocity and mobile dislocation density are becoming smaller. Very little stress relaxation is observed in either pure Au metal or alloys in the last relaxation cycle.

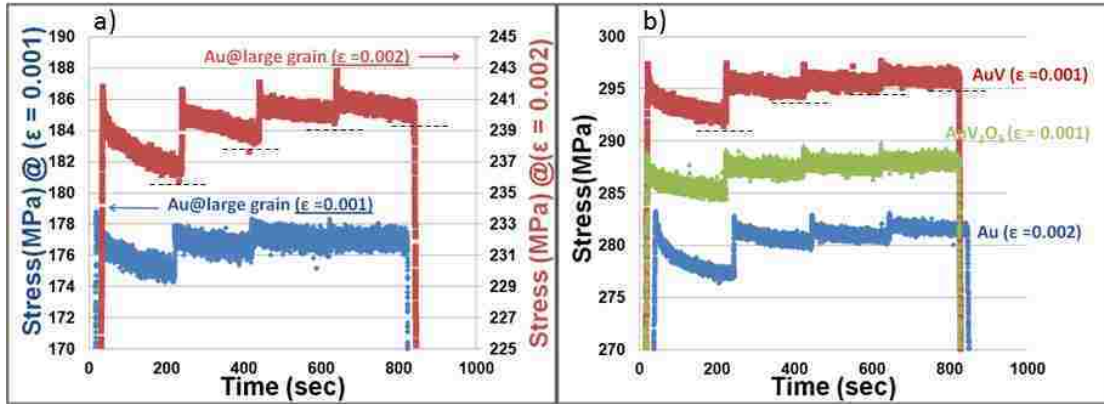


Figure 7.2 Repeated stress relaxation curves at steady state showing four cycles with time interval of 200 second a) large grain Au and b) Au, AuV and AuV₂O₅.

7.2 Activation volume results and discussion

7.2.1 Apparent activation volume

The apparent activation volume (V_a) can be determined from the first stress relaxation cycle of 200 sec of each run using⁸²

$$\Delta\tau(t) = -\frac{kT}{V_a} \ln\left(1 + \frac{t}{C_r}\right) \quad 7.3)$$

where $\Delta\tau$ is the decay of shear stress as a function of time (t), and C_r is the time constant. A 200 second time period was chosen for each cycle, since this is the time over which there is a good fit for only one time constant in the natural logarithmic expression of apparent activation volume in Eq 7.3). The first 200 sec relaxation cycle from every run from the first run until the final run at steady state is used to determine the apparent activation volume. Figure 7.3 shows an example of

determining V_a by the fitting curve (solid line) of stress decay during the first relaxation cycle of 200 second at steady state condition (run4) at room temperature of large grain size Au (605nm), giving $V_a \sim 336.5 b^3$ (b: Burgers vector). The time $t=0$ of stress decay is taken at the beginning of stress relaxation at the first cycle. The fitted time constant is 5.5 second and $\Delta\tau$ is about 2.1 MPa.

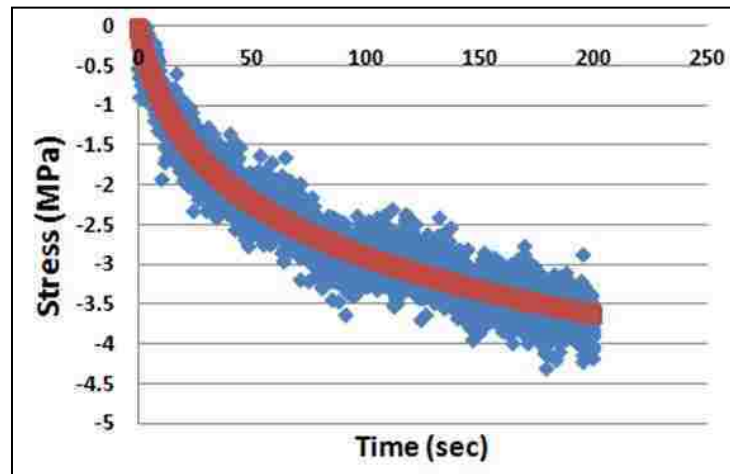


Figure 7.3 Example of the fitting curve of the first stress relaxation for apparent activation volume in Au.

At steady state condition, we can choose the fitting of the first 200 sec relaxation from repeated stress relaxation experiments or the beginning 200 seconds of a 3 hour relaxation to determine the apparent activation volume. They give essentially the same results. The relationship of stress decay between the 3 hour relaxation experiment and repeated stress relaxation of the Au film including the fitting of apparent activation volume and the fitting curve by the Prony series for the 3 hour relaxation is shown in the Figure 7.4.

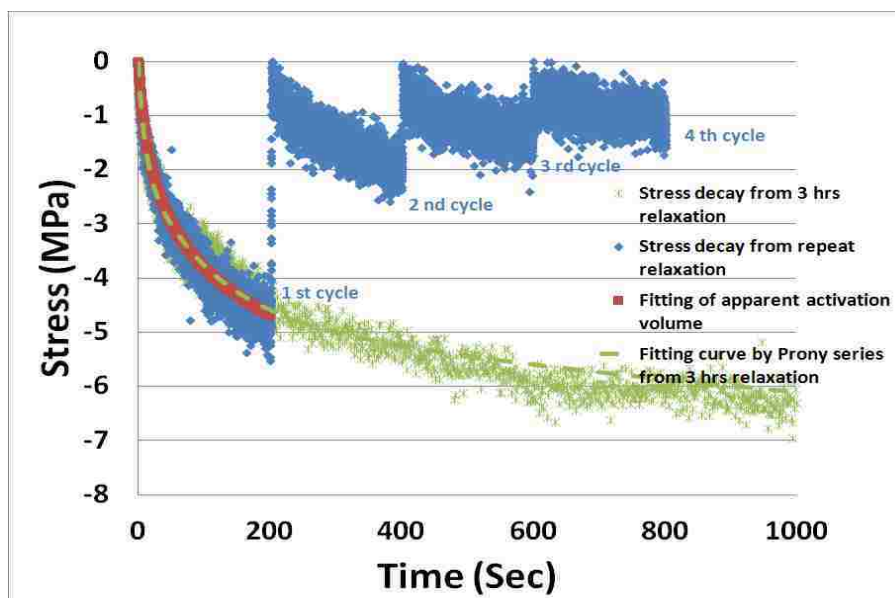


Figure 7.4 Repeated stress relaxation and 3 hour stress relaxation including the fitting of apparent activation volume of Au film.

Following Eq. 7.3, the apparent activation volume for viscoelastic stress relaxation of Au and Au alloy films is obtained by fitting stress vs. time plots. The results are shown in units of b^3 as a function of run number in Figure 7.5. The measured activation volume has a small increase with increasing run number. This trend is due to the smaller decay of shear stress with increasing run number as viscoplastic deformation capacity is being lost while the films are getting to the steady state. This implies that the average area swept out by the moving dislocations is increasing as viscoplastic deformation is decreasing, perhaps because those dislocations associated with the smallest activation volumes (the shortest glide distances) are becoming permanently pinned by strong obstacles. There is a large variation in apparent activation volume at steady state, with an average of approximately $330 b^3$ and a range of $\pm 210 b^3$.

Note that the observed V_a values in this study are much higher compared to the typical values in other research efforts that are primarily concerned with behavior of nanocrystalline metals near yielding, i.e., shortly after the onset of plastic flow. Values in the range of 12-50 b^3 have been reported for these materials.^{78, 112} This difference is because the change in stress in our study at the first relaxation cycle is so small by comparison. The stress drops for our Au and AuV₂O₅ films in the initial strain of 0.001 or 0.002 are about 4.7 and 2.3 MPa respectively, while the published stress drops for post-yield tests of the aforementioned nanocrystalline metals are 70-100 MPa when the initial strain is set to 0.008.^{78, 112} On the other hand, values reported for bulk materials with large grains can be on the order of 1000 b^3 . Our grain size is in between the reported bulk and nanocrystalline metal ranges so it may make some sense that our activation volume parameter fall in between if the grain boundaries play a role in the stress relaxation process as was suggested in a prior chapter. However, it is difficult to draw any conclusions because the initial strain conditions are very different.

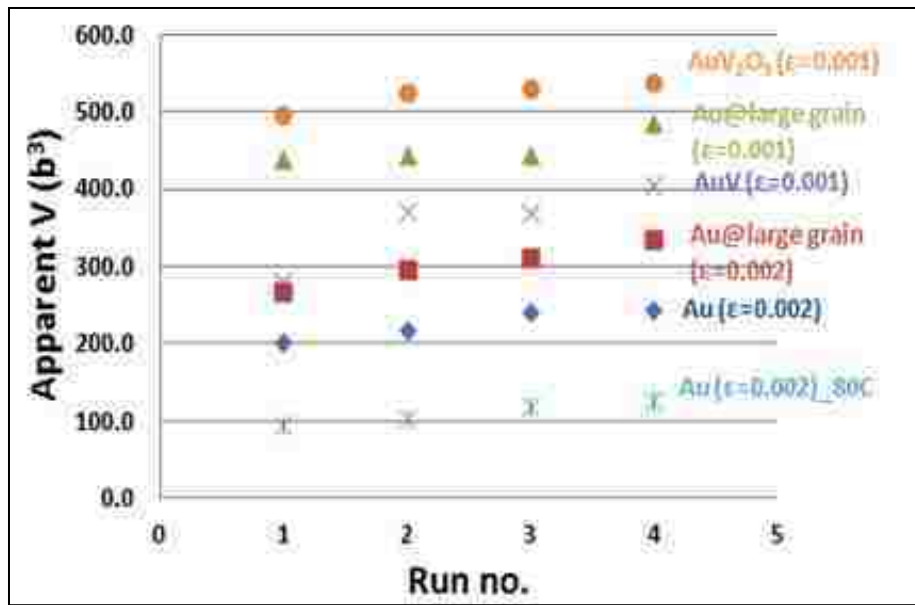


Figure 7.5 Apparent activation volume as a function of run number for Au and Au alloy films.

Considering the steady state condition (run4), the values of activation volume are approximately inversely proportional to the stress decay ($\Delta\tau$) in Eq.7.1. The difference in the fitted time constant has only a minor effect. The trend of 200 sec stress drop with apparent activation volume is shown in Figure 7.6 : the lower $\Delta\tau$, the higher V_a .

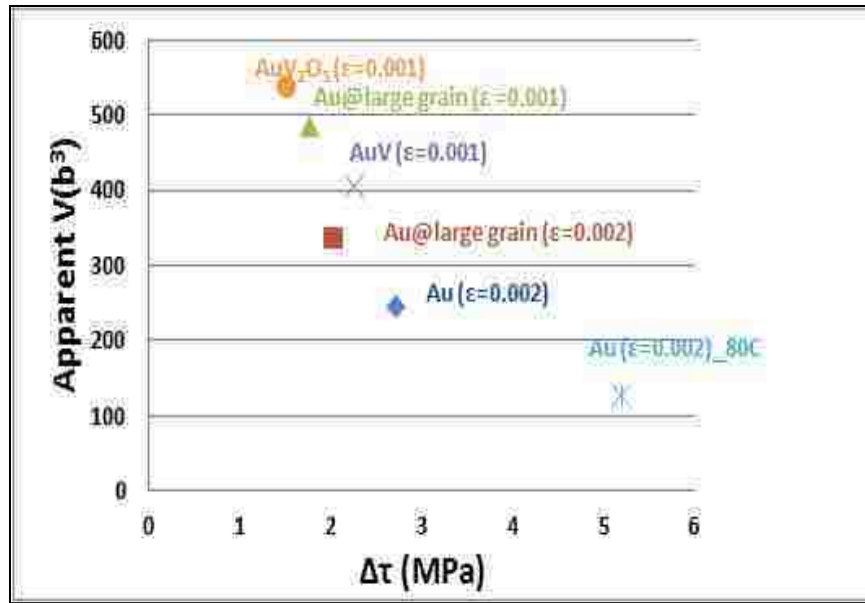


Figure 7.6 A plot of apparent activation volume at steady state vs. stress decay ($\Delta\tau$) of Au and Au alloy films.

7.2.2 Physical activation volume

To separate the contributions of the dislocation velocity (v) and mobile dislocation density (ρ_m) to the strain rate based on the Orowan Equation,⁸¹ the physical activation volume (V^*) is determined by

$$V^* = kT \frac{\ln \left(\frac{\dot{\gamma}_{i2}}{\dot{\gamma}_{f1}} \right)}{\Delta\tau} \quad 7.4)$$

where $\dot{\gamma}_{i2}$ and $\dot{\gamma}_{f1}$ are the initial and final shear strain rates measured at the onset of stress relaxation cycle 2 and the end of stress relaxation cycle 1, respectively, when the shear strain is increased suddenly by $\Delta\tau$ as the applied pressure is increased.

The physical activation volume V^* determined by Eq.7.2, which depends on the ratio of the relaxation rate before and after the stress increment $\Delta\tau$ is plotted in Figure 7.7. The differences in physical activation volume from one material to another and from one run to another are small compared to the apparent activation volumes shown in Figure 7.5. Of particular note, the physical activation volume values are all in a similar range, especially when the films are close to steady state condition ($40b^3 \pm 25$). This similarity implies that the same fundamental viscoelasticity mechanism is active for all of the Au and Au alloy films during the testing.

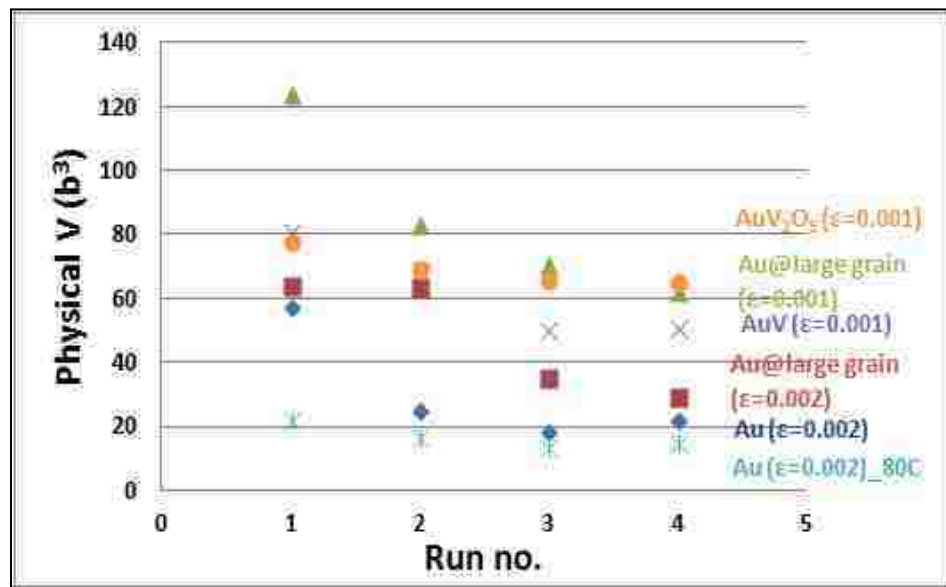


Figure 7.7 Physical activation volume as a function of run number for Au and Au alloy films.

Continuing to compare the trends of apparent and physical activation volume, we observe in Figure 7.8 that both V_a and V^* increase with a decrease of fixed strain in the films. Also, Au with the larger grain size and Au alloys have larger activation volumes than Au with normal grain size. The trend of both values is probably due to

the applied stress. The value of V_a and V^* are inversely related to the applied stress, and hence also to the magnitude of the stress relaxation. Figure 7.8 shows a clear decrease of activation volume with increasing applied stress which is consistent with the behavior seen when a metal deforms plastically by a dislocation mechanism.^{113, 114} This implies that a dislocation mechanism not only occurs during plastic deformation but also during viscoelastic deformation.

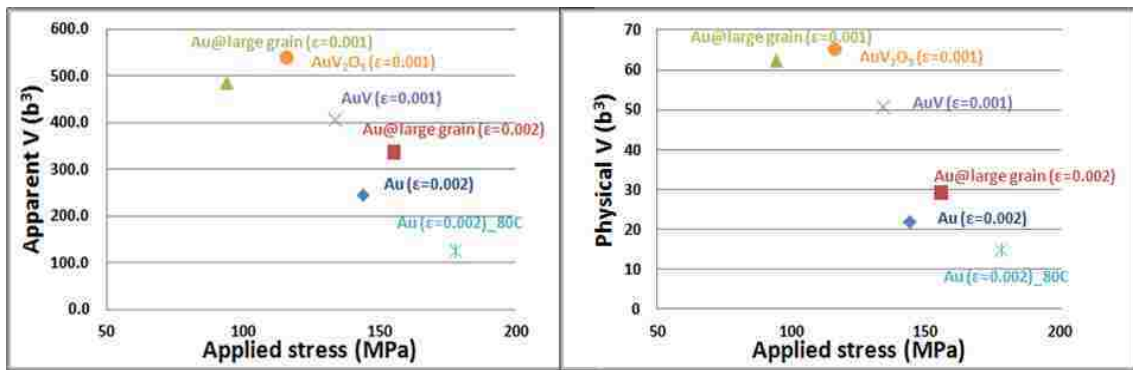


Figure 7.8 Apparent and physical activation volume as a function of applied stress.

Multiple-cycle stress relaxation experiments were performed at 80°C to assess the effect of temperature on activation volume. The results in Figure 7.9 indicate a decrease of the apparent activation volume and the physical activation volume with increasing temperature. The dependence of apparent and physical activation volume on Vanadium concentration and on grain size is shown in Figure 7.10 and Figure 7.11, respectively. Activation volume increases with increasing V concentration, and thus with increasing alloy strength, but also increases with increasing grain size, which probably implies decreasing strength. This shows that the activation volume is not a simple function of the metal yield strength, but instead depends on a combination of factors. For example, the initial total dislocation density and initial

mobile dislocation density values are likely to be different in each of the films in a way that is difficult to predict based purely on the composition and the prior processing conditions.

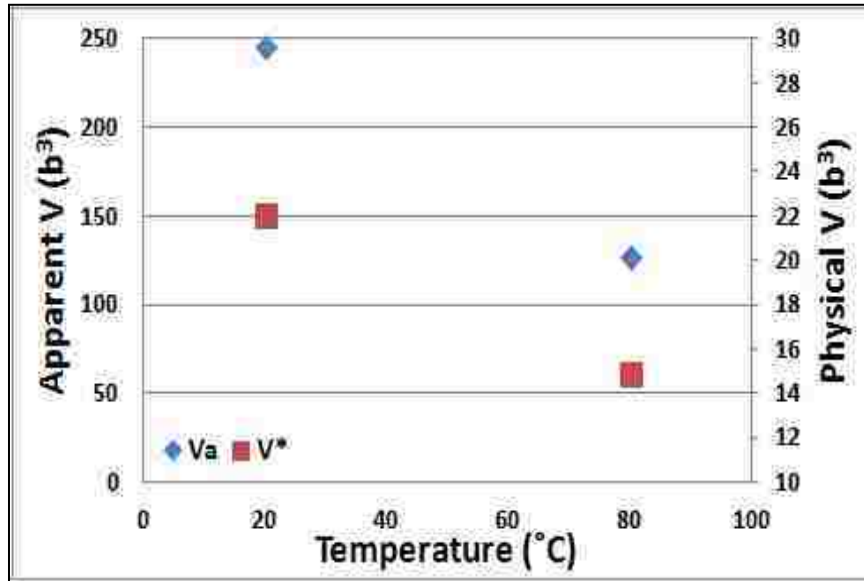


Figure 7.9 The effect of temperature on activation volume for Au thin films.

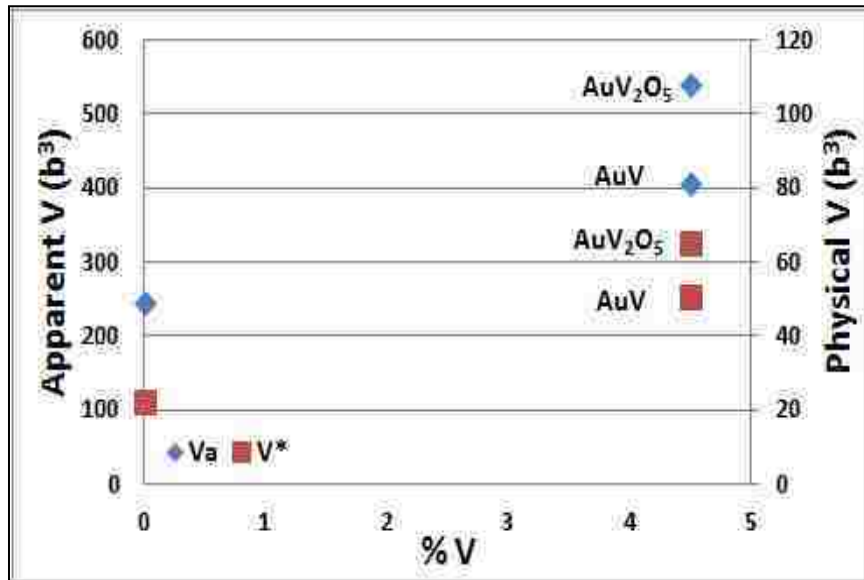


Figure 7.10 The effect of alloy compositions on activation volume of Au alloy thin films.

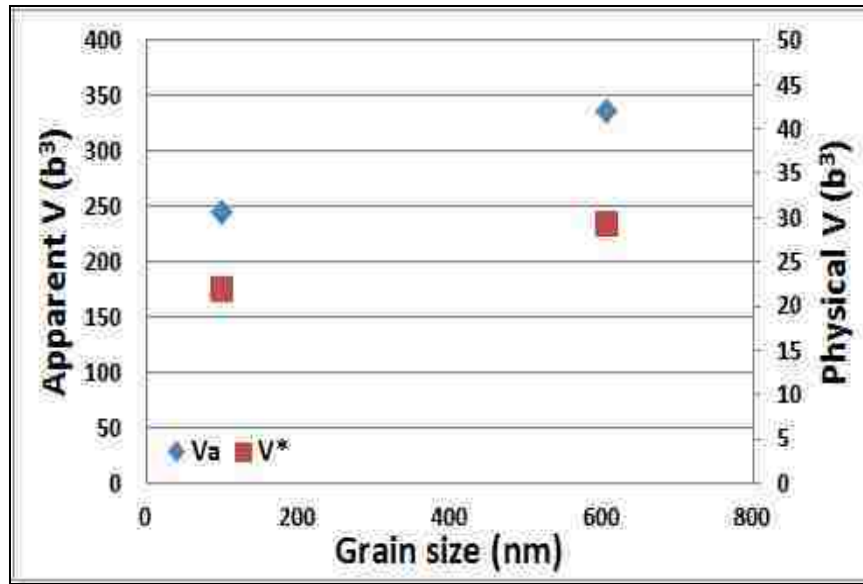


Figure 7.11 The effect of grain size on activation volume for Au thin films.

7.3 The density of mobile dislocation results and discussion

The mobile dislocation density (ρ_m) during the first stress relaxation can be determined by⁸²

$$\frac{\rho_m}{\rho_{m0}} = \left(\frac{C_r}{C_r + t} \right)^{\beta/(1+\beta)} \quad 7.5)$$

where ρ_{m0} is initial mobile dislocation density, β is defined as $\beta = \frac{\Omega}{1+K/M} - 1$, K is the strain-hardening coefficient, M is the elastic modulus of the specimen-machine system, and Ω is the ratio of V_a to V^* . The elastic modulus of the specimen-machine system, M , is roughly approximated by the elastic modulus of Au because the bulge system is very stiff compared to the film being tested. The parameter Ω is available from the experimental data. However, K is not known for the materials being tested

here. The strain hardening coefficient describes the potential for a change in flow stress with a change in plastic strain (i.e., a change in dislocation density). It is a function of material constants such as the stacking fault energy which, itself, is a function of composition and atomic structure. A significant difference in strain hardening capability might be expected for the films being evaluated in this study. In order to evaluate the change of dislocation mobility in our Au and Au alloy films, the sensitivity of the calculation to K must therefore be determined. The strain-hardening coefficient for Au and its alloys, which cannot be determined directly by the bulge test, is likely to be in the range of 100-30,000 MPa.

Figure 7.12 shows the evolution of mobile dislocation density with time in pure Au deposited at room temperature during 200 seconds of relaxation based on Eq.7.5. Four curves are plotted assuming four different strain-hardening coefficients that represent the entire range of probable behavior. Although the higher the strain-hardening coefficient, the larger the value of ρ_m/ρ_{m0} , the dependence of mobile dislocation on K is relatively small and can safely be ignored.

The general trend seen from this analysis is that the mobile dislocation density is greatest at the beginning of the relaxation test and decreases very rapidly over time. After 200 sec the fraction of dislocations that is still mobile is very small, on the order of 2%. The rapid decrease of ρ_m at the early stage of relaxation correlates well with the high rate of reduction of the effective modulus which is the fastest at the beginning of a relaxation test.⁴

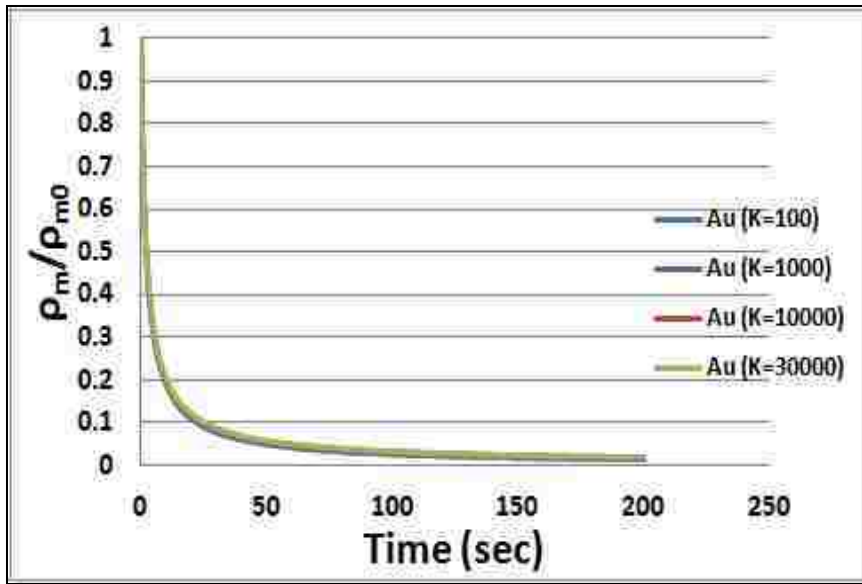


Figure 7.12 The mobile dislocation density as a function of time assuming various strain-hardening coefficients (K) for Au films deposited at room temperature.

Figure 7.13 shows the mobile dislocation fraction at the end of the first relaxation ($t=200$ sec) for all films derived from different K values. This plot provides the estimated upper and lower limits of the possible mobile dislocation density of the Au and Au alloy films. For example, for pure Au deposited at room temperature the value of mobile dislocation fraction after 200 sec is between approximately 1.5% and 1.8% when tested at 20°C while and between approximately 5.5% and 6.3% when tested at 80°C. Regardless of which K value is assumed, the order of the films is consistent. Since the mobile dislocation density has only a small dependence on K and all Au films are expected to have a relatively small K,⁸⁹ a single K value may be assumed for the purpose of drawing conclusion. Figure 7.14 therefore shows the comparative results of mobile dislocation density fraction for Au and Au alloy films as a function of time at a K value of 1000 MPa.

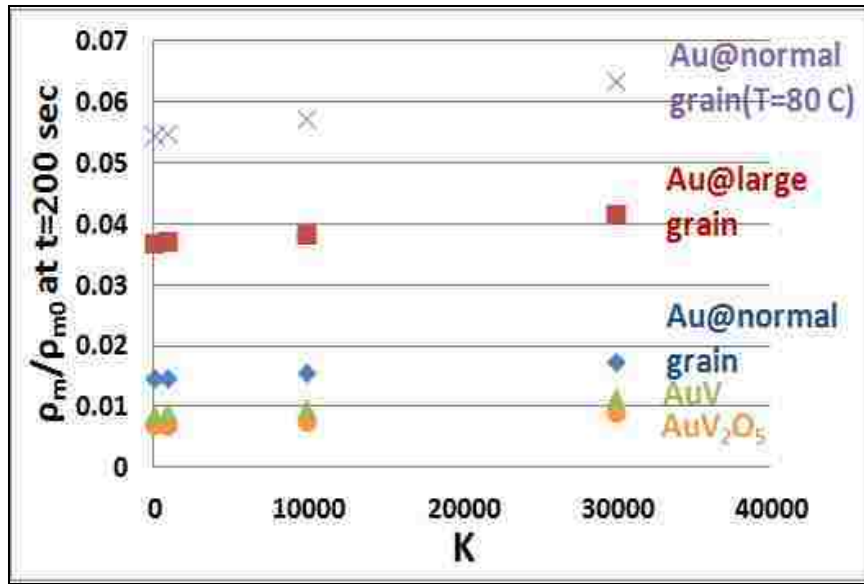


Figure 7.13 The estimated value of the mobile dislocation density at $t = 200$ seconds assuming various value of K for Au and Au alloy films.

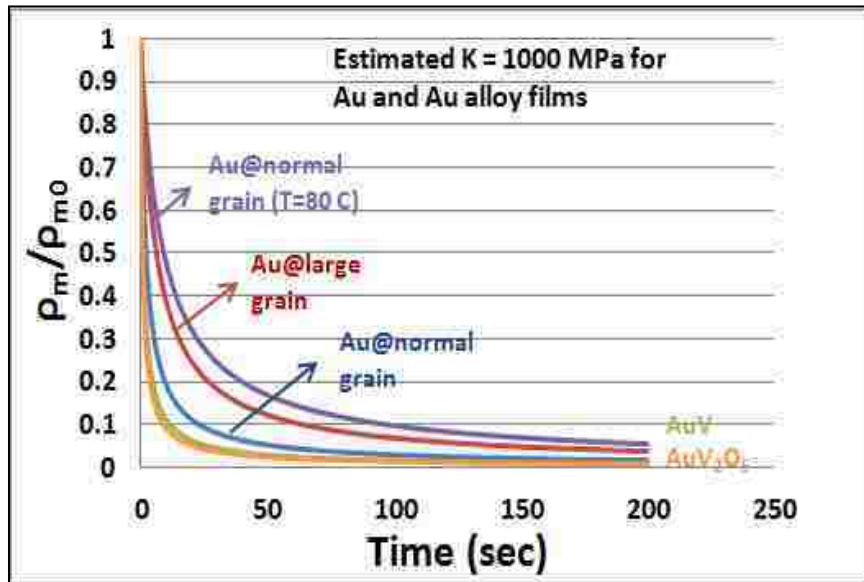


Figure 7.14 Comparison of mobile dislocation density as a function of time for Au and Au alloy films when K is reasonably estimated at 1000 MPa.

The curves for all of the Au and Au alloy films show a similar trend in which the mobile dislocation fraction decreases very rapidly at the beginning of relaxation.

The alloy films experience the fastest change in mobile dislocation density, leaving few mobile dislocations to participate in further stress relaxation after a short time. The mobile dislocation density fraction remains relatively high in the pure Au (especially at 80°C), consistent with the tendency of these films to experience significant relaxation for a longer time than the alloy films. The higher mobile dislocation fraction in the pure Au at a given time could be due to either a lower rate of dislocation pinning or a higher rate of dislocation nucleation. We assume, however, that at the low stresses imposed in our viscoelasticity studies the nucleation rate is very low so we attribute the differences in dislocation density among the films to differences in the rate of pinning. In all cases, continuing relaxation deformation causes more pinning of dislocations and so hardening occurs due to exhaustion of mobile dislocations. Presumably, the pinning rate is greatest for the alloy films, the films with smaller grains, and the films tested at lower temperatures. Conversely, film purity, large grain size, and elevated temperature appear to discourage rapid pinning.

The magnitude of V^* can also be used to obtain insight into the rate-controlling deformation mechanism. Based on our V^* values, grain boundary diffusion (Coble creep) and grain boundary sliding can be ruled out. For these mechanisms, V^* is expected to be a very small value, probably less than b^3 .^{79, 112} The calculated V^* of our Au films is closer to that of the dislocation glide seen in nanocrystalline and ultra-fine grained (sub- μm) metal films, for which the value is between $1b^3$ and $100b^3$.^{79, 115}

However, the trend with grain size is the opposite of that reported for FCC nanocrystalline Cu. In that case, a Hall-Petch type relation was found in which increasing grain size was associated with decreased activation volume.¹¹² The plasticity mechanism proposed for the nanocrystalline Cu treated the grain boundary as a source for dislocations that interact according to a Hall-Petch type mechanism.¹¹² For this mechanism, larger grains are associated with smaller activation volumes. In our case, the activation volume increased with increasing grain size.

Instead of a Hall-Petch type of trend, the results of our dislocation density analysis are consistent with the proposed mechanism that we described before in which dislocations pinned at grain boundaries bow out by a double kink nucleation and propagation process. A dislocation loop will expand by separating a double kink under an applied stress. When the applied stress is removed, the line tension of the dislocation loop will bias the motion of the dislocation loop back to the original location. Viscoelasticity occurs when the dislocation loops can return to their original size, and thus be fully recoverable. Larger grain size may be associated with greater distances between loop pinning points so that larger areas may be swept out by propagating dislocations. Viscoplasticity occurs when there is some final displacement of dislocation loops that thus cannot be fully recoverable, perhaps through the pile-up model proposed for nanocrystalline Cu. This demonstrates the uniqueness of the viscoelasticity process observed in the current study.

Activation volume has also been measured for plasticity in nanocrystalline Ni. The high exhaustion rate of mobile dislocation in our Au films is consistent with the

report of plastically deforming nanocrystalline Ni by Wang et al.^{78, 79} They proposed a possible process which involves the interaction of dislocations loop with grain boundaries.¹¹⁶ However, this mechanism calls for expansion of a dislocation loop by motion of the loop along the boundary that is dependent on a de-pinning process. The thermal activation of this process is associated with the de-pinning event and not with the expansion of the loop by double-kink formation. It should be pointed out that in our discussion we did not make the assumption of de-pinning dislocations, since we believe the line tension in an expanding pinned dislocation will provide the bias on the motion of a dislocation loop needed to return it to its original location during viscoelastic recovery. The proposed depinning process cannot account for viscoelastic deformation because there is no driving force for the pinning point to return to its original location. There is no fundamental problem with both mechanisms being active, however, with pinned bowing as the dominant viscoelastic relaxation mechanism at low applied strains and de-pinning loop growth as the dominant mechanism at high applied strains (and perhaps during the viscoplastic relaxation seen initially at low strains in our tests). Once again, it appears that there are fundamental differences between the viscoplastic deformation measured at large strains in nanocrystalline metals and the viscoelastic deformation measured at small strains in our Au films.

The obstacles causing pinning of dislocations can be grain boundaries, solutes or oxide dispersions which can interact with the moving dislocations. It can be seen that the fraction of mobile dislocations in pure Au is larger for a longer time than in a

Au alloy during the relaxation process. The solute or oxide dispersion in Au alloys can be the main obstacles which can cause the pinning of dislocation and a corresponding decrease in mobile dislocation fraction and in the stress relaxation rate. Based on the results of dislocation mobility, the oxide particles in AuV₂O₅ can impede the dislocation motion more effectively than substitutional atoms of V in AuV solid solution.

7.4 Summary

We have studied the relaxation behavior of Au and Au alloy films by using repeated stress relaxation tests to determine the apparent and physical activation volume at different condition tests. Results of both activation volumes show consistent trends. Activation volume of the viscoelastic relaxation process is inversely proportional to the applied stress and temperature, while it increases with alloy concentration. The rapid decrease of ρ_m is observed for all films which supports the fast relaxation in the effective modulus in the previous study. The lower value of dislocation mobility of AuV and AuV₂O₅ compared to Au presents the effect of solutes or oxide particles to impede the dislocation motions. We propose a mechanism based on a mobile dislocation loop with double kink generation emerging from a grain boundary as the possible rate controlling mechanism for viscoelastic deformation in Au and Au alloy films.

8. Conclusions and future work

8.1 Conclusions

It has been reported that stress relaxation in a metal membrane or bridge can increase the tendency for the mechanical failure of RF MEMS capacitive switches. In order to reduce the probability of device failure due to stress relaxation, we have investigated the viscoelastic behavior of Au and Au alloy films by using gas pressure bulge testing in the range of 20 - 80 °C. We observed that complete viscoelasticity in these thin films can be reached when the relaxation tests are performed multiple times to eliminate initial film plasticity. AuV and AuV₂O₅ films exhibit more relaxation resistance than pure Au in the temperature range of 20-80 °C which makes them attractive as candidate membrane materials for improving the lifetime of switches.

We also investigated some detailed factors that affect the material's viscoelasticity. Increasing the temperature increases the amount and rate of relaxation, and is therefore detrimental to RF MEMS reliability. The effect of the concentration of dissolved solute is established to have a $C^{1/3}$ contribution to stress relaxation from 20 – 80 °C, with increasing solute concentration leading to increasing relaxation resistance. The grain size effect on the viscoelastic modulus is shown to be proportional to D^2 , with decreasing grain size leading to increasing relaxation resistance. Alloying contributes to establishing and stabilizing a small grain size, so alloying has the potential to make multiple positive contributions to improving RF MEMS reliability.

The quantitative analysis of the viscoelastic model was used to predict the time dependent stress in thin films based on the proven linear viscoelasticity behavior. The model provides an excellent fit for Au films with a complex loading history and has the ability to predict stress relaxation at other strain rates during loading.

We proposed that a mobile dislocation loop pinned at its ends on a grain boundary and propagating under the influence of an applied stress by double kink nucleation is the most probable mechanism for relaxation in the Au and Au alloy films investigated at low strains. This proposed mechanism is based on small activation energies of approximately 0.1 eV extracted from the temperature dependence of the relaxation rate over the temperature range investigated. Also, the value of the activation volume and the high exhaustion rate of mobile dislocations determined by repeated stress relaxation tests are consistent with the dislocation-based mechanism. Critical differences between the viscoelastic relaxation observed in our films and the viscoplastic stress relaxation measured in nanocrystalline and ultra-fine grained metals were identified, motivating further study of the viscoelasticity process.

8.2 Future work

This research includes the detailed study of time and temperature dependence of viscoelastic stress relaxation in Au and Au alloy thin films. However, there is other work that can be done to advance the current understanding of stress relaxation behavior. The list below shows the recommendations for future work.

1. The effect of chemistry on relaxation behavior can be expanded to include other AuX solid solution alloys and to explore metals other than Au. We have previously discussed that relaxation resistance can be enhanced by solid solution strengthening as we did with AuV. Au films with different solutes should be fabricated and tested to characterize the solid solution hardening effect of different solutes. In order to select a potential solute element other than V, we need to evaluate the hardening effect which is the combination of solute misfit and modulus change. Based on specific hardening of Au alloys in Figure 1.6 in section 1, the hardening of AuV is found to be similar to AuZn and AuCd. AuIn is a more attractive selection since it is expected to show large relative solid solution hardening based on the combination of solute misfit and modulus effect. It is noted that we had a chance to investigate electrodeposited AuCo films, in collaboration with Purdue University. However, these films have different parameters, such as thickness and preparation method, compared to our films and are probably not a very good choice for further study of fundamental relaxation processes. AuIn should be the same thickness and use the same preparation method of

sputtering to simplify the comparison to AuV in the range of 20 – 80 °C. Based on the phase diagram of AuIn,¹¹⁷ the composition of AuIn alloys for the proposed study will be less than 8 at % to avoid any possible two-phase alloys or intermetallic compound formation. Furthermore, we can choose to study interesting elements which are commonly used in MEMS switches other than Au, such as Al and Cu.¹¹⁸ Pure Al, Cu and their promising alloys are also worth investigating for stress relaxation.

2. Preliminary results describing the effect of grain size on activation volume were presented in the present study, but films with a wider range of grain sizes should be measured to conclusively determine if the behavior is opposite to that seen in nanocrystalline Cu films.
3. Further study of some parameters that might influence the viscoelastic behavior of thin films, such as thickness or a wider range of temperature, should be investigated. If dislocations contribute to the relaxation behavior as we described, the strength of the films should increase when the film thickness decreases due to constraints on dislocation motions imposed by the substrate. The Au films can be fabricated by varying the thickness in the range of 100-4000 nm. The maximum thickness of Au film is presently limited by the capability of our bulge system which can provide a maximum pressure at 600 torr, enough to produce a strain of 0.001 for 4000 nm Au film. The grain sizes of the film are most likely to be changed with the thickness. Anyhow, the comparison of thickness dependence of stress relaxation can be

compared with the same grain size based on our predictive results D^2 for grain size on stress relaxation.

Higher temperature of bulge test can be investigated to extend the experimental results. Further investigation of the temperature capability of the bulge system at higher temperature must not damage the parts inside such as the o-ring seals that separate the vacuum and the pressure parts, plastic insulating rings or the wires inside the bulge system. Also, the residual tensile stress of the film is one of the main considerations which limit the range of the highest investigated temperature. If that temperature causes the film to buckle or wrinkle, the results might not be reliable.

4. Comparing results from different types of mechanical testing. Alternative testing methods, such as microtensile test or nanoindentation, should be tested to compare and check the consistency with our results from bulge testing.
5. The most attractive thin films identified in this study, such as AuV or AuV₂O₅, are worth applying to actual MEMS switches and tested in a real switch configuration. Also, it is useful to apply analytical modeling of viscoelasticity on restoring force in RF MEMS capacitive switches to simply predict the restoring force loss from stress relaxation and compare to pure Au films at different temperatures.
6. Transmission Electron Microscopy (TEM) can be used to investigate the addition microstructure of the films, especially the cross section-view images.

These TEM images can tell us that the grains are formed in the columnar or equiaxed grains.

7. The amount of plastic exhaustion or recovery should be investigated in terms of time and temperature dependence. In the present research, we have focused on viscoelastic stress relaxation behavior of the films and very little on plasticity.
8. If possible, a numerical technique, such as a kinetic Monte Carlo simulation, can be used to provide visualization of dislocation mobility on such parameters as stress, solute concentration and solute type. The simulation results of the dislocations within the framework of the kink model can be compared with our results which can support or oppose our proposed mechanism of dislocation double kink mechanism.

9. References

1. R. E. Strawser, K. D. Leedy, R. Cortez, J. L. Ebel, S. R. Dooley, C. F. Herrmann Abell and V. M. Bright, *Sensors and Actuators A: Physical* **134** (2), 600-605 (2007).
2. J. C. M. Hwang, *IEEE RFIT*, 168-171 (2007).
3. B. A. Samuel and M. A. Haque, *J. Micromech. Microeng.* **16**, 929-934 (2006).
4. X. Yan, W. L. Brown, Y. Li, J. Papapolymerou, C. Palego, J. C. M. Hwang and R. P. Vinci, *J. Microelectromech. Syst.* **18** (3), 570-576 (2009).
5. H. J. Frost and M. F. Ashby, *Deformation-Mechanism Maps: The Plasticity and Creep of Metals and Ceramics* (Pergamon Press, Oxford, UK, 1982).
6. S. Melle, C. Bordas, D. Dubuc, K. Grenier, Vendier, J. L. Muraro, J. L. Cazaux and R. Plana, *IEEE*, 173-176 (2007).
7. M. McLean, W. L. Brown and R. P. Vinci, *J. Microelectromech. Syst.* **19** (6), 1299-1308 (2010).
8. A. J. Kalkman, A. H. Verbruggen and G. C. A. M. Janssen, *Review of Scientific Instruments* **74** (3), 1383-1385 (2003).
9. S. Hyun, W. L. Brown and R. P. Vinci, *Appl. Phys. Lett.* **83** (21), 4411-4413 (2003).
10. T. Bannuru, W. L. Brown, S. Narksitipan and R. P. Vinci, *J. Appl. Phys.* **103** (8), 083522-083526 (2008).
11. Z. H. Barber and M. G. Blamire, *Mater. Sci. Technol.* **24** (7), 757-770 (2008).
12. J. E. Mahan, *Physical Vapor Deposition of Thin films* (John Wiley&Sons, NY 2000).
13. A. Eishabini-Riad and F. D. Barlow, *Thin Film Technology Handbook* (McGraw-Hill, New York 1998).
14. K. Wasa, M. Kitabatake and H. Adachi, *Thin Film Material Technology: Sputtering of Compound Materials* (William Andrew Publishing, NY 2004).
15. J. Smith, *Journal of Phase Equilibria* **2** (3), 344-347 (1981).
16. I. Safi, *Surface and Coatings Technology* **127** (2-3), 203-218 (2000).
17. W. D. Sproul, D. J. Christie and D. C. Carter, *Thin solid films* **491** (1-2), 1-17 (2005).
18. D. L. Smith, *Thin film deposition: Principles and practice* (McGraw-Hill, 1995).
19. A. J. Kalkman, A. H. Verbruggen and G. C. A. M. Janssen, *Applied Physics Letters* **78** (18), 2673-2675 (2001).
20. P. S. Alexopoulos and T. C. O'Sullivan, *Annual Review of Materials Science* **20** (1), 391-420 (1990).
21. D. Peckner, *The strengthening of metals* (Reinhold publishing, New York, 1964).
22. P. Jax, P. Kratochvil and P. Haasen, *Acta Metallurgica* **18** (2), 237-245 (1970).
23. R. L. Fleischer, *Acta Metallurgica* **11** (3), 203-209 (1963).
24. R. Labusch, *Phys. Status Solidi B* **41** (2), 659-669 (1970).
25. J. O. Linde and S. Edwardson, *Arch. Phys.* **8**, 511 (1954).
26. I. Wesemann, A. Hoffmann, T. Mrotzek and U. Martin, *International Journal of Refractory Metals and Hard Materials* **28** (6), 709-715 (2010).
27. R. W. Hertzberg, *Deformation and Fracture Mechanics of Engineering Materials* (John Wiley&Son, New York, 1996).
28. W. D. Callister, *Materials Science and Engineering: An Introduction* (John Wiley & Sons, 2006).
29. T. G. Nieh and J. Wadsworth, *Scripta Metallurgica et Materialia* **25** (4), 955-958 (1991).
30. E. Arzt, *Acta Materialia* **46** (16), 5611-5626 (1998).

31. A.H.Chokshi, Scripta metall. **23**, 1679 (1989).
32. H. Conrad and J. Narayan, Scripta metall. **42**, 1025-1030 (2000).
33. C. L. Goldsmith, Y. Zhimin, S. Eshelman and D. Denniston, Microwave and Guided Wave Letters, IEEE **8** (8), 269-271 (1998).
34. G. M. Rebeiz, *RF MEMS Theory, Design, and Technology*. (John Wiley & Sons, 2003).
35. R. Lagers, *Viscoelastic Materials* (Cambridge university press, New York, 2009).
36. R. D. Emery and G. L. Povirk, Acta Materialia **51** (7), 2067-2078 (2003).
37. R. D. Emery and G. L. Povirk, Acta Materialia **51** (7), 2079-2087 (2003).
38. I. Chasiotis, C. Bateson, K. Timpano, A. S. McCarty, N. S. Barker and J. R. Stanec, Thin Solid Films **515** (6), 3183-3189 (2007).
39. S.-J. Hwang, Y.-C. Joo and J. Koike, Thin solid films **516** (21), 7588-7594 (2008).
40. H. Huang and F. Spaepen, Acta Materialia **48** (12), 3261-3269 (2000).
41. W. C. Oliver and G. M. Pharr, J.Mater, Res **19** (1), 3 (2004).
42. J. J. Vlassak and W. D. Nix, Materials Research **7** (12), 3242-3249 (1992).
43. G. G. Stoney, Proceedings of the Royal Society of London. **A82** (553), 172 (1909).
44. B. Groenewald, J. Tapson, A. B. Mann and T. P. Weihs, presented at the Dielectric Materials, Measurements and Applications, 2000. Eighth International Conference on (IEE Conf. Publ. No. 473), 2000 (unpublished).
45. J. M. M. de Lima, R. G. Lacerda, J. Vilcarromero and F. C. Marques, Journal of Applied Physics **86** (9), 4936-4942 (1999).
46. R. P. Vinci and J. J. Vlassak, Annual Review of Materials Science **26**, 431 (1996).
47. F. vonPreissig, J. Appl. Phys. **66** (9), 4262-4268 (1989).
48. R. Liu, H. Wang, X. Li, G. Ding and C. Yang, Journal of Micromechanics and Microengineering **18** (6), 065002 (2008).
49. W. N. Sharpe, Jr., B. Yuan and R. L. Edwards, Microelectromechanical Systems, Journal of **6** (3), 193-199 (1997).
50. I. Chasiotis and W. G. Knauss, Proc. SPIE **3512**, 66-75 (1998).
51. M. A. Haque and M. T. A. Saif, Experimental Mechanics **42** (1), 123-128 (2002).
52. M. A. Haque and M. T. A. Saif, Scripta Materialia **47** (12), 863-867 (2002).
53. A. C. Fischer-Cripps, *Nanoindentation*, 2nd Ed. (Springer-Verlag New York, 2004).
54. W. C. Oliver and G. M. Pharr, J.Mater, Res. **7**, 1564 (1992).
55. W. Nix, Metallurgical and Materials Transactions A **20** (11), 2217-2245 (1989).
56. R. P. Vinci and J. C. Bravman, presented at the Solid-State Sensors and Actuators, 1991. Digest of Technical Papers, TRANSDUCERS '91., 1991 International Conference on, 1991 (unpublished).
57. M. K. Small and W. D. Nix, Journal of Materials Research **7**, 1553-1563 (1992).
58. J. D. Hall, N. E. Apperson, B. T. Crozier, C. Xu, R. F. Richards, D. F. Bahr and C. D. Richards, Review of Scientific Instruments **73** (5), 2067-2072 (2002).
59. E. I. Bromley, J. N. Randall, D. C. Flanders and R. W. Mountain, Journal of Vacuum Science & Technology B: Microelectronics and Nanometer Structures **1** (4), 1364-1366 (1983).
60. A. J. Kalkman, A. H. Verbruggen, G. C. A. M. Janssen and F. H. Groen, Review of Scientific Instruments **70** (10), 4026-4031 (1999).
61. F.R.N.Naberro, *Report of a Conference on the Strength of Solids*, Physical Society, London, 75-90 (1948).
62. C.Herring, J.Appl.Phys. **21**, 437-445 (1950).

63. M.A.Meyers, R.W.Armstrong and H.O.K.Kirchner, *Mechanical and Materials: Fundamentals and linkages*, (John Wiley & Sons, 1999).
64. R.L.Coble, *J.Appl.Phys.* **34**, 1679 (1963).
65. R.W.Evans and B.Wilshire, *Introduction to creep*, (Bourne Press Limited, Bournemouth, 1993).
66. A.S.Nowick and B.S.Berry, *Anelastic relaxation in crystalline solids* (Academic Press, New York, 1972).
67. C. Zener, *Physical Review* **60** (12), 906-908 (1941).
68. N. E. Dowling, *Mechanical behavior of Materials: Engineering methods for deformation, Fracture, and Fatigue*, (Prentice Hall, Englewood cliffs, NJ, 1993).
69. P. L. Raffo, *Journal of the Less Common Metals* **17** (2), 133-149 (1969).
70. I. M. Ward, *Mechanical Properties of Solid Polymers*, 2 nd Ed. (John Wiley & Sons, England, 1983).
71. U. F. Kocks, A. S. Argon and M. F. Ashby, *Prog. Mater. Sci* **19**, 1 (1975).
72. M. Kato, *Materials Science and Engineering: A* **516** (1–2), 276-282 (2009).
73. F. Dalla Torre, H. Van Swygenhoven and M. Victoria, *Acta Materialia* **50** (15), 3957-3970 (2002).
74. R. J. Asaro and S. Suresh, *Acta Materialia* **53** (12), 3369-3382 (2005).
75. C. D. Gu, J. S. Lian, Q. Jiang and W. T. Zheng, *Journal of Physics D: Applied Physics* **40** (23), 7440 (2007).
76. R. Schwaiger, B. Moser, M. Dao, N. Chollacoop and S. Suresh, *Acta Materialia* **51** (17), 5159-5172 (2003).
77. S. Cheng, E. Ma, Y. M. Wang, L. J. Kecskes, K. M. Youssef, C. C. Koch, U. P. Trociewitz and K. Han, *Acta Materialia* **53** (5), 1521-1533 (2005).
78. Y. M. Wang, A. V. Hamza and E. Ma, *Applied Physics Letters* **86** (24), 241917 (2005).
79. Y. M. Wang, A. V. Hamza and E. Ma, *Acta Materialia* **54** (10), 2715-2726 (2006).
80. D.Caillard and J. L. Martin, *Thermally activated mechanisms in crystal plasticity* (Pergamon, 2003).
81. E. Orowan, *Proc. Phys. Soc.* **52** (8) (1940).
82. J. L. Martin and T. Kruml, *Journal of Alloys and Compounds* **378** (1–2), 2-12 (2004).
83. M. J. Kobrinsky and C. V. Thompson, *Acta Materialia* **48** (3), 625-633 (2000).
84. Y. Xiang, X. Chen and J. J. Vlassak, *Journal of Materials Research* **20** (09), 2360-2370 (2005).
85. R. P. Vinci, T. Bannuru, S. Hyun and W. L. Brown, *Key Engineering Materials* **345-346**, 735-740 (2007).
86. T. Bannuru, W. L. Brown, S. Narksitipan and R. P. Vinci, *Journal of Applied Physics* **103** (8), 083522-083526 (2008).
87. R. Edwards, G. Coles and W. Sharpe, *Experimental Mechanics* **44** (1), 49-54 (2004).
88. M.Hershkovitz, I.A.Blech and Y.Komen, *Thin solid films* **130**, 87 (1985).
89. P. A. Gruber, S. Olliges, E. Artz and R. Spolenak, *Mater. Res. Soc.* **23** (9), 2406 (2008).
90. M.D.Thouless, J.Gupta and J.M.Harper, *Journal of Materials Research* **8** (8), 1845 (1993).
91. R. E. Hummel and H. J. Geier, *Thin Solid Films* **25** (2), 335-342 (1975).
92. S. Kilgore, C. Gaw, H. Henry, D. Hill and D. Schroder, *Mater. Res. Soc. Symp Proc* **863**, 313-318 (2005).
93. L. E. Benatar, D. Redfield and R. H. Bube, *J. Appl. Phys.* **73** (12), 8659-8661 (1993).

94. L.Chen and L.Yang, Non-Cryst. Sol. **137-138**, 1185 (1991).
95. D. Gan, P. S. Ho, R. Huang, J. Leu, J. Maiz and T. Scherban, J. Appl. Phys. **97** (10), 103531 (2005).
96. R. Huang, D. Gan and P. S. Ho, J. Appl. Phys. **97** (10), 103532 (2005).
97. G. Fantozzi, C. Esnouf, W. Benoit and I. G. Ritchie, Progress in Materials Science **27** (3-4), 311-451 (1982).
98. J. P. Hirth and J. Lothe, *Theory of Dislocations* (Wiley, New York, 1982).
99. J. Lothe and J. P. Hirth, Phys. Rev. **115** (3), 543 (1959).
100. S. Lytton, and Dorn, Trans. Am. Inst. Mining, Met., Petrol. Engrs., **212**, 220 (1958).
101. W. Benolt, M.Bujard and G. Gremaud, Phys. Stat. sol. (a) **104**, 427 (1987).
102. A. O. Moreno-Gobbi, G. Paolini and F. R. Zypman, Comp. Mat. Sci. **11** (3), 145-149 (1998).
103. C. S. Deo, D. J. Srolovitz, W. Cai and V. V. Bulatov, Journal of the Mechanics and Physics of Solids **53** (6), 1223-1247 (2005).
104. C. S. Deo, D. J. Srolovitz, W. Cai and V. V. Bulatov, Phys. Rev. B **71** (1), 014106 (2005).
105. J. Goldstein, D. Newbury, D. Joy, C. Lyma, P. Echlin, E. Lifshin, L. Sawyer and J. Michael, *Scanning Electron Microscopy and X-Ray Microanalysis*, 3rd Ed. (Springer, 2003).
106. A. A. Volinskya, N. R. Moody and W. W. Gerbericha, Journal of Material research **19**, 2650-2657 (2004).
107. D.Tabor, *The hardness of Metals* (Claredon Press, Oxford, U.K., 1951), 174.
108. S.Sakai, H.Tanimoto and H.Mizubayashi, Acta Materials **47**, 211 (1999).
109. Y. Cao, Z. Zong and W. Soboyejo, Materials Research Society **875**, 561 (2005).
110. G. B. Gibbs, Phil. Mag. **20**, 867-872 (1969).
111. C. S. Hartley, Phil. Mag. **83**, 3783-3808 (2003).
112. L. Lu, T. Zhu, Y. Shen, M. Dao, K. Lu and S. Suresh, Acta Materialia **57** (17), 5165-5173 (2009).
113. F. Dalla Torre, P. Spätig, R. Schäublin and M. Victoria, Acta Materialia **53** (8), 2337-2349 (2005).
114. D.Yau and W.Yu, *Microtensile testing of free-standing and supported metallic thin films* (PhD thesis, Harvard university, 2003).
115. C.Duhamel, Y.Brechet and Y.Champion, International Journal of Plasticity **26**, 747-757 (2010).
116. S. Cheng, J. A. Spencer and W. W. Milligan, Acta Materialia **51** (15), 4505-4518 (2003).
117. S. E. R. Hiscocks and W. Hume-Rothery, Proceedings of the Royal Society of London. Series A, Mathematical and Physical Sciences **282** (1390), 318-330 (1964).
118. A.K.Sharma and N. Gupta, Progress in Electromagnetics Research Letters **31**, 147-157 (2012).

VITA

Name: Mr. Kittisun Mongkolsuttirat

Date of Birth: March 13, 1981

Place of Birth: Bangkok, Thailand

Parents: Panyawat Mongkolsuttirat and Vipada Mongkolsuttirat

Education:

M.S. Mechanical Engineering, Lehigh University, PA, USA, May 2009

Thesis: "Mechanical properties and resistivity of Au and Au-V₂O₅ thin films"

B.Sci. Industrial Engineering, Chulalongkorn University, Thailand, March 2003

Professional experience:

Production Planning Engineer at Production Department, Thai Plastic and

Chemicals Public Company Limited, Thailand (15Apr2003-1Jan2005)